LIGAND ARCHITECTURE EFFECTS UPON PRIMARY COPPER-DIOXYGEN ADDUCT CHEMISTRY

By

Jung Yoon Lee

A dissertation submitted to Johns Hopkins University in conformity with the requirements for the degree of Doctor of Philosophy

Baltimore, Maryland

July, 2015

© 2015 Jung Yoon Lee

All Rights Reserved

Abstract

The investigation into the chemical/physical properties of synthetic copper complexes provide fundamental insights into the understanding of the enzyme chemistry overviewed in this dissertation.

In **Chapter 1**, copper monooxygenases and oxidases involved in C–H/O–H bond oxidation are introduced, along with biological functions, coordination environment of their metal active sites and their proposed mechanisms. Recent investigations of various synthetic oxygen-derived copper intermediates, including their characteristics and reactivity, are described. Possible reaction mechanisms are also highlighted by comparison to aqueous O_2-reduction chemistry.

In **Chapter 2**, with the goal of understanding the mechanism of phenol oxidation by mononuclear cupric superoxo species, kinetic studies were performed with the reaction of a new copper(II) superoxo complex $[(\text{DMM-tmpa})\text{Cu}^{\text{II}}(\text{O}_2^{\bullet-})]^+$ and a series of *para*-substituted-2,6-di-*tert*-butylphenols (*p*-X-DTBP's) affording 2,6-di-*tert*-butyl-1,4-benzoquinones (DTBQ's). Significant deuterium kinetic isotope effects (KIE's) and a positive correlation of second-order-rate constants (k_2's) compared to rate constants for *p*-X-DTBP's plus cumylperoxyl radical reactions indicate a mechanism involves rate-limiting hydrogen atom transfer (HAT). Product analyses, ^{18}O-labeling experiments, and separate reactivity employing the 2,4,6-tri-*tert*-butylphenoxyl radical provide further mechanistic insights.

Chapter 3 reports the first example of sulfur-ligated mononuclear superoxo species which mimics the putative $\text{Cu}^{\text{II}}(\text{O}_2^{\bullet-})$ active species of the peptidylglycine-α-hydroxylating monooxygenase, PHM. This complex exhibits enhanced reactivity towards both O-H and

C-H substrates in comparison to close analogues $[(L)Cu^{II}(O_2^{\bullet-})]^+$, where L contains only nitrogen donor atoms. Cu-$S_{(thioether)}$ ligation with its weaker donor ability (relative to an N-donor) are demonstrated by comparisons to the chemistry of analogue compounds.

Chapter 4 provides the coordination chemistry and reactivity study of primary Cu^I/O_2 species featuring an intramolecular hydrogen bonding substituent, $(^{X}BA)Cu^{II}(O_2^{\bullet-})$ (**^{X}S**). The stability of **^{X}S** compounds are ascribed to internal H-bond, from the secondary coordination sphere, to the proximal superoxide 'O' atom. Direct evidence for hydrogen atom transfer from phenol substrates by **^{X}S** complexes was obtained, and enhanced reactivity of copper(II) superoxo complexes possessing electron-withdrawing groups (i.e., X) compared with other $Cu^{II}(O_2^{\bullet-})$ analogues was observed. This behavior is discussed and correlated to the H-bonding ability of the ^{X}BA ligands and the copper ion centered redox behavior for varying **^{X}S** complexes.

In **Chapter 5**, we describe an overview of the copper proteins with respect to their preference for tautomeric histidine binding sites (δN_{His} vs εN_{His}) and a unique histidine-chelated ligand environment. Newly designed copper-histidine complexes are introduced, which possess ligands mimicking the copper center of certain enzymes. Dioxygen-derived copper species are determined to be (*trans*-peroxo)Cu^{II}_2 and (bis-μ-oxo)Cu^{III}_2 complexes based on spectroscopic studies.

Advisor: Professor Kenneth D. Karlin

Chair, Department of Chemistry

Ira Remsen Chair in Chemistry

Thesis Committee:

Professor David P. Goldberg

Professor John P. Toscano

Acknowledgement

I am greatly indebted to Prof. Kenneth D. Karlin for his guidance and support. His mentorship nurtured my scientific enthusiasm and ultimately led this thesis to fruition. Furthermore, his guidance deepened my knowledge and broadened my research interest in the field of synthetic bioinorganic chemistry. I appreciate his dedication for my graduate education.

I am grateful to Profs. David P. Goldberg and John P. Toscano for being my thesis committee members. I would also like to thank Prof. Gerald J. Meyer for serving on my Graduate Board Organization (GBO) committee and his support.

I would like to extend a heartfelt gratitude to Profs. Wonwoo Nam, Joan S. Valentine, and Shunichi Fukuzumi who have helped and encouraged me to pursue a Ph. D. with Dr. Karlin by cultivating my scientific curiosity.

I would like to thank Drs. Ryan L. Peterson and Sunghee Kim who I have closely worked with throughout my training as well. They taught me the fundamentals of synthetic chemistry in laboratory and closely guided me throughout this thesis work. It would have been impossible to complete this thesis without scientific advice from all current and former Karlin group members.

Special thanks to Prof. Edward I. Solomon, Jake W. Ginbach, and Dr. Ryan E. Cowley for their effort to help my experiments. I also want to extend my special thanks to department of chemistry staffs, Dr. Maxime Siegler, Dr. Joel Tang, Dr. Cathy Moore, Dr. Phil Mortimer, Meghan Carter, Boris Steinberg, Jean Goodwin and Rosalie Elder.

I am grateful to my classmates and the Korean community for sharing joyful and precious moments of their lives in Baltimore. Lastly, I want to thank my father, Hosung

Lee, my mother, Hong Sook Kim, and my brother Seyoung Lee for their endless support throughout my life, and Benjamin Park for being a wonderful and understanding husband.

July 21, 2015

Table of Contents

Chapter 1: Copper Monooxygenases/Oxidases Mediated C–H/O–H Activation and Their Model Chemistry

1 Introduction……………………………………………..…………………………2

1.1 Lytic Polysaccharide Monooxygenases (LPMOs)…………………...………….4

1.2 Peptidylglycine-α-Hydroxylating Monooxygenase (PHM) and Dopamine-β-Monooxygenase (DβM)……………………………………………………………………6

1.3 Particulate Methane Monooxygenase (pMMO)……………………...……..…...8

1.4 Galactose Oxidase (GO)…………………………………………...…………...10

1.5 Copper Amine Oxidase (CAO)……………………………………...……....12

2 Synthetic Cu_2/O_2 Complexes…………………………………………...……….....15

3 Primary Cu^I/O_2 Adducts and Reactivity…………………………………..……17

3.1 Synthetic Copper(II) Superoxo Complexes…………………………...…….17

3.2 Copper(II) Hydroperoxo Model Studies……………………………..……...20

3.3 Cupric Oxyl Radical Species……………………………………………...……21

4 Aqueous O_2-Reduction, Cu^I/O_2 Oxidase or Monooxygenase Chemistries…....…22

5 Conclusion and Perspectives……………………………………………………..25

6 References…...………………………………………………………………..……28

Chapter 2: Mechanistic Insights into the Oxidation of Substituted Phenols via Hydrogen Atom Abstraction by a Cupric Superoxo Complex

1 Introduction……………………………………………………………………..…..….36

2 Experimental Section……………………………………………………….…......41

2.1 General...41

2.2 Ligand Synthesis……………………………………………..……………..42

2.3 Synthesis of Substrates………………..…………..………………………… 43

2.4 Redox Potentials of *para*-Substituted-2,6-di-*tert*-butylphenols (*p*-X-DTBP's)…..46

2.5 Synthesis of [(DMM-tmpa)Cu^{I}(CO)]$B(C_6F_5)_4$ (1)……………………………..46

2.6 Generation of [(DMM-tmpa)$Cu^{II}(O_2^{\bullet -})$]$B(C_6F_5)_4$ (2) and Reaction with *p*-X-DTBP Derivatives……………………………………………………………………...47

2.7 Quantification of 2,6-Di-*tert*-butyl-1,4-benzoquinone (DTBQ) with Gas Chromatography-Mass Spectrometry (GC-MS)………………………………………48

2.8 ^{18}O-Labeling Experiments…………………………………………...…………49

2.9 OR Product Analysis using ^{2}H-NMR……………………………………………..50

2.10 Oxidation of Phenols by the Cumylperoxyl Radical (4)…………………...……50

2.11 Hydrogen Peroxide Quantification…………………..……………………………51

2.12 Attempt to Detect Formaldehyde…………………………..…………………51

2.13 Attempt to Detect Isobutylene……………………….………………………..…52

2.14 Resonance Raman Spectroscopy……………………………………..……..…52

3 Results and Discussion……………………………………………………..…..…53

3.1 Spectroscopic Characterization of [(DMM-tmpa)$Cu^{II}(O_2^{\bullet -})$]$^{+}$ (2)………………..…53

3.2 Reactivity of [(DMM-tmpa)$Cu^{II}(O_2^{\bullet -})$]$^{+}$ (2) towards *para*-Substituted-2,6-di-*tert*-butylphenols……………………………………………………………………………56

3.3 Kinetic and Thermodynamic Studies……………………………………...……57

3.3.1 Demonstration of hydrogen atom transfer chemistry……………………………57

3.3.2 Comparison of KIEs to other metal-superoxo mediated oxidations……………59

3.3.3 Cumylperoxyl radical (4) plus phenol substrate HAT reactions for comparison………………………………………………………………………61

3.3.4 Rate constants (k_2) correlation to phenol redox potentials?...............................62

3.3.5 Mechanistic considerations…………………………………………………64

3.3.6 Activation parameters and comparisons………………………………………66

3.3.7 KIE temperature dependence?...67

3.3.8 Summary of the kinetic-thermodynamic studies………………………………67

3.4 Product Analyses and Further Mechanistic Insights…………………………….68

3.4.1 Phenol oxidations lead to benzoquinone products……………………………68

3.4.2 Reaction of [(DMM-tmpa)Cu^{II}($O_2^{\bullet-}$)]$^+$ (2) with *p*-alkoxy-2,6-di-*tert*-butylphenols (*p*-OR-DTBP's)…………………………………………………………………69

3.4.3 Proposed pathway for [Cu^{II}($O_2^{\bullet-}$)]$^+$ (2) reaction with *p*-OR-DTBP substrates (Scheme 4)……………………………………………………………………………70

3.4.4 Reaction of [(DMM-tmpa)Cu^{II}($O_2^{\bullet-}$)]$^+$ (2) with *p*-alkyl-2,6-di-*tert*-butylphenols (*p*-R-DTBP's)……………………………………………………………………....72

3.4.5 [Cu^{II}($O_2^{\bullet-}$)]$^+$ (2) coupling with 2,4,6-tri-*tert*-butylphenoxyl radical……………73

3.4.6 A minor reaction pathway contributing to *p*-R-DTBP oxidation………………74

3.4.7 Precedent and comparison with cobalt and nickel superoxide phenol oxidations……………………………………………………………………………..75

3.4.8 A prior computational study of [Cu^{II}($O_2^{\bullet-}$)]+ reaction with 2,6-di-*tert*-butylphenol (*p*-H-DTBP) leading to a 2,6-di-*tert*-butyl-1,4-benzoquinone (DTBQ)……………....76

4 Conclusion……………………………………………………………...……..……....77

5 References…………………………………………………………………....…….79

6 Supporting Information…………………………………………………….….....85

6.1 Proposed Mechanisms of Copper Oxidases………………………………...…..85

6.2 Generation of SO_2…………………………………………………..…………..86

6.3 EPR Spectra of Cu Complexes……………………………………...….….…87

6.4 Kinetic Study of $[(NMe_2\text{-tmpa})Cu^{II}(O_2^{\bullet-})]^+$……………………………..……….88

6.5 Kinetic Isotope Effect of Cumylperoxyl Radical and Phenol Derivatives………..89

6.6 Derivation of the Equation for the plot of $(k_BT/e)\ \ln k_2$ vs E_{ox}……………….………..90

6.7 Temperature Effect of Kinetic Isotope Effect Values…………………...………91

6.8 EPR Spectra of Reaction Solution………………………...……………………92

6.9 Synthesis of $[(DMM\text{-tmpa})Cu^{II}(CH_3CN)](ClO_4)_2 \bullet 0.5\ (O(CH_2CH_3)_2)$…………...93

6.10 X-ray crystallography………...……………...…………………….…………..94

6.11 NMR Experiment…………………………..………………………96

6.12 Pseudo-First-Order Plots……………………………………………...…….…97

6.13 Yields of Products……………………………………..………………….….108

6.14 Titration of 2 with TEMPO-H……………………………………….....…..108

6.15 Protonation of $[(DMM\text{-tmpa})Cu^{II}(OOH)]^+$ (3)……………………………….…...109

6.16 Quantification of H_2O_2 Formed…………………………………………..…109

6.17 Comparison of *d-d* Bands for Possible Cu(II) Products………………………..110

6.18 MALDI-TOF Experiment…………………………………………...….…111

6.19 Reactivity Study toward Catechol Derivatives…………………………………112

6.19.1 Reaction with 3,5-di-*tert*-butylcatechol……………………………......112

6.19.2 Kinetic studies with *p*-substituted-catechol series………………………......113

Chapter 3: A $N_3S_{(thioether)}$-Ligated Cu^{II}-Superoxo with Enhanced Reactivity

1 Introduction………………………………………………………………..…….117

2 Physical Properties of Cu-Complexes……………………………………………..120

3 O_2 Chemistry of Cu(I)-Complexes……………………………………..…..…...121

4 Reactivity of $[(^{DMA}N_3S)Cu^{II}(O_2^{\bullet-})]^+$ (2^S)……………………………………………123

5 Cu-S Interaction……………………………………………………...……….125

6 Conclusion……………………………………………………...……….…...126

7 References…………………………………………………………………….…...127

8 Supporting Information……………………………………………..….…....130

8.1 Materials and Methods……………………………………..……………130

8.1.1 General……….…………………………………...………………….....130

8.1.2 Instrumentation……………………………………...…………….….130

8.2 Synthesis of Ligands…………………………………………………...……...132

8.3 Synthesis of Copper (I)/(II) Complexes…………………….……...…....134

8.4 X-ray Crystallography………………………………...………..…….…….137

8.5 Cyclic Voltammetry (CV) Data………………………...……………………......141

8.6 Oxygenation of a $[(^{DMA}N_3S)Cu^{I}]^+$ (1) in MeTHF at -135 °C……………….……143

8.7 Resonance Raman (rR) Data……………......………………..…………….…144

8.8 Oxygenation of a $[(^{DMA}N_3S)Cu^{I}]^+$ (1) in 20 % Polar Solvents/MeTHF at -135 °C……………………………………………………………………………...145

8.9 Reactivity Study and Product Analyses……………..………………………..…..146

8.9.1 Detection of the product from $\mathbf{2^S}$ + 2,6-di-*tert*-butyl-4-methoxyphenol (*p*-OMe-DTBP) by GC-MS…………………………...……………..….…………147

8.9.2 Identification of the product from $\mathbf{2^S}$ + N-methyl-9,10-dihydroacridine ($AcrH_2$) by ^{1}H-NMR……………………………………………………………………….147

8.10 Comparison of Cu/O_2 Adducts of Different Ligands…………………….…..…148

8.11 DOSY NMR Experiments…………………………...……………………150

8.12 References…………………………...………………………….………..151

Chapter 4: Primary Cu^I/O_2 Adduct with Tunable H-bond from Secondary Coordination

1 Introduction…………………………………………………………...…….153

2 Physical Properties of Cu-Complexes………………………………...……..157

2.1 Geometry and Crystal Structure…………………………………..………....157

2.2 Redox Potentials of $[(^{X}BA)Cu^{II}(CH_3COCH_3)](ClO_4)_2$ ($^{X}2$) Complexes…..……158

3 O_2 Chemistry of Cu(I)-Complexes………………………………..………..……159

4 Reactivity of $[(^{X}BA)Cu^{II}(O_2^{\bullet-})]^+$ (^{X}S) Complexes……………………….…..…162

4.1 The Oxidation of Phenol Derivatives…………………………………..……..163

4.2 The Reaction with N-methyl-9,10-dihydroacridine ($AcrH_2$)……………….…..166

5 Conclusion………………...……………………………………………..……..167

6 References……………………………………………………...…..…………...168

7 Supporting Information…………………………………………………..…...……170

7.1 Materials and Methods…………………………………………………….……..170

7.1.1 General……………………………………………………...…………..170

7.1.2 Instrumentation…………………………………………...……………171

7.2 Synthesis of Ligands……………………………………………...…...172

7.3 Synthesis of Copper (I)/(II) Complexes………………………………………..172

7.4 X-ray Crystallography……………………………...……………………176

7.5 Cyclic Voltammetry (CV) Data…………………………………..……..…184

7.6 Oxygenation of a [(^{DMA}N$_3$S)Cu^I]$^+$ (1) in MeTHF at -50 °C…………………....185

7.7 Resonance Raman (rR) Data…………………...……………………….186

7.8 Reactivity Study……………………………...…………………….…..188

Chapter 5: Dioxygen-Derived Copper Species Ligated by His-Braced Peptide Ligands

1 Introduction………………………………………………………...…….192

2 Cu-dipeptide Complex Chemistry……………………………….....………196

2.1 Dipeptide Ligand Design…………………………………...……..……..196

2.2 Oxygen-Derived Copper Species in Different Solvent Systems………………….197

2.3 Reactivity of the [{(NδHεH)Cu^{II}}$_2$(μ-1,2-O$_2^{2-}$)]$^{2+}$ Complex………..…………200

2.4 Protonation of *trans*-Peroxo Dicopper(II) Complex……………..…………...…200

2.5 Generation of Mononuclear Cupric Hydroperoxide Species………………......…201

3 Cu^I/O$_2$ Chemistry of a (^{Trt}His)Cu(I) Complex……………………..…………..203

4 Conclusion and Future Directions…………………...………………………205

5 References………………………...…………………………………………....205

6 Supporting Information……………………………...………………….……209

6.1 Materials and Methods……………………………………..…………………..…...209

6.1.1 General………………………………...…………………………………….…..209

6.1.2 Instrumentation………………………...………………………………..….210

6.2 Ligand Synthesis………………..……………………...…………………...211

6.2.1 NεHis (**Scheme S1**)[2]……………………………………………………...…..….211

6.2.2 Ligand NδHεH (**Scheme S2**)…………………………………..……..…….212

6.2.3 The ligand triphenylmethylhistamine (**^{Trt}His**) synthesized as in the literature.[3]……………………...………………………………………………213

6.3 Synthesis of Copper(I) Complexes…………………………...……………….214

6.4 Generation of Cpd A and Cpd B……………………………………...……......215

6.5 EPR Experiments……………………………………………………………...216

6.6 References……………………………………………………………………….217

List of Figures and Tables

Chapter 1: Copper Monooxygenases/Oxidases Mediated C–H/O–H Activation and Their Model Chemistry

		Page Number
Table 1.	Copper enzymes involved in C–H/O–H bond oxidation	**3**
Scheme 1.	Polysaccharides degradation process	**4**
Figure 1.	Copper active site of one of the lytic polysaccharide monooxygenase in the cellulose-active fungal AA9 group. A putative superoxide moiety is observed at 3.0 Å from the Cu center (PDB: 4EIR)	**5**
Figure 2.	Proposed mechanisms of LPMOs. The C-H bond of substrate is oxidatively cleaved by either cupric superoxo (I) or copper-oxyl (II) species.	**5**
Scheme 2.	Biological functions of PHM and DβM	**6**
Figure 3.	The oxidized form of PHM active site exhibiting the non-coupled two copper ions; dioxygen-bound Cu_M site and Cu_H site located apart.	**7**
Figure 4.	A possible substrate hydroxylation mechanism of PHM proposed by Klinman.	**8**
Scheme 3.	pMMO-catalyzed oxidation of methane to methanol in the presence of NADH.	**8**
Figure 5.	Two copper centers found in pMMOs; dicopper and monocopper active sites (PDB: 1YEW)	**9**
Scheme 4.	The two-electron oxidation of D-galactose to D-galactohexodialdose along with reduction of dioxygen to hydrogen peroxide.	**10**
Figure 6.	X-ray structure of an inactive form at mononuclear copper active site in GO (PDB: 1GOG)	**11**
Figure 7.	Proposed catalytic cycle of GO by active form of copper(II)-tyrosyl radical species.	**12**
Scheme 5.	CAO-catalayzed oxidative deamination of 1° amine to aldehyde via reduction of dioxygen.	**12**
Figure 8.	The reduced state of the mononuclear copper active site in CAO (PDB: 1D6U)	**13**
Scheme 6.	TPQ generation from tyrosine moiety.	**13**
Figure 9.	Two proposed pathways for cofactor reoxidation occurring in copper amine oxidase.	**14**
Figure 10.	O_2-derived copper species proposed as reactive intermediates in copper-containing enzymes.	**15**

Figure 11. A high-valent dicopper(III) species **O** ligated by the primary amine, 1,3-propylenediamine, is capable of H-atom abstraction from the C−H bond in 9,10-dihydromethylacridine. **17**

Figure 12. Spectroscopically characterized Cu^{II}(O$_2^{\bullet-}$) species: (a) Itoh's ^{E}**S** complex effecting intramolecular benzylic oxygenation (net hydroxylation), (b) Hydrogen-bond stabilized ^{E}**S** complex effecting exogenous (weak) C-H bond HAT chemistry, (c) Oxidative cleavage of O-H bond by ^{E}**S** possessing electron-donating groups on ligand donors and (d) Thioether-ligated ^{E}**S** complex with enhanced reactivity, here, toward 9,10-dihydromethylacridine. Also, see text. **19**

Scheme 7. The oxidative N-dealkylation by synthetic Cu(II) hydroperoxo complex. **20**

Figure 13. The full mechanism of amine oxidative N-dealkylation via cupric hydroperoxide Cu-(OOH) homolytic cleavage followed by site-specific Fenton chemistry. **21**

Scheme 8. C-H Activation by copper-oxyl intermediate generated from hemolytic O-O cleavage of Cu(II)-alkylperoxo species **21**

Figure 14. (a) Aqueous four-electron four-proton O$_2$-reduction to water; reduction potentials shown are for pH = 7. (b) Copper oxidase reactivity and intermediates relevant for single copper site chemistry. (c),(d),(e) Single-copper site stepwise monooxygenase chemistry. As must be the case, overall four-electron reduction chemistry occurs, where two derive from a substrate R–H bond; the other two electrons come from donors such as ascorbic acid. All O$_2$-derived species, superoxo (^{E}**S**), (hydro)peroxo (**Hp**) or cupryl (**Cp**), must be generated (in some form). The variations in chemistry, (c) vs (d) vs (e), are that for each, initial HAT chemistry with the substrate (R–H → R•) is effected by a different copper-oxygen intermediate, (^{E}**S**), (**Hp**) or (**Cp**). Still, other pathways or mechanisms are possible. Also, see text. **23**

Chapter 2: Mechanistic Insights into the Oxidation of Substituted Phenols via Hydrogen Atom Abstraction by a Cupric Superoxo Complex

Page Number

Chart 1. Oxygen-derived copper species. **37**

Figure 1. Reduction of molecular oxygen in galactose oxidase (GO). See Supporting Information (**Figure S1a**) for fuller details. **38**

Chart 2. Ligands and phenol-derivative substrate. **39**

Scheme 1. The generation and reaction of $[(\text{DMM-tmpa})\text{Cu}^{\text{II}}(\text{O}_2^{\bullet-})]^+$ (**2**). **40**

Figure 2. Structural representation of $[(\text{TMG}_3\text{tren})\text{Cu}^{\text{II}}(\text{O}_2^{\bullet-})]^+$. **53**

Figure 3. (a) Absorption spectra of **1** (0.27 mM) and **2** after addition of $\text{O}_{2\,(g)}$ in acetone (10 % MeTHF) at 183 K. (b) rR spectra of **2** (0.7 mM) measured in MeTHF (λ_{ex} = 407 nm). Red, $^{16}\text{O}_2$; blue, $^{18}\text{O}_2$. **55**

Table 1. Phenol BDE's, Redox Potentials (E_{ox}), Second-Order Rate Constants (183 K) for *p*-X-DTBP Phenol Oxidations by **2** and **4** and Reaction Yields (See **Figure S10** for kinetics details) **58**

Figure 4. (a) UV-vis spectral changes observed by addition of *p*-Et-DTBP (20 mM) to **2** (0.27 mM) in acetone (10 % MeTHF) at 183 K. $k_{\text{obs}} = 5.73 \times 10^{-4}$ s^{-1}. (b and c) Plots of k_{obs}'s against the concentrations of substrates (circles) and deuterated ^{2}H-O substrates (squares) for *p*-OMe-DTBP (b) and *p*-Me-DTBP (c) to determine second-order-rate constants and KIE's. **59-60**

Scheme 2. **61**

Figure 5. Correlation between log k_2 of **2** and log k_2^{C} of **4** with *p*-X-DTBP's, respectively. Slope is 4.85. **62**

Figure 6. Plots of $(k_{\text{B}}T/e)\ \ln k_2$ for the reactions of *p*-X-DTBP's with **2** (squares) and **4** (circles) against the one-electron oxidation potentials (E_{ox}) of substrates. The slopes are –0.29 and -0.05, respectively. **63**

Scheme 3. Three possible reaction pathways for hydrogen-atom transfer from *p*-X-DTBP to $[\text{Cu}^{\text{II}}(\text{O}_2^{\bullet-})]^+$. **64**

Table 2. Kinetic Parameters in Various Metal Complexes plus Phenol Oxidation Reactions. **66**

Table 3. Temperature Dependence on the KIEs of the HAT Reactions from *p*-OMe-DTBP to $[(\text{DMM-tmpa})\text{Cu}^{\text{II}}(\text{O}_2^{\bullet-})]^+$ (**2**) **67**

Scheme 4. Proposed Pathways for $[\text{Cu}^{\text{II}}(\text{O}_2^{\bullet-})]^+$ Reactivity with *p*-OR-DTBP or *p*-R-DTBP Substrates Leading to Observed Products.[a] **71**

Scheme 5. Oxygen-incorporating reaction releasing formaldehyde and isobutylene. **72**

Scheme 6. The reaction of $[\text{Cu}^{\text{II}}(\text{O}_2^{\bullet-})]^+$ (**2**) and $^t\text{Bu}_3\text{ArO}\bullet$. **74**

Scheme 7. Phenol oxidation by cobalt(III) superoxo complex. **75**

Figure 7. Chemdraw and X-ray crystal structure of cobalt peroxy species Co^{III}-OO-(ArO') **76**

Scheme 8. The proposed catalytic cycle of phenol oxidation by $[\text{Cu}^{\text{II}}(\text{O}_2^{\bullet-})]^+$ based on computational chemistry. 77

Figure S1. Proposed pathways for the primary alcohol oxidation/dioxygen reduction by galactose oxidase (GO) (a) and for copper amine oxidase (CAO) catalytic mechanism illustrating the two pathways for cofactor reoxidation (b).[a] **85**

Figure S2. An apparatus setup for sulfur dioxide (SO_2, gas) generation. **86**

Figure S3. Low-temperature EPR spectra of [(DMM-tmpa)Cu^I(CO)]$B(C_6F_5)_4$ (**1**) (**black**), [(DMM-tmpa)$Cu^{II}(O_2^{\bullet-})$]$B(C_6F_5)_4$ (**2**) (**red**), and **2** + one equiv *para*-methoxy-2,6-di-*tert*-butylphenol (**blue**) (2 mM; 3X-band, ν = 9.426 GHz; acetone at 23 K): $g_{\|} = 1.96$, $A_{\|} = 76$ G, $g\perp = 2.20$, $A\perp = 97$ G. The results indicate **1** and **2** are EPR "silent", as expected, exhibiting only impurity (~ 5%) quantities of a typical copper(II) paramagnetic compound, i.e., that copper(II) complex forming by the reaction of **2** with one equiv phenol substrate. Also, see **Figure S7**. **87**

Figure S4. The table of pseudo-first-order rate constants (k_{obs}'s) from the reactions of *p*-OMe-DTBP plus [(NMe_2-tmpa)$Cu^{II}(O_2^{\bullet-})$]$^+$ and the plot of k_{obs}'s against the concentrations of *p*-OMe-DTBP to obtain second-order-rate constant ($k_2 = 4.6$ $M^{-1}s^{-1}$). **88**

Figure S5. Plots of k_{obs}'s against the concentrations of *p*-OMe-DTBP(**black circles**) and deuterated ^{2}H-O *p*-OMe-DTBP (**red circles**) to determine second-order-rate constants and KIE (= 9.0). **89**

Figure S6. Table of pseudo-first-order rate constants (k_{obs}'s), second-order rate constants (k_2's) and kinetic isotope effects (KIEs) for the reactions of [(DMM-tmpa)$Cu^{II}(O_2^{\bullet-})$]$^+$ (**2**) and *para*-methoxy-2,6-di-*tert*-butylphenol (*p*-OMe-DTBP; H-O *vs* ^{2}H-O) in acetone over the temperature range of –100 ºC ~ –85 ºC (upper panel). Eyring plots of k_2's against 1/T for the oxidation of *p*-OMe-DTBP (H-O for **blue** and ^{2}H-O for **red**) to determine the reaction activation parameters (lower panel). **91**

Figure S7. EPR spectra of [(DMM-tmpa)$Cu^{II}(O_2^{\bullet-})$]$B(C_6F_5)_4$ (**2**) + one equiv *para*-methoxy-2,6-di-*tert*-butylphenol (*p*-OMe-DTBP) at low temperature (**blue**) and solution of **2** + one equiv *p*-OMe-DTBP which was warmed up to room temperature and then frozen again (**red**) (2 mM; 3X-band, ν = 9.426 GHz; acetone at 23 K). For both samples, **blue** and **red**, $g_{\|} = 1.96$, $A_{\|} = 76$ G, $g\perp = 2.20$, $A\perp = 97$ G. Thus, the **red** spectrum is representative of [(DMM-tmpa)Cu^{II}-OH(H)]$^+$. **92**

Figure S8. Left: Dicationic portion of [(DMM-tmpa)$Cu^{II}(CH_3CN)$]$(ClO_4)_2$. Right: Selected bond distances and angles are given below; τ = 0.9495 where a τ value = 0 would represent a perfect square-pyramid and a value of 1.0 would equal a perfect trigonal-bipyramid. See Experimental details concerning the X-ray crystallographic analysis, just below. **94**

Figure S9. Low temperature ^{2}H-NMR spectra collected at –90 ºC for the reaction solution of [(DMM-tmpa)Cu^{II}(O$_2^{\bullet-}$)]$^+$ (**2**) mixed with five equiv of (a) *p*-OCD$_3$-DTBP and (b) *p*-OCD$_2$CD$_3$-DTBP in acetone. (a) The blue spectrum is the reaction mixture at –90 ºC. The red spectrum is the reaction mixture after it is allowed to be warmed to room temperature (RT). {Note: The deuterated methanol product (CD$_3$OH) is only observed in the red spectrum, which forms after the reaction mixture is allowed to warm to RT.} (b) The blue spectrum is the reaction mixture at –90 ºC. Displayed in the red spectrum is the NMR spectrum obtained after the reaction mixture is allowed to warm to RT. The black spectrum is the room temperature reaction mixture (blue) which was spiked with d_6-ethanol. The NMR spectral ^{2}H resonances corresponding to *p*-OCD$_2$CD$_3$-DTBP and CD$_3$CD$_2$OH are indicated with arrows, respectively. *denotes solvent, $^{\#}$denotes C$_6$H$_6$ used as an internal reference. **96**

Figure S10. Pseudo-first-order plots for the reactions of [(DMM-tmpa)Cu^{II}(O$_2^{\bullet-}$)]$^+$ (**2**) and *p*-X-DTBP's to determine pseudo-first-order rate constants (k_{obs}'s). (see **Table 1** for second-order-rate constants) **97-107**

Table S1. Product yields **108**

Figure S11. UV-vis spectral changes of the titration of [(DMM-tmpa)Cu^{II}(O$_2^{\bullet-}$)]B(C$_6$F$_5$)$_4$ (**2**) 0.4 mM acetone solution with 0.2 ~ 1 equiv. TEMPO-H at 183 K affording new species presumed to be [(DMM-tmpa)Cu^{II}(OOH)] (**3**) ($\square_{max}$ = 374 nm, ε = 2000 M^{-1} cm^{-1}). **108**

Figure S12. UV-vis spectral changes of 0.4 mM [(DMM-tmpa)Cu^{II}(OOH)]B(C$_6$F$_5$)$_4$ (**3**) acetone solution (which was generated from **2** + 0.2 ~ 1 equiv. TEMPO-H; **Figure S12**) with H[B(C$_6$F$_5$)$_4$] acid titration. **109**

Figure S13. UV-vis spectra for *d-d* band comparison of possible Cu(II) products in acetone; [(DMM-tmpa)Cu^{II}(O$_2^{\bullet-}$)]B(C$_6$F$_5$)$_4$ (**2**) + phenol at low temperature, warmed up solution of **2** + phenol, [(DMM-tmpa)Cu^{II}(OOH)]$^+$ (**3**), [(DMM-tmpa)Cu^{II}(CH$_3$CN)](ClO$_4$)$_2$, [(DMM-tmpa)Cu^{II}(CH$_3$CN)](ClO$_4$)$_2$ + ^{t}Bu$_4$OH, and **2** + ^{t}Bu$_3$ArO·. **110**

Figure S14. MALDI-TOF spectra of possible Cu(II) products; warmed up solution of [(DMM-tmpa)Cu^{II}(O$_2^{\bullet-}$)]$^+$ + phenol, [(DMM-tmpa)Cu^{II}(CH$_3$CN)]$^{2+}$, [(DMM-tmpa)Cu^{II}(CH$_3$CN)]$^{2+}$ + ^{t}Bu$_4$OH, and [(DMM-tmpa)Cu^{II}(CH$_3$CN)]$^{2+}$ + H$_2$O. **111**

Figure S15. Left: Scheme for the oxidation of 3,5-di-*tert*-butylcatechol to 3,5-di-*tert*-butyl-1,2-benzoquinone by [(DMM-tmpa)Cu^{II}(O$_2^{\bullet-}$)]$^+$. Right: Second-order-rate constants and fitting for the reaction of [(DMM-tmpa)Cu$_{II}$(O$_{2}$•-)]$_{+}$ (**2**) and 3,5-di-*tert*-butylcatechol. **112**

Figure S16. (a) UV-vis spectra of the reaction of 0.26 mM [(DMM-tmpa)Cu^{II}(O$_2^{\bullet-}$)]$^+$ (**2**) with 10 equiv of 4-methylcatechol in acetone at –90 °C. Inset: Time traces at 409 and 516 nm. (b) Pseudo-first-order fitting of the reaction. **113**

Table S2. Pseudo-first-order values of the reaction of $[(\text{DMM-tmpa})\text{Cu}^{II}(\text{O}_2^{\bullet-})]^+$ (**2**) with 4-substituted-catechol derivatives. **114**

Figure S17. Second-order-rate constants and fitting for the reaction of $[(\text{DMM-tmpa})\text{Cu}^{II}(\text{O}_2^{\bullet-})]^+$ (**2**) and (a) 4-methoxycatechol, (b) 4-methylcatechol, (c) catechol, and (d) 4-chlorocatechol. **115**

Figure S18. Hammett plots of the catechol reactions against (a) σ_P and (b) σ_P^+. **115**

Chapter 3: A $N_3S_{(thioether)}$-Ligated Cu^{II}-Superoxo with Enhanced Reactivity

Page Number

Scheme 1. (a) Dioxygen-bound Cu_M site of PHM and (b) a new mononuclear cupric superoxo complex with thioether ligation. **118**

Scheme 2. Dicopper-oxygen species possessing sulfur-containing ligands. **119**

Figure 1. Displacement ellipsoid plots of the cations; (a) $[(^{DMA}\text{N}_3\text{S})\text{Cu}^I]^+$ (**1**) and (b) $[(^{DMA}\text{N}_3\text{S})\text{Cu}^{II}(\text{H}_2\text{O})(\text{ClO}_4)]^+$ (**3**). Hydrogen atoms were removed for clarity. **120**

Figure 2. Low-temperature UV-vis absorption spectra of the reaction of **1** with O_2 at –135 ºC in MeTHF (0.2 mM). The superoxo product $\mathbf{2^S}$ is observed immediately upon O_2 addition (red) and converted to the peroxo $\mathbf{2^P}$ (t = 50 s, blue). **121**

Figure 3. (a) Low-temperature (–135 °C) UV-vis absorption spectrum of $\mathbf{2^S}$ (containing ~11% $\mathbf{2^P}$, $\lambda_{max} = 526$ nm, $\varepsilon = 6500$)[12] as recorded ~40 s after bubbling O_2 into a MeTHF:TFE (4:1) solution of 1 (0.098 mM), and (b) rR spectra of frozen $\mathbf{2^S}$ (0.62 mM, $\lambda_{ex} = 413$ nm, 77 K) in MeTHF:TFE (4:1).[7] **122**

Table 1. Comparison of $\text{LCu}^{II}/\text{LCu}^I$ Redox Potentials and Reactivity of Derived $[(\text{L})\text{Cu}^{II}(\text{O}_2^{\bullet-})]^+$ Complexes. **124**

Scheme 3. Oxygenated products of ligand-Cu^I complexes. **126**

Sheme S1. Ligand synthesis scheme **134**

Figure S1. EPR spectrum of $[(^{DMA}\text{N}_3\text{S})\text{Cu}^{II}(\text{OClO}_3)(\text{H}_2\text{O})](\text{ClO}_4)$ (**3**) (2 mM). **136**

Figure S2. EPR spectrum of $[(^{DMA}\text{tmpa})\text{Cu}^{II}(\text{OClO}_3)(\text{H}_2\text{O})](\text{ClO}_4)$ (2 mM). **137**

Figuer S3. Displacement ellipsoid plot (50% probability level) of $[(^{DMA}N_3S)Cu^{I}]B(C_6F_5)_4$ (**1**) at 110(2) K. The H atoms are omitted for the sake of clarity. The structure is ordered. $[(^{DMA}N_3S)Cu^{I}]B(C_6F_5)_4$ (**1**)**:** Fw = 1192.24, irregular colorless lath, 0.54 × 0.18 × 0.08 mm^3, triclinic, *P*-1 (no. 2), a = 12.4367(3), b = 15.1159(3), c = 15.4174(4) Å, α = 69.996(2), β = 66.443(2), γ = 71.641(2)°, V = 2442.48(11) Å^3, Z = 2, D_x = 1.621 g cm^{-3}, μ = 2.115 mm^{-1}, T_{min}-T_{max}: 0.57–0.86. 32542 Reflections were measured up to a resolution of $(\sin \theta/\lambda)_{max}$ = 0.62 Å^{-1}. 9586 Reflections were unique (R_{int} = 0.0232), of which 8727 were observed [$I > 2\sigma(I)$]. 708 Parameters were refined. $R1/wR2$ [$I > 2\sigma(I)$]: 0.0307/0.0785. $R1/wR2$ [all refl.]: 0.0342/0.0811. S = 1.024. Residual electron density found between −0.43 and 0.36 e Å^{-3}. **138**

Figure S4. Displacement ellipsoid plot (50% probability level) of $[(^{DMA}N_3S)Cu^{II}(H_2O)(OClO_3)](ClO_4)$ (**3**). The H atoms are omitted for the sake of clarity. The structure is mostly ordered. Both counterions are found to be disordered over two orientations. The occupancy factors of the major components of the disorder refine to 0.727(7) and 0.9465(18). $[(^{DMA}N_3S)Cu^{II}(H_2O)(OClO_3)](ClO_4)$ (3)**:** Fw = 730.10, blue lath, 0.35 × 0.15 × 0.10 mm^3, monoclinic, $P2_1/c$ (no. 14), a = 15.0863(2), b = 11.06407(18), c = 19.2816(3) Å, β = 99.6221(14)°, V = 3173.13(8) Å^3, Z = 4, D_x = 1.528 g cm^{-3}, μ = 3.641 mm^{-1}, abs. corr. range: 0.65−1.00. 25665 Reflections were measured up to a resolution of $(\sin \theta/\lambda)_{max}$ = 0.62 Å^{-1}. 6227 Reflections were unique (R_{int} = 0.0302), of which 5302 were observed [$I > 2\sigma(I)$]. 496 Parameters were refined using 287 restraints. $R1/wR2$ [$I > 2\sigma(I)$]: 0.0355/0.0921. $R1/wR2$ [all refl.]: 0.0435/0.0990. S = 1.033. Residual electron density found between −0.50 and 0.81 e Å^{-3}. **139**

Figure S5. Displacement ellipsoid plot (50% probability level) of $[(^{DMA}tmpa)Cu^{II}(OClO_3)(H_2O)](ClO_4)$. The H atoms are omitted for the sake of clarity. The structure is mostly ordered. One of the two crystallographically independent perchlorate counterions is found to be disordered over two orientations, and the occupancy factor of the major component of the disorder refines to 0.936(9). The absolute configuration was established by anomalous-dispersion effects in diffraction measurements on the crystal. The Flack parameter refines to -0.013(8). $[(^{DMA}tmpa)Cu^{II}(OClO_3)(H_2O)](ClO_4)$: Fw = 700.03, green rod, 0.42 × 0.14 × 0.11 mm^3, hexagonal, $P6_5$ (no. 170), a = 15.05046(19), c = 22.7280(3) Å, V = 4458.52(13) Å^3, Z = 6, D_x = 1.564 g cm^{-3}, μ = 3.240 mm^{-1}, T_{min}-T_{max}: 0.486–0.752. 19557 Reflections were measured up to a resolution of $(\sin \theta/\lambda)_{max}$ = 0.62 Å^{-1}. 4703 Reflections were unique (R_{int} = 0.0323), of which 4565 were observed [$I > 2\sigma(I)$]. 430 Parameters were refined using 149 restraints. $R1/wR2$ [$I > 2\sigma(I)$]: 0.0248/0.0615. $R1/wR2$ [all refl.]: 0.0259/0.0623. S = 1.033. Residual electron density found between −0.23 and 0.21 e Å^{-3}. **140**

Figure S6. Cyclic voltammograms of ligand-Cu^{II} complexes in CH_3CN (mV *vs.* $[Fe(Cp)_2]^{+/0}$). Cu^{II} complexes (~ 1 mM) were employed for cyclic voltammetric measurements. CV measurements were undertaken in freshly distilled acetonitrile using a BAS 100B electrochemical analyzer with a glassy carbon working electrode and a platinum wire auxiliary electrode. Potentials were recorded versus a $Ag/AgNO_3$ electrode. Scans were run at 50 mV/s under Ar atmosphere using ca. 0.1 M $[Bu_4N][PF_6]$ as the supporting electrolyte. **141-142**

Figure S7. EPR spectra of $[(^{DMA}N_3S)Cu^I]B(C_6F_5)_4$ (**1**) (**black**), $[(^{DMA}N_3S)Cu^{II}(O_2^{\bullet-})]^+$ ($\mathbf{2^S}$) (**red**), and warmed up solution of $\mathbf{2^S}$ (**blue**) ($g_{\parallel} = 2.241$, $A_{\parallel} = 168$ G, $g_{\square} = 2.039$) taken with an X-band spectrometer ($\nu = 9.410$ GHz) in acetone at 70 K. Copper complex concentration: 0.1 mM. The spectra of **1** and $\mathbf{2^S}$ contain small amount of impurity of a typical copper(II) paramagnetic compound. The $[(L)Cu^{II}(O_2^{\bullet-})]^+$ complexes with N_4 tripodal tetradentate ligands have been shown to have S=1 triplet ground states, which usually do not exhibit EPR signals in typical X-band instrument conditions. $\mathbf{2^S}$ is EPR silent also assigned as an S = 1 species. On warming $\mathbf{2^S}$ to RT, a 'normal' Cu^{II} complex is generated, exhibiting a typical EPR signal at intensities expected. **143**

Figure S8. Resonance Raman spectra of $[\{(^{DMA}N_3S)Cu^{II}\}_2(\mu\text{-}1,2\text{-}O_2^{2-})]$ ($\mathbf{2^P}$) in MeTHF:acetone (4:1) with 720 nm excitation at 77 K. A control sample of $[(^{DMA}N_3S)Cu^I]B(C_6F_5)_4$ (**1**) in the same solvent mixture ("Cu(I)", black spectrum) is shown for comparison. The ^{16}O isotopologue of $\mathbf{2^P}$ shows two features at 544 and 561 cm^{-1} that are interpreted as a Fermi resonance of the ν(Cu–O) mode centered at the intensity-weighted average of 547 cm^{-1}. **144**

Figure S9. Comparison of resonance Raman spectra of $\mathbf{2^S}$ (413.1 nm) prepared in three solvent combinations (blue: $^{16}O_2$ spectra, red: $^{18}O_2$ spectra). The low concentration of $\mathbf{2^S}$ in neat MeTHF precluded observation of $\nu_{O\text{-}O}$. **144**

Figure S10. UV-vis spectra of $\mathbf{2^S}$ in mixed solvents of polar solvents with MeTHF at –135 ºC. **145**

Figure S11. Pseudo-first-order plots for the reactions of $[(^{DMA}N_3S)Cu^{II}\text{–}OO^{\bullet-}]^+$ ($\mathbf{2^S}$) and *p*-OMe-DTBP (left panel)/$AcrH_2$ (right panel) to determine pseudo-first-order rate constants (k_{obs}'s). The k_{obs}'s are 0.470 min^{-1} and 0.464 min^{-1}, respectively. **146**

Figure S12. UV-vis spectra of oxygenated adducts of Cu^I complexes with different ligand ($^{DMA}N_3$, $^{DMA}N_3O$, $^{DMA}N_4$ and $^{DMA}N_3S$) under different solvent with identical concentrations (–135 ºC). (See **Scheme 2**) **148-149**

Figure S13. DOSY NMR data of $[(^{DMA}N_3S)Cu^I]B(C_6F_5)_4$ (**1**), affording a diffusion coefficient (*D*) of $D = 10^{-9.09}$ m^{2}s^{-1} ($D_{THF\text{-}d8} = 10^{-8.50}$). **150**

Chapter 4: Primary Cu^I/O_2 Adduct with Tunable H-bond from Secondary Coordination

		Page Number
Figure 1.	Metalloenzymes containing mononuclear copper active sites and their biological functions by O_2 activation.	**153**
Scheme 1.	O_2-Derived copper adducts proposed as reactive intermediates.	**154**
Figure 2.	(a) and (b): Primary Cu^I/O_2 adducts stabilized by electron-donating groups, (c): mononuclear cupric superoxo species stabilized by potential H-bonding pivalamido group, $[(^{PV}tmpa)Cu^{II}(O_2^{\bullet-})]^+$ (d) the X-ray crystallographic structure of $Cu^{II}(O_2H)$ possessing two pivalamido groups, (e) $Cu^{II}(O_2H)$ activated by H-bond with distal O-atom, and (f) $(^{H}BA)Cu^{II}(O_2H)$.	**155**
Scheme 2.	Mononuclear copper(II)-hydroperoxo complexes, which are stabilized by a H-bond interaction with the proximal oxygen (left) and destabilized by a interaction with the distal oxygen (right).	**156**
Chart 1.	^{X}BA ligands utilized in this study.	**156**
Figure 3.	X-ray crystallographically derived structures of; (a) $[(^{OMe}BA)Cu^I]^+$ ($^{\mathbf{OMe}}\mathbf{1}$), (b) $[(^{OMe}BA)Cu^{II}(CH_3COCH_3)]^{2+}$ ($^{\mathbf{OMe}}\mathbf{2}$) and (c) $[(^{OMe}BA)Cu^{II}(N_3)]^+$ ($^{\mathbf{OMe}}\mathbf{3}$). Hydrogen atoms were removed for clarity. Displacement ellipsoid plots of the cations are illustrated in Supporting Information.	**157**
Figure 4.	Low-temperature UV-vis absorption spectra of the reaction of $^{\mathbf{X}}\mathbf{1}$ (X = OMe, H, and F5) with O_2 at –135 ºC in MeTHF (0.37 mM). The superoxo products $^{\mathbf{X}}\mathbf{S}$'s are observed after adding O_2 by bubbling for 40 s.	**160**
Figure 5.	Solvent-subtracted resonance Raman spectra of complex $^{\mathbf{F5}}\mathbf{S}$ (0.7 mM) measured in frozen MeTHF (77 K, λ_{ex} = 413 nm) showing A: ν(Cu–O) and B: ν(O–O) regions. Blue, $^{16}O_2$; red, $^{18}O_2$.	**161**
Table 1.	The redox potentials of LCu^{II} complexes and rR values of $LCu^{II}(O_2^{\bullet-})$, where L is tmpa-based tripodal N_4 ligand.	**162**
Chart 2.	O-H/C-H bond containing substrates utilized in the reactivity study.	**163**
Figure 6.	Low-temperature UV-vis absorption spectra of the reaction of $^{\mathbf{F5}}\mathbf{S}$ with 75 equiv *p*-OMe-DTBP at –135 ºC in MeTHF (0.37 mM).	**163**
Scheme 3.	Final major products of phenol oxidation reactions.	**164**
Table 2.	Physical properties of phenol derivatives and rate constants of reaction with $Cu^{II}(O_2^{\bullet-})$ complexes.	**165**

Scheme 4. Itoh's proposed reaction mechanism. **166**

Scheme 5. Proposed pathways of the reaction of $Cu^{II}(O_2^{\bullet-})$ and NADH analogues. **167**

Figure S1. EPR spectra of $^{\mathbf{OMe}}\mathbf{2}$ and $^{\mathbf{F5}}\mathbf{2}$ complexes taken with an X-band spectrometer (ν = 9.186 GHz) in acetone at 70 K. Copper(II) complex concentration: 2 mM. **174**

Figure S2. UV-vis spectrum of $[(^{OMe}BA)Cu^{II}(N_3)]ClO_4$ ($^{\mathbf{OMe}}\mathbf{3}$) At room temperature. **175**

Figure S3. Displacement ellipsoid plot (50% probability level) of the cation $[(^{OMe}BA)Cu^{I}]^+$ at 110(2) K. H atoms are omitted for clarity. A list of relevant bond distances and angles is also provided. **177**

Figure S4. Displacement ellipsoid plot (50% probability level) of the cation $[(^{F5}BA)Cu^{I}]_2^{2+}$ at 110(2) K. H atoms are omitted for clarity. A list of relevant bond distances and angles is also provided. **References**: Sheldrick, G. M. (2008). *Acta Cryst.* A64, 112-122; Flack, H.D. (1983). *Acta Cryst.* A39, 876-881. **179**

Figure S5. Displacement ellipsoid plot (50% probability level) of the cation $[(^{OMe}BA)Cu^{II}(CH_3COCH_3)]^{2+}$ at 110(2) K. H atoms are omitted for clarity. A list of relevant bond distances and angles is also provided. **180**

Figure S6. Displacement ellipsoid plot (50% probability level) of the cation $[(^{F5}BA)Cu^{II}(CH_3COCH_3)(OClO_3)]^+$ at 110(2) K. H atoms are omitted for clarity. A list of relevant bond distances and angles is also provided. **181**

Figure S7. Displacement ellipsoid plot of the cation $[(^{OMe}BA)Cu^{II}(N_3)]^+$ at 110(2) K. H atoms are omitted for clarity. A list of relevant bond distances and angles is also provided. **Reference**: Sheldrick, G. M. (2008). Acta Cryst. A64, 112-122. **183**

Figure S8. Cyclic voltammograms for copper(II) complexes in CH_3CN (mV *vs.* $[Fe(Cp)_2]^{+/0}$). **184**

Figure S9. Low-temperature UV-vis absorption spectra of the reaction of $^{\mathbf{X}}\mathbf{P}$ (X=OMe, H, and F5) with O_2 at –50 ºC in MeTHF (0.1 mM). **185**

Figure S10. Solvent-subtracted resonance Raman spectra of MeTHF solutions of $(BA)CuO_2$ (77 K, λ_{ex} = 413 nm) showing the (A) ν(Cu–O) and (B) ν(O–O) regions. **186**

Figure S11. Gaussian fit of the two Fermi-mixed (a) ν(O-O) modes of $[(^{H}BA)Cu^{II}(O_2^{\bullet-})]^+$ ($^{\mathbf{H}}\mathbf{S}$) (relative intensities 72:28 ($^{16}O_2$) and 42:58 ($^{18}O_2$)), and (b) ν(Cu-O) modes (relative intensities 70:30 ($^{16}O_2$)). An isotope-insensitive feature occurs at 447 cm^{-1}. **187**

Figure S12. Gaussian fits of the two Fermi-mixed (a) ν(O-O) modes of $[(^{F5}BA)Cu^{II}(O_2^{\bullet-})]^+$ ($^{\mathbf{F5}}\mathbf{S}$) (relative intensities 82:18 ($^{16}O_2$) and 29:71 ($^{18}O_2$)) and (b) ν(Cu-O) modes (relative intensities 75:25 ($^{16}O_2$) and 53:47 ($^{18}O_2$)). An isotope-insensitive feature occurs at 445 cm^{-1} in the spectra. **187**

Figure S13. Plots of k_{obs}'s against the concentrations of *p*-OMePh for the reaction of (a) $[(^{OMe}BA)Cu^{II}(O_2^{\bullet-})]^+$ (**^{OMe}S**), (b) $[(^{H}BA)Cu^{II}(O_2^{\bullet-})]^+$ (**^{H}S**), and (c) $[(^{F5}BA)Cu^{II}(O_2^{\bullet-})]^+$ (**^{F5}S**). **188-189**

Figure S14. UV-vis spectra for the reaction of $[(^{F5}BA)Cu^{II}(O_2^{\bullet-})]^+$ (**^{F5}S**) and 125 equiv N-methyl-9,10-dihydroacridine ($AcrH_2$) affording generation of radical species and *trans*-peroxo dicopper(II) complexes. **190**

Chapter 5: Dioxygen-Derived Copper Species Ligated by His-Braced Peptide Ligands

Page Number

Figure 1. Amino acids commonly found at copper active site as ligand donors. Donor atoms are colored and underlined. **192**

Table 1. Binding sites of His's at Cu centers in enzymes. **193**

Figure 2. (a) Copper active site of one of the lytic polysaccharide monooxygenase proteins in the cellulose-active fungal AA9 group (PDB: 4EIR). A putative superoxide moiety is observed at 3.0 Å from the Cu center. (b) Dicopper active sites found in pMMOs (PDB: 1YEW). (c) Structure of CopC (copper resistance protein, bacterial blue copper protein, copper carrier) (PDB: 2C9Q) **194**

Figure 3. A high-valent dicopper(III) species **O** ligated by the primary amine, 1,3-propylenediamine, is capable of H-atom abstraction from the C−H bond in 9,10-dihydromethylacridine. **195**

Chart 1. The ligands utilized in this study; NδHεH (left) and BocδHεH (right). Nitrogen donors are underlined. **197**

Figure 4. Low-temperature UV-vis absorption spectra of the oxygenated products of $[(N\delta H\varepsilon H)Cu^{I}]^+$ species in (a) THF at –100 °C forming **Cpd A** (final most absorbing green line spectrum); (b) MeTHF at –135 °C showing conversion of **Cpd A** (dark green lines) to **Cpd B** bright lighter green line spectrum; the black spectrum is that for the starting Cu(I) complex, and (c) **Cpd B** (green line) in acetone at –90 °C' the aqua blue line spectrum is that obtained after warmup to RT. **198**

Figure 5. (a) Low-temperature UV-vis absorption spectrum of the oxygenated products of $[(N\delta H\varepsilon H)Cu^{I}]^+$ species Cpd A in THF at –100 °C and (b) resonance Raman spectra λ_{ex} = 458 nm. **199**

Figure 6. Low-temperature UV-vis absorption spectra for the protonation of $[\{(N\delta H\varepsilon H)Cu^{II}\}_2(\mu\text{-}1,2\text{-}O_2^{2-})]^{2+}$ (**Cpd A**) by perchloric acid, $HClO_4$ in THF at –100 °C. **201**

Figure 7. (a) Low-temperature UV-vis absorption spectra of 0.25 mM $[(N\delta H\varepsilon H)Cu^{II}(OOH)]^+$ in THF at - 80 ^{o}C and its warmed-up solution, and (b) EPR spectra of the $[(N\delta H\varepsilon H)Cu^{II}(OOH)]^+$ complex. **202**

Figure 8. (a) Low-temperature UV-vis absorption spectra of the oxygenated products of $[(^{Trt}His)Cu^{I}]^+$ species with or without one equiv 1-methylimidazole in MeTHF at –135 °C and (b) resonance Raman spectra of the bis-μ-oxo dicopper(III) complex (λ_{ex} = 364 nm). **203**

Scheme S1. Synthesis of the NεH. **212**

Scheme S2. Synthetic pathway to the ligand NδHεH. **213**

Scheme S3. Synthetic pathway to protect the primary amino group; the precursor His-Phth **213**

Scheme S4. Synthetic pathway to block the $\varepsilon N_{histamine}$ with trityl group **214**

Scheme S5. Deprotection of the phthalimide moiety affording the ^{Trt}His ligand **214**

Figure S1. EPR spectra of $[(N\delta H\varepsilon H)Cu^{I}]B(C_6F_5)_4$, Cpd A, Cpd B, and decomposed product in THF (2 mM). **216**

Figure S2. EPR spectra of protonation of **Cpd A** with half equivalent of (a) $HClO_4$; X-band (ν = 9.431 GHz) spectrometer in THF at 70 K: $g_{\parallel} = 2.28$, $A_{\parallel} = 150$ G, $g_{\perp} = 2.05$ and (b) trifluoroacetic acid (TFA); X-band (ν = 9.431 GHz) spectrometer in THF at 70 K: $g_{\parallel} = 2.28$, $A_{\parallel} = 145$ G, $g_{\perp} = 2.06$. **216**

Figure S3. UV-vis spectra for oxygenation of $(^{Trt}His)Cu^{I}$ in MeTHF solution at –135 °C without addition of 1-methylimidazole. (0.24 mM). **217**

Chapter 1:

Copper Monooxygenases/Oxidases Mediated C–H/O–H Activation and Their Model Chemistry

A part of this work was co-written with collaborators and published under the following citations:

Jung Yoon Lee, and Kenneth D. Karlin*; "Elaboration of Copper-Oxygen Mediated C–H Activation Chemistry in Consideration of Future Fuel and Feedstock Generation"

Curr. Opin. Chem. Biol. **2015***, 25*, 184-193

Clarence J. Rolle III, Sunghee Kim and Jung Yoon Lee and Kenneth D. Karlin*; "Highlights and Directions in Copper-Dioxygen Chemistry of Bioinorganic Relevance"

Bull. Jpn. Soc. Coord. Chem. **2013**, *62*, 40-44

Abstract

In this chapter, copper monooxygenases and oxidases involved in C–H/O–H bond oxidation are overviewed, including biological functions, chemical/physical properties of their metal active sites and their proposed mechanisms. Copper monooxygenases are known to oxidatively activate strong C-H bonds under ambient conditions, and mononuclear copper oxidases are involved in O-H bond oxidation along with reduction of molecular oxygen to hydrogen peroxide. Recent investigation of various synthetic oxygen-derived copper intermediates including their characteristics and reactivity is described. Possible reaction mechanisms are discussed by comparison to aqueous O_2-reduction.

1. Introduction

The third most abundant transition metal "copper" is an essential constituent in nature. Copper in proteins has been regarded to play a critical biological role as a metal active site.[1-4] Many copper enzymes utilize molecular oxygen (O_2) to perform oxidation-reduction processes (plastocyanin, azurin), dioxygen transport (hemocyanin), superoxide scavenging (superoxide dismutase), H_2O_2 production along with O–H oxidation (oxidases) and substrate hydroxylation through the oxidative activation of C–H bonds (monooxygenases). Since the key process is "oxygen activation" by Cu ion centers in metalloenzymes, bioinspired copper-dioxygen chemistries provide information or concepts derived from biochemical or synthetic bioinorganic systems.[3] This chapter will focus on an overview of copper monooxygenases/oxidases relevant to the oxidation of C–H/O–H bonds (**Table 1**), which are fundamental reactions in biological systems.

The oxidative cleavage of C–H bonds is mediated by monooxygenases,[3, 4] *cf.*, $R–H + O_2 + 2e^- + 2H^+ \rightarrow R–OH + H_2O$, utilizing molecular oxygen as the 'O' atom source; the 'other' atom derived from O_2 is released in the reduced form of water. The elucidation of strong C–H bond activation pathway by copper monooxygenases may be applicable to solve current energy concerns.[5, 6] Copper oxidases reduce dioxygen to hydrogen peroxide while producing aldehydes from either primary alcohol or primary amines, including concomitant two-electron oxidation of O–H bond substrates, *cf.*, $O_2 + 2e^- + 2H^+ \rightarrow H_2O_2$.

There are various types of copper active sites. Hemocyanin, tyrosinase, catechol oxidase, and particulate methane monooxygenase (pMMO) contain dinuclear active sites, and unique noncoupled dicopper centers are found in peptidylglycine-α-hydroxylating monooxygenase (PHM) and dopamine-β-monooxygenase (DβM). Galactose oxidase (GO) and copper amine oxidase (CAO) possess a single active-site copper center.[1-4]

In fact, for C–H oxidative cleavage of methane, biopolymers (vide supra), or other substrates, enzymes with copper active sites include lytic polysaccharide monooxygenases (LPMOs), PHM, tyrosinases (phenol *o*-hydroxylases) and pMMO, which possess mononuclear (single Cu), non-coupled dicopper or adjacent dicopper active centers. The understanding of the formation, chemical-physical properties and reactivity of diverse biochemical or synthetic copper-oxygen adducts is of great interest.

To study the nature of copper active sites in enzymes can fundamental knowledge pertaining to the reactions occurring in biological as well as chemical systems. There have been considerable efforts to establish copper model complexes coordinated by newly designed/synthesized ligands and elucidate their characteristics and reactivity toward substrates. Here, copper monooxygenases (LPMOs, PHMs, and pMMOs) and oxidases (GO and CAO) mediating oxidative activation of C–H/O–H bond by utilizing molecular oxygen will be reviewed, along with recent biosynthetic model chemistry.

Table 1. Copper enzymes involved in C–H/O–H bond oxidation[1-4]

	Copper Proteins	*Biological function*
Monooxygenases	Lytic polysaccharide monooxygenases (LPMOs)	Polysaccharide degradation
	Peptidylglycine-*α*-hydroxylating monooxygenase (PHM)	Glycine-extended prohormone peptide hydroxylation
	Dopamine-β-monooxygenase (DβM)	Dopamine → norepinephrine
	Particulate methane monoxygenase (pMMO)	Methane →methanol
Oxidases	Galactose oxidase (GO)	1° alcohol → aldehyde
	Copper amine oxidase (CAO)	1° amine → aldehyde

1.1 Lytic Polysaccharide Monooxygenases (LPMOs)

LPMOs have aroused much attention due to their significant roles in production of potential alternative biofuel from currently plentiful and renewable biomass via oxidative polysaccharide breakdown (**Scheme 1**).[6, 7] Abundant biopolymers such as cellulose, chitin, lignin and starches may provide potential future sources of primary feedstock in the production of fuels.[7] Hydrolytic chemistry by enzymes or extreme chemical conditions, such as heating with sulfuric acid,[8] can lead to useful breakdown products. Recent advances have revealed that the C-H activation is a major reaction in polysaccharides degradation affording biopolymer conversion via oxidative chemistry.

Scheme 1. Polysaccharides degradation process

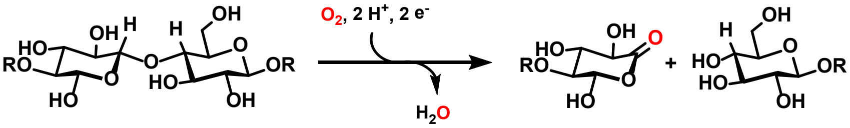

Several families of LPMOs have been categorized; cellulose-active fungal AA9, chitin-degradable bacterial AA10, and chitin-active fungal AA11.[7, 9] Most recently, other LPMOs are shown to be capable of degrading starch.[10] There are now many X-ray crystallographic studies showing that all LPMOs possess a mononuclear copper active site where binding to a chelating (bidentate) histidine amino terminus and a second His via εN imidazole ligation (**Figure 1**).[9, 11, 12] These three N-donors comprise a roughly T-shaped coordination (especially for reduced $\mathrm{Cu^{I}}$),[13] with the chelating histidine referred to as a 'His-brace'. In oxidized forms, additional waters coordinate and tyrosine or other aromatic amino-acids reside nearby. Subtle differences in the LPMO active-site structures occur. AA9 enzymes possess an εN-methylated His-brace, a highly unusual biochemical feature (**Figure 1**). The type of copper-oxygen intermediate formed during catalysis is unknown, but it must be highly reactive in order to cleave the very strong sugar C–H bond (C1 or C4). The generation and investigation of the plausible oxygen-derived monocopper species chelated by a His-brace ligand can contribute to an enhanced future application of C-H oxidation or oxygenation processes using air.

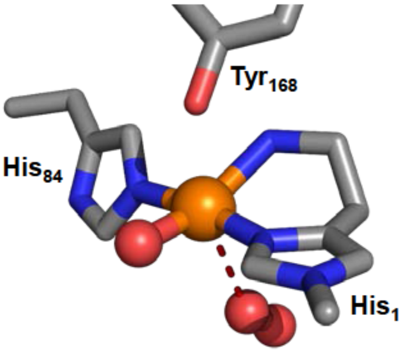
Tyr168
His84
His1

Figure 1. Copper active site of one of the lytic polysaccharide monooxygenase in the cellulose-active fungal AA9 group. A putative superoxide moiety is observed at 3.0 Å from the Cu center (PDB: 4EIR)[12]

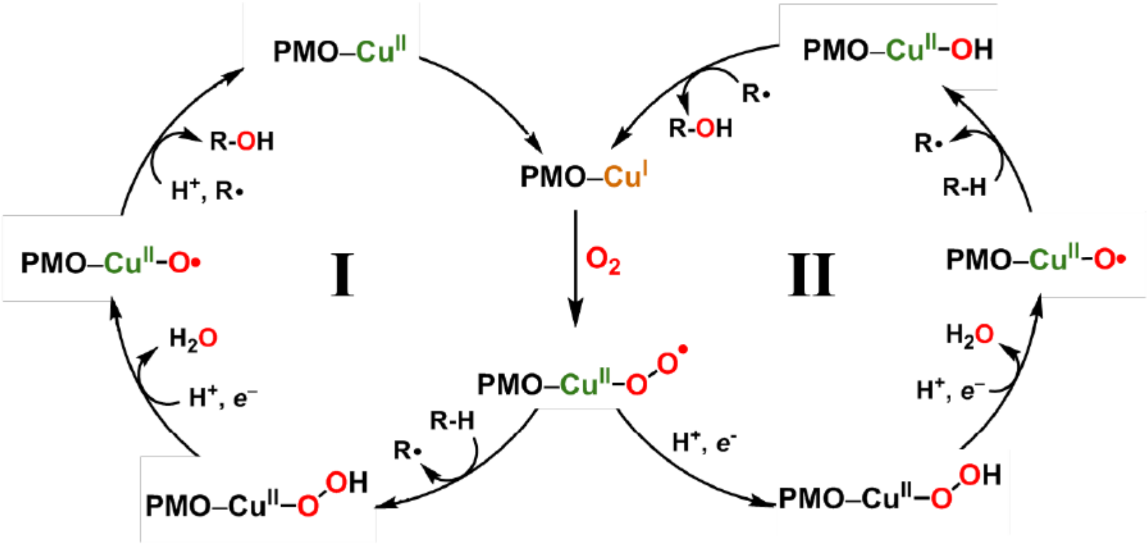
PMO–Cu^II
PMO–Cu^II-OH
R•
R-OH
R-OH
H+, R•
PMO–Cu^I
R•
R-H
PMO–Cu^II-O•
I
O2
II
PMO–Cu^II-O•
H2O
H+, e−
PMO–Cu^II-O-O•
H2O
H+, e−
R-H
R•
H+, e-
PMO–Cu^II-O-OH
PMO–Cu^II-O-OH

Figure 2. Proposed mechanisms of LPMOs. The C-H bond of substrate is oxidatively cleaved by either a cupric superoxo (I) or copper-oxyl (II) species.[14, 15]

There are a few mechanisms proposed by biochemists based on the studies of enzymes, relevant model systems and computational work (**Figure 2**). Beeson et al. suggested Pathway I that relies on hydrogen atom abstraction by the Cu(II)-superoxo intermediate followed by oxygen rebound by copper-oxyl species.[14] Whereas, in catalytic cycle II, the Cu(II)-oxyl radical intermediate is responsible for cleaving the strong C-H bond of polysaccharides.[15]

1.2 Peptidylglycine-α-Hydroxylating Monooxygenase (PHM) and Dopamine-β-Monooxygenase (DβM)

Peptidylglycine-α-hydroxylating monooxygenase (PHM) and dopamine-β-monooxygenase (DβM) are copper monooxygenases found in higher eukaryotes and mediate strong C-H bond activation.[16] PHM is a subunit of peptidylglycine-α-amidating monooxygenase (PAM) which is responsible for producing an active amidated hormone. A glycine-extended prohormone undergoes α-carbon hydroxylation by PHM. DβM, involved in the catecholamine biosynthetic pathway, catalyzes the benzylic hydroxylation of dopamine to give norepinephrine[17, 18] which is a neurotransmitter in nervous system (**Scheme 2**).

Scheme 2. Biological functions of PHM and DβM

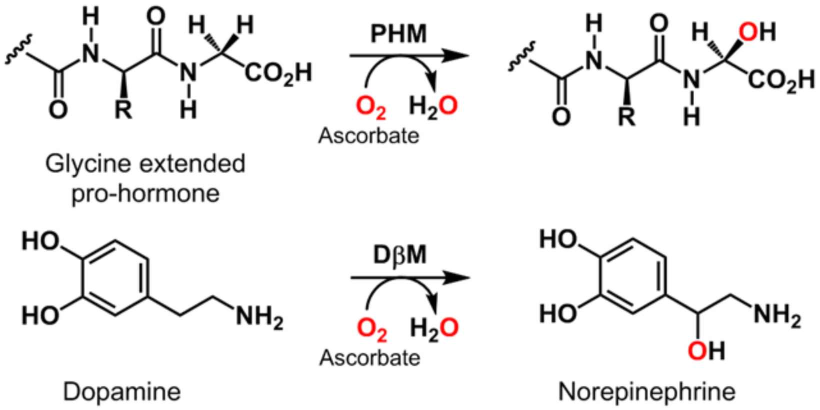

They possess a dicopper active site which is "noncoupled"; the two copper ions are about 11 Å apart (**Figure 3**).[19] One copper ion (Cu_H or Cu_A), coordinated by two or three δN_{His} residues, receives and passes reducing equivalents from ascorbate to Cu_M or Cu_B, where O_2 and substrate binding occurs. The Cu_M (Cu_B) site binds to two εN_{His}, and S_{Met} which is regarded as a unique coordination environment. The role of the methionine coordination is not fully elucidated. An X-ray crystallographic study on a PHM derivative reveals a dioxygen-derived species at the Cu_M site, judged to be a Cu^I/O_2 adduct, formally an end-on superoxide ($O_2^{\bullet -}$) ligand-Cu^{II} complex (^{E}S; **Figure 10**);[20] dioxygen binding to transition metals involves electron-transfer from metal ion to O_2. Other biochemical and computational studies implicate a Cu^{II}-$O_2^{\bullet -}$ species formed in PHM which effects substrate hydrogen-atom transfer (HAT), eventually leading to product.[17, 18, 21] With these protein studies and more recent model compound work, fundamental studies on the physical properties and reactivity of mononuclear cupric superoxo species have thus been evoked (vide infra).

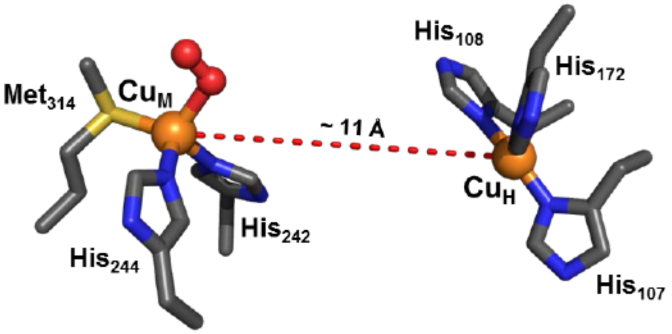

Figure 3. The oxidized form of PHM active site exhibiting the non-coupled two copper ions; dioxygen-bound Cu_M site and Cu_H site located apart.[20]

On the basis of many experimental and theoretical studies, there are several possible reaction mechanisms proposed that could lead to the substrate hydroxylation, which also requires the delivery of protons and electrons.[22-24] The generally accepted reaction pathway was suggested by Klinman (**Figure 4**)[22, 24] and in this catalytic cycle, a primary Cu^I/O_2 adduct formed at the Cu_M site is responsible for initiating C-H bond activation of substrate through a hydrogen atom transfer reaction, while Cu_H provides an electron to the Cu_M.

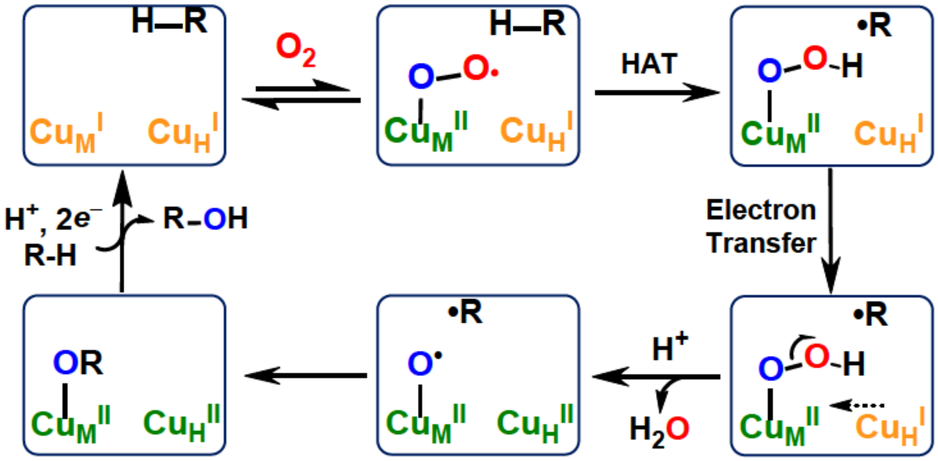

H—R
Cu_M^I
Cu_H^I
O₂
H—R
O—O•
Cu_M^II
Cu_H^I
HAT
•R
O-O-H
Cu_M^II
Cu_H^I
Electron Transfer
•R
O-O-H
Cu_M^II
Cu_H^I
H⁺
H₂O
•R
O•
Cu_M^II
Cu_H^II
OR
Cu_M^II
Cu_H^II
H⁺, 2e⁻
R-H
R-OH

Figure 4. A possible substrate hydroxylation mechanism of PHM proposed by Klinman.[24]

1.3 Particulate Methane Monooxygenase (pMMO)

pMMO, found in bacterial methanotrophs, is employed to oxidize methane to methanol in order to acquire a carbon source (**Scheme 3**).[25, 26] The activation of the inert methane C–H bond (BDE = 104 kcal/mol^{-1}) would be a key reaction to find efficient ways to efficiently utilize current energy resources such as natural gas (CH_4).[5] The development of new shale gas fracking technology has enabled the very recent steep growth in natural gas output. The efficient control of overflowed shale gas includes liquefaction of methane.

Scheme 3. pMMO-catalyzed oxidation of methane to methanol in the presence of NADH.

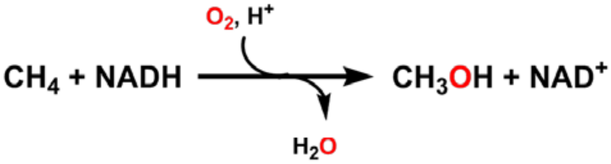

$$CH_4 + NADH \xrightarrow[H_2O]{O_2,\ H^+} CH_3OH + NAD^+$$

In general, high temperature and pressure (800 ºC, 40 atm) are required for the industrial partial oxidation of CH_4 to produce methanol (CH_3OH).[5] This energy-dense liquid can be a fuel (e.g. in fuel cells or as an additive to blended gasoline) or feedstock. Methanol also provides advantages in its utilization, as there would be minimal loss in transport from a storage site. The pMMO's capability of cleavage C-H bond at ambient environment has been of great interest in that selective oxidation of methane to methanol could minimize the loss in natural gas usage or produce feedstock for use as fuels.

X-ray crystallographic studies exhibit that pMMO possesses three different metal active sites; dicopper, monocopper, and a zinc center (**Figure 5**).[26-28] The mononuclear copper center, which is not present in some pMMOs, shows ligation from two δN_{His} residues with an adjacent glutamine. Biochemical studies implicate dicopper active site as an asymmetrical motif,[28-30] although Chan et al.[31] hold the view that an as yet unseen pMMO trinuclear Cu center constitutes the active site. The dicopper site displays a short Cu–Cu distance, where the ligands are provided by two His's for one copper and the bidentate N-terminal histidine ('His-brace', as in LPMOs) for the other (**Figure 1**).

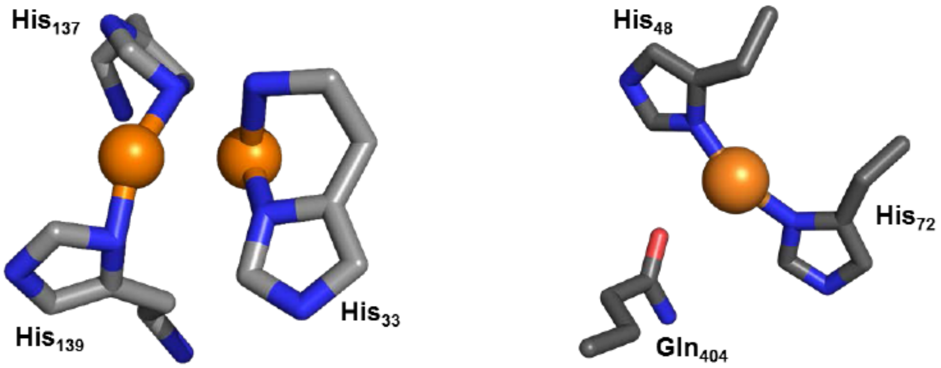

Figure 5. Two copper centers found in pMMOs; dicopper and monocopper active sites (PDB: 1YEW).[27]

Closer examination of the dicopper centers in X-ray structures (albeit the structures are not of high-resolution) reveals two very tilted Cu-N_{His} bonds (with the Cu-N vector reaching far out of the plane of the imidazole ring), not reasonable for inorganic coordination structures. As LPMO structures also having the His-brace are mononuclear in Cu, some biochemists[32] suggest the pMMO active site may possess only one copper, coordinated by the His-brace and one another His residue. Nevertheless, a dicopper center capable of methane or other alkyl C–H oxidations is worthy of studying, and there are many 2:1 Cu/O_2 derived entities in synthetic chemistry (vide infra).

1.4 Galactose Oxidase (GO)

Galactose oxidase (GO) is a copper enzyme involved in a catalytic reaction wherein primary alcohols undergo two-electron oxidation to the corresponding aldehydes with the concomitant reduction of molecular oxygen to hydrogen peroxide (H_2O_2). This process is believed to play vital roles in physiological systems, particularly in cell signaling (**Scheme 4**).[33]

Scheme 4. The two-electron oxidation of D-galactose to D-galactohexodialdose along with reduction of dioxygen to hydrogen peroxide.

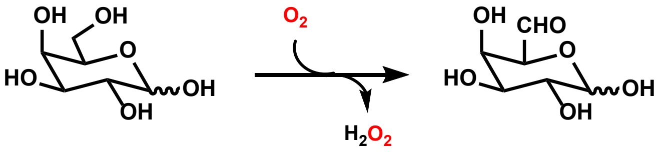

Substrate oxidation: $RCH_2OH \longrightarrow RCHO + 2e^- + 2H^+$

Dioxygen reduction: $O_2 + 2e^- + 2H^+ \longrightarrow H_2O_2$

X-ray crystallographic studies reveal that the inactive form of the metal active site of GO contains an unusual ligation; two histidines at εN$_{His}$ sites, two tyrosines and a water (**Figure 6**).[34] One tyrosine is cross-linked with cysteine forming a Tyr-Cys cofactor. This Tyr acts as radical center affording a unique free radical-coupled copper moiety.

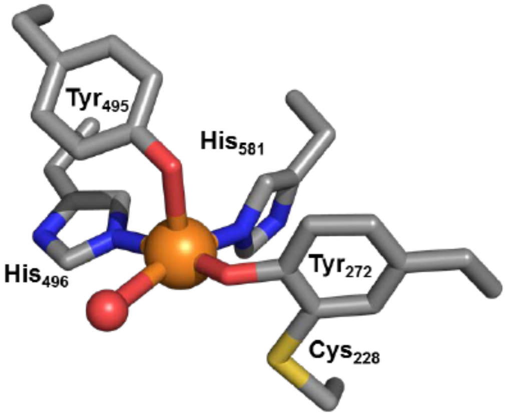

Figure 6. X-ray structure of an inactive form at the mononuclear copper active site in GO (PDB: 1GOG).[34]

According to the proposed mechanism for GO (**Figure 7**),[35] the inactive copper center becomes an 'active' form by oxidation of the Tyr-Cys moiety to generate a copper(II)-tyrosyl radical species. This is responsible for the oxidation of D-galactose in the catalytic cycle. Further reaction reduces copper ion which then reacts with dioxygen yielding a cupric superoxo intermediate. A copper(II)-tyrosyl radical is regenerated through hydrogen atom transfer via O-H bond oxidation and hydrogen peroxide is released as the two-electron reduced form of O_2.

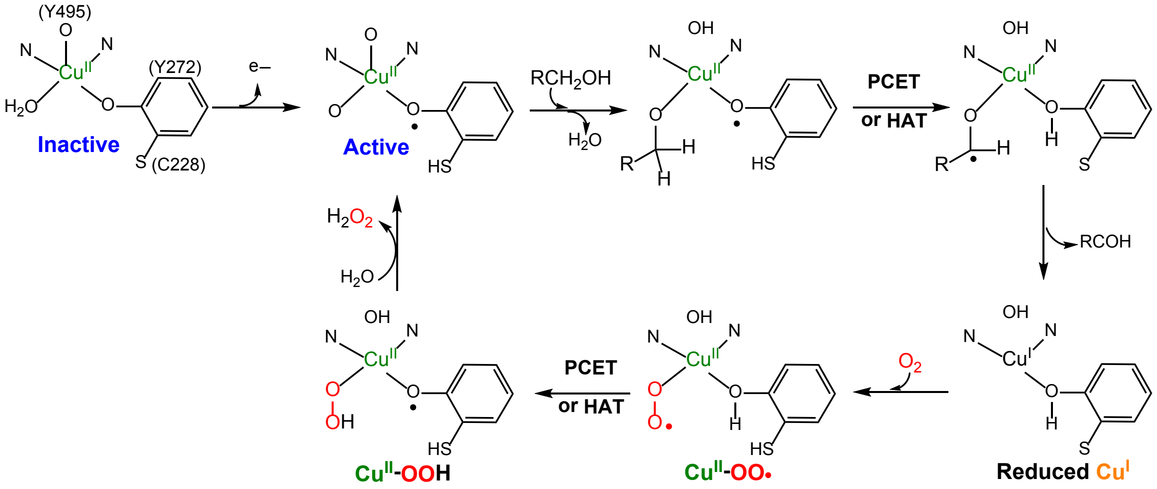
(Y495)
O
N
N
Cu^II
(Y272)
H2O
O
Inactive
S (C228)
e–
Active
HS
RCH2OH
H2O
PCET
or HAT
RCOH
H2O2
H2O
O2
Cu^II-OOH
Cu^II-OO•
Reduced Cu^I

Figure 7. Proposed catalytic cycle of GO by the active species, a copper(II)-tyrosyl radical.[35]

1.5 Copper Amine Oxidase (CAO)

Copper amine oxidase (CAO) catalyzes the two-electron oxidation of substrate primary amines to corresponding aldehydes along with the reduction of molecular oxygen to hydrogen peroxide (**Scheme 5**).[16]

Scheme 5. CAO-catalayzed oxidative deamination of 1° amines to aldehydes via coupled reduction of dioxygen.

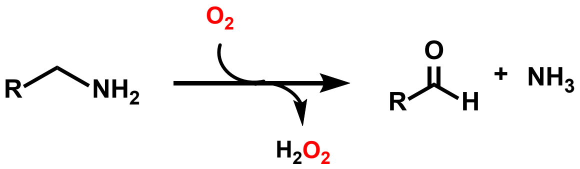
O2
R
NH2
H2O2
O
R
H
+
NH3

The structure of CAO, solved by X-ray crystallography, contains a monocopper active site ligated by three histidines through two εN_{His} and one δN_{His} residues. A reduced form binds to a well-ordered axial water molecule (**Figure 8**).[36] A protein-derived cofactor, 2,4,5-trihydroxyphenylalanine quinone (TPQ) is located within a six (6) Å distance to the copper ion.

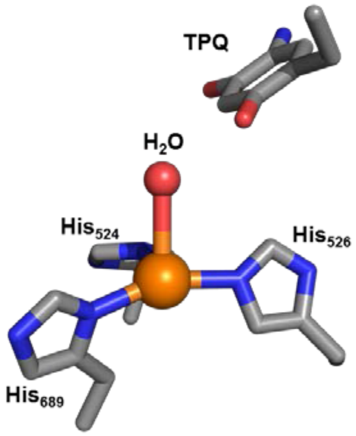

Figure 8. The reduced state of the mononuclear copper active site in CAO (PDB: 1D6U).[36]

The TPQ is derived from a tyrosine at active site through the biogenesis reaction.[37] The reaction is a catalytic reaction which requires molecular oxygen, water and active site copper(II) (**Scheme 6**).[38]

Scheme 6. TPQ generation from tyrosine moiety.

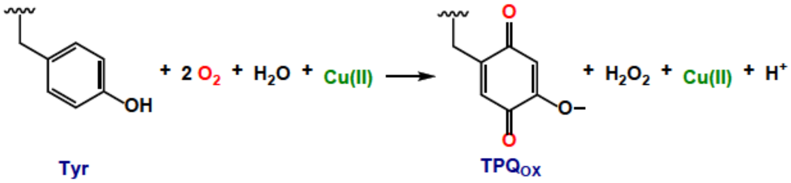

CAO utilizes this active-site TPQ cofactor to proceed through catalysis, via a two-electron oxidation ping–pong mechanism including two reductive/oxidative half-reactions.[16, 39] In the reductive half-reaction, a primary amine is oxidized to an aldehyde while producing a two-electron reduced aminoquinol form of the TPQ. In the oxidative half-reaction, the enzyme is oxidatively deaminated, going back to the resting state using dioxygen; NH_4^+ and hydrogen peroxide are released.

Reductive half-reaction:

$$\mathbf{E}_{ox} + RCH_2NH_3^+ \longrightarrow \mathbf{E}_{red} + RCHO + H_2O$$

Oxidative half-reaction:

$$\mathbf{E}_{red} + O_2 + H_2O \longrightarrow \mathbf{E}_{ox} + NH_4^+ + H_2O_2$$

The mechanism of oxidative deamination by CAO has been extensively studied.[40, 41] There are two plausible mechanisms for cofactor re-oxidation (**Figure 9**). In the inner-sphere pathway,[41, 42] the enzyme is reduced to the two-electron-reduced aminoquinol state (TPQ_{AMQ}) or the one-electron-reduced semiquinone state (TPQ_{SHQ}) releasing aldehyde. TPQ_{SHQ} reduces dioxygen affording copper(II) superoxo species and further protonation and electron transfer give a cupric hydroperoxide along with a iminoquinone species (TPQ_{IMQ}). This releases NH_4^+ and H_2O_2 by hydrolysis, leaving the starting cofactor, TPQ_{OX}. In the outer-sphere pathway,[40] TPQ_{AMQ} directly reduces dioxygen to superoxide ion. Although the mechanisms are well-studied, there still exists controversy about the role of copper ion.

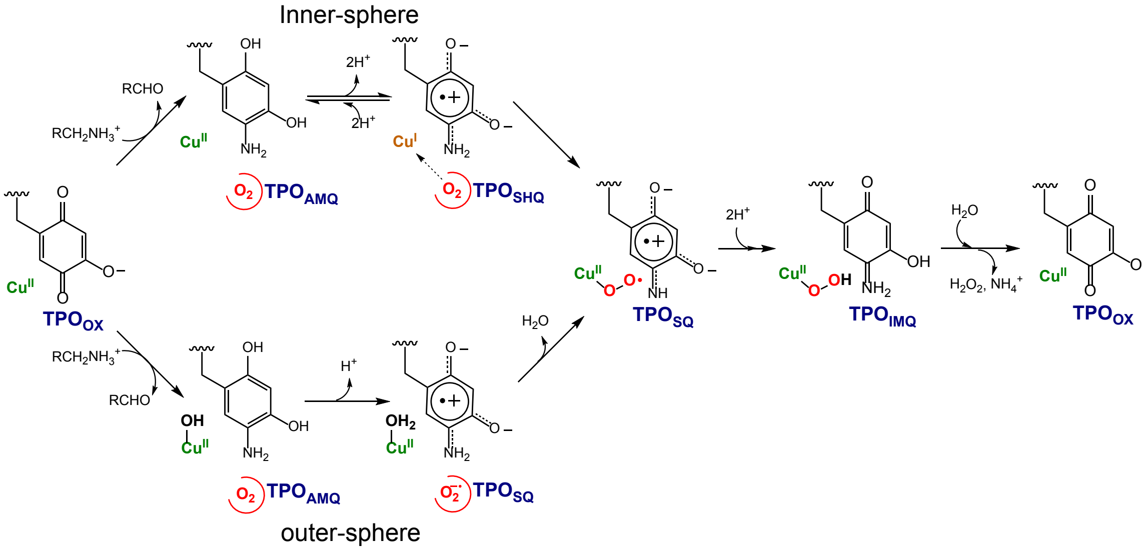
Inner-sphere
RCHO
RCH2NH3+
Cu^II
2H+
2H+
Cu^I
O2 TPO_AMQ
O2 TPO_SHQ
Cu^II
TPO_OX
2H+
H2O
H2O2, NH4+
TPO_SQ
TPO_IMQ
TPO_OX
RCH2NH3+
RCHO
OH Cu^II
H+
OH2 Cu^II
H2O
O2 TPO_AMQ
O2•− TPO_SQ
outer-sphere

Figure 9. Two proposed pathways for cofactor reoxidation occurring in copper amine oxidase.

2. Synthetic Cu$_2$/O$_2$ Complexes

As copper containing enzymes have different kinds of active sites (vide supra), it is critical to clarify fundamental aspects for the formation, structural/spectroscopic characteristics, and reactivity of the known Cu^{I}-O$_2$ derived species, **Figure 10.**[2, 43] Upon oxygenation of a reduced copper ion, an initial product is a mononuclear cupric superoxo (Cu^{II}-O$_2^{\bullet-}$, ^{E}**S**) species. Over the years, species ^{E}**S** have been difficult to observe because the reactions of ^{E}**S** or "side-on" η^2-bound forms (^{S}**S**) with a second mole-equiv of the starting ligand Cu(I) complex are very fast and the binuclear dicopper complexes (μ-1,2-peroxo)Cu$^{II}_2$ ("trans" ^{T}**P**[44]; or a newer "cis" ^{C}**P** form[45]), (μ-η^2: η^2-peroxo)Cu$^{II}_2$ (^{S}**P**)[46] and bis(μ-oxo)Cu$^{III}_3$ (**O**) (**Figure 10**) are stable if handled at cryogenic temperatures.[44, 46-48] The dicopper(III) complex **O** seems to be most stable among the three, possibly due to the strong Cu^{III}-oxo bonds, but the nature of the chelating ligand employed controls the chemistry and final structure. However, **O** is well known to attack exogenous substrates, including C–H bonds, in a wide variety of reactions as outlined by Stack, Tolman, Itoh and others.[47, 49, 50]

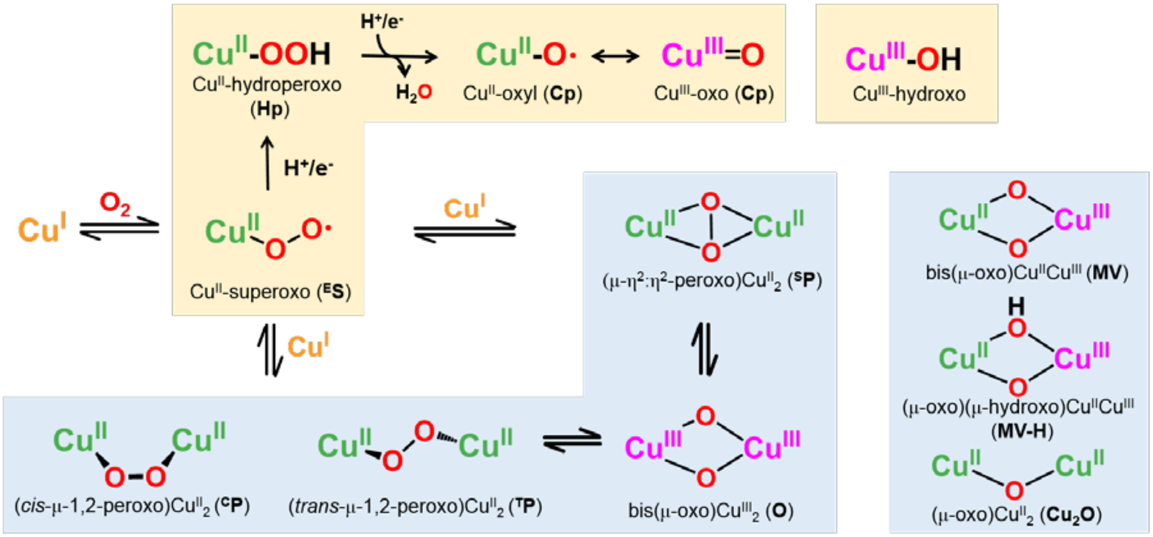
Cu^{II}-OOH
Cu^{II}-hydroperoxo (Hp)
H$^+$/e$^-$
H$_2$O
Cu^{II}-O·
Cu^{II}-oxyl (Cp)
Cu^{III}=O
Cu^{III}-oxo (Cp)
Cu^{III}-OH
Cu^{III}-hydroxo
H$^+$/e$^-$
Cu^{I}
O$_2$
Cu^{II}-superoxo (^{E}S)
Cu^{I}
Cu^{I}
(μ-η^2:η^2-peroxo)Cu$^{II}_2$ (^{S}P)
bis(μ-oxo)Cu^{II}Cu^{III} (MV)
(μ-oxo)(μ-hydroxo)Cu^{II}Cu^{III} (MV-H)
(μ-oxo)Cu$^{II}_2$ (Cu$_2$O)
(cis-μ-1,2-peroxo)Cu$^{II}_2$ (^{C}P)
(trans-μ-1,2-peroxo)Cu$^{II}_2$ (^{T}P)
bis(μ-oxo)Cu$^{III}_2$ (O)

Figure 10. O$_2$-derived copper species proposed as reactive intermediates in copper-containing enzymes.

As described, pMMO is well thought to effect dicopper methane oxygenation chemistry and **O** has been suggested as an intermediate which may form at the active site. Related species which are probably more reactive toward oxidative (oxygenative; overall O-atom insertion) chemistry involving very strong C–H bonds are bis(μ-oxo)$Cu^{II}Cu^{III}$ (**MV**) or (μ-oxo)(μ-hydroxo)$Cu^{II}Cu^{III}$ (**MV-H**) (**Figure 10**). **MV** is suggested by examination of the literature[28, 30, 31, 51] or from calculations;[52] Yoshizawa's newer computational analysis[53] suggests further activation, i.e., implementation of enhanced reactivity toward CH_4 as substrate, could come by starting with **O** and injecting a proton and an electron from a nearby tyrosine to give **MV-H**. However, neither **MV** nor **MV-H** species has ever been directly synthesized or identified. These remain as important synthetic targets.

Solomon, Schoonheydt and co-workers have shown that a (*μ*-oxo)Cu^{II}_2 (**Cu_2O**, **Figure 10**) attacks methane in Cu-loaded zeolites (Cu-ZSM-5),[54] producing CH_3OH at low temperature (~100 °C) with high selectivity. Some **Cu_2O** synthetic complexes have been reported,[55] but they have not yet been shown to undergo interesting C-H bond oxidation chemistry.

An important recent contribution from Stack and coworkers[50] establishes the chemistry of complexes **O** when ligated by a bidentate ligands where at least one donor is a primary amine ($-NH_2$) (**Figure 11**). A combination of experimental and computational studies leads to conclusions that might not be expected – the smaller size of the $–NH_2$ ligand (relative to $–NR_2$) allows for tight/strong Cu-N bonding and achievement of Cu high-valency in **O**, without loss of oxidative power. Also, the small $–NH_2$ ligand also allows a substrate closer approach to the O_2-derived copper-oxygen species. This study thus provides possible insight into the presence of the protein terminal His residue as chelating ligand in LPMOs (**Figure 1**) and/or pMMO (**Figure 5**), enzymes with very strong C–H bond containing substrates.

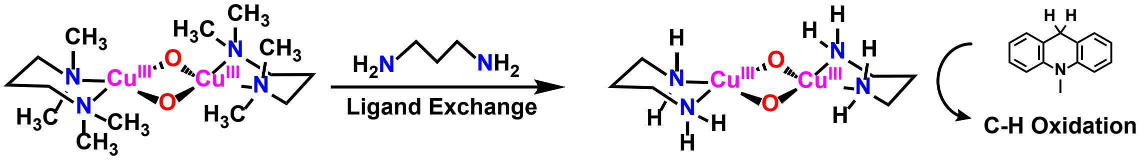

Figure 11. A high-valent dicopper(III) species **O** ligated by the primary amine, 1,3-propylenediamine, is capable of H-atom abstraction from the C−H bond in 9,10-dihydromethylacridine.

3. Primary Cu^I/O_2 Adducts and Reactivity

As stated above, a Cu^{II}-$O_2^{\bullet-}$ (**^{E}S**) species is the initial adduct produced from the internal electron transfer between a single ligand-Cu^I complex and O_2. Then, sequential electron-proton addition from reductants (e.g., ascorbate) and solvent, or H-atom transfer from substrates (see below) to species **^{E}S** may lead to a Cu^{II}-OOH species (**Hp**). Similar reduction-protonation accompanied by O-O bond homolysis should afford a cupric oxyl (**Cp**) (Cu^{II}-O• ↔ Cu^{III}=O) species (**Figure 10**); the latter has only been detected in the gas phase.[56]

3.1 Synthetic Copper(II) Superoxo Complexes

Cupric superoxo species are important entities to study.[13, 20, 57] In fact, previous work has led to X-ray structures of one Cu^{II}-$O_2^{\bullet-}$ (**^{E}S**) species with tris(tetramethylguanidino)tren, $[Cu(TMG_3tren)(O_2)]^+$ (see below),[58] along with two structures[59, 60] where the superoxo (or peroxo) [60] moiety is ligated in a "side-on" η^2-binding fashion (^{S}**S**), the latter exhibit limited or no exogenous substrate reactivity due to ligand imposed steric effects. The reactivity toward substrates where C–H/O–H oxidation chemistry is achieved has been a critically lacking aspect of this subfield. However, recent newer ligand designs, e.g., with electron-releasing ligand substituents,[61] or application of extreme cryogenic conditions (e.g., down to < 125 °C),[62] have enabled generation of new ^{E}**S** complexes which exhibit important reactivity (**Figure 12**).

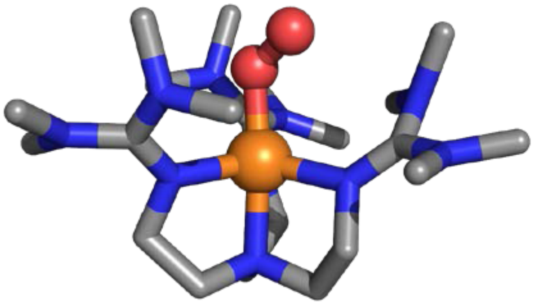

X-ray crystal structure of [Cu(TMG$_3$tren)(O$_2$)]$^+$

Itoh and co-workers[63] reported an exciting advance starting in 2009; their –80 °C stabilized ^{E}**S** complex with a tridentate alkylamino donor ligand, undergoes intramolecular benzylic C−H oxygenation (**Figure 12a**). Such reactivity is similar to that of DβM (**Scheme 2**), thus giving credence to the biochemical[18] and computational studies[21] suggesting that such a Cu^{II}-($O_2^{\bullet -}$) species ^{E}**S** (or ^{S}**S**) is responsible for the enzyme substrate HAT.

Karlin and co-workers[62] have also carried out detailed mechanistic examinations of ^{E}**S** species toward *exogenous* substrates with weak C-H bonds (**Figure 12b**). The ligand internal H-bonding group affords enough stability to generate the complex at –125 °C, yet substrate H-atom abstraction occurs.

Another set of –80 °C stabilized $^{\mathbf{E}}\mathbf{S}$ complexes possess 4-dimethylamino[61] or 4-methoxy-pyridyl ligand donors.[64] For the latter, an in-depth mechanistic study was carried out employing phenolic substrates: the $^{\mathbf{E}}\mathbf{S}$ complex effects initial and rate-determining substrate O–H bond HAT, then the phenoxyl radical produced is attacked by a second $^{\mathbf{E}}\mathbf{S}$ complex, all leading to phenol oxygenation and *p*-benzoquinone formation (**Figure 12c**).[64]

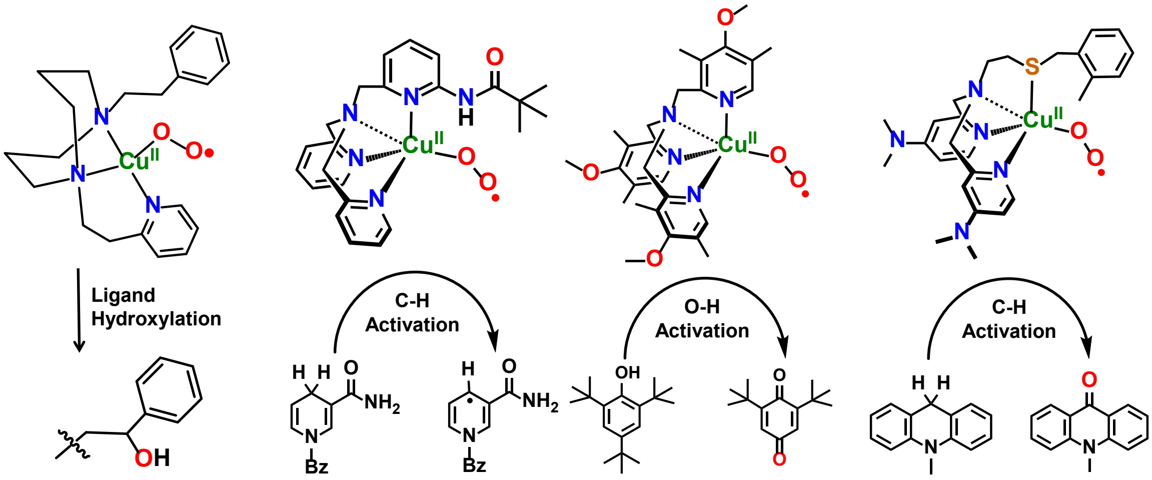

Figure 12. Spectroscopically characterized $Cu^{II}(O_2^{\bullet-})$ species: (a) Itoh's $^{\mathbf{E}}\mathbf{S}$ complex effecting intramolecular benzylic oxygenation (net hydroxylation), (b) Hydrogen-bond stabilized $^{\mathbf{E}}\mathbf{S}$ complex effecting exogenous (weak) C-H bond HAT chemistry, (c) Oxidative cleavage of O-H bond by $^{\mathbf{E}}\mathbf{S}$ possessing electron-donating groups on ligand donors and (d) Thioether-ligated $^{\mathbf{E}}\mathbf{S}$ complex with enhanced reactivity, here, toward 9,10-dihydromethylacridine. Also, see text.

Kim and co-workers recently employed a new thioether sulfur ligated (N_3S) complex (**Figure 12d**).[65] It exhibits enhanced reactivity compared to N_4 ligated $^{\mathbf{E}}\mathbf{S}$ analogs. This work is a breakthrough in synthetic biomimetic research in that the complex mimics the Cu_M center of PHM (**Figure 3**) and such studies should lead to a better understanding of the role of the PHM active site methionine ligand.

3.2 Copper(II) Hydroperoxo Model Studies

Mononuclear Cu^{II}-OOH (**Hp**) systems have been also generated and studied, again usually at low temperatures (–80 °C). They may derive from (i) addition of simple copper(II) complex precursors plus H_2O_2 in the presence of base,[66, 67] perhaps referred to as a shunt pathway (i.e., not derived from dioxygen chemistry), (ii) HAT from e^-/H^+ donors (e.g., phenols) to **^{E}S**, or (iii) addition of 1.5 equiv H_2O_2 to a fully reduced Cu^I complex, possibly initially a Fenton chemistry type reaction.[66] Well-characterized **Hp** complexes may effect oxidative N-dealkylation chemistry leading to a product 2° amine methyl group lost as formaldehyde (e.g, R_2-NCH_2R' →→ R_2NH + R'C(O)H) (**Scheme 7**), that analogous to PHM.[68]

Scheme 7. The oxidative N-dealkylation by synthetic Cu(II) hydroperoxo complex.

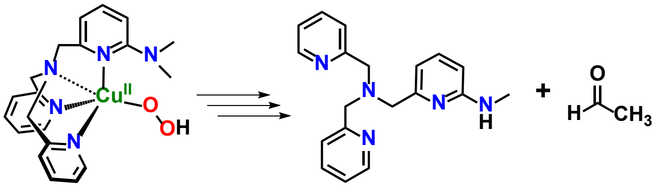

Recently, Cu–O homolytic cleavage of Cu^{II}–OOH along with subsequent site-specific Fenton chemistry was reported (**Figure 13**). The process was derived from the Cu(I) thus produced reacting with the excess H_2O_2 present.[69] In general, Cu^{II}-OOH (**Hp**) appear experimentally[66, 70] and computationally[71] to not be effective oxidants toward C–H/O–H substrates.

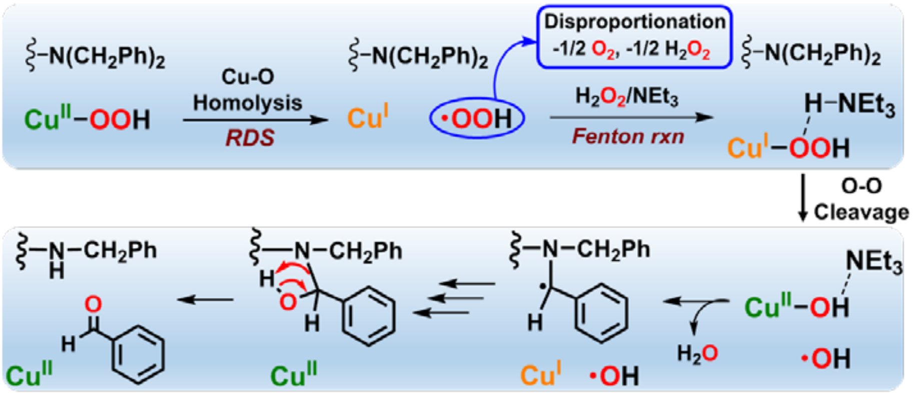

N(CH₂Ph)₂
Cu^II–OOH
Cu-O Homolysis
RDS
N(CH₂Ph)₂
Cu^I
•OOH
Disproportionation
-1/2 O₂, -1/2 H₂O₂
H₂O₂/NEt₃
Fenton rxn
N(CH₂Ph)₂
H–NEt₃
Cu^I–OOH
O-O Cleavage
NEt₃
Cu^II–OH
•OH
H₂O
N–CH₂Ph
H
Cu^I
•OH
N–CH₂Ph
H
O
H
Cu^II
N–CH₂Ph
H
O
H
Cu^II

Figure 13. The full mechanism of amine oxidative N-dealkylation via cupric hydroperoxide Cu-(OOH) homolytic cleavage followed by site-specific Fenton chemistry.

3.3 Cupric Oxyl Radical Species

There is yet no direct evidence or characterization of a Cu^{II}-oxyl (**Cp**) complex (**Figure 10**), in solution chemistry. However, in one study, Itoh and co-workers[72] provided compelling evidence for the generation of **Cp**, produced from O-O homolysis of a Cu^{II}-OOR complex, leading to a substrate C-H oxygenation (**Scheme 8**). In a DFT computational study, Beckham and co-workers[15] suggest that net C–H hydroxylation in fungal LPMOs may occur by generation of **Cp** (of course starting from Cu^{I}-O_2 chemistry). In relevant studies, Tolman and co-workers[73] have been able to study a high-valent Cu^{III}-

Scheme 8. C-H Activation by copper-oxyl intermediate generated from hemolytic O-O cleavage of Cu(II)-alkylperoxo species.

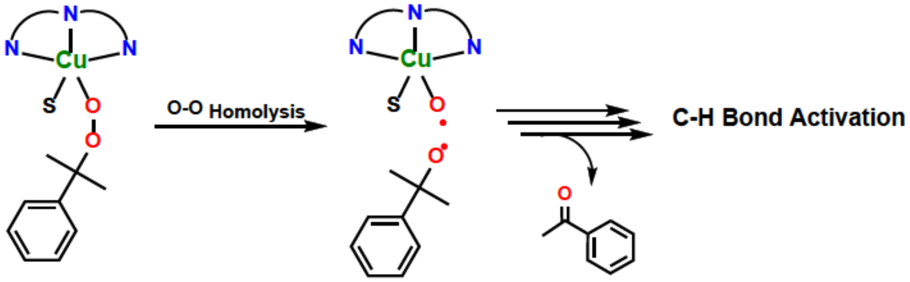

N
N
N
Cu
S
O
O
O-O Homolysis
N
N
N
Cu
S
O
O
C-H Bond Activation
O

OH species (**Figure 10**) (perhaps a protonated Cu^{II}-oxyl) which effects dihydroanthracene rate-limiting HAT oxidative chemistry.

4. Aqueous O_2-Reduction, Cu^I/O_2 Oxidase or Monooxygenase Chemistries

Aqueous reduction and protonation of molecular oxygen involve sequential electron-proton addition, as shown in **Figure 14a**. Note that as O_2 becomes further reduced, the products become stronger oxidants, such as superoxide, hydrogen peroxide ($H_2O_2 + 2e^- + 2H^+ \rightarrow 2H_2O$; E°= +1.35 V vs. NHE at pH=7), and hydroxyl radical (**Figure 14a**). In biochemical systems, reduced iron or copper complexes ‘reductively activate’ O_2 forming Fe^{III}/O_2 or Cu^I/O_2 derived species which themselves can continue to be reduced and protonated (**Figure 14b**) and/or they attack R–H substrates leading R-OH products (**Figure 14c,d,e**). In all cases, the overall reactions are four-electron four-proton processes.

Oxidase enzymes reduce O_2 to water (or H_2O_2 in some cases) where the electrons come from reductants (e.g., cytochrome *c* in cytochrome *c* oxidase (C*c*O)) or from substrates which undergo dehydrogenations (providing protons + electrons; e.g., in ascorbate, diphenols) or multicopper oxidase enzymes such as laccase.[4] Copper oxidases can be considered or compared to catalysts which mediate cathodic reactions in fuel cells,[75] further making an understanding of their chemistry of great relevance in the field of energy. **Figure 14b** depicts single-Cu site oxidase chemistry, with the point being that here we find O_2-derived copper-oxygen species which must form, i.e., they are critical to the whole process of capturing the energy stored in dioxygen when reduced to water, that being +0.82 V at pH = 7.[4]

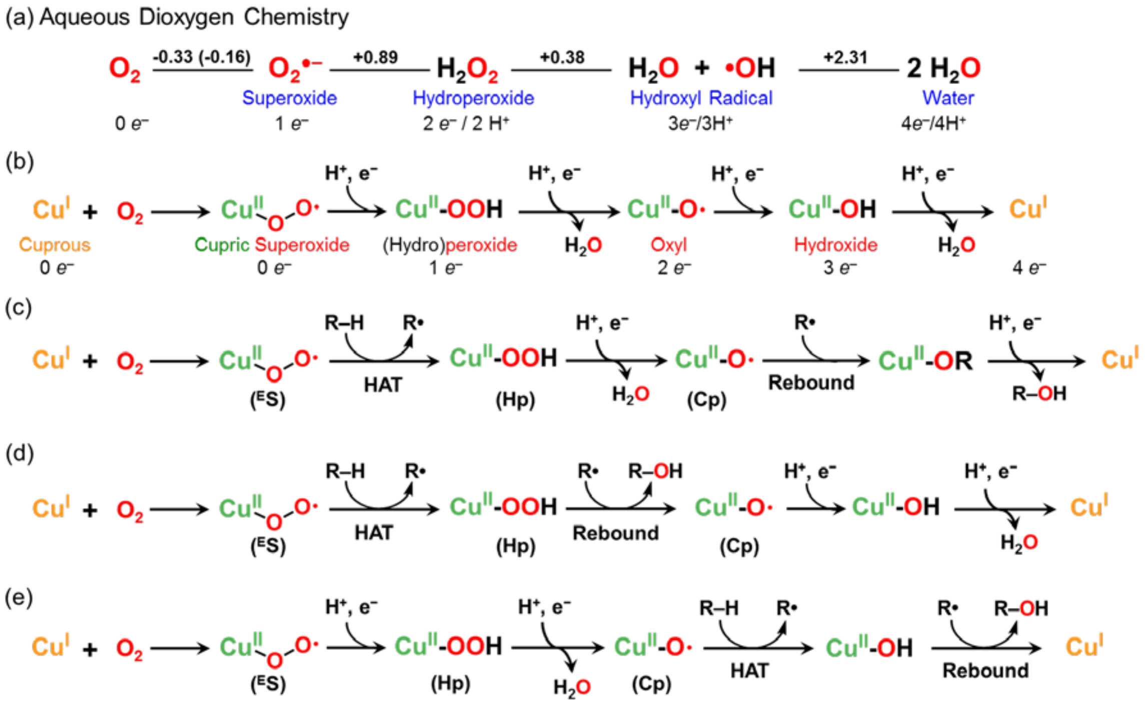
(a) Aqueous Dioxygen Chemistry
O2
-0.33 (-0.16)
O2•−
+0.89
H2O2
+0.38
H2O + •OH
+2.31
2 H2O
Superoxide
Hydroperoxide
Hydroxyl Radical
Water
0 e−
1 e−
2 e− / 2 H+
3e−/3H+
4e−/4H+
(b)
CuI + O2
CuII-O-O•
CuII-OOH
CuII-O•
CuII-OH
CuI
H+, e−
H2O
Cuprous
Cupric Superoxide
(Hydro)peroxide
Oxyl
Hydroxide
0 e−
1 e−
2 e−
3 e−
4 e−
(c)
R–H
R•
HAT
Rebound
R–OH
CuII-OR
(ES)
(Hp)
(Cp)
(d)
(e)

Figure 14. (a) Aqueous four-electron four-proton O_2-reduction to water; reduction potentials shown are for pH = 7. (b) Copper oxidase reactivity and intermediates relevant for single copper site chemistry. (c),(d),(e) Single-copper site stepwise monooxygenase chemistry. As must be the case, overall four-electron reduction chemistry occurs, where two derive from a substrate R–H bond; the other two electrons come from donors such as ascorbic acid. All O_2-derived species, superoxo (**^{E}S**), (hydro)peroxo (**Hp**) or cupryl (**Cp**), must be generated (in some form). The variations in chemistry, (c) vs (d) vs (e), are that for each, initial HAT chemistry with the substrate (R–H → R•) is effected by a different copper-oxygen intermediate, (**^{E}S**), (**Hp**) or (**Cp**). Still, other pathways or mechanisms are possible. Also, see text.

However, what is critically lacking is our knowledge of the details depicted in **Figure 14b**. Future research is required to elucidate fundamental information such as reduction potentials (E° or E°'(pH = 7)), e.g., for Cu^{II}-$O_2^{\bullet-}$ (**^{E}S** or **^{S}S**) species, and their reduction to Cu^{II}-peroxo complexes. Alternatively, stepwise or proton-coupled reduction to Cu^{II}-OOH (**Hp**) may be preferred or required; aqueous superoxide anion ($O_2^{\bullet-}$) cannot be reduced without the presence of a proton.[74]

Thus, we also need to learn about the basicity of the superoxo complex O-atoms, since a proton is normally required to effect an electron-transfer reduction, but what acid strength (pKa) is needed? The same kind of information, reduction potentials and O-atom basicities, is needed for each subsequent step, Cu^{II}-OOH (**Hp**) + H^+/e^- → Cu^{II}-O• (**Cp**) + H_2O, and **Cp** + H^+/e^- → Cu^{II}-OH (**Figure 14b**). The former step is the critically important reductive cleavage reaction, that important for oxidase chemistry (O_2-reduction to water) and for substrate oxygenation (e.g., **Figure 14c,d,e**). Such chemistries are thus widely applicable to heme, non-heme iron, copper biochemistries and metal-mediated stoichiometric or catalytic substrate oxidation-oxygenation chemistries, thus important for practical and/or industrial situations.

In reality, the amount of basic/fundamental information needed is in fact vastly multiplied from what is discussed and illustrated here; (i) the environment around the metal (the ligand and second sphere) very much influences or even controls factors such as reduction potentials and M-$(H)O_2^{n-}$ basicity, and (ii) all these chemistries need to be evaluated in more complex systems where 2 or 3 proximate copper ions constitute the catalyst center, as occurs in multi-copper oxidases or in C*c*O (with heme-Cu dimetal active site).[3, 4] (iii) Simultaneous multi-electron (i.e., $2e^-$) processes may occur,[3] so different with what is represented in **Figure 14**. Thus, in practice, nature does not utilize mononuclear Cu centers to effect oxidase chemistry; however, an understanding of the **Figure 14b** chemistry is a critical start.

Figure 14c, **d**, and **e** outline pathways in which a monooxygenase may function, as possibly occurs at the PHM Cu_M active site. See earlier works in which such comparisons of pathways have been presented.[76, 77] But which entity, $^{\mathbf{E}}$**S**, $^{\mathbf{S}}$**S**, **Hp** or **Cp** is the species that initially attacks the substrate to effect HAT from R–H, giving R•? Pathways **c** and **d** involve $^{\mathbf{E}}$**S** or $^{\mathbf{S}}$**S** substrate HAT, but they differ in that either ‘rebound’ of the O-atom to

R• occurs at different stages. Klinman and co-workers prefer pathway **c**, but calculations from Chen & Solomon suggest pathway **d**.[77] Other mechanisms have also been suggested.[77,78]

If, as strongly suggested, an **^{E}S** or **^{S}S** copper-superoxo intermediate effects substrate HAT in PHM, than this dramatically differs from the situation for cytochrome P-450 monooxygenase, the 'classic' system known for C–H oxygenation.[79] There, protons and electrons are stepwise added the ferrous-heme O_2-adduct, to form an iron^{IV}-porphrin-π-cation-radical (≡ Fe^{V}), that derived from heterolytic cleavage of an Fe^{III}-OOH intermediate. Closest to that by analogy would be that illustrated by pathway **Figure 14e**. But there, homolytic O-O reductive cleavage occurs to give a Cu^{II}-oxyl species (**Cp**). If a proton plus protein (or ligand)-derived electron could be further provided, heterolysis could occur, giving a (X$^{\bullet+}$)Cu^{II}-oxyl intermediate (≡ Cu^{IV}=O formally) plus H_2O.[78]

Figure 14e, itself, represents the situation where Cu^{I}/O_2 chemistry proceeds to a Cu^{II}–O• (**Cp**) species, the last reactive intermediate possible following reduction-protonation of O_2 at a mononuclear Cu site. As mentioned, based on one recent computational study, it is pathway **14e** and a **Cp** reactive intermediate which is relevant at polysaccharide monooxygenation at the active site of LPMOs.[15]

5. Conclusion and Perspectives

The chemistry represented by **Figure 14**, with all the possible Cu^{I}/O_2 derived reduced and/or protonated intermediates, is for coordination chemists or synthetic bioinorganic chemists, a vast field of research targets for study. The understanding of copper ion complexes as biochemical or synthetic entities able to catalyze oxidation reactions using readily available molecular oxygen is very important. As described, precedence exists for copper mediated oxidation, i.e., C–H activation and O–H oxidation, of substrates such as methane, polysaccharides, or tyrosine. The understanding of such chemistries can also be applied to the design of copper ion based fuel-cell catalysts. Elucidation of underlying principles and details of reduction, protonation, the timing of these preceding events, Cu-oxy species' (i.e., $^{\mathbf{E}}\mathbf{S}$, $^{\mathbf{S}}\mathbf{S}$**, Hp, Cp**, or even multicopper containing analogs**)** structure, and determination of reaction mechanisms are all important goals. Determination of reduction potentials for Cu^I/O_2 derived reduced species (e.g., $^{\mathbf{E}}\mathbf{S}$, $^{\mathbf{S}}\mathbf{S}$, $^{\mathbf{T}}\mathbf{P}$, $^{\mathbf{S}}\mathbf{P}$, $^{\mathbf{C}}\mathbf{P}$, **O**, **Hp** and **Cp**), and comparison in an absolute or relative sense, to those of free O_2-reduced species, is also of fundamental importance.

Looking to the chemistry involved at copper enzyme active sites can lead to new insights to the field of bio-inspired chemistry field. In addition to protein studies, establishing small molecule model systems and investigating their fundamental properties will be critical. Which $Cu\text{-}O_2$ intermediate is effective to carry out what chemistry? Although the dicopper complexes, $^{\mathbf{T}}\mathbf{P}$, $^{\mathbf{S}}\mathbf{P}$ and **O** are well studied, further insights are still needed. However, especially it is important to target the generation and investigations of the chemistry of mixed-valent species like **MV** or **MV-H**. Also, can different sorts of $\mathbf{Cu_2O}$ species be discovered that will enable the oxidative attack of strong C-H bonds. As the His-brace copper ion ligation is critical in LPMOs and pMMO, elucidation of its effect on Cu^I/O_2 chemistry is needed. Perhaps the recent study by Stack and co-workers[50] has already provided insight. Very recent breakthroughs in the generation and reactivity of $Cu^{II}\text{-}O_2^{\bullet -}$ species indicate that this sub-field can be further explored. The relationship between copper-ligation and $^{\mathbf{E}}\mathbf{S}$ or $^{\mathbf{S}}\mathbf{S}$ reactivity requires elucidation. An intriguing point for consideration of monocopper O_2-chemistry is that a new computational study[80] suggests that the reactive species in PHM is a $[Cu^{II}\text{-}O_2^{\bullet-}(H)]^{2+}$ entity, i.e., with a protonated superoxide. $HO_{2\,(aq)}$ is a much stronger HAT reagent than is the coordinated $O_2^{\bullet-}$ anion.[74] Even with the Lewis acidic Cu(II) ion present and ligated, perhaps $[Cu^{II}\text{-}O_2^{\bullet-}(H)]^{2+}$, as suggested,[80] is required to effect HAT chemistry producing R• + Cu^{II}-OOH plus release of that "extra" proton. In addition to the recently developed tetradentate sulfur-ligated N_3S-**^{E}S** complex, new reactive overall tridentate N_2S-**^{E}S** species are targets for synthetic studies, in relationship to the active site in PHM. Detailed mechanistic investigation of the reductive O–O cleavage of Cu^{II}-OOH (**Hp**), i.e., elucidating insights (into pKa of added acids, site of protonation, etc.) is not only critical to the field of Cu^{I}/O_2 chemistry, but also for all fields and aspects of metal-O_2 (bio)chemical reactivity. Such studies can also provide insights to the formation and chemistry of the cupryl Cu^{II}-O• (**Cp**) species. The study of Cu-oxyl (**Cp**) species is surely a critical, not only in how it forms but also as to what is its solution substrate reactivity profile. It is expected to be the most reactive, "hottest", Cu^{I}-O_2 derived species, and likely important is LPMOs or possibly in pMMO.

The field of biochemical and synthetic bioinorganic O_2-activation by copper ion is exciting. While numerous insights have been obtained in the last 30 years, many challenges for both fundamental and practical chemistry applications remain.

6. References

1. Solomon, E. I.; Hadt, R. G., *Coord. Chem. Rev.* **2011,** *255* (7–8), 774-789.

2. Hatcher, L.; Karlin, K., *J. Biol. Inorg. Chem.* **2004,** *9* (6), 669-683.

3. Solomon, E. I.; Heppner, D. E.; Johnston, E. M.; Ginsbach, J. W.; Cirera, J.; Qayyum, M.; Kieber-Emmons, M. T.; Kjaergaard, C. H.; Hadt, R. G.; Tian, L., *Chem. Rev.* **2014,** *114* (7), 3659-3853.

4. Peterson, R. L.; Kim, S.; Karlin, K. D., 3.07 - Copper Enzymes. In *Comprehensive Inorganic Chemistry II (Second Edition)*, Reedijk, J.; Poeppelmeier, K., Eds. Oxford: Elsevier: Amsterdam, 2013; Vol. 3, pp 149-177, http://dx.doi.org/10.1016/B978-0-08-097774-4.00309-0.

5. Casey, P. S.; McAllister, T.; Foger, K., *Ind. Eng. Chem. Res.* **1994,** *33* (5), 1120-1125.

6. Chang, M. C. Y., *Curr. Opin. Chem. Biol.* **2007,** *11* (6), 677-684.

7. Beeson, W. T.; Vu, V. V.; Span, E. A.; Phillips, C. M.; Marletta, M. A., *Ann. Rev. Biochem.* **2015**.

8. Nagasawa, K.; Tohira, Y.; Inoue, Y.; Tanoura, N., *Carbohydr. Res.* **1971,** *18* (1), 95-102.

9. Hemsworth, G. R.; Henrissat, B.; Davies, G. J.; Walton, P. H., *Nat Chem Biol* **2014,** *10* (2), 122-126.

10. Vu, V. V.; Beeson, W. T.; Span, E. A.; Farquhar, E. R.; Marletta, M. A., *Proc. Natl. Acad. Sci.* **2014,** *111* (38), 13822-13827; Lo Leggio, L.; Simmons, T. J.; Poulsen, J.-C. N.; Frandsen, K. E. H.; Hemsworth, G. R.; Stringer, M. A.; von Freiesleben, P.; Tovborg, M.;

Johansen, K. S.; De Maria, L.; Harris, P. V.; Soong, C.-L.; Dupree, P.; Tryfona, T.; Lenfant, N.; Henrissat, B.; Davies, G. J.; Walton, P. H., *Nat Commun* **2015,** *6*.

11. Gudmundsson, M.; Kim, S.; Wu, M.; Ishida, T.; Momeni, M. H.; Vaaje-Kolstad, G.; Lundberg, D.; Royant, A.; Ståhlberg, J.; Eijsink, V. G. H.; Beckham, G. T.; Sandgren, M., *J. Biol. Chem.* **2014,** *289* (27), 18782-18792.

12. Li, X.; Beeson Iv, William T.; Phillips, Christopher M.; Marletta, Michael A.; Cate, Jamie H. D., *Structure* **2012,** *20* (6), 1051-1061.

13. Kjaergaard, C. H.; Qayyum, M. F.; Wong, S. D.; Xu, F.; Hemsworth, G. R.; Walton, D. J.; Young, N. A.; Davies, G. J.; Walton, P. H.; Johansen, K. S.; Hodgson, K. O.; Hedman, B.; Solomon, E. I., *Proc. Natl. Acad. Sci.* **2014**, 8797–8802.

14. Phillips, C. M.; Beeson, W. T.; Cate, J. H.; Marletta, M. A., *ACS Chem. Biol.* **2011,** *6* (12), 1399-1406; Beeson, W. T.; Phillips, C. M.; Cate, J. H. D.; Marletta, M. A., *J. Am. Chem. Soc.* **2012,** *134* (2), 890-892.

15. Kim, S.; Ståhlberg, J.; Sandgren, M.; Paton, R. S.; Beckham, G. T., *Proc. Natl. Acad. Sci.* **2014,** *111* (1), 149-154.

16. Klinman, J. P., *Chem. Rev.* **1996,** *96* (7), 2541-2562.

17. Klinman, J. P., *Chem. Rev.* **1996,** *96*, 2541-2561.

18. Klinman, J. P., *J. Biol. Chem.* **2006,** *281*, 3013-3016.

19. Prigge, S. T.; Kolhekar, A.; Eipper, B. A.; Mains, R. E.; Amzel, M., *Science* **1997,** *278*, 1300-1305.

20. Prigge, S. T.; Eipper, B.; Mains, R.; Amzel, L. M., *Science* **2004,** *304*, 864-867.

21. Chen, P.; Solomon, E. I., *J. Am Chem. Soc.* **2004,** *126*, 4991-5000.

22. Evans, J. P.; Ahn, K.; Klinman, J. P., *J. Biol. Chem.* **2003,** *278* (50), 49691-49698.

23. Chen, P.; Solomon, E. I., *J. Am. Chem. Soc.* **2004,** *126* (15), 4991-5000.

24. Klinman, J. P., *J. Biol. Chem.* **2006,** *281* (6), 3013-3016.

25. Tinberg, C. E.; Lippard, S. J., *Acc. Chem. Res.* **2011,** *44* (4), 280-288.

26. Culpepper, M. A.; Rosenzweig, A. C., *Crit. Rev. Biochem. and Mo. Biol.* **2012,** *47* (6), 483-492.

27. Lieberman, R. L.; Rosenzweig, A. C., *Nature* **2005,** *434* (7030), 177-182.

28. Himes, R.; Barnese, K.; Karlin, K., *Angew. Chem. Intl. Ed.* **2010,** *49* (38), 6714-6716.

29. Himes, R. A.; Karlin, K. D., *Curr. Opin. Chem. Biol.* **2009,** *13* (1), 119-131.

30. Culpepper, M. A.; Cutsail Iii, G. E.; Gunderson, W. A.; Hoffman, B. M.; Rosenzweig, A. C., *J. Am. Chem. Soc.* **2014,** *136* (33), 11767-11775.

31. Chan, S. I.; Yu, S. S.-F., *Accounts Chem. Res.* **2008,** *41* (8), 969-979.

32. Quinlan, R. J.; Sweeney, M. D.; Lo Leggio, L.; Otten, H.; Poulsen, J.-C. N.; Johansen, K. S.; Krogh, K. B. R. M.; Jørgensen, C. I.; Tovborg, M.; Anthonsen, A.; Tryfona, T.; Walter, C. P.; Dupree, P.; Xu, F.; Davies, G. J.; Walton, P. H., *Proc. Natl. Acad. Sci.* **2011,** *108* (37), 15079-15084.

33. Whittaker, J. W., *Chem. Rev.* **2003,** *103* (6), 2347-2364.

34. Ito, N.; Phillips, S. E. V.; Stevens, C.; Ogel, Z. B.; McPherson, M. J.; Keen, J. N.; Yadav, K. D. S.; Knowles, P. F., *Nature* **1991,** *350* (6313), 87-90.

35. Que, L.; Tolman, W. B., *Nature* **2008,** *455* (7211), 333-340.

36. Wilmot, C. M.; Hajdu, J.; McPherson, M. J.; Knowles, P. F.; Phillips, S. E. V., *Science* **1999,** *286* (5445), 1724-1728.

37. Klinman, J. P., *Biochimica et Biophysica Acta (BBA) - Proteins and Proteomics* **2003,** *1647* (1–2), 131-137.

38. Cai, D.; Klinman, J. P., *J. Biol. Chem.* **1994,** *269* (51), 32039-32042.

39. Mure, M.; Mills, S. A.; Klinman, J. P., *Biochemistry* **2002,** *41* (30), 9269-9278.

40. Mills, S. A.; Klinman, J. P., *J. Am. Chem. Soc.* **2000,** *122* (41), 9897-9904; Schwartz, B.; Olgin, A. K.; Klinman, J. P., *Biochemistry* **2001,** *40* (9), 2954-2963.

41. Rokhsana, D.; Shepard, E. M.; Brown, D. E.; Dooley, D. M., Amine Oxidase and Galactose Oxidase. In *Copper-Oxygen Chemistry*, John Wiley & Sons, Inc.: 2011; pp 53-106.

42. Shepard, E. M.; Okonski, K. M.; Dooley, D. M., *Biochemistry* **2008,** *47* (52), 13907-13920.

43. Mirica, L. M. a. O. X. a. S. T. D. P., *Chem. Rev.* **2004,** *104* (2), 1013-1046.

44. Lucas, H. R.; Li, L.; Sarjeant, A. A. N.; Vance, M. A.; Solomon, E. I.; Karlin, K. D., *J. Am. Chem. Soc.* **2009,** *131* (9), 3230-3245; Würtele, C.; Sander, O.; Lutz, V.; Waitz, T.; Tuczek, F.; Schindler, S., *J. Am. Chem. Soc.* **2009,** *131* (22), 7544-7545.

45. Dalle, K. E.; Gruene, T.; Dechert, S.; Demeshko, S.; Meyer, F., *J. Am. Chem. Soc.* **2014,** *136* (20), 7428-7434.

46. Matsumoto, T.; Ohkubo, K.; Honda, K.; Yazawa, A.; Furutachi, H.; Fujinami, S.; Fukuzumi, S.; Suzuki, M., *J. Am. Chem. Soc.* **2009,** *131* (26), 9258-9267.

47. Que, L., Jr.; Tolman, W. B., *Angew. Chem. Int. Ed.* **2002,** *41* (7), 1114-1137.

48. Mirica, L. M.; Ottenwaelder, X.; Stack, T. D. P., *Chem. Rev.* **2004,** *104*, 1013-1045.

49. Itoh, S.; Nakao, H.; Berreau, L. M.; Kondo, T.; Komatsu, M.; Fukuzumi, S., *J. Am. Chem. Soc.* **1998,** *120* (12), 2890-2899; Shearer, J.; Zhang, C. X.; Zakharov, L. N.;

Rheingold, A. L.; Karlin, K. D., *J. Am. Chem. Soc.* **2005,** *127* (15), 5469-5483; Maiti, D.; Woertink, J. S.; Narducci Sarjeant, A. A.; Solomon, E. I.; Karlin, K. D., *Inorg. Chem.* **2008,** *47* (9), 3787-3800.

50. Citek, C.; Lin, B.-L.; Phelps, T. E.; Wasinger, E. C.; Stack, T. D. P., *J. Am. Chem. Soc.* **2014,** *136* (41), 14405-14408.

51. Himes, R. A.; Karlin, K. D., *Proc. Natl Acad. Sci. USA* **2009,** *106* (45), 18877-18878.

52. Shiota, Y.; Yoshizawa, K., *Inorg, Chem.* **2009,** *48* (3), 838-845.

53. Shiota, Y.; Juhász, G.; Yoshizawa, K., *Inorg. Chem.* **2013,** *52* (14), 7907-7917.

54. Woertink, J. S.; Smeets, P. J.; Groothaert, M. H.; Vance, M. A.; Sels, B. F.; Schoonheydt, R. A.; Solomon, E. I., *Proc. Natl Acad. Sci. USA* **2009,** *106* (45), 18908-18913.

55. Haack, P.; Limberg, C., *Angew. Chem. Int. Ed. Engl.* **2014,** *53* (17), 4293-4353.

56. Schröder, D.; Holthausen, M. C.; Schwarz, H., *J. Phys. Chem. B* **2004,** *108* (38), 14407-14416; Decker, A.; Solomon, E. I., *Curr. Opin. Chem. Biol.* **2005,** *9* (2), 152-163; Dietl, N.; Schlangen, M.; Schwarz, H., *Angew. Chem. Intl. Ed.* **2012,** *51* (23), 5544-5555.

57. Itoh, S., *Curr. Opin. Chem. Biol.* **2006,** *10* (2), 115-122.

58. Würtele, C.; Heinemann, F. W.; Schindler, S., *J. Coord. Chem.* **2010,** *63* (14-16), 2629-2641.

59. Fujisawa, K.; Tanaka, M.; Morooka, Y.; Kitajima, N., *J. Am. Chem. Soc.* **1994,** *116* (26), 12079-12080.

60. Aboelella, N. W.; Lewis, E. A.; Reynolds, A. M.; Brennessel, W. W.; Cramer, C. J.; Tolman, W. B., *J. Am. Chem. Soc.* **2002,** *124* (36), 10660-10661.

61. Maiti, D.; Fry, H. C.; Woertink, J. S.; Vance, M. A.; Solomon, E. I.; Karlin, K. D., *J. Am. Chem. Soc.* **2007,** *129* (2), 264-265.

62. Peterson, R. L.; Himes, R. A.; Kotani, H.; Suenobu, T.; Tian, L.; Siegler, M. A.; Solomon, E. I.; Fukuzumi, S.; Karlin, K. D., *J. Am. Chem. Soc.* **2011,** *133* (6), 1702-1705.

63. Kunishita, A.; Kubo, M.; Sugimoto, H.; Ogura, T.; Sato, K.; Takui, T.; Itoh, S., *J. Am. Chem. Soc.* **2009,** *131* (8), 2788-2789; Kunishita, A.; Ertem, M. Z.; Okubo, Y.; Tano, T.; Sugimoto, H.; Ohkubo, K.; Fujieda, N.; Fukuzumi, S.; Cramer, C. J.; Itoh, S., *Inorg. Chem.* **2012,** *51* (17), 9465-9480.

64. Lee, J. Y.; Peterson, R. L.; Ohkubo, K.; Garcia-Bosch, I.; Himes, R. A.; Woertink, J.; Moore, C. D.; Solomon, E. I.; Fukuzumi, S.; Karlin, K. D., *J. Am. Chem. Soc.* **2014,** *136* (28), 9925-9937.

65. Kim, S.; Lee, J. Y.; Cowley, R. E.; Ginsbach, J. W.; Siegler, M. A.; Solomon, E. I.; Karlin, K. D., *J. Am. Chem. Soc.*, **2015**, *137* (8), 2796–2799.

66. Kim, S.; Saracini, C.; Siegler, M. A.; Drichko, N.; Karlin, K. D., *Inorg. Chem.* **2012,** *51* (23), 12603-12605.

67. Kunishita, A.; Kubo, M.; Ishimaru, H.; Ogura, T.; Sugimoto, H.; Itoh, S., *Inorg. Chem.* **2008,** *47* (24), 12032-12039.

68. Maiti, D.; Narducci Sarjeant, A. A.; Karlin, K. D., *Inorg. Chem.* **2008,** *47* (19), 8736-8747.

69. Kim, S.; Ginsbach, J. W.; Lee, J. Y.; Peterson, R. L.; Liu, J. J.; Siegler, M. A.; Sarjeant, A. A.; Solomon, E. I.; Karlin, K. D., *Am. Chem. Soc.*, **2015**, *137* (8), 2867–2874

70. Choi, Y. J.; Cho, K.-B.; Kubo, M.; Ogura, T.; Karlin, K. D.; Cho, J.; Nam, W., *Dalton Trans.,* **2011,** *40* (10), 2234-2241.

71. Chen, P.; Fujisawa, K.; Solomon, E. I., *J. Am. Chem. Soc.* **2000,** *122* (41), 10177-10193.

72. Kunishita, A.; Ishimaru, H.; Nakashima, S.; Ogura, T.; Itoh, S., *J. Am. Chem. Soc.* **2008,** *130*, 4244-4245.

73. Dhar, D.; Tolman, W. B., *J. Am. Chem. Soc.* **2015,** *137*, 1322-1329.

74. Warren, J. J.; Tronic, T. A.; Mayer, J. M., *Chem. Rev.* **2010,** *110* (12), 6961-7001.

75. Thorseth, M. A.; Tornow, C. E.; Tse, E. C. M.; Gewirth, A. A., *Coord. Chem. Rev.* **2013,** *257* (1), 130-139.

76. Bollinger, J. J. M.; Krebs, C., *Curr. Opin. Chem. Biol.* **2007,** *11* (2), 151-158.

77. de la Lande, A.; Parisel, O.; Gérard, H.; Moliner, V.; Reinaud, O., *Chem. – Eur. J.* **2008,** *14* (21), 6465-6473.

78. Crespo, A.; Marti, M. A.; Roitberg, A. E.; Amzel, L. M.; Estrin, D. A., *J. Am. Chem. Soc.* **2006,** *128* (39), 12817-12828.

79. Groves, J. T., *Nat Chem* **2014,** *6* (2), 89-91; McQuarters, A. B.; Wolf, M. W.; Hunt, A. P.; Lehnert, N., *Angew. Chem. Intl. Ed.* **2014,** *53* (19), 4750-4752.

80. Abad, E.; Rommel, J. B.; Kaestner, J., *J. Biol. Chem.* **2014,** *289* (20), 13726-13738.

Chapter 2:

Mechanistic Insights into the Oxidation of Substituted Phenols *via* Hydrogen Atom Abstraction by a Cupric Superoxo Complex

This work was accomplished with the aid of the following collaborators and was published under the following citation:

Jung Yoon Lee, Ryan L. Peterson, Kei Ohkubo, Isaac Garcia-Bosch, Richard A. Himes, Julia Woertink, Cathy D. Moore, Edward I. Solomon, Shunichi Fukuzumi, and Kenneth D. Karlin

J. Am. Chem. Soc., **2014**, *136* (28), pp 9925−9937

Abstract

To obtain mechanistic insights into the inherent reactivity patterns for copper(I)-O_2 adducts, a new cupric-superoxo complex $[(\text{DMM-tmpa})\text{Cu}^{\text{II}}(O_2^{\bullet-})]^+$ (**2**) [DMM-tmpa = tris((4-methoxy-3,5-dimethylpyridin-2-yl)methyl)amine] has been synthesized and studied in phenol oxidation-oxygenation reactions. Compound **2** is characterized by UV-vis,

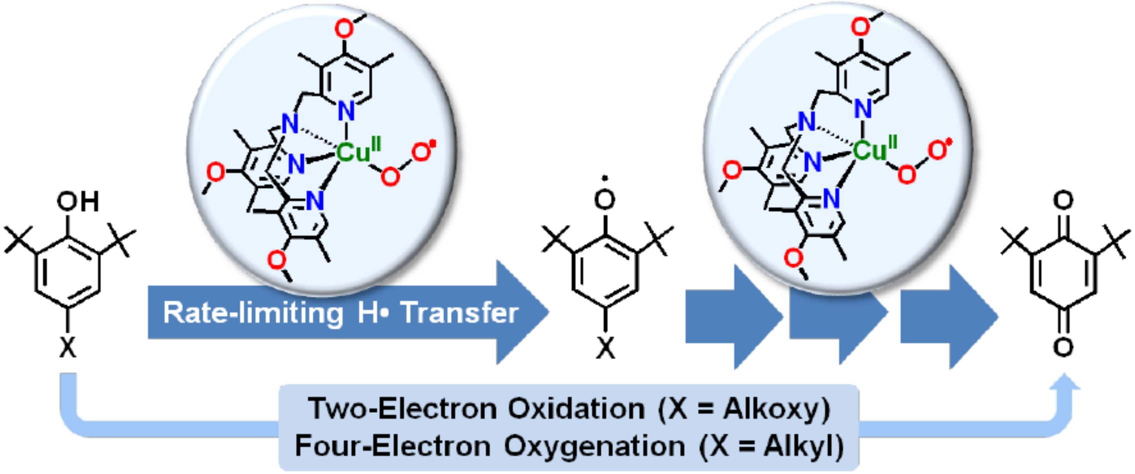
OH
X
N
N
N
Cu^II
Rate-limiting H• Transfer
X
O
O
Two-Electron Oxidation (X = Alkoxy)
Four-Electron Oxygenation (X = Alkyl)

resonance Raman and EPR spectroscopies. Its reactions with a series of *para*-substituted-2,6-di-*tert*-butylphenols (*p*-X-DTBP's) afford 2,6-di-*tert*-butyl-1,4-benzoquinone (DTBQ) in up to 50 % yields. Significant deuterium kinetic isotope effects (KIE's) and a positive correlation of second-order-rate constants (k_2's) compared to rate constants for *p*-X-DTBP's plus cumylperoxyl radical reactions indicate a mechanism involves rate-limiting hydrogen atom transfer (HAT). A weak correlation of (k_BT/e) lnk_2 *vs* E_{ox} of *p*-X-DTBP's indicates the HAT reactions proceed *via* a partial transfer of charge rather than a complete transfer of charge in the electron-transfer/proton-transfer (ET/PT) pathway. Product analyses, ^{18}O-labeling experiments, and separate reactivity employing the 2,4,6-tri-*tert*-butylphenoxyl radical provide further mechanistic insights. After initial HAT, a second mole equiv **2** couples to the phenoxyl radical initially formed, giving a Cu^{II}-OO-(ArO') intermediate, which proceeds in the case of *p*-OR-DTBP substrates *via* a two-electron oxidation reaction involving hydrolysis steps which liberate H_2O_2 and the corresponding alcohol. By contrast, four-electron oxygenation (O-O cleavage) mainly occurs for *p*-R-DTBP which gives ^{18}O-labeled DTBQ and elimination of the R group.

1. Introduction

Investigation of the structure and reactivity of various Cu^I/O$_2$ adducts (**Chart 1**), those derived from the reaction of reduced ligand-copper(I) complexes with molecular oxygen (dioxygen) occurs in large part due to their critical roles in metalloenzymes.[1] Monocopper complexes **A**-**C** or dinuclear species **E**-**G**, or their analogs, have been discovered and insights into their electronic structural characteristics and 3-D structures have been obtained.[1] Formally high-valent species **D** has been detected in the gas phase,[2] hinted at in coordination chemistry studies[3] or discussed computationally.[4] Among them, the mononuclear species such as cupric superoxide (**A** and **B**), cupric hydroperoxide (**C**), and copper oxyl (**D**) species all have been considered as highly reactive intermediates which likely participate in overall reaction sequences occurring in copper enzyme bio-transformations.[5]

Chart 1. Oxygen-derived copper species.

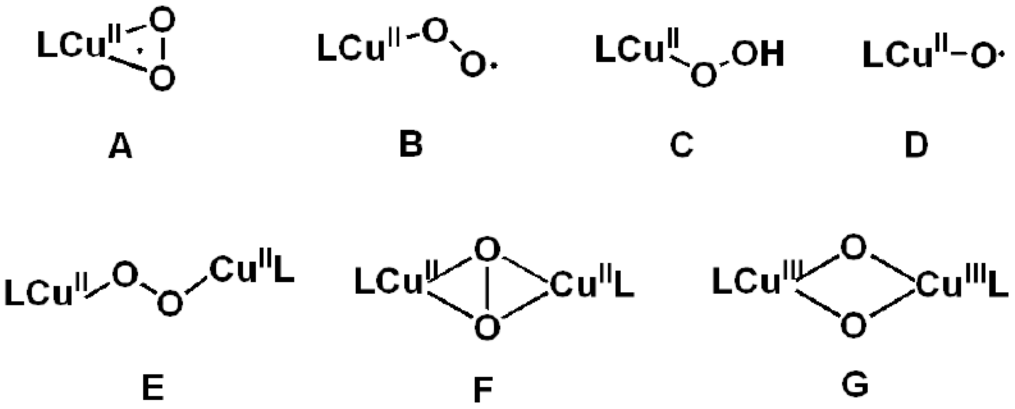

They may hydroxylate the substrate C-H bond in copper enzymes such as peptidylglycine-*α*-hydroxylating monooxygenase (PHM) and dopamine-*β*-monooxygenase (D*β*M)[6, 7] or initiate O-H oxidation in copper oxidases such as galactose oxidase (GO)[6, 8, 9] or copper amine oxidase (CAO).[6, 10] From relatively recent experimental and computational studies, the $[\mathrm{Cu^{II}}(\mathrm{O_2^{\bullet-}})]^+$ (**A** or **B**) moiety has been declared as the reactive intermediate which effects C–H[11,12] or O–H[7, 8] hydrogen-atom transfer (HAT) reactions. Relevant to this is an X-ray crystallographic study on a PHM derivative, which reveals a dioxygen-derived species assigned as an end-on bound cupric superoxo species (**B**) (also discussion below).[13] As is relevant to part of the GO catalytic cycle, recent experimental studies support a mechanism wherein O_2-binding to this fully reduced copper ion affords a cupric superoxo species (**Figure 1**) and that this mediates the oxidation of the ligated tyrosine residue resulting in the formation of a cupric hydroperoxide species (**C**) plus phenoxyl radical.[9] Hydrolysis leads to the release of hydrogen peroxide, the observed stoichiometric O_2 reduction product in the overall mechanism.

With this background, one of the research goals that we have recently been emphasizing is on the chemistry of cupric superoxo complexes. It is critical to elucidate chemical/physical properties, spectroscopic characteristics and reactivity toward substrates possessing C-H or O-H bonds. An understanding of such aspects is critical in order to fully elucidate fundamentals involved in oxidative processes and the reduction of dioxygen by copper centers in chemical systems or at the active sites of metalloenzymes.

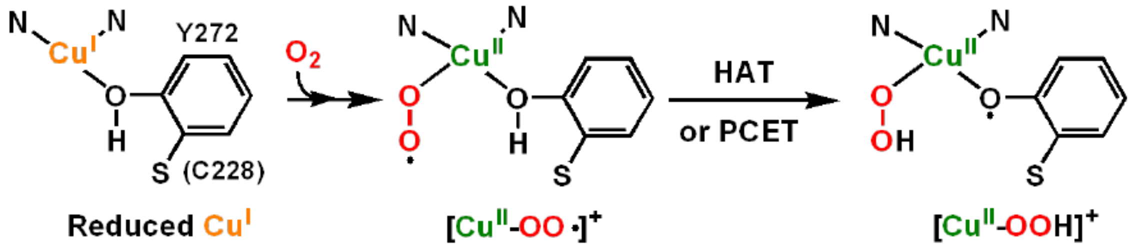

Figure 1. Reduction of molecular oxygen in galactose oxidase (GO). See Supporting Information (**Figure S1a**) for fuller details.

In this report, we describe the chemistry of a new $[Cu^{II}(O_2^{\bullet -})]^+$ complex and a detailed investigation into its reactions with phenolic substrates. As discussed above, the net hydrogen atom abstraction reaction from a phenol derivative is directly relevant to the enzyme chemistry in GO. Similar reactivity occurs in copper amine oxidase (CAO) where a cupric superoxo species is thought to undergo a proton-coupled electron transfer (PCET) process converting TPQ_{SQ} (2,4,5-trihyroxyphenylalanine semiquinone) to TPQ_{IMQ}, the one-electron oxidized iminoquinone form (**Figure S1b**).[10] As mentioned, phenols can undergo oxidation by two pathways, both resulting in formation of the neutral phenoxyl radical and transfer of a hydrogen atom to the oxidant, eq 1. Mechanistically, the process can occur by PCET[14] or hydrogen atom transfer (HAT) and these are fundamentally important reactions occurring in many biological systems.

$$\mathrm{ArOH} \rightarrow \mathrm{ArO}\bullet + \mathrm{H}\bullet \qquad (1)$$

Itoh, Fukuzumi and co-workers[15] previously investigated phenol (and C-H) oxidation chemistry using binuclear complexes of the type (μ-η^2:η^2-peroxo)dicopper(II) (**F**) and/or bis(μ-oxo)dicopper (III) (**G**). For a series of phenols, kinetic/mechanistic studies demonstrated that these oxidations proceeded *via* PCET rather than HAT. However, studies on the reactivity of mononuclear Cu^{I}/O$_2$ species are scarce and in fact no detailed mechanistic investigations have been described. Only recently have ligand design and synthetic methodologies better allowed for the formation of discrete [Cu^{II}(O$_2^{\bullet-}$)]$^+$ adducts making it possible for the systematic investigation into their inherent chemical and physical properties, along with substrate reactivity. Recently, Itoh and coworkers reported on the "redox reactivity" of a [Cu^{II}(O$_2^{\bullet-}$)]$^+$ complex first described in 2009.[16, 17] The complex with tridentate N$_3$ ligand does not oxidize phenols but only reacts with them in an acid−base fashion.

Chart 2. Ligands and phenol-derivative substrate.

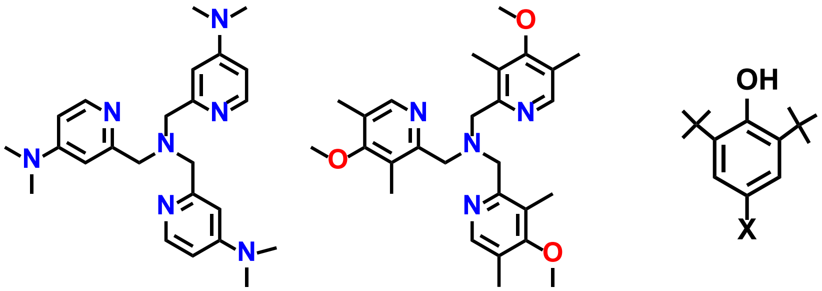

NMe$_2$-tmpa **DMM-tmpa** ***p*-X-DTBP**

Furthermore, the investigation into exogenous phenolic substrate O-H oxidation by $[\mathrm{Cu^{II}}(\mathrm{O_2}^{\bullet-})]^+$ complexes has been limited to the report of product yields for a few phenol or catechol substrates. Thus, utilizing the tripodal tetradentate ligand $\mathrm{NMe_2}$-tmpa (**Chart 2**), which forms a low-temperature stable end-on bound superoxo copper(II) complex, we found that 2,6-di-*tert*-butylphenol derivatives (*p*-X-DTBP; X = OMe, ^{t}Bu, H) were oxidized to corresponding 2,6-di-*tert*-butyl-1,4-benzoquinones (DTBQ) (**Scheme 1**).

Scheme 1. The generation and reaction of $[(\mathrm{DMM\text{-}tmpa})\mathrm{Cu^{II}}(\mathrm{O_2}^{\bullet-})]^+$ (**2**).

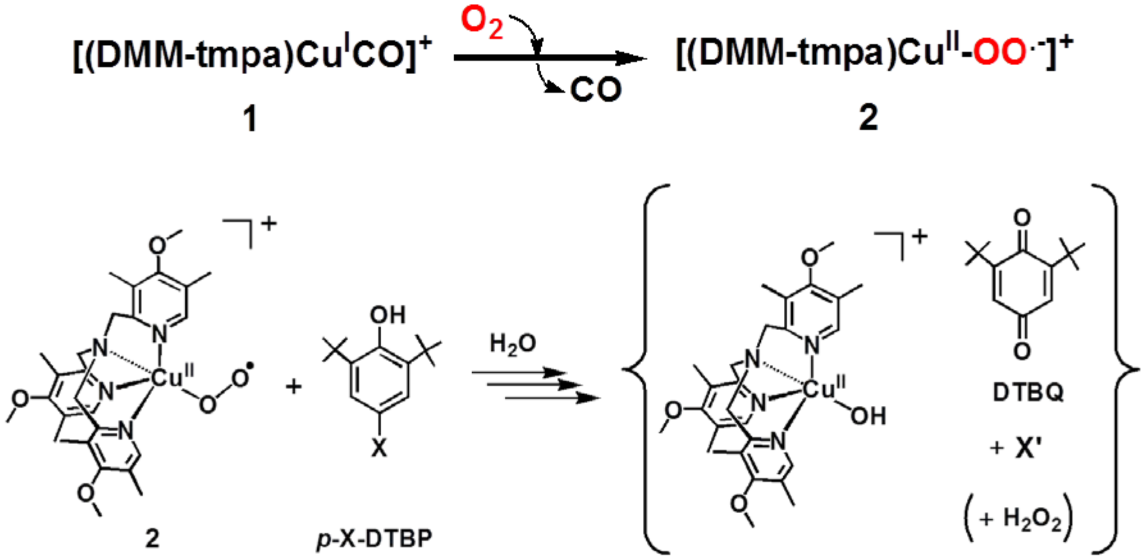

We herein describe a detailed study employing a new electron-rich ligand supporting the cupric superoxo complex, $[(\mathrm{DMM\text{-}tmpa})\mathrm{Cu^{II}}(\mathrm{O_2}^{\bullet-})]^+$ (**2**), (**Scheme 1**) which is capable of mediating this chemistry for a large series of *p*-X-DTBP (X = alkoxy/alkyl) substrates. We provide decisive kinetic evidence supporting cupric superoxo complex mediated HAT as the rate-limiting step in phenol O-H bond activation and two- and/or four- electron reduction of molecular oxygen, *vide infra*. There are three possible reaction pathways in the overall hydrogen-atom transfer from *p*-X-DTBP to $[Cu^{II}(O_2^{\bullet-})]^+$; (1) electron transfer (ET) followed by proton transfer (PT), (2) PT followed by ET and (3) concerted ET and PT. The former two pathways correspond to PCET processes, whereas the third one, i.e., concerted ET and PT corresponds to a direct HAT process. The mechanistic conclusions are drawn by several corroborating studies employing physical measurements leading to i) kinetic isotope effect (KIE) determination, ii) correlation of the relative reactivity for hydrogen atom abstraction using cumylperoxyl radical (**4**) as a mechanistic benchmark, iii) comparison of the rate-dependences in the phenol oxidations by **2** and **4** on the one-electron oxidation potentials of the *p*-X-DTBP's, and iv) activation parameters determined from the reaction kinetics. We also discuss the experimental results from product analysis showing that either overall two-electron oxidation or four-electron oxygenation of the *p*-X-DTBP's can occur; the results depend on the identity of the substituent X. Detailed pathways leading to the products observed are proposed.

2. Experimental Section

2.1 General

All materials used were of commercially available reagent quality unless otherwise stated. Acetone was distilled from Drierite under argon atmosphere. Tetrahydrofuran (THF) and 2-methyltetrahydrofuran (MeTHF) inhibitor free was purchased from Sigma-Aldrich and distilled under argon from Sodium/benzophenone prior to use. Pentane was distilled under argon over CaH_2. Acetonitrile was purified *via* passage through a double alumina column solvent purification system from Innovative Technologies, Inc. Di-*tert*-butyl peroxide was purchased from Nacalai Tesque Co., Ltd and purified by chromatography through alumina which removes traces of the hydroperoxide. Cumene was purchased from Tokyo Kasei Industry Co., Ltd. Air-sensitive compounds were synthesized and transferred under an argon atmosphere using standard Schlenk techniques and stored in an MBraun glovebox filled with N_2. $[Cu^I(CH_3CN)_4]B(C_6F_5)_4$ was synthesized as previously reported.[18] 2,4,6-Tri-*tert*-butylphenoxyl radical (^{t}Bu$_3$ArO•) was synthesized following a procedure reported in the literature[19] and characterized with UV-vis absorption band at 384 and 402 nm and sharp EPR signal at $g = 2.00$. Elemental analyses were performed by Desert Analytics, Tucson, AZ. The ^{1}H-NMR spectrum was measured on a Bruker 300 MHz or a Bruker 400 MHz spectrometer. ^{2}H-NMR was recorded on the broadband coil on a 300 MHz instrument with ^{2}H resonance at 46 MHz. Chemical shifts are reported in ppm downfield against TMS or residual solvent signals unless otherwise specified. Benchtop low temperature UV-vis experiments were carried out on a Cary bio-50 spectrophotometer equipped with a Unisoku USP-203A cryostat using a 1 cm modified Schlenk cuvette. EPR measurements were performed on a Bruker X band EPR 5 mm quartz EPR tubes (Willmad). Electrospray ionization (ESI) mass spectra were acquired using a Finnigan LCQDeca ion-trap mass spectrometer equipped with an electrospray ionization source (Thermo Finnigan, San Jose, CA). Sulfur dioxide (SO_2, gas) was prepared by mixing sodium metabisulfite-saturated water and diluted sulfuric acid solution (**Figure S2**). 2,4,6-Tri-*tert*-butyl-4-hydroperoxycyclohexa-2,5-dienone was prepared as in the literature,[20] and characterized by ^{1}H-NMR spectroscopy.

2.2 Ligand Synthesis

DMM-tmpa [tris((4-methoxy-3,5-dimethyl pyridin-2-yl)methyl)amine] ligand utilized in this report was synthesized following a procedure described in the literature.[21]

2-Phthalimidomethyl-4-methoxy-3,5-dimethylpyridine. TLC on Alumina (1:1 = EtOAc : Hexane), R_f = 0.63;^{1}H-NMR $CDCl_3$ – 8.05 (s, 1H), 7.89-7.86 (dd, 2H, j = 4), 7.72-7.70 (dd, 2H, j = 4), 4.93 (s, 2H), 3.75 (s, 3 H), 2.31 (s, 3H), 2.17 (s, 3H); FAB-MS Calculated MH^+ = 297.12392 Found 297.12352

(4-Methoxy-3,5-dimethylpyridin-2-yl)methanamine. TLC on Alumina (95:5 = DCM : MeOH), R_f = 0; ^{1}H-NMR $CDCl_3$ – 8.16 (s, 1 H), 3.87 (s, 2H), 3.71 (s, 3H), 2.20 (s, 3H), 2.16 (s, 3H), 1.98 (s (br), 2 H)

DMM-tmpa. TLC on Alumina (95:5 = DCM : MeOH), R_f = 0.29;^{1}H-NMR $CDCl_3$ - 8.18 (s, 3H), 3.74 (s, 6H), 3.65 (s, 9H), 2.22 (s, 9H), 1.61 (s, 9H); ^{1}H-NMR Acetone-d_6 - 8.16 (s, 3H), 3.68 (s, 9H), 3.67 (s, 6H), 2.21 (s, 9H), 1.62 (s, 9H). FAB-MS Calculated MH^+ = 465.28657 Found 465.28582

2.3 Synthesis of Substrates

4-Bromo-2,6-di-*tert*-butyl-2,5-cyclohexadienone. The preparation of 4-bromo-2,6-di-*tert*-butyl-2,5-cyclohexadienone was accomplished using a modified published procedure.[22] ^{1}H-NMR $CDCl_3$ – 6.77-6.75 (d, 2H), 5.38-5.36 (t, 1H), 1.24 (s, 9H); ^{13}C-NMR $CDCl_3$ – 185.05, 143.74, 136.60, 77.31

***para*-Alkoxyl-2,6-di-*tert*-butylphenols (*p*-OR-DTBP's).** Selected phenols were synthesized from adapted published procedures.[23] A 22 mL vial was charged with 810.7 mg of silver triflate and a magnetic stir bar. To this vial, 10 mL of the corresponding alcohol

(RO-H) was added. If needed, a minimal amount of dimethylethanol (DME) was used to dissolve the silver salt. To this solution, 900 mg of 4-bromo-2,6-di-*tert*-butyl-2,5-cyclohexadienone dissolved in 2.5 mL DME was rapidly added resulting in the immediate formation of a precipitate and the solution to turn yellow. After 3 min the solution was poured into a 50 mL solution containing ~1 g of NaSH. The organics were separated by extraction with four times 50 mL portions of pentane. This pentane solution was dried over sodium sulfate and filtered using a 0.45 μm filter. The pentane was removed by vacuum and the phenol was purified by flash chromatography using silica gel eluting with 0~2.5 % gradient of EtOAc: petroleum ether. The phenols were isolated as pale yellow to white solids and the purity was checked by NMR and GC-MS. If necessary, phenols were crystallized from petroleum ether. Phenol purity for kinetic analysis was >95%. The yields of phenols varied according to substituent but were typically 25~70 %.

***p*-OCH_2CH_3-DTBP** ^{1}H-NMR $CDCl_3$ - 6.758 (s, 2H), 4.757 (s, 1H), 4.02-3.95 (q, 2H, j= 6.9), 1.43 (s, 18H), 1.419-1.372 (t, 3H, j= 6.9); ^{13}C-NMR $CDCl_3$ – 151.83, 147.66, 137.17, 111.262, 63.80, 34.576, 30.22, 15.10; FAB-MS Calculated M^+ = 250.19328 Found 250.19312

***p*-OCD_2CD_3-DTBP** ^{1}H-NMR $CDCl_3$ - 6.758 (s, 2H), 4.757 (s, 1H), 4.02-3.95 (q, 2H, j= 6.9), 1.43 (s, 18H), 1.419-1.372 (t, 3H j= 6.9); ^{13}C-NMR $CDCl_3$ – 151.83, 147.66, 137.17, 111.262, 63.80, 34.576, 30.22, 15.10; FAB-MS Calculated M^+ = 255.22466 Found 255.22453

***p*-OCD$_3$-DTBP** ^{1}H-NMR CDCl$_3$ - 6.766 (s, 2H), 4.773 (s, 1H), 1.43 (s, 18H); ^{2}H-NMR CDCl$_3$ - 3.759(s); ^{13}C-NMR CDCl$_3$ – 152.41, 147.68, 110.53, 34.57, 30.18; FAB-MS Calculated M$^+$ = 239.19696 Found 239.19629

***p*-OCH$_2$CF$_3$-DTBP** ^{1}H-NMR CDCl$_3$ - 6.86 (s, 2H), 4.975(s, 1H), 4.40-4.316 (q, 2H, j= 8.4), 1.49 (s, 18H); ^{13}C-NMR CDCl$_3$– 150.64, 149.17, 137.49, 129.14-118.082 (q, j = 278) 112.19, 67.71-66.316 (q, j= 35.3) 34.59, 30.121; ^{19}F-NMR 74.61-74.67 (t, j=8.5); FAB-MS Calculated M$^+$ = 304.16501 Found 304.16607

***p*-OMPP-DTBP (2-methyl-1-phenylpropan-2-yloxy)** ^{1}H-NMR CDCl$_3$ - 7.332-7.31 (m, 5H), 6.778 (s, 2H), 4.931 (s, 1H), 2.989 (s, 2H), 1.431 (s, 18H), 1.235 (s, 6H); ^{13}C-NMR CDCl$_3$ – 149.82, 147.18, 138.50, 136.15, 130.77, 127.83, 126.19, 120.88, 79.83, 48.85, 34.27, 30.28, 30.25, 26.23; FAB-MS Calculated M$^+$ = 354.25588 Found 354.25570

Preparation of ^{2}H-O-2,6-di-*tert*-butyl-4-methoxyphenol. A Schlenk flask containing 1.25 g of *p*-OMe-DTBP and a stir bar was dissolved in 20 mL of freshly distilled THF. The sample was then chilled to –78 °C and 1.1 equiv of *n*-butyllithium dissolved in pentane was slowly added to the solution. The solution was allowed to react at low temperature for 30 min, after which 1.4 mL of D$_2$O was added to the solution in ~150 μL portions. The solution was slowly allowed to warm to room temperature and the solvent removed *in vacuo* yielding a white precipitate. The desired phenol was extracted from the flask by the addition of ~20 mL of freshly distilled pentane and the resulting pentane solution was filtered through a plug of celite. The pentane was removed *in vacuo* yielding the desired product as a white solid. The sample was stored in the glove box and the ^2H content was assessed by the absence of the RO-H proton resonance at ~ 4.8 ppm. ^2H content was determined to be >98%.

2.4 Redox Potentials of *para*-Substituted-2,6-di-*tert*-butylphenols (*p*-X-DTBP's)

The redox potentials were measured by second harmonic AC voltammetry (SHACV) in CH_3CN containing 0.10 M $Bu_4N^+PF_6^-$ as a supporting electrolyte using an ALS-630B Electrochemistry Analyzer with a three electrode set up consisting of a platinum disk working electrode, platinum wire counter electrode and an $Ag/AgNO_3$ reference electrode. The voltammograms are plotted against the $[Fe(Cp)_2]^{+/0}$ potential which was measured as an external standard. The E^0 values (*vs* $Ag/AgNO_3$) were converted to those *vs* the $[Fe(Cp)_2]^{+/0}$ (Fc/Fc^+) potential which was measured as an external standard. All electrochemical measurement was carried out at 25 °C under argon atmosphere. Scans were run at 4 mV s^{-1}.

2.5 Synthesis of $[(DMM\text{-}tmpa)Cu^I(CO)]B(C_6F_5)_4$ (1)

This complex was synthesized in a manner very similar to that for the previously reported complex $[(NMe_2\text{-}tmpa)Cu^I(CO)]B(C_6F_5)_4$.[24] A 100 mL Schlenk flask containing a stir bar, 100 mg of DMM-tmpa, and 195 mg of $[Cu^I(CH_3CN)_4]B(C_6F_5)_4$ was evacuated and the flask purged with argon on the vacuum line. To this reaction flask, a Claisen adapter fitted with two air-free addition funnels consisting of ~50 mL of THF and ~125 mL of pentane, respectively, was attached. The argon line was replaced with a carbon monoxide (CO) line and the resulting solutions deaerated with briskly flowing $CO_{(g)}$ for 20 min.

Approximately 10 mL of the CO-saturated THF solution was used to dissolve the ligand and copper salt. The yellow solution was allowed to stir for ~5 min under a positive pressure of CO. The CO-saturated pentane was added to the THF solution resulting in the solution to turn cloudy and an oil to settle to the bottom of the flask. Excess solvent was decanted off under a $CO_{(g)}$ atmosphere and the resulting oil dried under vacuum yielding a white solid (70 % yield). ^{1}H-NMR Acetone-d_6 - 8.39 (s, 3H), 4.13 (s, 6H), 3.82 (s, 9H), 2.29 (s, 9H), 2.24 (s, 9H). Cu-CO stretch 2085 cm^{-1} in CH_3CN, Elemental (Calc. C 50.56, H 2.94, N 4.54; Found C 50.96, H 2.95, N 4.52). Note: The use of the CO-adduct of the copper(I) complex is required in order to prevent disproportionation. The counteranion, $B(C_6F_5)_4$, is utilized for better solubility of the superoxo-copper(II) complex and products derived from its reactions, at very low temperatures.

2.6 Generation of [(DMM-tmpa)Cu^{II}($O_2^{\bullet-}$)]$B(C_6F_5)_4$ (2) and Reaction with *p*-X-DTBP Derivatives

Kinetic Measurements. In the glove box, 0.27 mM solution of [(DMM-tmpa)Cu^{I}(CO)]$B(C_6F_5)_4$ (**1**) was prepared in a 2.5 mL acetone solvent mixture (10 % MeTHF), and the 1 cm Schlenk cuvette was sealed with a rubber septum. Out of the glove box and at RT, the solution was immediately purged for 15 s with $CO_{(g)}$ using a long syringe needle. The solution was then cooled to the appropriate temperature (–100 °C ~ –85 °C) and dioxygen was gently bubbled through the solution. Clean isosbestic conversion to **2** is obtained within 15 min monitored by UV-vis spectroscopy.[24] This green intermediate is stable for hours at –90 °C. Phenol oxidation reactions were initiated by the addition of a stock solution of phenol to the fully generated **2** after three times of Ar/Vacuum purge cycles. Pseudo-first-order rate plots were performed by observing the disappearance of 409 nm band to obtain plots of ln [(*A* - A_f)/(A_i - A_f)] *vs* time(s), which were found to be linear for three or more half-lives. {General Notes: (i) Complex **2** is stable for hour at –90 °C in acetone, as judged by any absorbance loss at λ_{max} = 409 nm. This "lifetime" is well beyond times needed for kinetic studies. (ii) The superoxo complex **2** can also be generated in other solvents such as THF or MeTHF, but it is less stable than in acetone. (iii) If CO $_{(g)}$ is not present in excess in the initial solution of **1** (in 10 % MeTHF/acetone at –90 °C), the binuclear peroxodicopper(II) species $[\{(\text{DMM-tmpa})\text{Cu}^{\text{II}}\}_2(\mu\text{-}1,2\text{-}O_2^{2-})]^{2+}$ readily forms upon addition of O_2. (iv) Further, this dicopper species is formed when higher concentrations of **1** (> 1 mM) are employed in the generation of the **2**, thus confining the range of concentrations used in all of the studies described. (v) Superoxo complex **2** does slowly decay with warming to above –85 °C, however $[\{(\text{DMM-tmpa})\text{Cu}^{\text{II}}\}_2(\mu\text{-}1,2\text{-}O_2^{2-})]^{2+}$ is not the product.}

2.7 Quantification of 2,6-Di-*tert*-butyl-1,4-benzoquinone (DTBQ) with Gas Chromatography-Mass Spectrometry (GC-MS)

A Schlenk flask was charged with 10 mL of 0.25 mM acetone solution of $[(\text{DMM-tmpa})\text{Cu}^{\text{I}}(\text{CO})]\text{B}(C_6F_5)_4$ (**1**) in the glove box, and out of the glove box, the solution was immediately purged with $CO_{(g)}$ at room temperature. The solution was then cooled to the –90 °C acetone/liquid nitrogen cooling bath and dioxygen was gently bubbled through the solution to generate $[(\text{DMM-tmpa})\text{Cu}^{\text{II}}(O_2^{\bullet-})]\text{B}(C_6F_5)_4$ (**2**). After **2** was fully formed, three times of Ar/Vacuum purge cycles were applied to remove excess dioxygen and a stock solution of substrates (1 ~ 50 equiv) was added to the solution. When the reaction ended, the Schlenk flask was warmed up to room temperature. (Note: we also analyzed solutions quenched at low temperature by addition of SO_2, but the results and yields of reactions were not affected). The solvent was removed *in vacuo*, redissolved in 300 μL of the solvent and transferred in a GC-MS vial with addition of 0.8 μmol of naphthalene as a standard. Then 1 μL was injected into the GC-MS. The area ratio was converted to mole ratio to quantify the yield of DTBQ by using standard curve. All GC-MS experiments were carried out and recorded using a Hewlett-Packard 6890 Series Gas Chromatograph System equipped with 5973N Mass Selective Detector. The GC-MS conditions for the product analysis were: Injector Port Temperature: 250 ^{o}C; Column Temperature: Initial Temperature 80 ^{o}C; Initial Time, 2 min; Final Temperature 280 °C; Final Time, 2 min; Gradient Rate 10 °C/min; Flow Rate: 14.2 mL/min; Ionization voltage: 1.3 kV.

2.8 ^{18}O-Labeling Experiments

A Schlenk cuvette was charged with 2.5 mL of 1 mM acetone solution of [(DMM-tmpa)Cu^{I}(CO)]B(C_6F_5)$_4$ (**1**) in the glove box, and out of the glove box, the solution was immediately purged with $CO_{(g)}$ at room temperature. The solution was then cooled to the –90 ^{o}C temperature and $^{18}O_2$ was gently bubbled through the solution to generate [(DMM-tmpa)Cu^{II}($O_2^{\bullet -}$)]B(C_6F_5)$_4$ (**2**) monitored by UV-vis spectroscopy. $^{18}O_2$ (Icon 6393) was prepared in 100 mL of Hamilton gastight syringe equipped with a three-way valve and needle outlet. After **2** was fully formed, three times of Ar/Vacuum purge cycles were applied to remove excess dioxygen and a stock solution of substrates was added to the solution. When the reaction ended, the Schlenk cuvette was taken out to be warmed up at room temperature. The solvent was removed *in vacuo*, redissolved in 300 μL of the solvent and transferred in a GC-MS vial. Then 1 μL was injected into the GC-MS.

2.9 OR Product Analysis using ^{2}H-NMR

Reactions were performed using a 0.75 mM solution of [(DMM-tmpa)Cu^{I}(CO)] B(C_6F_5)$_4$ (**1**) in acetone. The [(DMM-tmpa)Cu^{II}($O_2^{\bullet-}$)]B(C_6F_5)$_4$ (**2**) was generated in a similar fashion described above at -95 °C. After oxygenation a solution containing 5 equiv of *p*-OR-DTBP (OR = OCD_3 or OCD_2CD_3) and d_6-benzene (as internal reference) was added to the NMR tube. The sample was loaded to the spectrophotometer at low temperature and the spectrum recorded. After which, the sample was removed from the instrument allowed to be warmed to room temperature and the spectrum of the solution recorded.

2.10 Oxidation of Phenols by the Cumylperoxyl Radical (4)

Kinetic measurements were performed on a JEOL X-band spectrometer (JES-ME-LX) at 183 K. Typically, photoirradiation of an oxygen-saturated acetone solution containing di-*tert*-butyl peroxide (1.0 M) and cumene (1.0 M) with a 1000 W Mercury lamp resulted in formation of cumylperoxyl radical (g = 2.0156) which could be detected at low temperatures. The g values were calibrated by using a Mn^{2+} marker. Upon cutting off the light, the decay of the EPR intensity was recorded with time. The decay rate was accelerated by the presence of *p*-X-DTBP's (1.0×10^{-2} M). Rates of hydrogen transfer from *p*-X-DTBP's to $PhCMe_2OO\bullet$ were monitored by measuring the decay of EPR signal of $PhCMe_2OO\bullet$ in the presence of various concentrations of *p*-X-DTBP's in acetone at 183 K. Pseudo-first-order rate constants were determined by a least-squares curve fit using a personal computer. The first-order plots of ln (I - I_∞) *vs* time (I and I_∞ are the EPR intensity at time t and the final intensity, respectively) were linear for three or more half-lives with the correlation coefficient, $\rho > 0.99$. In each case, it was confirmed that the rate constants derived from at least five independent measurements agreed within an experimental error of ±5 %.

2.11 Hydrogen Peroxide Quantification

Detection of H_2O_2 as a product has been performed with CH_3CN-saturated NaI solution as in a recent report.[25] 2.5 mL of a 0.6 mM solution of $[(\text{DMM-tmpa})\text{Cu}^{II}(O_2^{\bullet-})]B(C_6F_5)_4$ (**2**) was generated in a Schlenk cuvette as a typical way. After the reaction with *p*-X-DTBP was ended, the solution was taken out and warmed to room temperature. 70 µL of solution was added into 2.0 mL of a CH_3CN-saturated NaI solution at room temperature in the darkness. The UV-vis spectrum of this solution displayed the formation of triiodide (I_3^-) at 362 nm and the yield was calculated by comparing with a standard H_2O_2 solution of known concentrations. 2,4,6-Tri-*tert*-butyl-4-hydroperoxycyclohexa-2,5-dienone was also found to oxidize the iodide ion.

2.12 Attempt to Detect Formaldehyde

The detection of the formaldehyde was accomplished spectrophotometrically *via* an aqueous-based Nash assay.[26] The Nash reagent was prepared by dissolving 7.5 g ammonium acetate, 100 µL of 2,4-pentadione and 150 µL acetic anhydride in 50 mL water. A 8 mg of $[(\text{DMM-tmpa})\text{Cu}^{I}(\text{CO})]B(C_6F_5)_4$ (**1**) was dissolved in 5 mL acetone and transferred to a Schlenk flask, capped with a rubber septum and bubbled with $CO_{(g)}$ for ~ 30 seconds. This reaction vesicle was put in a –95 °C acetone bath. The formation of $[(\text{DMM-tmpa})\text{Cu}^{II}(O_2^{\bullet-})]B(C_6F_5)_4$ (**2**) was achieved by O_2 displacement for ~10 min at which time 7.4 mg of *para*-methoxy-2,6-di-*tert*-butylphenol dissolved in 200 µL acetone was added to the solution. The reaction was allowed to react at –95 °C for 45 min at which time the reaction was quenched at low temperature with $SO_{2\,(g)}$. The solution was allowed to be warmed up to room temperature and a 250 μL aliquot of the reaction solution was added to a vial charged with 2 mL of the Nash reagent cocktail. The reaction mixture was capped, sealed and heated to 60 °C for 90 min at which time the absorbance at 413 nm was recorded.

2.13 Attempt to Detect Isobutylene

The attempt for detecting isobutylene$_{(gas)}$ as one of the products was performed by using GC-MS. An isobutylene-saturated acetone solution was injected as an authentic standard and it could be well detected by GC-MS. However, when the reaction solution was tested, there was no evidence of isobutylene. We attribute this to the low concentrations (maximum 1 mM) used for reaction. If higher concentrations of $[(\text{DMM-tmpa})\text{Cu}^{II}(\text{O}_2^{\bullet-})]^+$ (**2**) are employed, **2** reacts with $[(\text{DMM-tmpa})\text{Cu}^{I}(\text{CO})]^+$ (**1**), forming dicopper(II) species; see Introduction (structure type E) and the Experimental Section concerning the synthesis of **1** and the generation of **2**.

2.14 Resonance Raman Spectroscopy

Resonance Raman spectra were recorded on a Princeton Instruments ST-135 back-illuminated CCD detector and on a Spex 1877 CP triple monochromator with 1200, 1800, and 2400 grooves/mm holographic spectrograph gratings. Excitation was provided by a Coherent I90C-K Kr^+ ion laser ($\lambda_{ex} = 407$nm). The spectral resolution was <2 cm^{-1}. Spectra were recorded at 5 mW power at the sample, and the samples were cooled to 77 K in a quartz liquid nitrogen finger Dewar (Wilmad). Baseline spectra were collected using ground, activated charcoal. Isotopic substitution was achieved by oxygenating with $^{18}O_2$ (Icon, Summit, NJ).

3. Results and Discussion

3.1 Spectroscopic Characterization of [(DMM-tmpa)Cu^{II}($O_2^{\bullet-}$)]$^+$ (2)

There exist three structurally characterized cupric-superoxo complexes. One is a synthetic complex from Fujisawa-Kitajima with side-on η^2-bound $O_2^{\bullet-}$ fragment. It is a ground state singlet species (S = 0) and from resonance Raman (rR) spectroscopy $\nu_{O\text{-}O}$ = 1043 cm^{-1}.[27] There is also the already mentioned case of the PHM protein X-ray structure, considered to have the Cu^{II}($O_2^{\bullet-}$) formulation and end-on bound O_2 fragment.[13] The physical properties of this species within the protein are still lacking. Closely related to our own case here, **2**, is the now very well-known complex from Sundermeyer and Schindler,[28] [(TMG$_3$tren)Cu^{II}($O_2^{\bullet-}$)]$^+$ (TMG$_3$tren = (1,1,1-tris[2-[*N*^{2}-(1,1,3,3-tetramethyl guanidino)] ethyl]amine), with analogous tripodal tetradentate ligand, and end-on superoxo binding ($\angle$ Cu-O-O = 123°) (X-ray structure, **Figure 2**) with $\nu_{O\text{-}O}$ = 1120 cm^{-1} ($\Delta^{18}O_2$ = –63 cm^{-1}). The electronic structure of this molecule has been delineated by Solomon and coworkers[29]

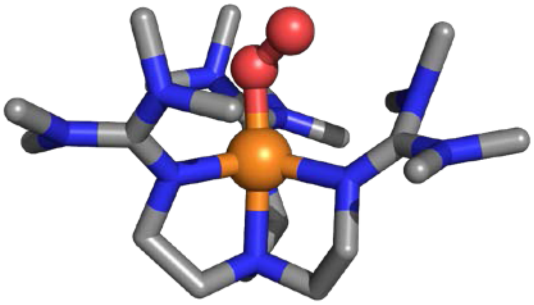

Figure 2. Structural representation of [(TMG$_3$tren)Cu^{II}($O_2^{\bullet-}$)]$^+$.[28]

and the molecule possesses a triplet ground state with ferromagnetically coupled spins on both the Cu(II) ion and superoxo fragment. In fact, the finding of a triplet ground state for cupric-superoxo complexes possessing tripodal tetradentate ligands is general.[30]

Based on the physical properties of $[(\text{DMM-tmpa})\text{Cu}^{\text{II}}(\text{O}_2^{\bullet-})]^+$ (**2**), as described here, it has a physical and electronic structure very similar to that of $[(\text{TMG}_3\text{tren})\text{Cu}^{\text{II}}(\text{O}_2^{\bullet-})]^+$. Complex **2** was generated in acetone and/or MeTHF at –90 °C *via* displacement of $\text{CO}_{(g)}$ by bubbling O_2 gas through a solution of $[(\text{DMM-tmpa})\text{Cu}^{\text{I}}(\text{CO})]^+$ (**1**); a further discussion of why/how this procedure is employed, with references, is given in the Experimental Section. Thus, **2** has been presently characterized by UV-vis and resonance Raman (rR) spectroscopies. The absorption spectrum of this green colored complex is shown in **Figure 3a** and three primary absorption bands are observed: 409, 587 and 743 nm with ε = 4250, 1100 and 1030 $\text{M}^{-1}\,\text{cm}^{-1}$, respectively. This complex is EPR silent (**Figure S3**). Complex **2** is stable enough ($t_{1/2} > \sim 3$ h; –90 °C) to investigate its reactivity toward external substrates. Compared to the parent tmpa ligand (without any pyridyl substituents) Cu^{II}-superoxo complex, which can only be observed as a fleeting intermediate at –128 °C in MeTHF,[31] the electron donating groups on the DMM-tmpa ligand (as also for NMe_2-tmpa; **Chart 2**),[24] provide significant electron density to the copper center resulting in stabilization of $[(\text{ligand})\text{Cu}^{\text{II}}(\text{O}_2^{\bullet-})]^+$ species.

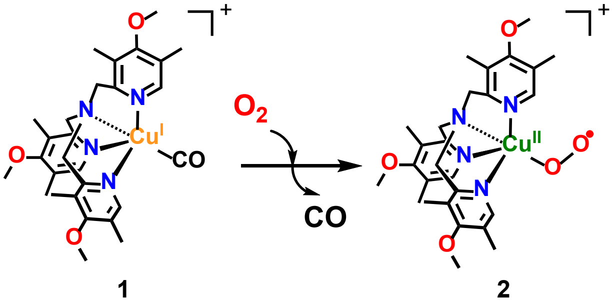

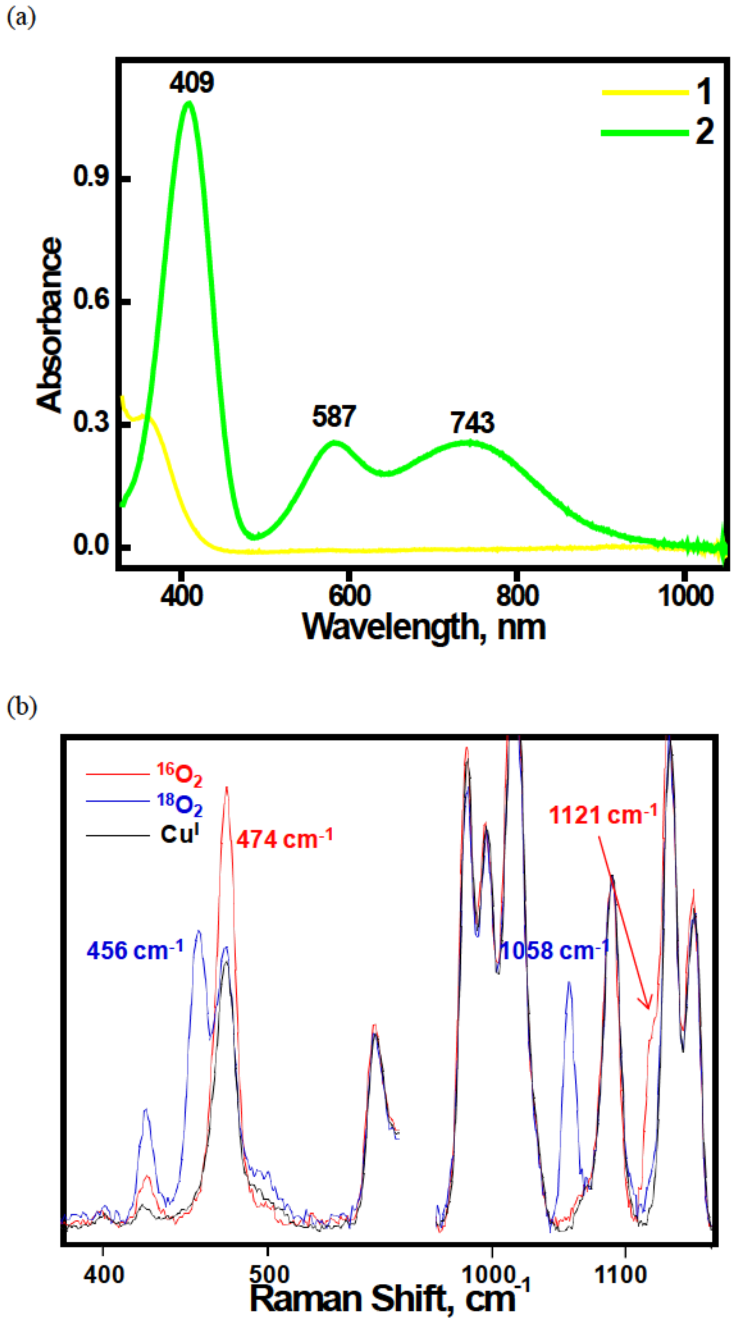

Figure 3. (a) Absorption spectra of **1** (0.27 mM) and **2** after addition of $O_{2\,(g)}$ in acetone (10 % MeTHF) at 183 K. (b) rR spectra of **2** (0.7 mM) measured in MeTHF (λ_{ex} = 407 nm). Red, $^{16}O_2$; blue, $^{18}O_2$.

Resonance Raman (rR) spectra of $[(\text{DMM-tmpa})\text{Cu}^{\text{II}}(O_2^{\bullet-})]^+$ (2) (λ_{ex} = 407 nm) reveal two dioxygen isotope sensitive vibrations (**Figure 3b**). An O-O vibration is observed at 1121 cm^{-1} which shifts to 1058 cm^{-1} ($\Delta^{18}O_2$ = –63 cm^{-1}) upon $^{18}O_2$ substitution. An additional isotope sensitive vibration attributed to the Cu-O stretch occurs at 474 cm^{-1} ($\Delta^{18}O_2 = -18$ cm^{-1}). These parameters closely match those for [(TMG$_3$tren)Cu^{II}($O_2^{\bullet-}$)]$^+$ and other cupric-superoxo complexes with tripodal tetradentate N$_4$ ligands.[24, 29, 32]

3.2 Reactivity of [(DMM-tmpa)Cu^{II}($O_2^{\bullet-}$)]$^+$ (2) towards *para*-Substituted-2,6-di-*tert*-butylphenols

As mentioned in the Introduction, the broader perspective for why the present study was undertaken is our general knowledge of [Cu^{II}($O_2^{\bullet-}$)]$^+$ reactivity is very limited. There are a few highly interesting examples of C–H oxidation reaction (vide infra), and as also indicated, initial descriptions of phenol oxygenation (giving benzoquinones) with both [(NMe$_2$-tmpa)Cu^{II}($O_2^{\bullet-}$)]$^+$ (**Chart 2**)[24] and [(TMG$_3$tren)Cu^{II}($O_2^{\bullet-}$)]$^+$ (**Figure 2**)[33] will be provided. At first, we planned to employ either or both of these complexes for detailed phenol oxidation/oxygenation reactivity studies, but found them to have a very narrow range of substrates that could be oxidized (in terms of O–H BDE) and even where oxidation occurred the reactions were exceptionally slow (**Figure S4**), thus not amenable to kinetic investigations, as compared to what we find here for reactions of complex **2**. A very simple analysis and conclusion would be that the superoxo moiety in [(NMe$_2$-tmpa)Cu^{II}($O_2^{\bullet-}$)]$^+$, with its very electron releasing pyridyl *p*-NMe$_2$ substituents, is less electrophilic than the superoxo complex in **2**, with its pyridyl *p*-OMe substituents. As to how this translates to reactivity of phenols with varying O-H BDE, we can judge from the BDE values of substrates in **Table 1**, the BDE of the Cu-OOH complex must be larger than 79.6 kcal mol^{-1}, but smaller than 82.7 kcal mol^{-1}. Initial survey of reaction of **2** with a variety of phenols indicated the kinetic studies and product analyses were viable for a good range of phenols, both *p*-alkoxy-2,6-di-*tert*-butylphenols (*p*-OR-DTBP's) and *p*-alkyl-2,6-di-*tert*-butylphenols (*p*-R-DTBP's) (**Table 1**).

3.3 Kinetic and Thermodynamic Studies

3.3.1 Demonstration of hydrogen atom transfer chemistry

Kinetic isotope labeling studies on the oxidation of the two phenol substrates *p*-OMe-DTBP and *p*-Me-DTBP by $[(\text{DMM-tmpa})\text{Cu}^{\text{II}}(\text{O}_2^{\bullet -})]^{+}$ (**2**) were performed under pseudo-first-order conditions at 183 K by following the disappearance of the 409 nm band as shown in **Figure 4a**. It is only for the *p*-alkyl-DTBP cases that it was convenient to take a large number of full spectra, as in **Figure 3a**, to follow the kinetics. For all other cases, reactions which were much faster; only the 409 nm absorption value changes were monitored to deduce pseudo-first-order rate constants. In both cases, the decay behavior observed fits to a first-order kinetics and yields an observed rate constant (k_{obs}) which was linear with respect to the substrate concentration as shown in **Figure 4b**. A second-order-rate constant (k_2) of 23 $\text{M}^{-1}\ \text{s}^{-1}$ was obtained for the oxidation of proteo *p*-OMe-DTBP. Using substrate which had been subjected to deuterium (^{2}H-O) exchange (see Experimental Section), a significant deceleration of the reaction rate was observed, yielding a second-order-rate constant of 2.1 $\text{M}^{-1}\ \text{s}^{-1}$. Thus, a primary kinetic isotope effect (KIE) of 11 was obtained. Using *p*-Me-DTBP, a lower but significant KIE of 4.2 was observed based on the determination of $k_2 = 4.2 \times 10^{-2}\ \text{M}^{-1}\ \text{s}^{-1}$ and $1.0 \times 10^{-2}\ \text{M}^{-1}\ \text{s}^{-1}$ obtained for the oxidation of the proteo and deuterium labeled phenols, respectively. Thus, it appears that the oxidations of both the *p*-alkoxy-DTBP and *p*-alkyl-DTBP by **2** occur *via* a rate limiting O-H activation event.

Table 1. Phenol BDE's, redox potentials (E_{ox}), second-order rate constants (183 K) for *p*-X-DTBP phenol oxidations by **2** and **4** and reaction yields (See **Figure S10** for kinetics details)

	Substituent (X)	BDE [a] (kcal mol^{-1})	E_{ox}, V (vs Fc/Fc^{+})[c]	k_2 of **2**[d] (M^{-1} s^{-1})	k_2^{C} of **4**[d] (M^{-1} s^{-1})	DTBQ yield (%)
OR	OCH_2CH_3	-	0.532	24	714	-
	OCH_3	79.6	0.526	23	520	49
	OCD_3	-	0.496	21	513	-
	OCH_3, -OD	-	0.585	2.1	58	-
	OMPP [b]	-	0.614	0.84	350	44
	OCH_2CF_3	-	0.805	0.81	329	-
R	CH_3	80.1	0.81	0.042	185	-
	CH_2CH_3	80.0	0.875	0.027	160	-
	sec-butyl	-	0.884	0.023	152	-
	CH_3, -OD	-	0.896	0.010	-	-
	tert-butyl	82.3	0.927	0.008	106	38
	H	82.7	1.074	NR	-	-

[a] Bond Dissociation Energy in DMSO.[34] [b] OMPP = 2-methyl-1-phenylpropan-2-yloxy. [c] These were determined from SHACV measurements, see Experimental Section. The experimental error is ± 0.01 V. [d] The experimental error is ±5 %.

3.3.2 Comparison of KIEs to other metal-superoxo mediated oxidations

There have been no prior reports of O–H KIEs by cupric superoxo complexes. However, a primary KIE of 10.6 and 10.9 are reported for the C–H activation of hippuric acid and dopamine by PHM and DBM, respectively,[35, 36] thought to be effected by a protein cupric superoxide moiety.[7,12] In a bioinspired synthetic system, a value of 12.1 was reported for the oxidation of BNAH (1-benzyl-1,4-dihydronicotinamide) for the PV-tmpa [bis(pyrid-2-ylmethyl) ([6-(pivalamido)pyrid-2-yl]methyl)amine] cupric superoxo complex.[32] A lower magnitude of 4.1 was reported for the intramolecular benzylic C–H oxidation of a phenethyl ligand arm in a chelated copper(II)-superoxo complex reported by Itoh and coworkers.[16, 17] In addition, this value (KIE = 12) is approximately equal to what is observed for the oxidation of a water-soluble tri-substituted phenol by a chromium superoxo described by Bakac and coworkers.[37] All of these results are consistent with the substrate activation *via* homolytic O–H bond cleavage.

(a)

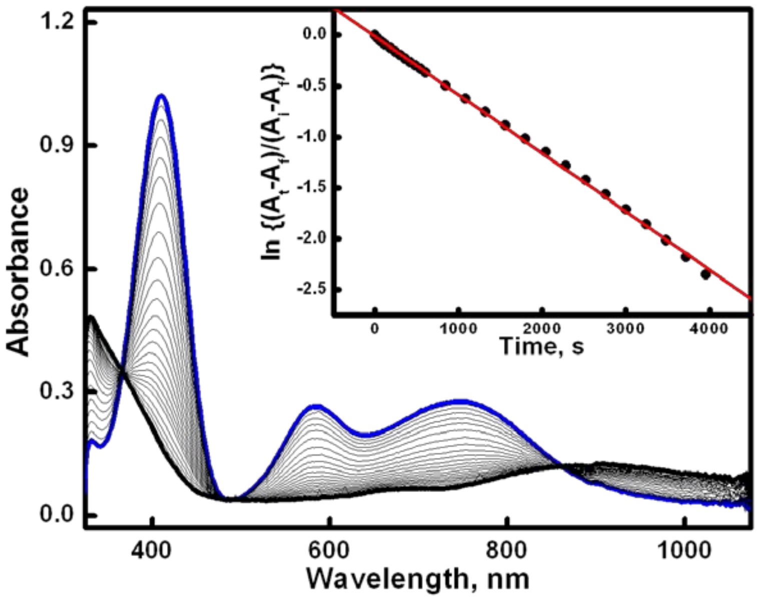

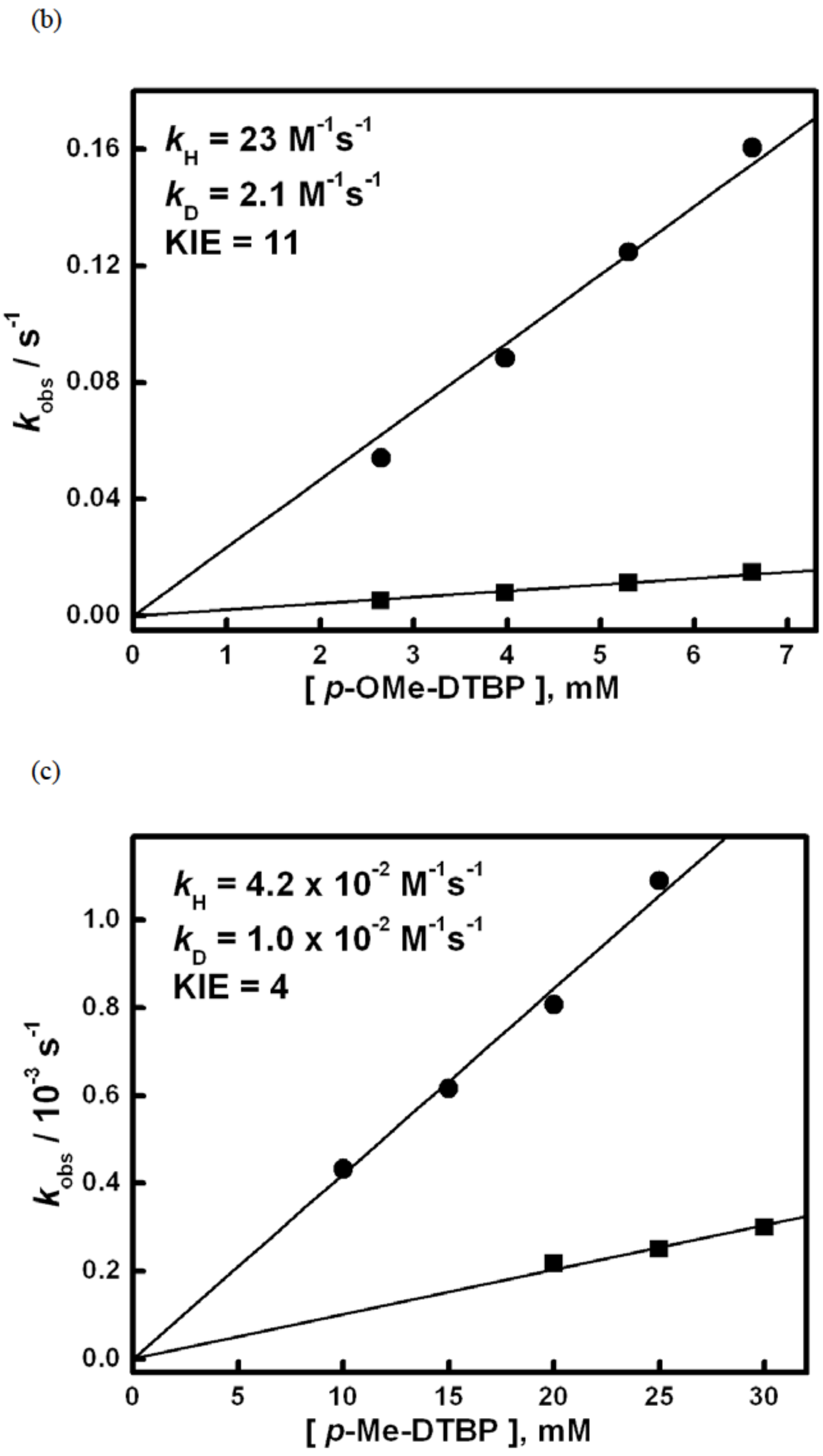

Figure 4. (a) UV-vis spectral changes observed by addition of *p*-Et-DTBP (20 mM) to **2** (0.27 mM) in acetone (10 % MeTHF) at 183 K. $k_{obs} = 5.73 \times 10^{-4}\ s^{-1}$. (b and c) Plots of k_{obs}'s against the concentrations of substrates (circles) and deuterated ^{2}H-O substrates (squares) for *p*-OMe-DTBP (b) and *p*-Me-DTBP (c) to determine second-order-rate constants and KIE's.

3.3.3 Cumylperoxyl radical (**4**) plus phenol substrate HAT reactions for comparison

To provide further evidence that hydrogen atom transfer (HAT) is the rate-determining step (*r.d.s.*) in these reactions, we studied the same substrates with cumylperoxyl radical (**4**); the latter is known to effect "pure" HAT chemistry with phenols (and *N*,*N*-dimethylanilines).[15, 38] This hydrogen atom acceptor reacts with phenols to yield cumene hydroperoxide and phenoxyl radical, here, we wished to compare the behavior of 4 with phenols to that of the reactions of [(DMM-tmpa)Cu^{II}($O_2^{\bullet-}$)]$^+$ (**2**) and phenols (**Scheme 2**). Thus, to understand the relationship between second-order-rate constants for **2** (k_2) and **4** (k_2^C) (**Table 1**), the reaction of the whole series of substrates with **2** and **4** has been explored monitoring the chemistry with the use of UV-vis and EPR spectroscopies, respectively (see Experimental Section). A large KIE value (KIE = 9.0) was observed for hydrogen atom transfer from *p*-OMe-DTBP to **4** as shown in **Figure S5**. The k_2 values display a linear correlation with k_2^C, which further indicates HAT is involved in rate-

Scheme 2.

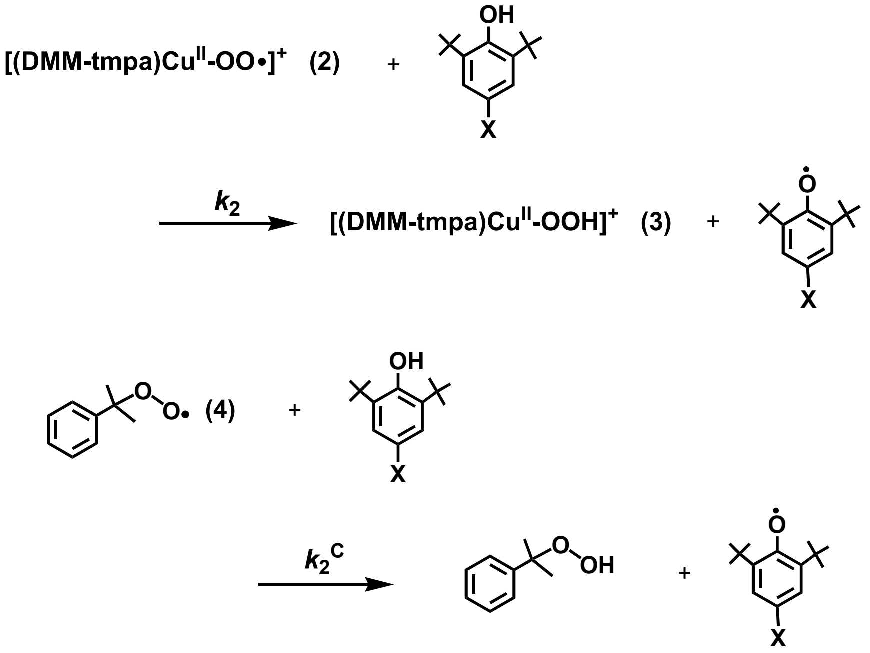
[(DMM-tmpa)Cu^{II}-OO•]$^+$ (2)
+
OH
X
k_2
[(DMM-tmpa)Cu^{II}-OOH]$^+$ (3)
+
O
X
O
O• (4)
+
OH
X
k_2^C
O
OH
+
O
X

limiting step of phenol oxidations by **2** (**Figure 5**). If the *r.d.s.* was to be pure HAT, as in case of **4**, the slope would be one. The larger slope observed (= 4.85) from the plot obtained indicates that some degree of contribution of partial transfer of charge is also involved in the *r.d.s.* for **2** plus phenol reactions.

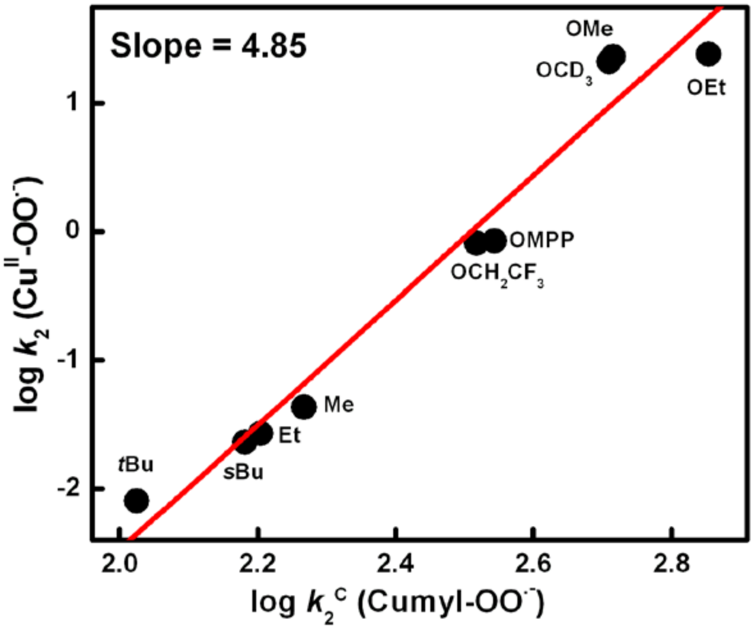

Figure 5. Correlation between log k_2 of **2** and log k_2^C of **4** with *p*-X-DTBP's, respectively. Slope is 4.85.

3.3.4 Rate constants (k_2) correlation to phenol redox potentials?

We also considered possible relationships between the second-order-rate constants for the reaction of $[(\text{DMM-tmpa})\text{Cu}^{\text{II}}(\text{O}_2^{\bullet-})]^+$ (**2**) with phenols (k_2) and substrate redox potentials. In fact, k_2 values for the reactions increase with decreasing the redox potentials, i.e., with increasing driving force of electron transfer from phenols to **2**. The plot of (k_BT/e) $\ln k_2$ *vs* E_{ox} exhibits a linear correlation with a negative slope = –0.29 as shown in **Figure 6** (See Supporting Information for derivation). By contrast, for the case of cumylperoxyl radical (**4**), the plot of $(k_B\text{T/e})$ $\ln k_2^C$ *vs* E_{ox} exhibits a much weaker dependence on the E_{ox}

values and the slope is only –0.05. Although the bond dissociation energy (BDE) of *p*-X-DTBP is known to decrease by electron-donating substituents,[39] the difference in BDE between OCH_3 and *tert*-butyl group is only 2.7 kcal mol^{-1}, which is equivalent to 0.12 eV, whereas the difference in E_{ox} between OCH_3 and *tert*-butyl group is 0.40 eV (**Table 1**). Based on thermochemical cycles,[38] the difference in BDE (ΔBDE) is given by eq 2,

$$\Delta BDE = e\Delta E_{ox} + k_B T \Delta pK_a \qquad (2)$$

where ΔpK_a is the difference in the pK_a values of *p*-X-$DTBP^{\bullet+}$ and entropy changes are neglected. The pK_a value becomes smaller with increasing in the E_{ox} value and the constant BDE value (eq 2) indicates that an increase in the E_{ox} value is partially cancelled by a decrease in the pK_a value. Such cancellation may be the reason why the BDE value is much less sensitive to electron-donating substituents in **Table 1** as compared to the E_{ox} value.

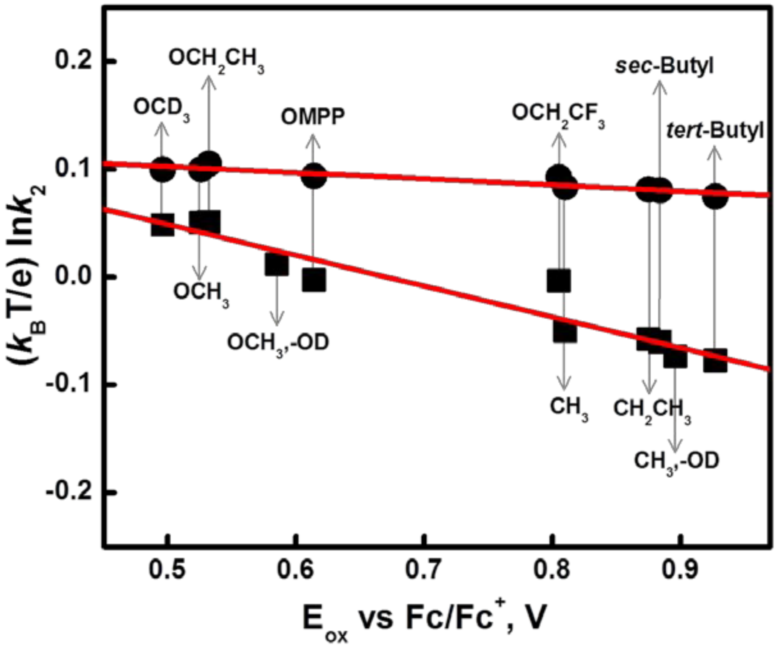

Figure 6. Plots of $(k_B T/e) \ln k_2$ for the reactions of *p*-X-DTBP's with **2** (squares) and **4** (circles) against the one-electron oxidation potentials (E_{ox}) of substrates. The slopes are –0.29 and –0.05, respectively.

3.3.5 Mechanistic considerations

There are three possible reaction pathways in the apparent hydrogen-atom transfer from *p*-X-DTBP to $[\mathrm{Cu^{II}}(\mathrm{O_2^{\bullet-}})]^+$; (1) electron transfer (ET) followed by proton transfer (PT), (2) PT followed by ET and (3) concerted ET and PT (**Scheme 3**). The observation of large KIEs in **Figure 4** indicates that PT should be involved in the rate-determining step.

Scheme 3. Three possible reaction pathways for hydrogen-atom transfer from *p*-X-DTBP to $[\mathrm{Cu^{II}}(\mathrm{O_2^{\bullet-}})]^+$.

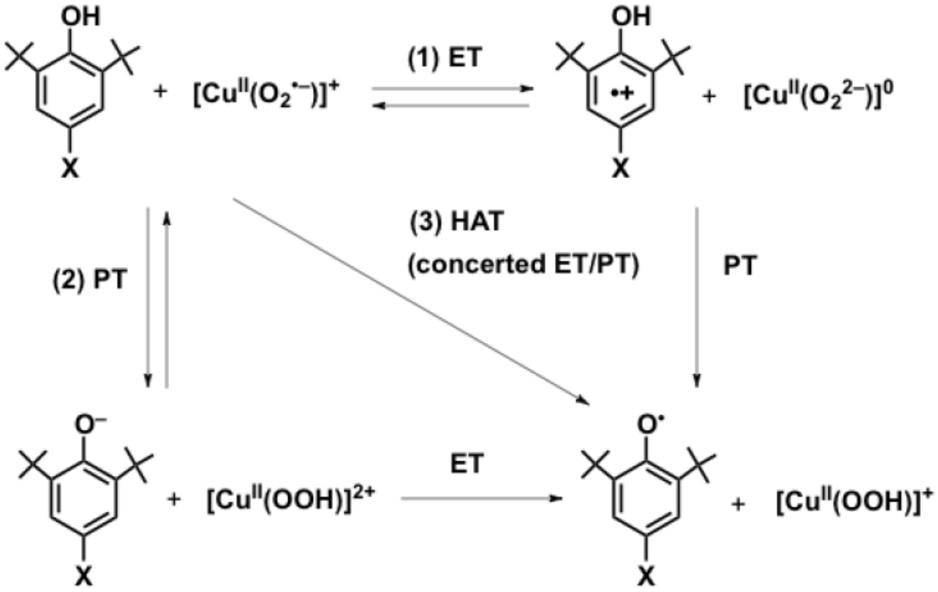

In such a case, PT should be the rate-determining step following the ET equilibrium, which is endergonic, in the ET/PT pathway (1). If the ET step is exergonic, this should occur first, followed by rate-determining PT. In such a case, phenol radical cation derivatives should be observed, but they were not. If an exergonic ET were the rate-determining step, followed by rapid PT, no KIE would be observed in contrast to our experimental observations. We further note that $[\mathrm{Cu^{II}}(\mathrm{O_2^{\bullet-}})]^+$ complex **2** is unreactive to the strong reductant decamethylferrocene. In this case the observed second-order-rate constant (k_2) is given by eq 3,

$$k_2 = k_p K_{et} \quad (3)$$

where k_p is the rate constant of proton transfer from *p*-X-DTBP$^{\bullet+}$ to $[Cu^{II}(O_2^{2-})]^0$ and K_{et} is the ET equilibrium constant between *p*-X-DTBP and $[Cu^{II}(O_2^{\bullet-})]^+$ ($K_{et} << 1$). Because the Brønsted slope of k_p is between 0 and 0.5 for an exergonic proton-transfer reaction,[40] and the slope of the plot of $(k_BT/e)\ \ln K_{et}$ *vs* E_{ox} is –1.0, the predicted slope of a plot of (k_BT/e) $\ln k_2$ *vs* E_{ox} is between –0.5 and –1.0.

In the case of the PT/ET pathway (2), PT should also be the rate-determining step followed by fast ET. In this case the slope of the plot of (k_BT/e) $\ln k_2$ *vs* E_{ox} is positive, because an increase in the E_{ox} value with electron-withdrawing substituents results in an decrease in the p*K'*$_a$ value (more acidic) when the proton transfer from *p*-X-DTBP to $[Cu^{II}(O_2^{\bullet-})]^+$ becomes thermodynamically more favorable. The observed negative slope (-0.29) clearly rules out the PT/ET pathway. Although the ET/PT pathway affords the negative slope of a plot of (k_BT/e) $\ln k_2$ *vs* E_{ox} is between -0.5 and -1.0, the observed slope (-0.29) is less negative than -0.5. In the case of the concerted ET/PT pathway (one-step hydrogen atom transfer), the slope is -0.05 as observed for hydrogen atom transfer from *p*-X-DTBP to **4**. The smaller slope than expected for transfer of a full unit of charge has been reported to result from only partial transfer of charge in hydrogen-atom transfer reactions from hydrogen donors to the triplet excited state of benzophenone.[41] Thus, it is most likely that hydrogen transfer from *p*-X-DTBP proceeds *via* a partial transfer of charge rather than an ET/PT pathway in which a full unit of charge is transferred. Thus, more electron deficient ligands may be required in order to increase the hydrogen-transfer reactivity of $[Cu^{II}(O_2^{\bullet-})]^+$ by facilitating charge transfer from *p*-X-DTBP to $[Cu^{II}(O_2^{\bullet-})]^+$.

3.3.6 Activation parameters and comparisons

The rates of the [(DMM-tmpa)Cu^{II}(O$_2^{\bullet-}$)]$^+$ (**2**) + *p*-X-DTBP's reactions were of course temperature dependent. However, we could only examine a narrow temperature range, as colder (than 173 K) conditions involved solution freezing, while self-decomposition of **2** was too extensive when warming above 188 K. Also, the slow self-decomposition precluded the generation of good quality data except for the fastest reaction, that being with the *p*-OMe-DTBP substrate. Never-the-less, an Eyring plot developed from data between 173 K and 188 K for this substrate yielded activation parameters as follows: $\Delta H^{\ddagger} = 3.6 \pm 0.6$ kcal mol^{-1} and $\Delta S^{\ddagger} = -32 \pm 3$ cal mol^{-1} K^{-1} (**Figure S6**). The large negative activation entropy suggests that the *r.d.s.* involves a well ordered transition state.

Although no comparable activation parameters for *p*-X-DTBP oxidation by cupric superoxide or other Cu-oxygen complexes have been reported, there are a few values measured for oxidation of phenol derivatives by various other metal ion complexes, including Cu^{III}, Ru^{VI}, Mn^{V}, and Ru^{III} (**Table 2**).[42-45] Excepting the case of reaction of a Ru^{III}-pterin complex which was concluded to involve PCET, all other cases are stated as involving HAT in the rate-limiting step. In particular, the HAT reaction of a manganese(V)-oxo corrolazine complex plus 2,4-di-*tert*-butylphenol (2,4-DTBP)

Table 2. Kinetic Parameters in Various Metal Complexes plus Phenol Oxidation Reactions

Reactants		$\Delta H^{\ddagger}$, kcal mol^{-1}	$\Delta S^{\ddagger}$, cal mol^{-1} K^{-1}
Cu^{II}-O$_2^{\bullet-}$ [a]	*p*-OMe-DTBP	3.6 ± 0.6	-32 ± 3
Cu(III)[42]	2,4-DTBP	8.3 ± 1.1	-27 ± 3
Ru(VI)[43]	Phenol	11.3 ± 0.8	-14 ± 2
Mn(V)[44]	2,4-DTBP	6.3 ± 1.4	-35.6 ± 2.3
Ru(III)[45]	*p*-^{t}Bu-DTBP	1.6 ± 0.2	-36 ± 2

[a] This work

affording $Mn^{IV}(OH)$ plus 2,4-di-*tert*-butylphenoxyl radical, gives both $\Delta H^{\ddagger}$ and $\Delta S^{\ddagger}$ values close to those obtained from our reaction of **2** and *p*-OMe-DTBP.

3.3.7 KIE temperature dependence?

We also investigated the temperature dependence of the KIE values for the reaction with deuterated *p*-OMe-DTBP (**Table 3**, **Figure S6**). While the temperature range is again limited, the results suggest there is no temperature dependence on the magnitude of the primary KIEs. Thus, the Arrhenius pre-exponential factor for the phenol O-H and O-D isotopically labeled analogues remain essentially constant as a function of temperature. This behavior is consistent with a substrate oxidation mechanism involving classical rate limiting H–atom abstraction.[46]

Table 3. Temperature Dependence on the KIEs of the HAT Reactions from *p*-OMe-DTBP to $[(DMM\text{-}tmpa)Cu^{II}(O_2^{\bullet -})]^+$ (**2**)

	k_H, M^{-1} s^{-1}	k_D, M^{-1} s^{-1}	k_H/k_D
173 K	11	1.0	11
178 K	14	1.2	12
183 K	23	2.1	11
188 K	26	2.7	10

3.3.8 Summary of the kinetic-thermodynamic studies

As detailed above, our in-depth studies are consistent with conclusion that the cupric superoxo complex $[(DMM\text{-}tmpa)Cu^{II}(O_2^{\bullet -})]^+$ (**2**), as a kind of prototype for the initial adducts formed in chemical or biological Cu^I/O_2 interactions, reacts with *p*-OMe-DTBP (and the other phenols) *via* a HAT oxidative mechanism. Likewise, as mentioned above, rate-limiting HAT occurs for the galactose oxidase (GO) active-site special Tyr, but PCET in copper amine oxidase (CAO) has been suggested by Klinman[9] and Roth.[10] In relevant C-H bond activation by $[Cu^{II}(O_2^{\bullet -})]^+$ species, Klinman and Blackburn reported C-H bond cleavage in *N*-benzoylglycine by PHM having large intrinsic isotope effects.[35] They also demonstrated hydrogen tunneling as occurring in PHM with a lack of a temperature dependence of an intrinsic isotope effect on the C-H bond cleavage of the substrate hippuric acid.[47] As also mentioned, Itoh and co-workers reported intramolecular C-H hydroxylation (HAT) by a cupric superoxo species supported by tridentate ligand possessing a distorted tetrahedral geometry.[16]

3.4 Product Analyses and Further Mechanistic Insights

3.4.1 Phenol oxidations lead to benzoquinone products

As described above in detail, the initial products generated after rate-limiting hydrogen atom transfer occurs are presumed to be a $[(\text{DMM-tmpa})Cu^{II}(OOH)]^+$ (**3**) and a *para*-X-2,6-di-*tert*-butylphenoxyl radical (**Scheme 2**). Such a phenoxyl radical would possess distinctive λ_{max} = 384 and 402 nm absorptions and exhibit a sharp *g* ~ 2.0 EPR spectroscopically detectable signal. However, neither of these spectroscopic signals could be observed. Thus, qualitative and quantitative product analyses were carried out allowing us to understand and build up the proposed overall mechanism and stoichiometry of the reactions observed. In fact, for all phenolic substrates, benzoquinones are produced. As mentioned above, reactions of **2** with *p*-OR-DTBP and *p*-R-DTBP proceed *via* different pathways, two-electron oxidation and four-electron oxygenation, respectively, and these further aspects of the overall chemistry are now detailed.

3.4.2 Reaction of $[(\text{DMM-tmpa})\text{Cu}^{\text{II}}(\text{O}_2^{\bullet-})]^+$ (**2**) with *p*-alkoxy-2,6-di-*tert*-butylphenols (*p*-OR-DTBP's)

All synthetic reactions were carried out by mixing excess phenol substrate with **2**, at –90 °C. The cryogenic solutions were interrogated by UV-vis, NMR and EPR spectroscopies. As described for the initial kinetics of the system (vide supra), **2** rapidly disappears. Low-temperature UV-vis (new *d*-*d* bands) and EPR (EPR silent to EPR active) spectroscopies reveal that a new mononuclear Cu^{II} complexes has formed, but NMR spectroscopy suggests that no quinone has yet formed and only starting extra phenol is present. However, warming of these initial reaction solutions to RT followed by NMR and GC-MS analyses indicates that up to 50 % yields of 2,6-di-*tert*-butyl-1,4-benzoquinones (DTBQ's) form (**Scheme 1**). An ^{18}O labeling experiment (see Experimental Section) where **2** was generated using $^{18}\text{O}_2$ gas revealed that no ^{18}O was incorporated into the DTBQ. This is explained below; only the overall two-electron oxidation of the substrate phenol takes place while hydrogen peroxide and alcohol products are also formed. The fate of the initial *para*-OR fragment, after warming, was identified by ^{2}H(D)-labeling experiments using *p*-OCD_3/OCD_2CD_3-DTBP substrates (**Figure S9**). In each case, the product detected was the corresponding alcohol (methanol and ethanol), not the oxidized form (formaldehyde and acetaldehyde). The inorganic product is a mononuclear copper(II) complex $[(\text{DMM-tmpa})\text{Cu}^{\text{II}}\text{-(OH(H))}]^{+/2+}$, and H_2O_2 is produced (~50 % yield), as determined by EPR/UV-vis spectroscopy (**Figures S7**, **S8** & **S13**) and iodometric titration, respectively. The smaller yield of H_2O_2 than expected from **Scheme 4** may result from partial decomposition during the reaction. The DMM-tmpa ligand in Cu(II) reaction products remains intact (based on direct TLC and MS analyses); no ligand oxidation occurred.

3.4.3 Proposed pathway for $[Cu^{II}(O_2^{\bullet-})]^+$ (**2**) reaction with *p*-OR-DTBP substrates (**Scheme 4**).

Initially, a hydrogen atom is transferred from the phenol to $[Cu^{II}(O_2^{\bullet-})]^+$ as the (low-temperature) *r.d.s.*, where $[Cu^{II}(OOH)]^+$ and the corresponding phenoxyl radical form (**Scheme 4**, step i). The $[Cu^{II}(OOH)]^+$ intermediate would 'hydrolyze' giving H_2O_2 and $[Cu^{II}(OH)]^+$ (**Scheme 4**, step iii), (upon warming up to RT). Strong support for this claim comes from our independent generation of authentic complex $[Cu^{II}(OOH)]^+$ (**3**), and demonstration that it releases H_2O_2 (which was directly identified) and forms the hydroxide complex, $[Cu^{II}(OH)]^+$. This was identified as the Cu product by matching EPR and UV-vis spectroscopic data with authentically generated compounds (see Supporting Information). The formation of the eventual benzoquinone and other products is explained by (a) a fast radical-radical coupling reaction of the newly generated ArO• moiety and a second equiv $[Cu^{II}(O_2^{\bullet-})]^+$, affording a peroxy Cu^{II}-OO-(ArO') species ***A*** (**Scheme 4**, step ii), (b) then this reacts with solvent water to give ***B***, which eliminates the alcohol (RO-H) derived from the *p*-OR-DTBP substrate, step iv. {Note: if this hydrolysis step involved Cu^{II}–OOH rather than Cu^{II}-OO–(ArO') bond cleavage, then the corresponding hydroperoxo intermediate ***C*** (HOO-(ArO')) (**Scheme 5**) forms, rather than our postulated ***B*** with HO-(ArO') formulation. However, ***C*** would be incapable of producing methoxide/methanol plus benzoquinone, our observed products. If ***C*** or Cu^{II}-peroxo derivative ***A*** were to form, $CH_2=O$ would be produced (**Scheme 5**), but none was observed (Experimental Section)}. Kinetic aspects for quinone formation were not investigated in detail, as this step occurs later, with warming of the reaction solutions (see Experimental Section).

Scheme 4. Proposed Pathways for $[Cu^{II}(O_2^{\bullet-})]^+$ Reactivity with *p*-OR-DTBP or *p*-R-DTBP Substrates Leading to Observed Products.[a]

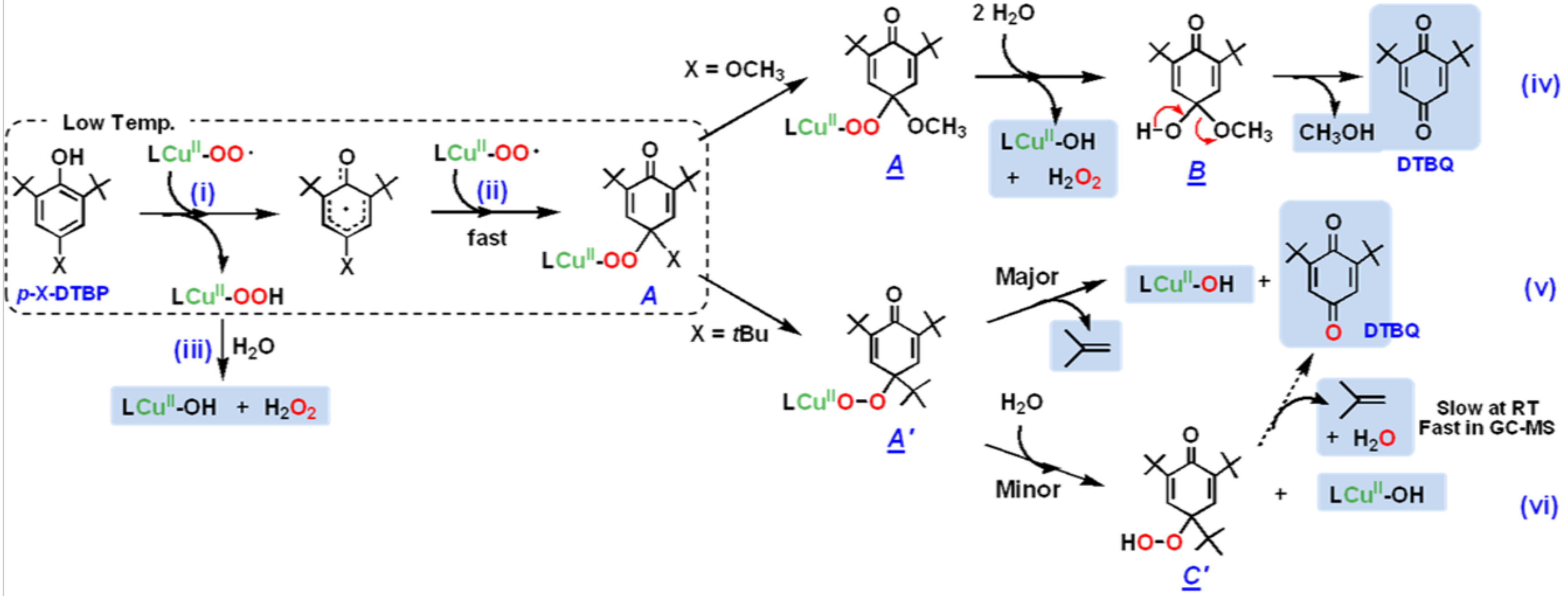

Low Temp.
OH
X
p-X-DTBP
LCuII-OO·
(i)
LCuII-OOH
O
X
LCuII-OO·
(ii)
fast
O
LCuII-OO
X
A
(iii)
H2O
LCuII-OH + H2O2
X = OCH3
X = tBu
O
LCuII-OO
OCH3
A
2 H2O
LCuII-OH + H2O2
O
H-O
OCH3
B
CH3OH
O
O
DTBQ
(iv)
O
LCuIIO-O
A′
Major
LCuII-OH +
O
O
DTBQ
(v)
H2O
Minor
O
HO-O
C′
+ H2O
Slow at RT
Fast in GC-MS
+
LCuII-OH
(vi)

[a]See text for detailed descriptions of direct/indirect evidence or literature support for the individual reaction steps or intermediates described. EPR spectra observed for (*A* ≡ *A'*) (from mixing **2** & *p*-X-DTBP at –90 °C), for LCu^{II}-OH(H) (observable at RT and re-freezing to record EPR spectra) are indistinguishable, see **Figure S7** and caption.

Scheme 5. Oxygen-incorporating reaction releasing formaldehyde and isobutylene

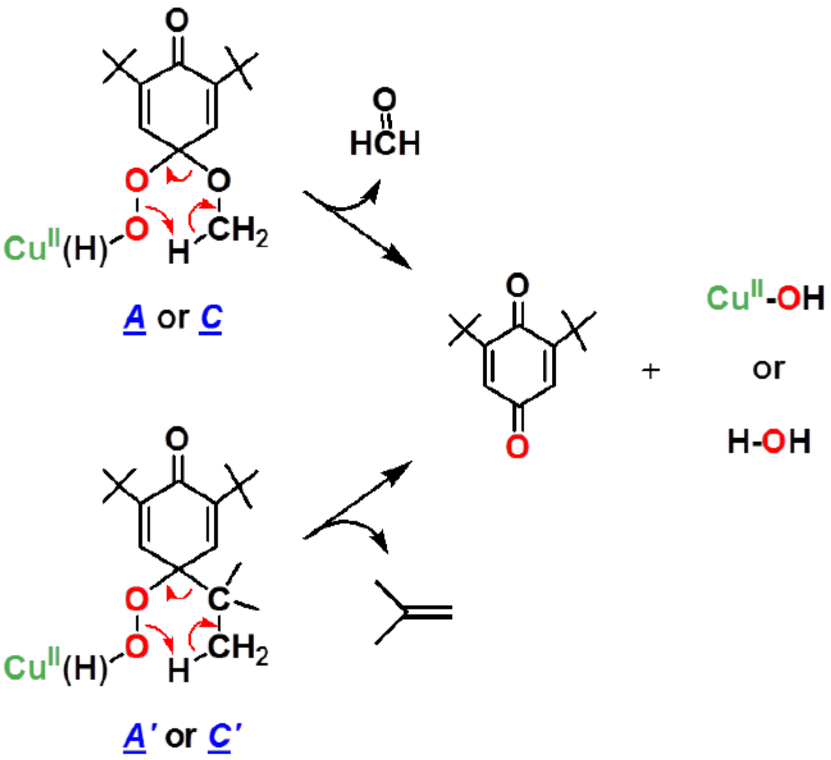

3.4.4 Reaction of $[(DMM\text{-}tmpa)Cu^{II}(O_2^{\bullet-})]^+$ (**2**) with *p*-alkyl-2,6-di-*tert*-butylphenols (*p*-R-DTBP's)

For the case where the *para-* substituent is an alkyl group like *tert*-butyl, the reaction of *p*-R-DTBP plus $[(DMM\text{-}tmpa)Cu^{II}(O_2^{\bullet-})]^+$ (**2**) proceeds differently, *via* an overall four-electron substrate oxygenation. The initial reaction, steps i and ii proceed analogously, producing the Cu^{II}-OO–(ArO') species A′ (**Scheme 4**). This however, can undergo a *tert*-butyl substituent oxidation *via* elimination of isobutylene, then directly giving the DTBQ and Cu(II) products observed (**Scheme 4**, steps v). In fact, we were not able to detect isobutylene as a product; see the Experimental Section for details and explanation. Isobutylene or ^{t}BuOH (= isobutylene + H_2O) elimination from *tert*-butyl substituted phenols under oxidative conditions is well precedented.[48] We, however, were not able to detect isobutylene as a product.[49] For the substrate *p*-Me-DTBP, which was studied for its kinetics (**Table 1**), there is a question as to what the final organic product could be. The mechanism applied to the *p*-^{t}Bu-DTBP substrate which would eliminate isobutylene, cannot apply to *p*-Me-DTBP; methanol or a Cu(II)−OMe species might be formed, but a detailed analysis was not performed.

As can be seen from **Scheme 4** (step v), the product DTBQ in the [(DMM-tmpa)$Cu^{II}(O_2^{\bullet-})]^+$ (**2**) plus *p*-R-DTBP substrate reaction, should have one of its O-atoms derived from molecular oxygen (derived from **2**). Indeed, this appears to be the case. The reaction of *p*-^{t}Bu-DTBP with **2** provides for a quantitative yield of DTBQ (based on the stoichiometry of two molecules of **2** per one mole of phenol substrate). For ^{18}O-labeled **2** (derived from **1** plus $^{18}O_2$), reaction with *p*-^{t}Bu-DTBP affords a 40 % of ^{18}O-incorporated DTBQ (GC-MS). The smaller isotope incorporation yield than expected may result from the ^{18}O-^{16}O exchange reaction with water, because carbonyl compounds are known to undergo oxygen exchange reactions with water, catalyzed by acids or bases.[50]

3.4.5 $[Cu^{II}(O_2^{\bullet-})]^+$ (**2**) coupling with 2,4,6-tri-*tert*-butylphenoxyl radical

A set of experiments that provides further and strong support for our mechanistic picture of the chemistry comes from reacting [(DMM-tmpa)$Cu^{II}(O_2^{\bullet-})]^+$ (**2**) with isolated $^tBu_3ArO$• (**Scheme 6**). The addition of one equiv $^tBu_3ArO$• to **2** was monitored by UV-vis and EPR spectroscopies. A fast reaction occurs; the intermediate **2** quickly disappears (UV-vis monitoring) and the Cu(II) EPR spectrum previously observed for the [(DMM-tmpa)$Cu^{II}(OH(H))]^{+/2+}$ product appears. The yield of DTBQ was 98 % and a 70~80 % ^{18}O-incorporation into the DTBQ product was observed. Thus, the **2** + $^tBu_3ArO$• occurs with a

1:1 stoichiometry (**Scheme 4**, step ii), and this then supports the $[\mathrm{Cu^{II}(O_2^{\bullet -})}]^+$: phenol = 2 : 1 overall stoichiometry. Upon benchtop mixing of **2** and $^t\mathrm{Bu_3ArO}$• (less than 1 min, with 1:1 ratios of reagents), the reaction is already over by the time the first UV−vis spectrum could be recorded, as indicated by the complete loss of the UV−vis signals ascribed to **2** (**Figure 3**) and an expected 402 nm peak for $^t\mathrm{Bu_3ArO}$•. It is outside the scope of this study to attempt stopped-flow (triple mixing) experiments which would be required. In contrast to the case of *p*-OR-DTBP, the oxygen incorporated into the oxidized product (DTBQ) obtained from the reaction of *p*-R-DTBP with **2** originates from **2** *via* O-O bond cleavage followed by the elimination of the oxidized R group (**Scheme 4**, step v).

Scheme 6. The reaction of $[\mathrm{Cu^{II}(O_2^{\bullet -})}]^+$ (**2**) and $^t\mathrm{Bu_3ArO}$•

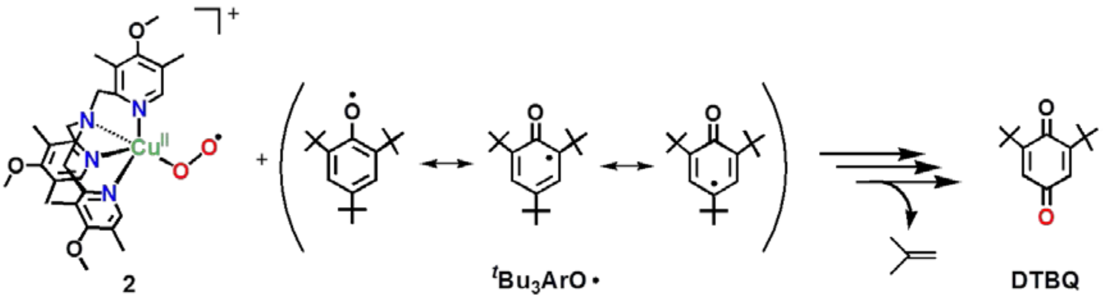

3.4.6 A minor reaction pathway contributing to *p*-R-DTBP oxidation

If the reaction of $[(\mathrm{DMM\text{-}tmpa})\mathrm{Cu^{II}(O_2^{\bullet -})}]^+$ (**2**) with *p*-*R*-DTBP (or that of 2 + $^t\mathrm{Bu_3ArO}$•) occurred only *via* step v (**Scheme 4**), the product solution should not oxidize iodide since no H_2O_2 would have been generated. However, we observed 20~30 % of triiodide absorption band formation when testing for peroxide. We explain this by invoking the "minor" step vi, where hydrolysis of *A′* occurs giving 2,4,6-tri-*tert*-butyl-4-hydroperoxycyclohexa-2,5-dienone (*C′*), which (i) does itself oxidize iodide ion (see

Experimental Section), and (ii) slowly converts to DTBQ (at RT) but (iii) fully converts to DTBQ in the GC-MS experiment.

3.4.7 Precedent and comparison with cobalt and nickel superoxide phenol oxidations

In the overall process involving reaction of the *p*-X-DTBP, steps i and ii (top line; Scheme 4), a second mole-equiv of $[(\text{DMM-tmpa})\text{Cu}^{\text{II}}(\text{OH})]^+$ and H_2O_2 are produced, all consistent with the identity and yields of products obtained, and thus the reaction stoichiometry. Nishinaga and coworkers, in classical studies of the reactions of $[\text{Co}^{\text{III}}(\text{O}_2^{\bullet-})]^+$ (formed from Co^{II} and O_2), also observed this same reaction stoichiometry, involving two $[\text{Co}^{\text{III}}(\text{O}_2^{\bullet-})]^+$ moieties with one phenol substrate. Further, Nishinaga's work provides precedent for the proposed (**Scheme 4**) reaction of $[(\text{DMM-tmpa})\text{Cu}^{\text{II}}(\text{O}_2^{\bullet-})]^+$ (**2**) with the initially generated phenoxyl radical intermediate;[51, 52] Nishinaga[52] also obtained a cobalt peroxy species Co^{III}-OO-(ArO'), and its X-ray structure for a *para*-^{t}Bu phenol substrate (**Figure 7**). Further, in order to explain the products observed in very recent investigations by Driess and co-workers,[53] involving phenol reactions with a new $[\text{Ni}^{\text{II}}(\text{O}_2^{\bullet-})]^+$ complex, an intermediate analogous to *A′* was proposed to form from *p*-R-DTBP's (R = H, Me, ^{t}Bu) substrates.

Scheme 7. Phenol oxidation by cobalt(III) superoxo complex

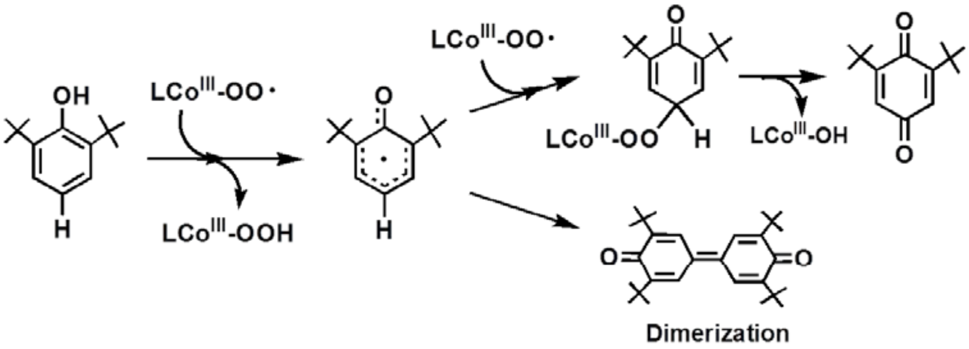

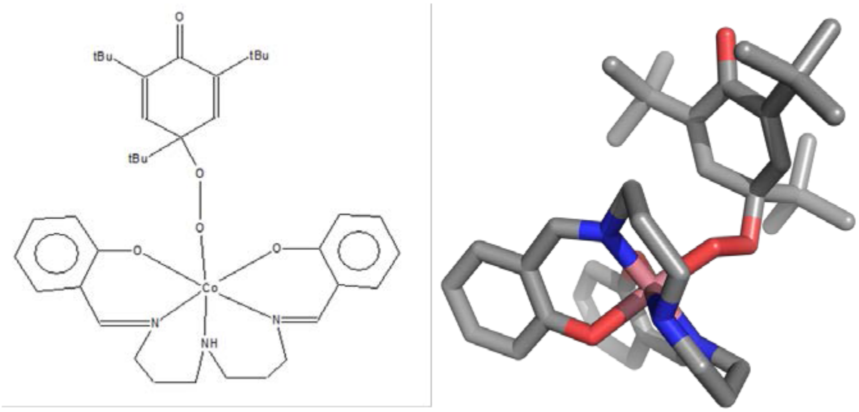

Figure 7. Chemdraw and X-ray crystal structure of cobalt peroxy species Co^{III}-OO-(ArO')

3.4.8 A prior computational study of $[Cu^{II}(O_2^{\bullet-})]^+$ reaction with 2,6-di-*tert*-butylphenol (*p*-H-DTBP) leading to a 2,6-di-*tert*-butyl-1,4-benzoquinone (DTBQ)

In 2009, based on DFT calculations, Güell et al.[54] proposed a mechanism (**Scheme 8**) of *p*-H-DTBP oxidation by a cupric superoxide complex close analogue of **2**, $[(NMe_2\text{-}tmpa)Cu^{II}(O_2^{\bullet-})]^+$ (see Introduction), which differs considerably from what we have found and proposed in the present study (**Scheme 4**). They suggest HAT occurs at the first step (as we observe), but then it is suggested that the LCu^{II}-OOH species formed undergoes Cu–OOH homolytic cleavage and the hydroperoxyl radical thus formed attacks the phenoxyl radical, overall leading to copper(I) and hydroperoxy organic. This C-O bond formation process is described as the *r.d.s*. Then, the resulting copper(I) facilitates O–O homolytic cleavage forming hydroxyl radical plus a copper(II)-O-ArO' complex. The last step involves HAT (or PCET) from the ring to hydroxyl radical leading to the formation of copper(I), a water molecule and DTBQ. Thus, their overall chemistry is formally a catalytic reaction (regenerating copper(I), to react again with more O_2 to give the cupric superoxo species), with different stoichiometry than we observed and a different *r.d.s.* as mentioned. However, we should point out that the substrate used in their calculations was *p*-H-DTBP, a perhaps rather special case compared to the series of substrates we examined, **Table 1**. In fact, we find that *p*-H-DTBP is unreactive toward $[(\text{DMM-tmpa})\text{Cu}^{\text{II}}(\text{O}_2^{\bullet-})]^+$ (**2**).

Scheme 8. The proposed catalytic cycle of phenol oxidation by $[\text{Cu}^{\text{II}}(\text{O}_2^{\bullet-})]^+$ based on computational chemistry

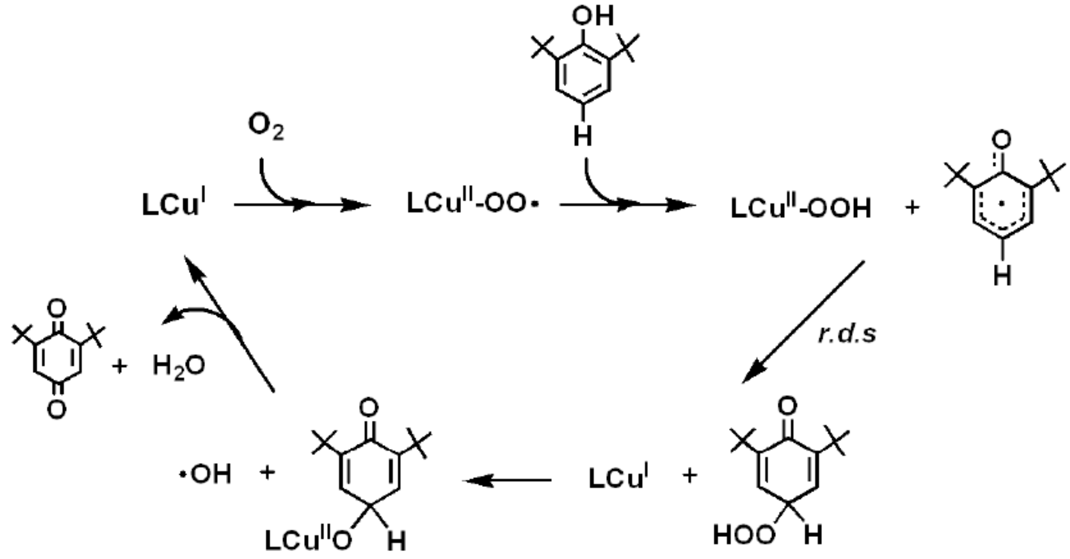

4. Conclusion

In this report, we have obtained detailed mechanistic insights into the oxidation of a wide series of *para*-substituted-2,6-di-*tert*-butyl-phenols (*p*-X-DTBP's) by a newly synthesized cupric superoxo complex supported by an electron-rich ligand, $[(\text{DMM-tmpa})\text{Cu}^{\text{II}}(\text{O}_2^{\bullet-})]^+$ (**2**). With detailed kinetic investigations, we proved that hydrogen atom abstraction is the first step and the rate-determining-step for the oxidation of *p*-X-DTBP's. The key observations supporting this were the finding of a large deuterium kinetic isotope effect, a good correlation with reactivity of the cumylperoxyl radical toward the same substrates, comparison of the rate-dependences in the phenol oxidations on the one-electron oxidation potentials of the *p*-X-DTBP substrates, and the observed activation parameters for the reaction. The hydrogen atom transfer from *p*-X-DTBP's proceeds *via* a partial transfer of charge rather than a complete transfer of charge in the ET/PT pathway. The qualitative and quantitative product analyses and reactivity study carried out with the 2,4,6-tri-*tert*-butylphenoxyl radical (^{t}Bu$_3$ArO•) reacting with **2**, allowed us to build the case for the proposed overall stoichiometry of reaction and furthermore, the detailed mechanism. Two moles of copper(II) superoxo species are required to oxidize *para*-substituted-2,6-di-*tert*-butylphenols to 2,6-di-*tert*-butyl-1,4-benzoquinones. It is found that the reaction of **2** toward *para*-alkoxy-2,6-di-*tert*-butylphenol proceeds *via* two-electron oxidation with hydrolysis while reaction with *para*-alkyl-2,6-di-*tert*-butylphenol proceeds *via* a process involving four-electron oxygenation chemistry.

This study contributes significantly to our understanding of the fundamental chemistry and oxidative capabilities of initial copper(I)-dioxygen adducts, i.e., cupric-superoxide complexes. As described in the Introduction, $Cu^{II}(O_2^{\bullet-})$ species are implicated in reactions with both C–H and O–H containing substrates, and the latter biomimetic chemistry was the focus of attention here. The supporting ligand is well known to modulate the structural, electronic structure/bonding, as well as the reactivity nature of copper complexes, here with O_2 derived fragments bound to the copper ion. Thus, future efforts will include the generation of $Cu^{II}(O_2^{\bullet-})$ complexes with rather differing supporting ligands, to explore the range of reactivity possible for such primary copper-dioxygen adducts.

5. References

1. Mirica, L. M.; Ottenwaelder, X.; Stack, T. D. P., *Chem. Rev.* **2004,** *104*, 1013-1045; Lewis, E. A.; Tolman, W. B., *Chem. Rev.* **2004,** *104*, 1047-1076; Hatcher, L. Q.; Karlin, K. D., *J. Biol. Inorg. Chem.* **2004,** *9*, 669-683; Peterson, R. L.; Kim, S.; Karlin, K. D., 3.07 - Copper Enzymes. In *Comprehensive Inorganic Chemistry II (Second Edition)*, Reedijk, J.; Poeppelmeier, K., Eds. Oxford: Elsevier: Amsterdam, 2013; Vol. 3, pp 149-177, http://dx.doi.org/10.1016/B978-0-08-097774-4.00309-0.

2. Schröder, D.; Holthausen, M. C.; Schwarz, H., *J. Phys. Chem. B* **2004,** *108* (38), 14407-14416; Dietl, N.; van der Linde, C.; Schlangen, M.; Beyer, M. K.; Schwarz, H., *Angew. Chem., Int. Ed.* **2011,** *50* (21), 4966-4969.

3. Hong, S.; Huber, S. M.; Gagliardi, L.; Cramer, C. C.; Tolman, W. B., *J. Am. Chem. Soc.* **2007,** *129* (46), 14190-14192; Donoghue, P. J.; Tehranchi, J.; Cramer, C. J.; Sarangi, R.; Solomon, E. I.; Tolman, W. B., *J. Am. Chem. Soc.* **2011,** *133* (44), 17602-17605; Kunishita, A.; Ishimaru, H.; Nakashima, S.; Ogura, T.; Itoh, S., *J. Am. Chem. Soc.* **2008,** *130*, 4244-4245; Maiti, D.; Narducci Sarjeant, A. A.; Karlin, K. D., *Inorg. Chem.* **2008,** *47* (19), 8736-8747.

4. Nakao, Y.; Hirao, K.; Taketsugu, T., *J. Chem. Phys.* **2001,** *114* (18), 7935-7940; Decker, A.; Solomon, E. I., *Curr. Opin. Chem. Biol.* **2005,** *9* (2), 152-163; Yoshizawa, K.; Kihara, N.; Kamachi, T.; Shiota, Y., *Inorg. Chem.* **2006,** *45* (7), 3034-3041.

5. Itoh, S., *Curr. Opin. Chem. Biol.* **2006,** *10* (2), 115-122.

6. Klinman, J. P., *Chem. Rev.* **1996,** *96*, 2541-2561.

7. Klinman, J. P., *J. Biol. Chem.* **2006,** *281*, 3013-3016.

8. McGuirl, M. A.; Dooley, D. M., *Curr. Opin. Chem. Biol.* **1999,** *3*, 138-144; Rokhsana, D.; M., S. E.; Brown, D. E.; Dooley, D. M., Amine Oxidase and Galactose Oxidase. In *Copper-Oxygen Chemistry*, Itoh, S.; Karlin, K. D., Eds. John Wiley & Sons, Inc.: Hoboken, 2011; Vol. 4, pp 53-106.

9. Humphreys, K. J.; Mirica, L. M.; Wang, Y.; Klinman, J. P., *J. Am. Chem. Soc.* **2009,** *131* (13), 4657-4663.

10. Liu, Y.; Mukherjee, A.; Nahumi, N.; Ozbil, M.; Brown, D.; Angeles-Boza, A. M.; Dooley, D. M.; Prabhakar, R.; Roth, J. P., *J. Phys. Chem. B* **2012,** *117* (1), 218-229.

11. Evans, J. P.; Ahn, K.; Klinman, J. P., *J. Biol. Chem.* **2003,** *278* (50), 49691-49698.

12. Chen, P.; Solomon, E. I., *J. Am Chem. Soc.* **2004,** *126*, 4991-5000; Chen, P.; Bell, J.; Eipper, B. A.; Solomon, E. I., *Biochemistry* **2004,** *43* (19), 5735-5747.

13. Prigge, S. T.; Eipper, B.; Mains, R.; Amzel, L. M., *Science* **2004,** *304*, 864-867.

14. Warren, J. J.; Tronic, T. A.; Mayer, J. M., *Chem. Rev.* **2010,** *110* (12), 6961-7001.

15. Osako, T.; Ohkubo, K.; Taki, M.; Tachi, Y.; Fukuzumi, S.; Itoh, S., *J. Am Chem. Soc.* **2003,** *125* (36), 11027-11033.

16. Kunishita, A.; Kubo, M.; Sugimoto, H.; Ogura, T.; Sato, K.; Takui, T.; Itoh, S., *J. Am. Chem. Soc.* **2009,** *131* (8), 2788-2789.

17. Kunishita, A.; Ertem, M. Z.; Okubo, Y.; Tano, T.; Sugimoto, H.; Ohkubo, K.; Fujieda, N.; Fukuzumi, S.; Cramer, C. J.; Itoh, S., *Inorg. Chem.* **2012,** *51* (17), 9465-9480.

18. Liang, H.-C.; Kim, E.; Incarvito, C. D.; Rheingold, A. L.; Karlin, K. D., *Inorg, Chem.* **2002,** *41* (8), 2209-2212.

19. Manner, V. W.; Markle, T. F.; Freudenthal, J. H.; Roth, J. P.; Mayer, J. M., *Chem. Commun.* **2008,** (2), 256-258.

20. Nishinaga, A.; Shimizu, T.; Matsuura, T., *J. Org. Chem.* **1979,** *44* (17), 2983-2988.

21. Zhang, C. X.; Kaderli, S.; Costas, M.; Kim, E.-i.; Neuhold, Y.-M.; Karlin, K. D.; Zuberbühler, A. D., *Inorg. Chem.* **2003,** *42*, 1807-1824.

22. Fyfe, C. A.; Vanveen, L., *J. Am. Chem. Soc.* **1977,** *99* (10), 3366-3371.

23. Omura, K., *J. Org. Chem.* **1996,** *61* (20), 7156-7161.

24. Maiti, D.; Fry, H. C.; Woertink, J. S.; Vance, M. A.; Solomon, E. I.; Karlin, K. D., *J. Am. Chem. Soc.* **2007,** *129* (2), 264-265.

25. Kim, S.; Saracini, C.; Siegler, M. A.; Drichko, N.; Karlin, K. D., *Inorg. Chem.* **2012,** *51* (23), 12603-12605.

26. Nash, T., *Biochem. J.* **1953,** *55*, 416-421; Zhang, C. X. Synthetic Analogues for Copper Metalloenzymes: Effects of Ligand Electronic and Structural Variations on the Formation, Stability and Reactivity of Biomimetic Copper-Dioxygen Adducts. The Johns Hopkins University, Baltimore, 2001.

27. Fujisawa, K.; Tanaka, M.; Morooka, Y.; Kitajima, N., *J. Am. Chem. Soc.* **1994,** *116* (26), 12079-12080; Chen, P.; Root, D. E.; Campochiaro, C.; Fujisawa, K.; Solomon, E. I., *J. Am Chem. Soc.* **2003,** *125* (2), 466-474.

28. Würtele, C.; Gaoutchenova, E.; Harms, K.; Holthausen, M. C.; Sundermeyer, J.; Schindler, S., *Angew. Chem. Int. Ed.* **2006,** *45*, 3867-3869.

29. Woertink, J. S.; Tian, L.; Maiti, D.; Lucas, H. R.; Himes, R. A.; Karlin, K. D.; Neese, F.; Würtele, C.; Holthausen, M. C.; Bill, E.; Sundermeyer, J.; Schindler, S.; Solomon, E. I., *Inorg. Chem.* **2010,** *49* (20), 9450-9459.

30. Ginsbach, J. W.; Peterson, R. L.; Cowley, R. E.; Karlin, K. D.; Solomon, E. I., *Inorg. Chem.* **2013,** *52* (22), 12872-12874.

31. Lucas, H. R.; Meyer, G. J.; Karlin, K. D., *J. Am. Chem. Soc.* **2010,** *132* (37), 12927-12940.

32. Peterson, R. L.; Himes, R. A.; Kotani, H.; Suenobu, T.; Tian, L.; Siegler, M. A.; Solomon, E. I.; Fukuzumi, S.; Karlin, K. D., *J. Am. Chem. Soc.* **2011,** *133* (6), 1702-1705.

33. Maiti, D.; Lee, D.-H.; Gaoutchenova, K.; Würtele, C.; Holthausen, M. C.; Sarjeant, A. A. N.; Sundermeyer, J.; Schindler, S.; Karlin, K. D., *Angew. Chem., Int. Ed.* **2008,** *47* (1), 82-85.

34. Bordwell, F. G.; Zhang, X.-M., *J. Phys. Org. Chem.* **1995,** *8*, 529-535.

35. Francisco, W. A.; Merkler, D. J.; Blackburn, N. J.; Klinman, J. P., *Biochemistry* **1998,** *37* (22), 8244-8252.

36. Miller, S. M.; Klinman, J. P., *Biochemistry* **1983,** *22* (13), 3091-3096.

37. Nemes, A.; Bakac, A., *Inorg. Chem.* **2001,** *40* (4), 746-749.

38. Fukuzumi, S.; Shimoosako, K.; Suenobu, T.; Watanabe, Y., *J. Am. Chem. Soc.* **2003,** *125* (30), 9074-9082.

39. Pratt, D. A.; Dilabio, G. A.; Mulder, P.; Ingold, K. U., *Acc. Chem. Res.* **2004,** *37* (5), 334-340.

40. Matsumoto, T.; Ohkubo, K.; Honda, K.; Yazawa, A.; Furutachi, H.; Fujinami, S.; Fukuzumi, S.; Suzuki, M., *J. Am. Chem. Soc.* **2009,** *131* (26), 9258-9267; Marcus, R. A., *J. Phys. Chem.* **1966,** *72*, 891.

41. Guttenplan, J. B.; Cohen, S. G., *J. Am. Chem. Soc.* **1972,** *94* (11), 4040-4042; Wagner, P. J.; Lam, H. M. H., *J. Am. Chem. Soc.* **1980,** *102* (12), 4167-4172.

42. Lockwood, M. A.; Blubaugh, T. J.; Collier, A. M.; Lovell, S.; Mayer, J. M., *Angew. Chem. Int. Ed.* **1999,** *38*, 225-227.

43. Yiu, D. T. Y.; Lee, M. F. W.; Lam, W. W. Y.; Lau, T.-C., *Inorg. Chem.* **2003,** *42* (4), 1225-1232.

44. Lansky, D. E.; Goldberg, D. P., *Inorg. Chem.* **2006,** *45* (13), 5119-5125.

45. Miyazaki, S.; Kojima, T.; Mayer, J. M.; Fukuzumi, S., *J. Am. Chem. Soc.* **2009,** *131* (32), 11615-11624.

46. Kohen, A.; Klinman, J. P., *Acc. Chem. Res.* **1998,** *31* (7), 397-404; Kwart, H., *Acc. Chem. Res.* **1982,** *15* (12), 401-408.

47. Francisco, W. A.; Knapp, M. J.; Blackburn, N. J.; Klinman, J. P., *J. Am. Chem. Soc.* **2002,** *124* (28), 8194-8195.

48. Wali, A.; Das, J.; Pillai, S. M.; Ravindranathan, M., *Green Chem.* **2002,** *4*, 587-591; Mandal, S.; Macikenas, D.; Protasiewicz, J. D.; Sayre, L. M., *J. Org. Chem.* **2000,** *65* (16), 4804-4809; Nishinaga, A.; Itahara, T.; Shimizu, T.; Matsuura, T., *J. Am. Chem. Soc.* **1978,** *100* (6), 1820-1825; Peters, A.; Trumm, C.; Reinmuth, M.; Emeljanenko, D.; Kaifer, E.; Himmel, H.-J. r., *Eur. J. Inorg. Chem.* **2009,** *2009* (25), 3791-3800; Gupta, R.; Mukherjee, R., *Tet. Lett.* **2000,** *41* (40), 7763-7767; Cvetkovic, M.; Batten, S. R.; Moubaraki, B.; Murray, K. S.; Spiccia, L., *Inorg. Chim. Acta* **2001,** *324* (1,Äì2), 131-140; Gupta, M.; Upadhyay, S. K.; Sridhar, M. A.; Mathur, P., *Inorg. Chim. Acta* **2006,** *359* (13), 4360-4366; Singla, M.; Mathur, P.; Gupta, M.; Hundal, M. S., *Transition Met Chem* **2008,** *33* (2), 175-182; Mukherjee, C.; Weyhermuller, T.; Bothe, E.; Chaudhuri, P., *C. R. Chimie* **2007,** *10* (4-5), 313-325; Singh, A. P.; Gupta, R., *Eur. J. Inorg. Chem.* **2010,** (28), 4546-4554; Bakshi, R.; Mathur, P., *Inorg. Chim. Acta* **2010,** *363* (13), 3477-3488; Ahuja, G.; Mathur, P., *Inorg. Chem. Commun.* **2012,** *17* (0), 42-48.

49. We were not able to detect isobutylene as a product.

50. Damuel, D.; Silver, B. L., *Adv. Phys. Org. Chem.* **1965,** *3*, 123-186; Kawanishi, Y.; Suzuki, Y.; Miyazawa, A., *Chem. Eng. J.* **2011,** *167* (2-3), 531-535.

51. Nishinaga, A.; Tomita, H.; Matsuura, T., *Tet. Lett.* **1980,** *21* (35), 3407-3408.

52. Nishinaga, A.; Tomita, H.; Nishizawa, K.; Matsuura, T.; Ooi, S.; Hirotsu, K., *J. Chem. Soc. Dalton Trans.* **1981,** (7), 1504-1514.

53. Company, A.; Yao, S.; Ray, K.; Driess, M., *Chem.-Eur. J.* **2010,** *16* (31), 9669-9675.

54. Güell, M.; Luis, J.; Solà, M.; Siegbahn, P., *J. Biol. Inorg. Chem.* **2009,** *14* (2), 229-242.

6. Supporting Information

6.1 Proposed Mechanisms of Copper Oxidases

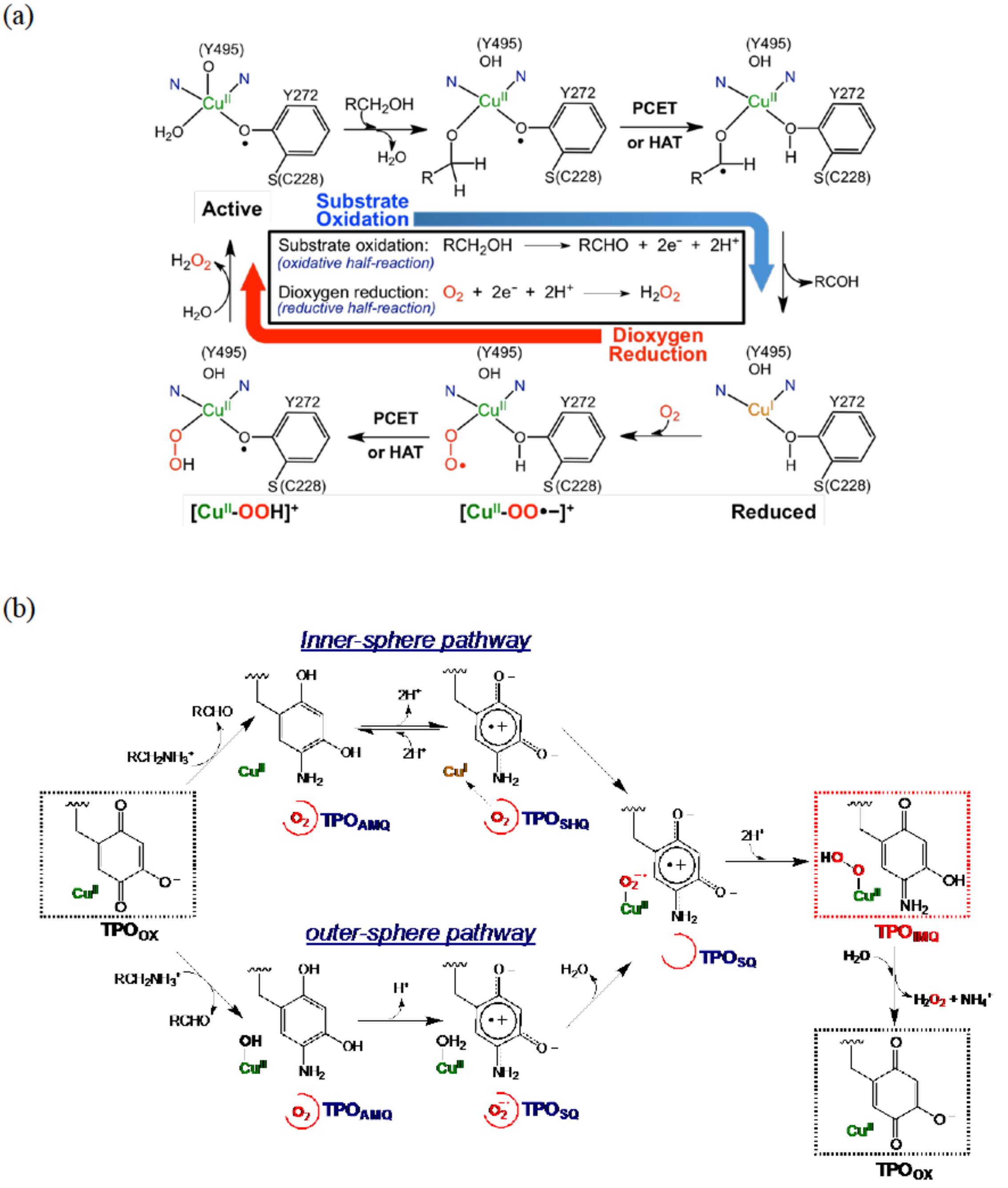
(a)
(Y495)
Y272
S(C228)
RCH2OH
H2O
PCET
or HAT
Active
Substrate Oxidation
Substrate oxidation: RCH2OH → RCHO + 2e⁻ + 2H⁺
(oxidative half-reaction)
Dioxygen reduction: O2 + 2e⁻ + 2H⁺ → H2O2
(reductive half-reaction)
H2O2
H2O
RCOH
Dioxygen Reduction
O2
[CuII-OOH]+
[CuII-OO•−]+
Reduced
(b)
Inner-sphere pathway
RCHO
RCH2NH3+
2H+
TPOAMQ
TPOSHQ
TPOox
outer-sphere pathway
H+
H2O
TPOSQ
TPOIMQ
H2O2 + NH4+

Figure S1. Proposed pathways for the primary alcohol oxidation/dioxygen reduction by galactose oxidase (GO) (a) and for copper amine oxidase (CAO) catalytic mechanism illustrating the two pathways for cofactor reoxidation (b).[a]

---

[a] R. L. Peterson, S. Kim, K. D. Karlin "3.07 - Copper Enzymes," In Comprehensive Inorganic Chemistry II (Second Edition); Editors-in-Chief:, J. Reedijk, K. Poeppelmeier, Ed.; Elsevier: Amsterdam, 2013; pp 149-177.

6.2 Generation of SO_2

$$H_2SO_{4\,(aq)} + Na_2S_2O_5 \rightarrow Na_2SO_4 + H_2O + 2\ SO_{2(g)}$$

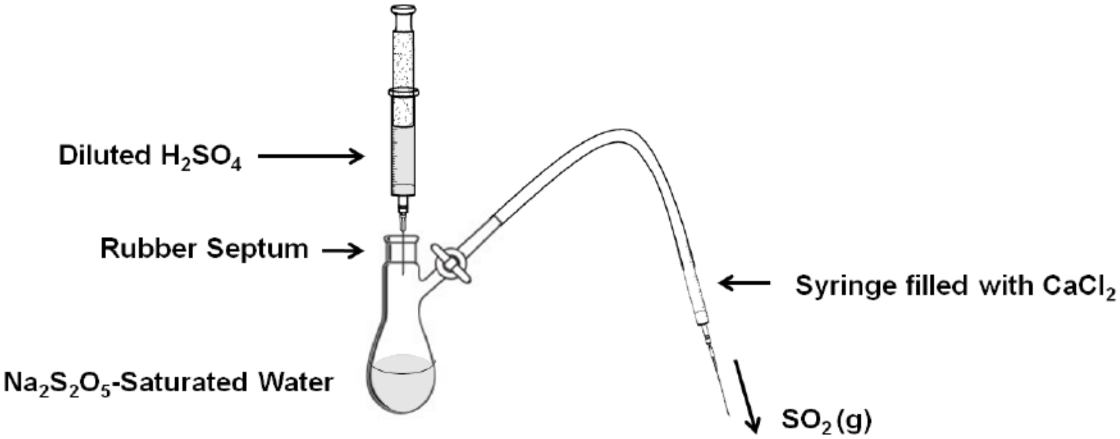
Diluted H_2SO_4
Rubber Septum
Syringe filled with $CaCl_2$
$Na_2S_2O_5$-Saturated Water
SO_2(g)

Figure S2. An apparatus setup for sulfur dioxide (SO_2, gas) generation.

6.3 EPR Spectra of Cu Complexes

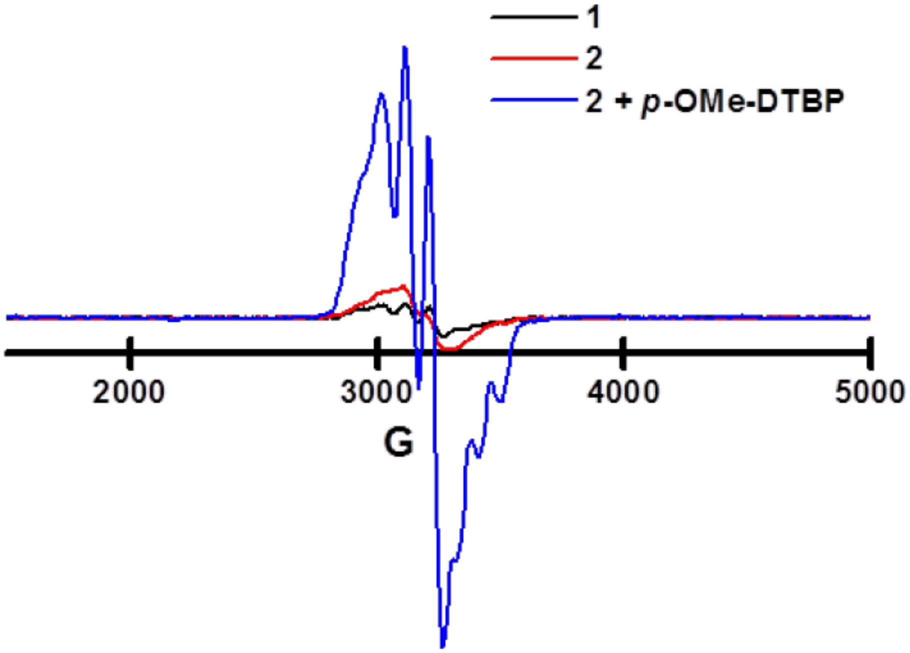

Figure S3. Low-temperature EPR spectra of [(DMM-tmpa)Cu^I(CO)]B(C_6F_5)$_4$ (**1**) (**black**), [(DMM-tmpa)Cu^{II}($O_2^{\bullet -}$)]B(C_6F_5)$_4$ (**2**) (**red**), and **2** + one equiv *para*-methoxy-2,6-di-*tert*-butylphenol (**blue**) (2 mM; 3X-band, $\nu = 9.426$ GHz; acetone at 23 K): $g_{\|} = 1.96$, $A_{\|} = 76$ G, $g_{\perp} = 2.20$, $A_{\perp} = 97$ G. The results indicate **1** and **2** are EPR "silent", as expected, exhibiting only impurity (~ 5%) quantities of a typical copper(II) paramagnetic compound, i.e., that copper(II) complex forming by the reaction of **2** with one equiv phenol substrate. Also, see **Figure S7**.

6.4 Kinetic Study of $[(NMe_2\text{-tmpa})Cu^{II}(O_2^{\bullet-})]^+$

mM	s^{-1}
2.7	0.0104
4.1	0.0179
5.4	0.0234
6.8	0.0331

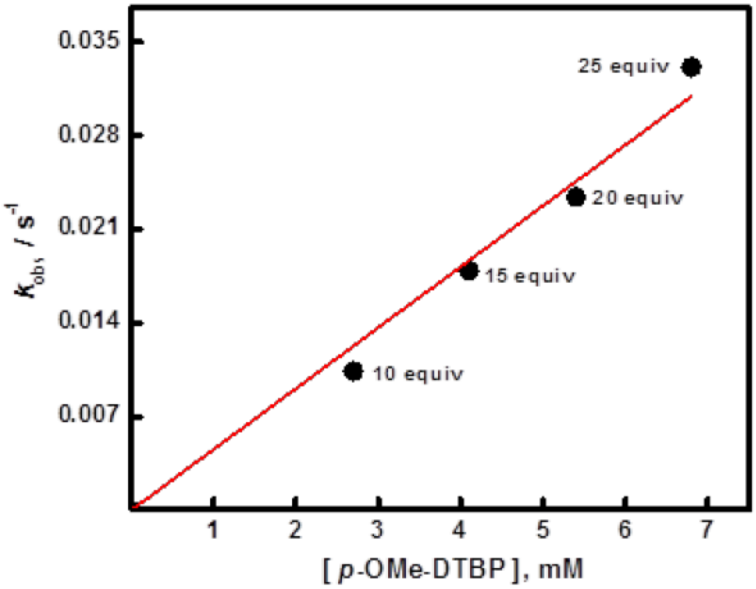

Figure S4. The table of pseudo-first-order rate constants (k_{obs}'s) from the reactions of *p*-OMe-DTBP plus $[(NMe_2\text{-tmpa})Cu^{II}(O_2^{\bullet-})]^+$ and the plot of k_{obs}'s against the concentrations of *p*-OMe-DTBP to obtain second-order-rate constant ($k_2 = 4.6\ M^{-1}s^{-1}$).

6.5 Kinetic Isotope Effect of Cumylperoxyl Radical and Phenol Derivatives

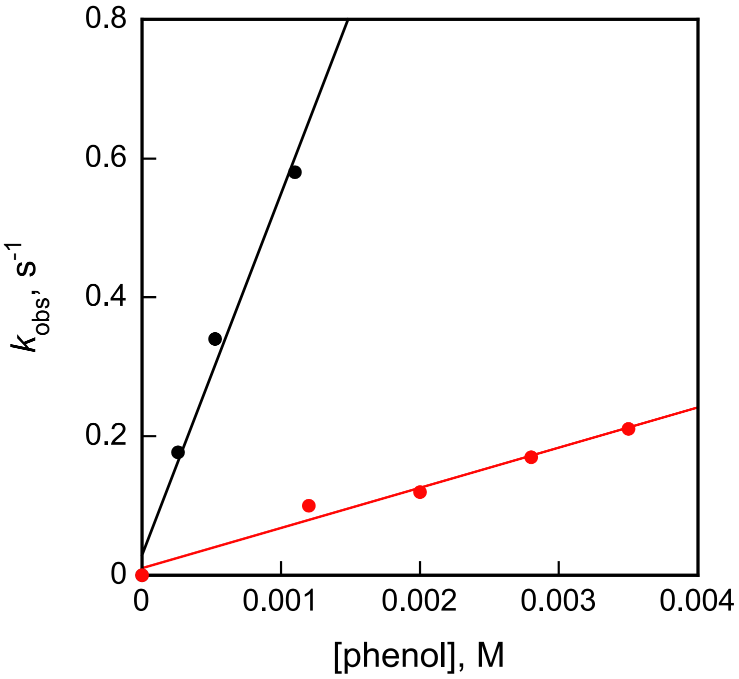

Figure S5. Plots of k_{obs}'s against the concentrations of *p*-OMe-DTBP (**black circles**) and deuterated ^{2}H-O *p*-OMe-DTBP (**red circles**) to determine second-order-rate constants and KIE (= 9.0).

6.6 Derivation of the Equation for the plot of ($k_B T/e$) lnk_2 *vs* E_{ox}

$$\Delta G° = -\,n\,F\,\Delta E°$$

$$\Delta G° = -\,RT \ln K$$

$$\rightarrow n\,F\,\Delta E° = RT \ln K$$

$$\rightarrow \Delta E° = \frac{RT}{nF} \ln K$$

"Electron transfers in chemical and biology" R.A. Marcus, N. Sutin; Biochimica et Biophysica Acta, **1985**, *811*, 265

$$\ln k_2 = \alpha \ln K \quad (\alpha = \frac{1}{2}(1 + \frac{\Delta G°'}{\lambda}))$$

$$\rightarrow \ln K = \frac{1}{\alpha} \ln k_2$$

$$\rightarrow \quad \Delta E° = \frac{RT}{nF} \bullet \frac{1}{\alpha} \ln k_2$$

$$\frac{RT}{nF} \ln k_2 = \alpha\,\Delta E°$$

$$R = k_B N_A,\ F = eN_A$$

$$\rightarrow \quad \frac{RT}{nF} = \frac{kBT}{ne} \quad (n = 1\ \text{mol})$$

$$\therefore \quad \frac{kBT}{e} \ln k_2 = \alpha\,\Delta E°$$

ΔG° = Standard Free Energy

n = Number of Electrons per Mole

F = Faraday Constant

ΔE° = Standard Electrode Potential

R = Gas Constant

T = Absolute Temperature

K = Equilibrium Constant

k_2 = Rate Constant

λ = Reorganization Energy

ΔG°′ = Free Energy of Reaction

k_B = Boltzmann Constant

N_A = Avogadro Constant

e = Electric Charge

6.7 Temperature Effect of Kinetic Isotope Effect Values

	O-H					O-D					
℃	10 equiv	15 equiv	20 equiv	25 equiv	k_2	10 equiv	15 equiv	20 equiv	25 equiv	k_2	**KIE**
-100	0.0297	0.0425	0.058	0.0791	**11**	0.0021	0.004	0.0052	0.0063	**0.96**	**11**
-95	0.0336	0.0571	0.0784	0.0928	**14**	0.0028	0.0048	0.0069	0.0077	**1.2**	**12**
-90	0.054	0.0883	0.1248	0.1606	**23**	0.0051	0.0078	0.0112	0.0148	**2.1**	**11**
-85	0.0599	0.0984	0.1338	0.1877	**26**	0.0068	0.0099	0.0119	0.0133	**2.7**	**9.6**

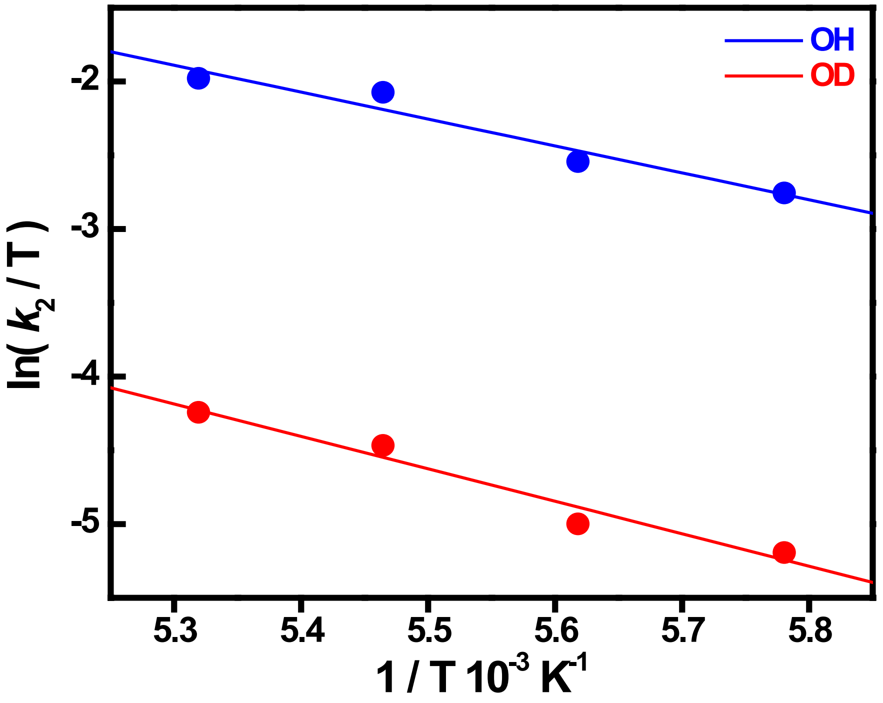

Figure S6. Table of pseudo-first-order rate constants (k_{obs}'s), second-order rate constants (k_2's) and kinetic isotope effects (KIEs) for the reactions of [(DMM-tmpa)Cu^{II}(O$_2^{\bullet-}$)]$^+$ (**2**) and *para*-methoxy-2,6-di-*tert*-butylphenol (*p*-OMe-DTBP; H-O *vs* ^{2}H-O) in acetone over the temperature range of –100 °C ~ –85 °C (upper panel). Eyring plots of k_2's against 1/T for the oxidation of *p*-OMe-DTBP (H-O for **blue** and ^{2}H-O for **red**) to determine the reaction activation parameters (lower panel).

6.8 EPR Spectra of Reaction Solution

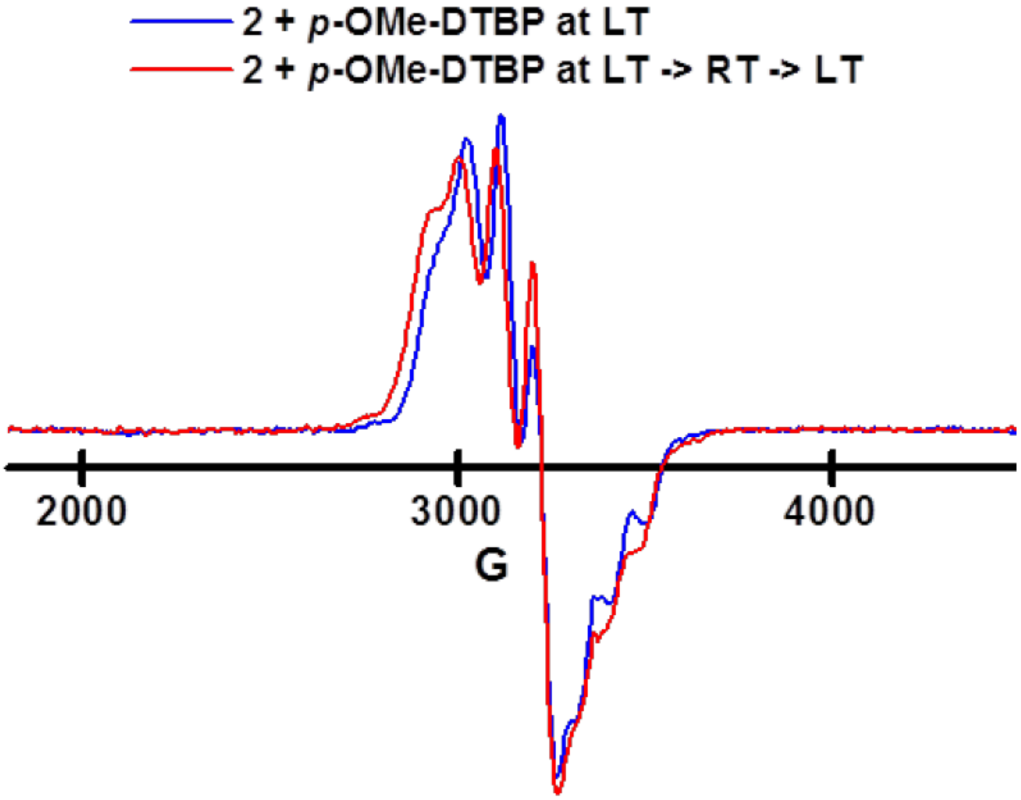

Figure S7. EPR spectra of [(DMM-tmpa)Cu^{II}($O_2^{\bullet-}$)]B(C_6F_5)$_4$ (**2**) + one equiv *para*-methoxy-2,6-di-*tert*-butylphenol (*p*-OMe-DTBP) at low temperature (**blue**) and solution of **2** + one equiv *p*-OMe-DTBP which was warmed up to room temperature and then frozen again (**red**) (2 mM; 3X-band, ν = 9.426 GHz; acetone at 23 K). For both samples, **blue** and **red**, $g_{\|} = 1.96$, $A_{\|} = 76$ G, $g\perp = 2.20$, $A\perp = 97$ G. Thus, the **red** spectrum is representative of [(DMM-tmpa)Cu^{II}-OH(H)]$^+$.

NOTE: EPR spectra observed for (***A*** ≡ ***A'***) (from mixing **2** & ArOH at –90 °C), for [(DMM-tmpa)Cu^{II}-OH(H)]$^+$ (observable at RT) are indistinguishable, and further are identical to spectra of (i) [(DMM-tmpa)Cu^{II}(CH_3CN)](ClO_4)$_2$•0.5(O(CH_2CH_3)$_2$), (ii) that species generated by reaction of [(DMM-tmpa)Cu^{II}(CH_3CN)](ClO_4)$_2$•0.5(O(CH_2CH_3)$_2$) plus hydroxide, and (iii) that species [(DMM-tmpa)Cu^{II}(OOH)] (**3**) generated by reaction of [(DMM-tmpa)Cu^{II}(CH_3CN)](ClO_4)$_2$•0.5(O(CH_2CH_3)$_2$) with a small excess of $H_2O_{2(aq)}$/Et_3N or by addition of 3/2 $H_2O_{2(aq)}$ to copper(I) complex **1**. See the next section for details of the synthesis and characterization of [(DMM-tmpa)Cu^{II}(CH_3CN)](ClO_4)$_2$ •0.5(O(CH_2CH_3)$_2$), including its X-ray structure.

6.9 Synthesis of [(DMM-tmpa)Cu^{II}(CH_3CN)](ClO_4)$_2$ • 0.5 (O(CH_2CH_3)$_2$)

In a Schlenk flask containing 100 mg of DMM-tmpa ligand and 79.7 mg of $Cu^{II}(ClO_4)_2$ • 6 H_2O were dissolved in ~ 5 mL acetonitrile. The resulting solution was precipitated as blue solid upon addition of diethyl ether (100 mL) and crystals were obtained by vapor diffusion of diethyl ether into a solution of the complex in acetonitrile yielding 160 mg (92%) of blue crystals. **Elemental analysis:** Calculated: C (46.24), H (5.51), N (8.70); found: C (46.30), H (5.32), N (9.0).

6.10 X-ray crystallography

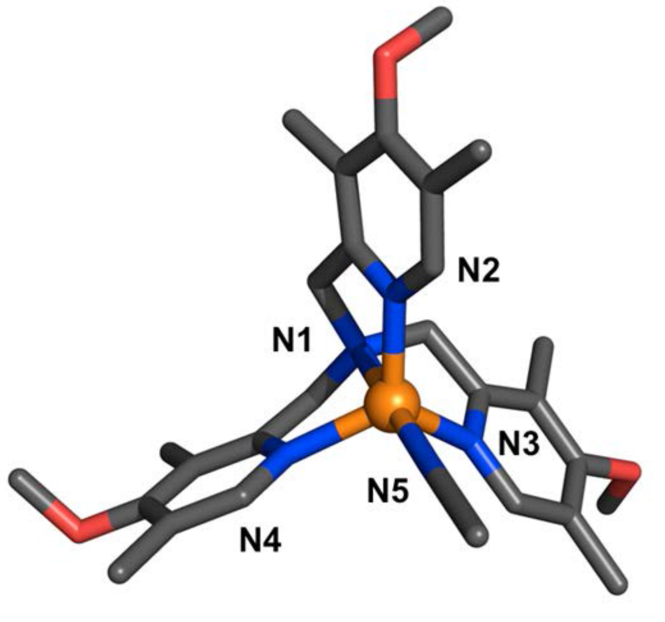

Selected Bond Lengths and Angles	
Atoms	**Bond Length(Å)**
N1-Cu1(tripod)	1.999
N2-Cu1	2.051
N3-Cu1	2.045
N4-Cu1	2.081
N5-Cu1(ACN)	1.970
	Bond Angle (°)
N1-Cu1-N5	179.15
N1-Cu1-N2	81.54
N1-Cu1-N3	81.00
N1-Cu1-N4	81.14
N2-Cu1-N5	97.83
N2-Cu1-N3	122.18
N2-Cu1-N4	117.34
N3-Cu1-N4	113.62
N3-Cu1-N5	98.87
N4-Cu1-N5	99.67

Figure S8. Left: Dicationic portion of [(DMM-tmpa)Cu^{II}(CH$_3$CN)](ClO$_4$)$_2$. Right: Selected bond distances and angles are given below; $\tau = 0.9495$ where a τ value = 0 would represent a perfect square-pyramid and a value of 1.0 would equal a perfect trigonal-bipyramid. See Experimental details concerning the X-ray crystallographic analysis, just below.

All reflection intensities were measured at 110(2) K using a KM4/Xcalibur (detector: Sapphire3) with enhance graphite-monochromated Mo *Kα* radiation (λ = 0.71073 Å) under the program CrysAlisPro (Version 1.171.33.31, Oxford Diffraction Ltd., 2009). The program CrysAlisPro (Version 1.171.33.31, Oxford Diffraction Ltd., 2009) was used to refine the cell dimensions. Data reduction was done using the program CrysAlis RED (Version 1.171.33.31, Oxford Diffraction Ltd., 2009). The structure was solved with the program SHELXS-86 (Sheldrick, 2008) and was refined on F^2 with SHELXL-97 (Sheldrick, 2008). Multi-scan semi-empirical absorption corrections based on symmetry-related measurements were applied to the data using SADABS (Version 2.10). The temperature of the data collection was controlled using the system Cryojet (manufactured by Oxford Instruments). The H-atoms were placed at calculated positions using the instructions AFIX 23, AFIX 43 or AFIX 137 with isotropic displacement parameters having values 1.2 or 1.5 times *U*eq of the attached C atom.

The structure is mostly ordered. One of the two perchlorate anions is found to be disordered over three orientations, and the occupancy factors refine to 0.519(4), 0.281(5) and 0.200(3). A first refinement against F^2 was problematic because some unresolved residual electron density was found in one large void located at (0, 0.5, 0), which includes 34 electrons in a volume of 169 Å^3. This void is likely to contain a very disordered solvent molecule (likely to be diethyl ether with no full occupancy). The contribution for such solvent molecules was then taken out for the subsequent stages of the refinement using the program SQUEEZE.

Fw = 768.09*, blue block, 0.54 × 0.24 × 0.19 mm^3, triclinic, *P*-1 (no. 2), a = 11.8100(3), b = 12.4184(3), c = 14.5410(3) Å, α = 79.3859(19), β = 67.8701(19), γ = 69.185(2)°, V = 1843.44(8) Å^3, Z = 2, D_x = 1.38 g cm^{-3},* μ = 0.78 mm^{-1},* abs. corr. range: 0.65–0.86. 27175 Reflections were measured up to a resolution of (sin $\theta/\lambda)_{max}$ = 0.65 Å^{-1}. 8443 Reflections were unique (R_{int} = 0.0397), of which 7363 were observed [$I > 2\sigma(I)$]. 524 Parameters were refined with 349 restraints. $R1/wR2$ [$I > 2\sigma(I)$]: 0.0309/0.0808. $R1/wR2$ [all refl.]: 0.0362/0.0833. S = 1.041. Residual electron density found between −0.52 and 0.44 e Å^{-3}.

* excluding the unresolved entity contribution.

6.11 NMR Experiment

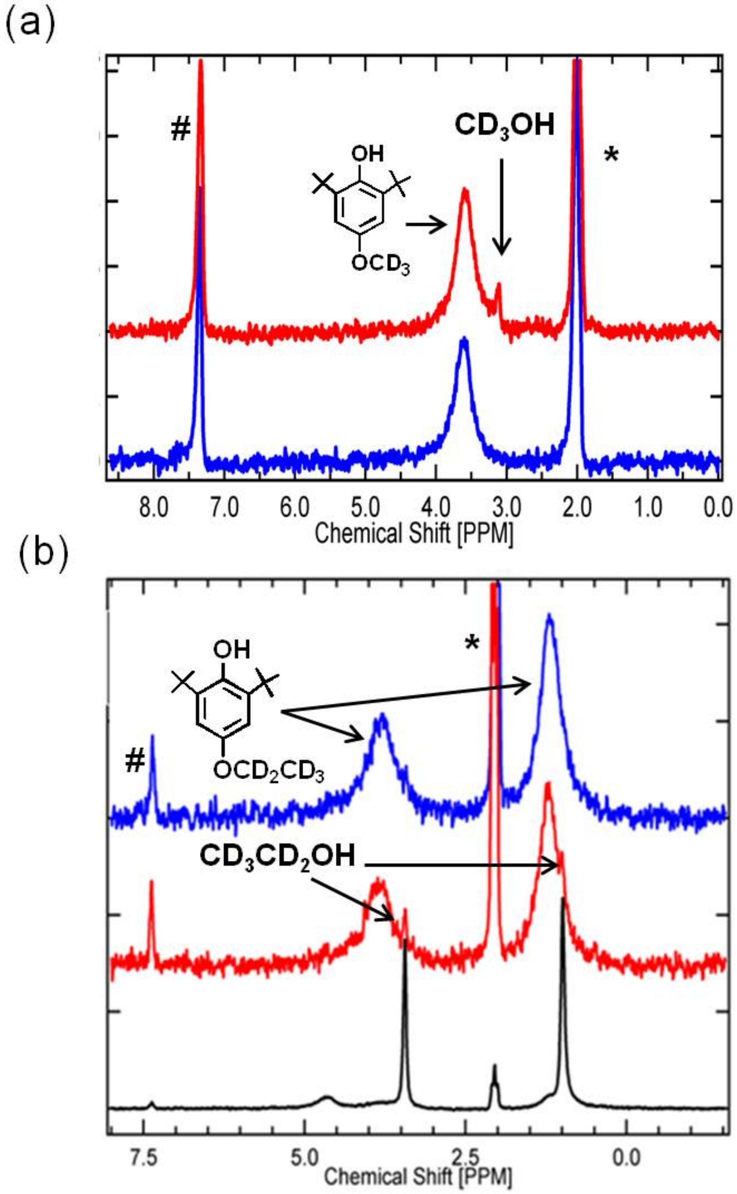

Figure S9. Low temperature ^{2}H-NMR spectra collected at –90 °C for the reaction solution of [(DMM-tmpa)Cu^{II}(O$_2^{\bullet-}$)]$^+$ (**2**) mixed with five equiv of (a) *p*-OCD$_3$-DTBP and (b) *p*-OCD$_2$CD$_3$-DTBP in acetone. (a) The blue spectrum is the reaction mixture at –90 °C. The red spectrum is the reaction mixture after it is allowed to be warmed to room temperature (RT). {Note: The deuterated methanol product (CD$_3$OH) is only observed in the red spectrum, which forms after the reaction mixture is allowed to warm to RT.} (b) The blue spectrum is the reaction mixture at –90 °C. Displayed in the red spectrum is the NMR spectrum obtained after the reaction mixture is allowed to warm to RT. The black spectrum is the room temperature reaction mixture (blue) which was spiked with *d*$_6$-ethanol. The NMR spectral ^{2}H resonances corresponding to *p*-OCD$_2$CD$_3$-DTBP and CD$_3$CD$_2$OH are indicated with arrows, respectively. *denotes solvent, $^\#$denotes C$_6$H$_6$ used as an internal reference.

6.12 Pseudo-First-Order Plots

Figure S10. Pseudo-first-order plots for the reactions of [(DMM-tmpa)Cu^{II}($O_2^{\bullet -}$)]$^+$ (**2**) and *p*-X-DTBP's to determine pseudo-first-order rate constants (k_{obs}'s). (see **Table 1** for second-order-rate constants)

(a) *p*-OCH_2CH_3-DTBP

OCH_2CH_3	
mM	s^{-1}
2.7	0.0551
4.1	0.0821
5.4	0.1233
6.8	0.1517

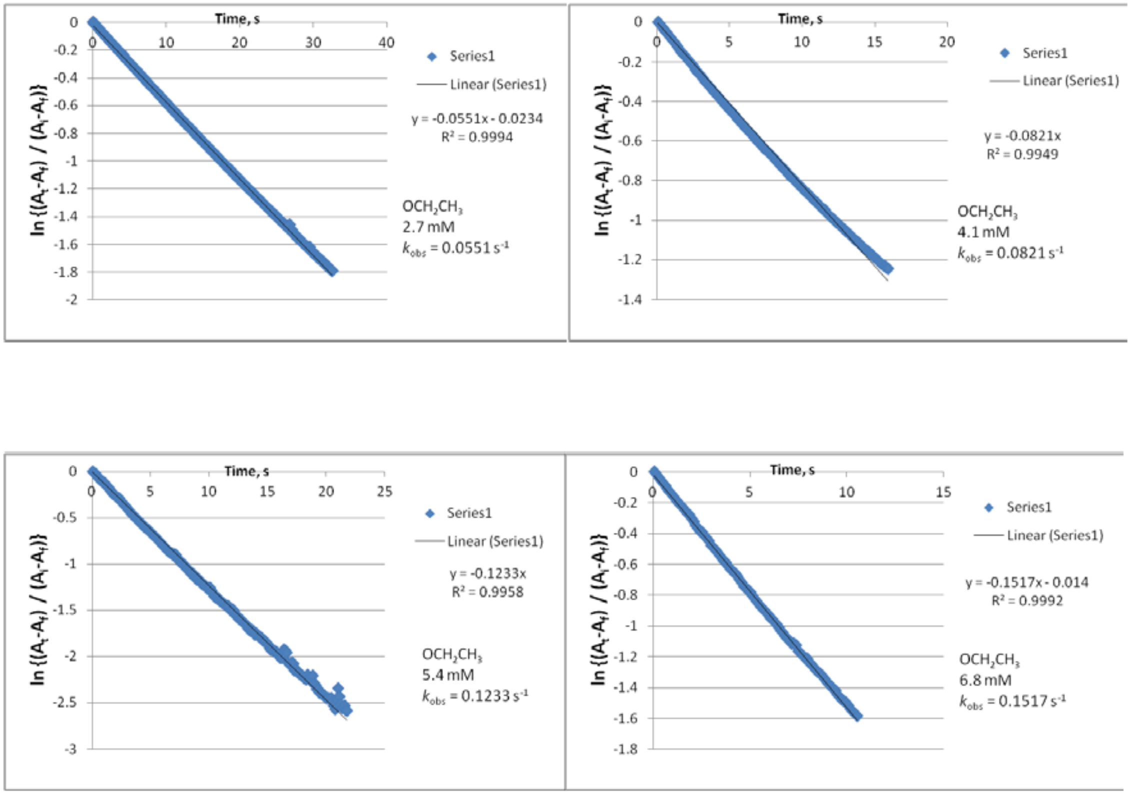

(b) *p*-OCH_3-DTBP

OCH_3	
mM	s^{-1}
2.7	0.054
4.1	0.0815
5.4	0.1248
6.8	0.1606

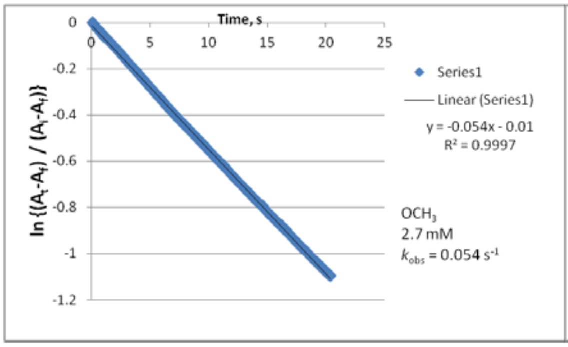

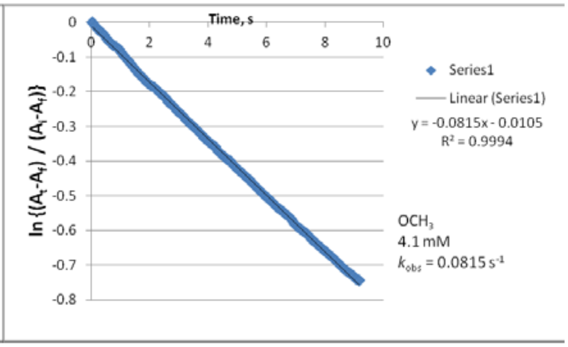

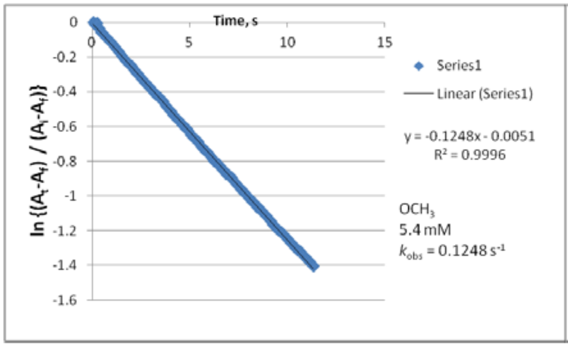

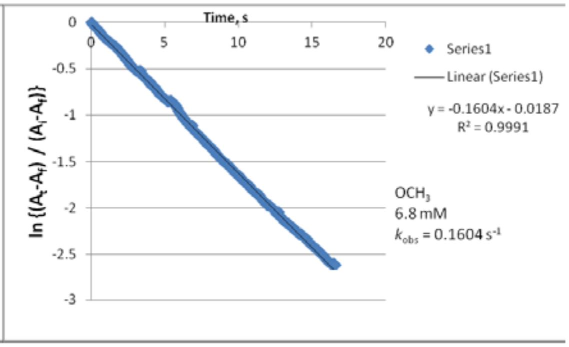

(c) *p*-OCD_3-DTBP

OCD_3	
mM	s^{-1}
3	0.0628
5	0.0948
7	0.1518
10	0.2001

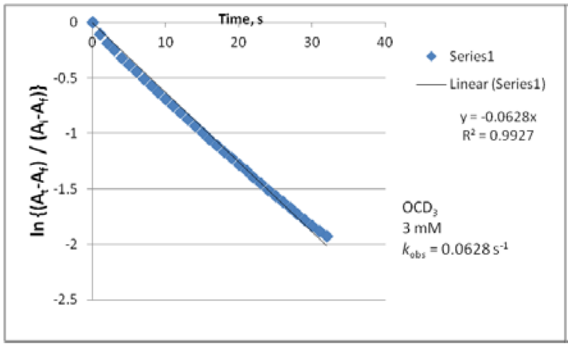

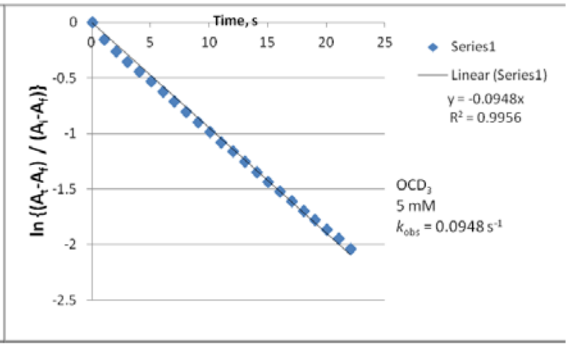

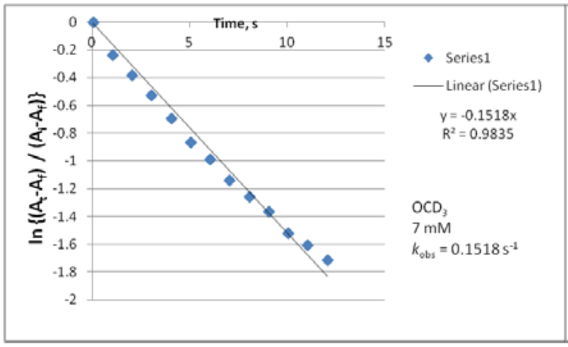

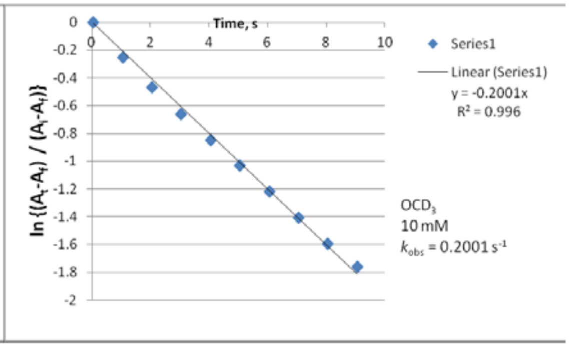

(d) *p*-OCH_3-DTBP (^{2}H-O)

OCH_3, -OD	
mM	s^{-1}
2.7	0.0054
4.1	0.0078
5.4	0.0112
6.8	0.0147

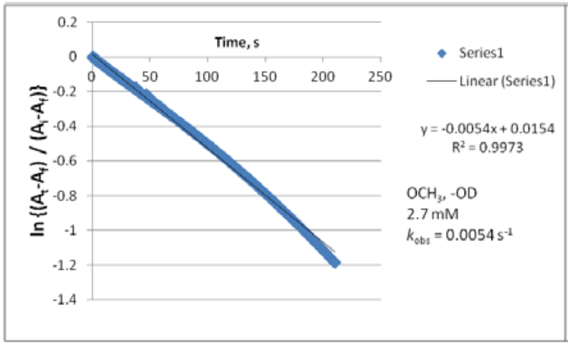

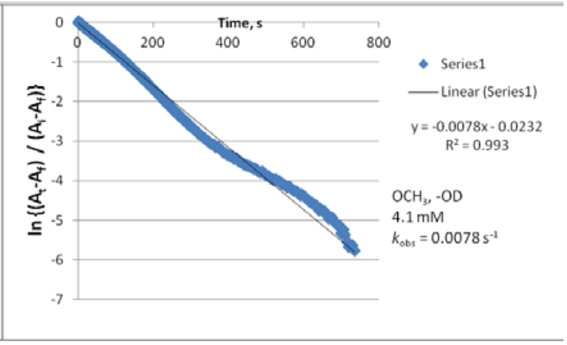

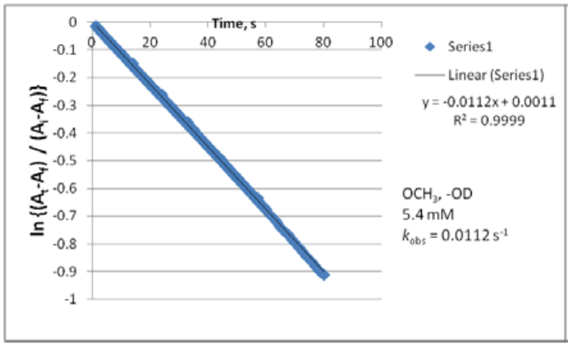

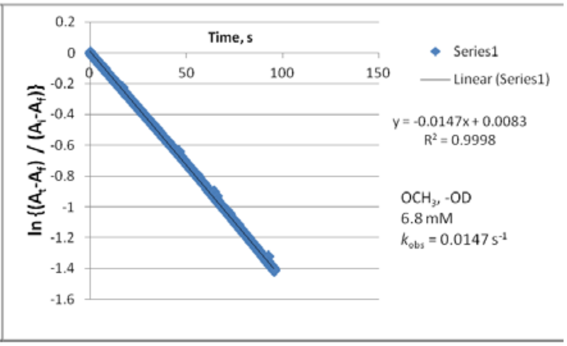

(e) *p*-OMPP-DTBP (OMPP = 2-methyl-1-phenylpropan-2-yloxy)

OMPP	
mM	s^{-1}
2.7	0.0022
4.1	0.0031
5.4	0.0041
6.8	0.0058

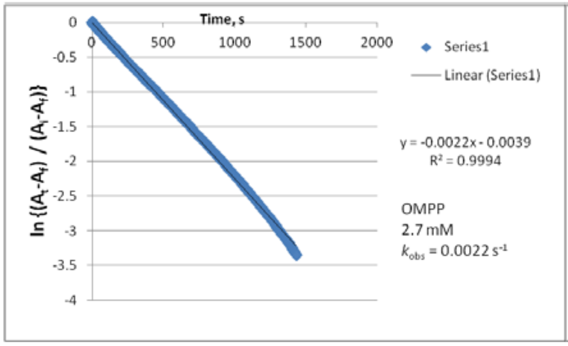

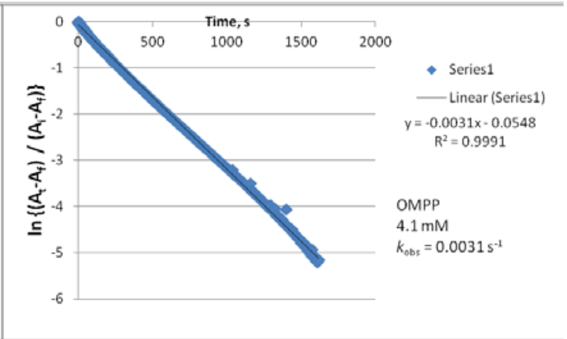

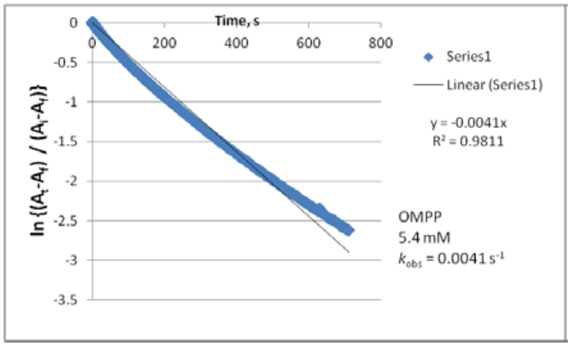

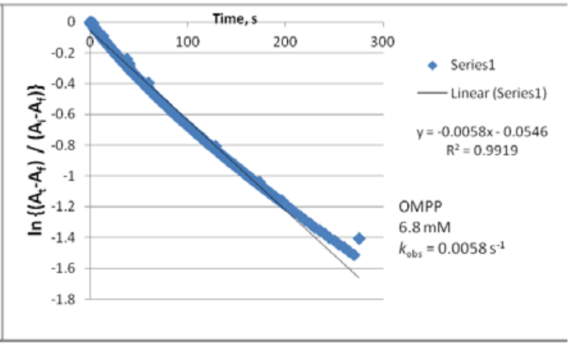

(f) *p*-OCH_2CF_3-DTBP

OCH_2CF_3	
mM	s^{-1}
3	0.0024
6	0.0051
9	0.0072
12	0.0096

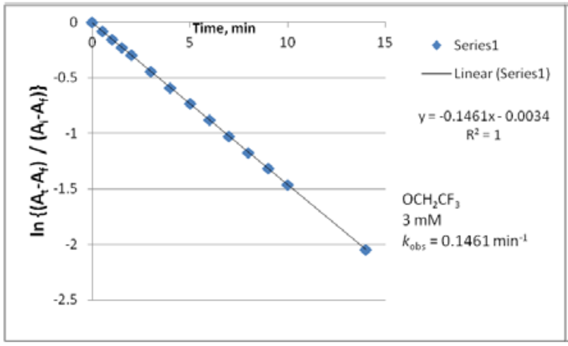

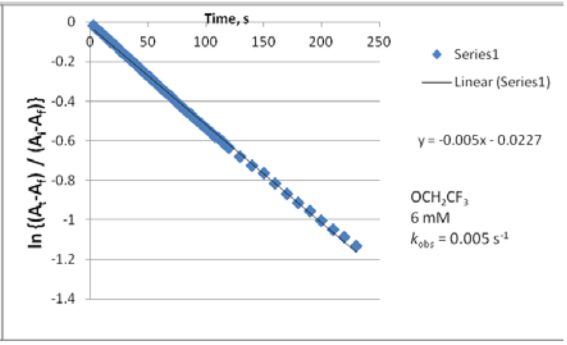

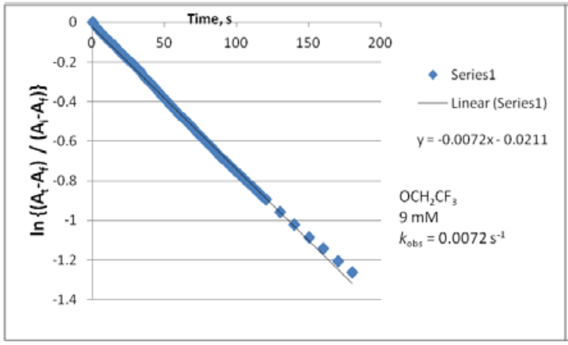

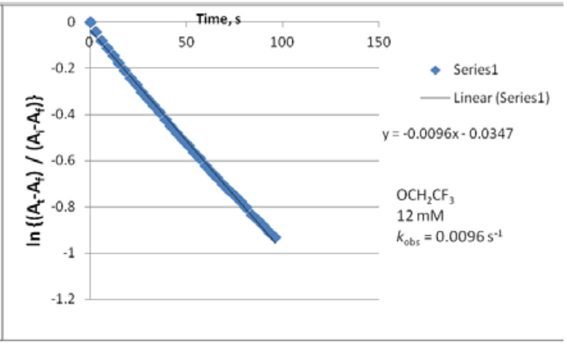

(g) *p*-CH$_3$-DTBP

CH$_3$	
mM	s^{-1}
10	4.33×10^{-4}
15	6.22×10^{-4}
20	8.07×10^{-4}
25	1.09×10^{-3}

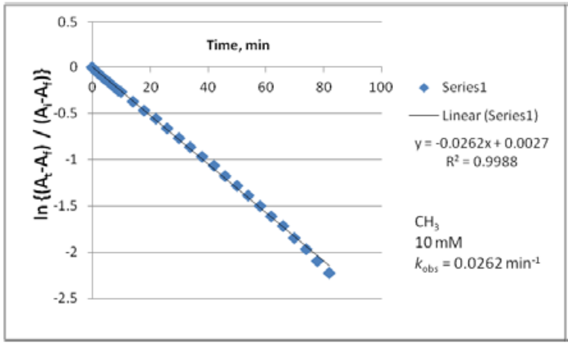

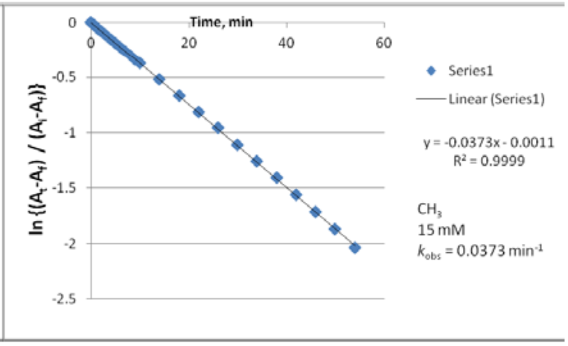

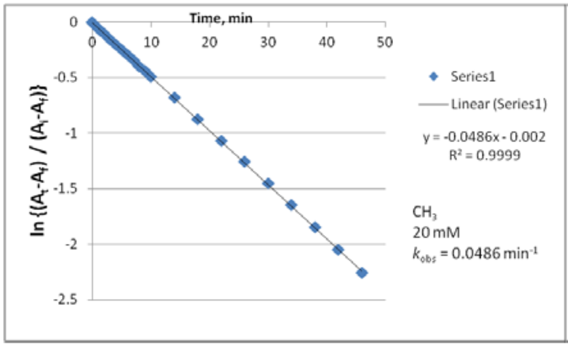

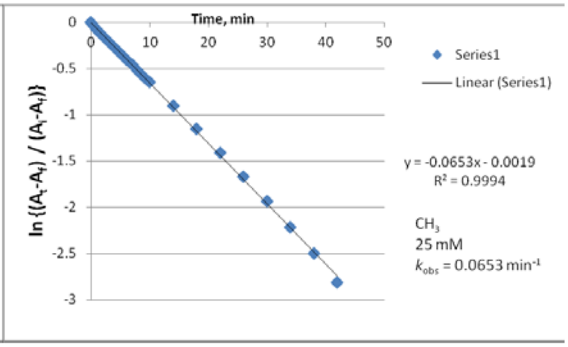

(h) *p*-CH_2CH_3-DTBP

CH_2CH_3	
mM	s^{-1}
20	5.6×10^{-4}
30	7.22×10^{-4}
40	1.03×10^{-3}
50	1.34×10^{-3}

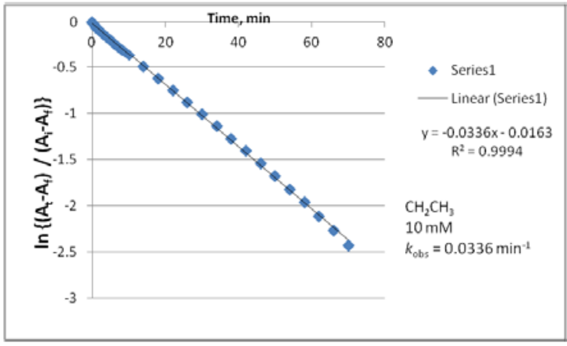

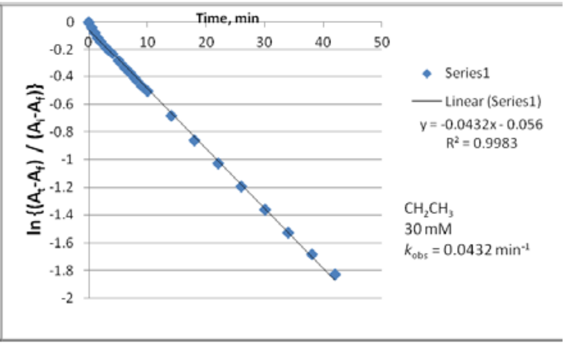

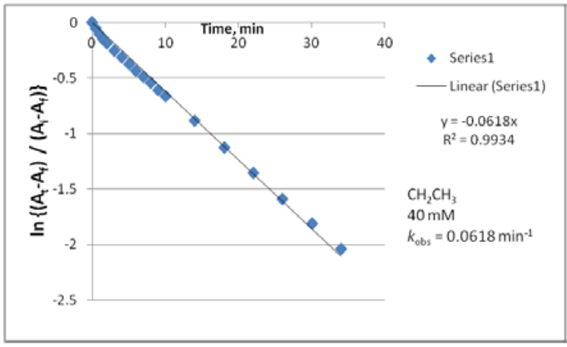

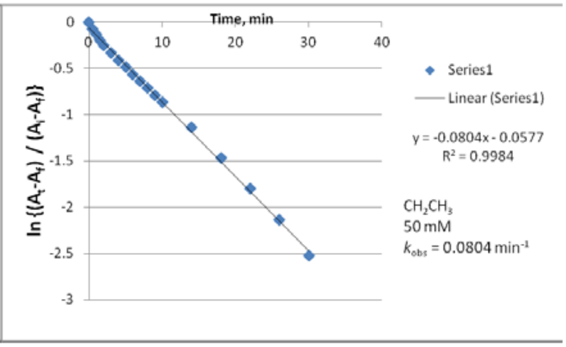

(i) *p*-*sec*Butyl-DTBP

sec-Butyl	
mM	s^{-1}
10	4.87×10^{-4}
30	9.38×10^{-4}
50	1.34×10^{-4}
70	1.87×10^{-4}

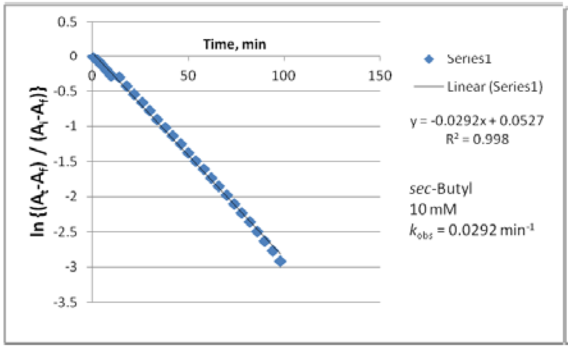

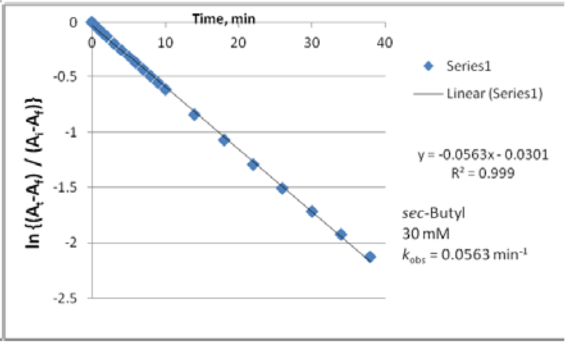

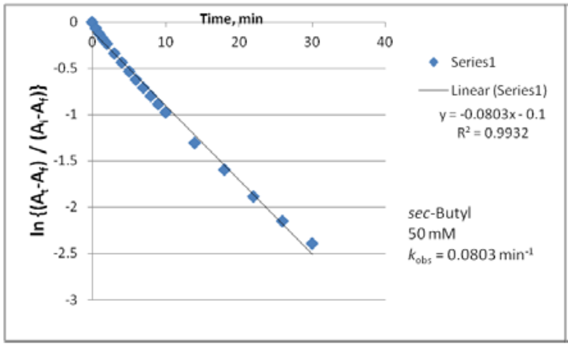

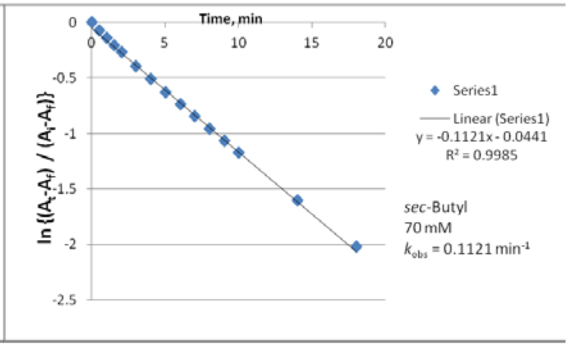

(j) *p*-CH_3-DTBP (^{2}H-O)

CH_3, -OD	
mM	s^{-1}
20	2.17×10^{-4}
25	2.5×10^{-4}
30	3.0×10^{-4}

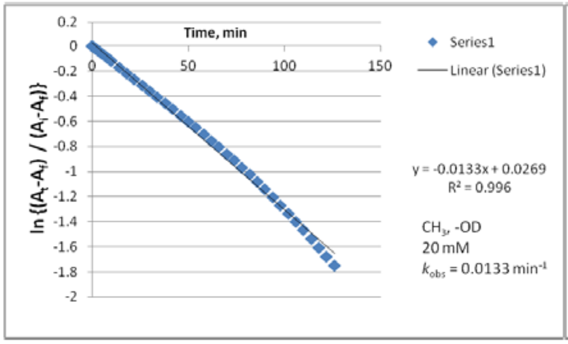

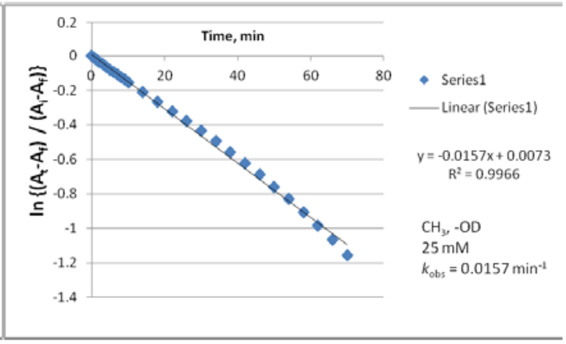

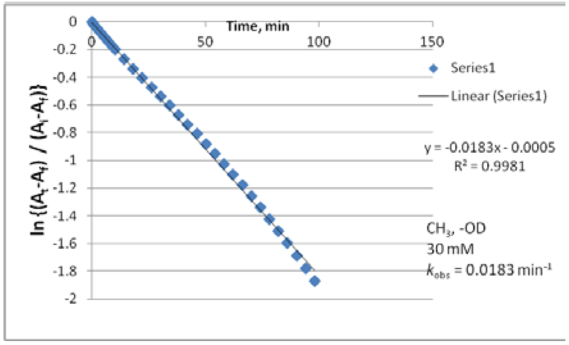

(k) *p-tert*Butyl-DTBP

tert-Butyl	
mM	s^{-1}
20	2.47×10^{-4}
25	2.82×10^{-4}
30	3.32×10^{-4}
40	4.05×10^{-4}

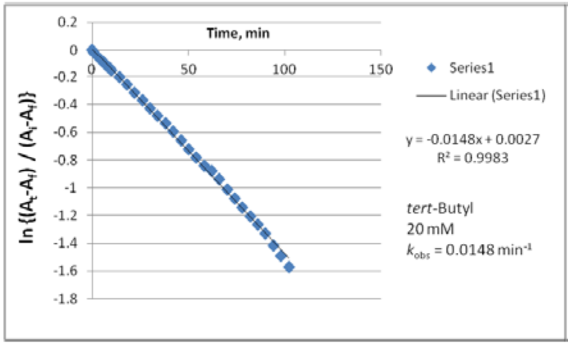

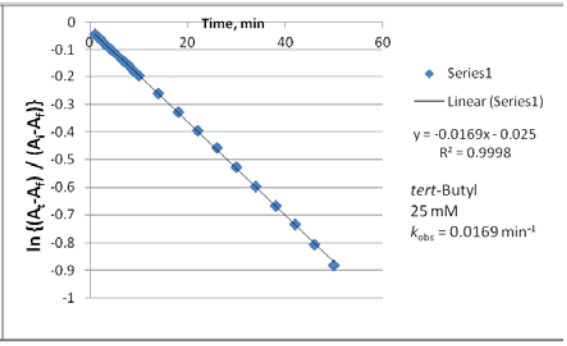

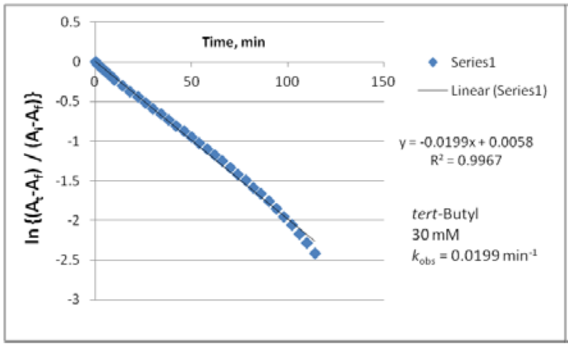

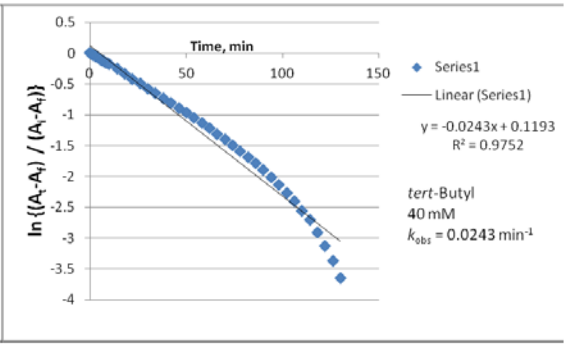

6.13 Yields of Products

Table S1. Product yields

	DTBQ [a]	H_2O_2 [b]	Cu complex [c]	OR / R
2 + *p*-OMe-DTBP	50 %	50 %	~ 95 %	MeOH 25 % [d]
2 + *p*-^{t}Bu-DTBP	38 %	44 %	~ 95 %	ND
2 + ^{t}BuArO·	99 %	20 ~ 30 %	~ 95 %	ND

[a] Determined by GC-MS, [b] quantified by UV-vis spectroscopy, [c] by EPR spectroscopy, and [d] by ^{2}H-NMR

6.14 Titration of 2 with TEMPO-H

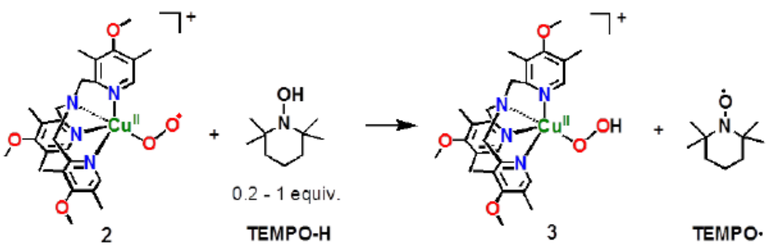

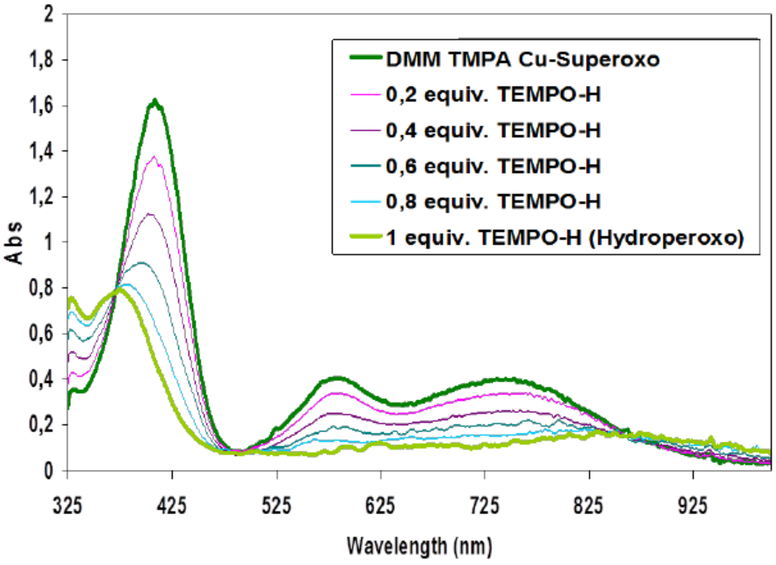

Figure S11. UV-vis spectral changes of the titration of [(DMM-tmpa)Cu^{II}($O_2^{\bullet-}$)]B(C_6F_5)$_4$ (**2**) 0.4 mM acetone solution with 0.2 ~ 1 equiv. TEMPO-H at 183 K affording new species presumed to be [(DMM-tmpa)Cu^{II}(OOH)] (**3**) (λ_{max} = 374 nm, ε = 2000 M^{-1} cm^{-1}).

6.15 Protonation of $[(\mathrm{DMM\text{-}tmpa})\mathrm{Cu^{II}(OOH)}]^+$ (3)

$$\underset{\mathbf{3}}{[(\mathrm{DMM\text{-}tmpa})\mathrm{Cu^{II}\text{-}OOH}]\,\mathrm{B(C_6F_5)_4}} + \mathrm{HB(C_6F_5)_4} \longrightarrow [(\mathrm{DMM\text{-}tmpa})\mathrm{Cu^{II}B(C_6F_5)_4}]\,\mathrm{B(C_6F_5)_4} + \mathrm{H_2O_2}$$

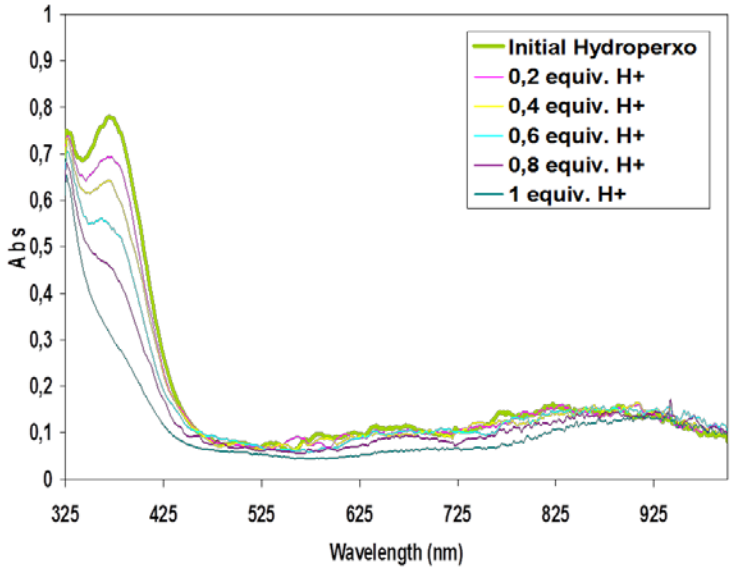

Figure S12. UV-vis spectral changes of 0.4 mM $[(\mathrm{DMM\text{-}tmpa})\mathrm{Cu^{II}(OOH)}]\mathrm{B(C_6F_5)_4}$ (**3**) acetone solution (which was generated from **2** + 0.2 ~ 1 equiv. TEMPO-H; **Figure S12**) with $\mathrm{H[B(C_6F_5)_4]}$ acid titration.

6.16 Quantification of H_2O_2 Formed

In order to quantify hydrogen peroxide formed from the titration of the $[(\mathrm{DMM\text{-}tmpa})\mathrm{Cu^{II}(OOH)}]^+$ (**3**) with acid, the following reaction was used:

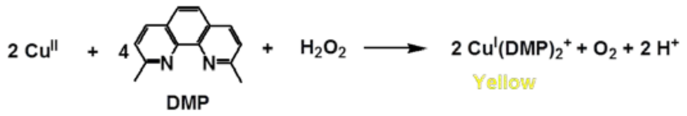

Hydrogen peroxide is an efficient reagent for the reduction of Cu(II)-2,9-dimethyl-1,10-phenanthroline (DMP) to Cu(I) species which has yellow color and exhibits specific absorption band (λ_{max} = ~460 nm).[b] To 3 ml of reaction solution, 1 ml of 4 mM $\mathrm{Cu^{II}(ClO_4)_2}$ solution and 1 ml of 8 mM DMP solution were added. The absorption obtained was compared to H_2O_2 standard and the yield was 40 %.

[b] Florence, T. M.; Stauber, J. L.; Mann, K. J. *J. Inorg. Biochem.* **1985**, *24*, 243-254.

6.17 Comparison of *d-d* Bands for Possible Cu(II) Products

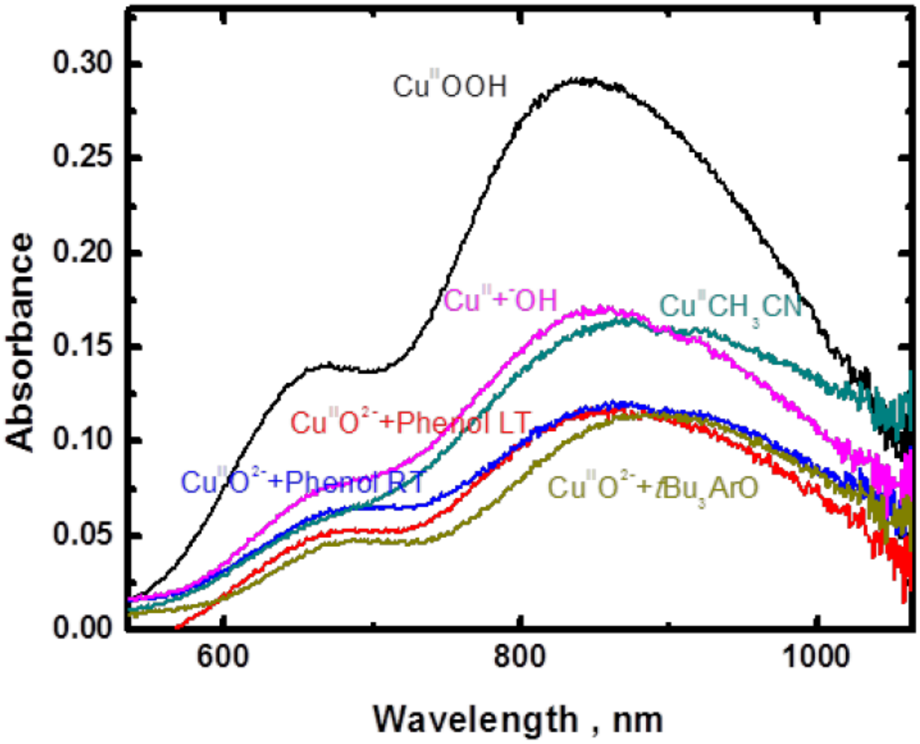

Figure S13. UV-vis spectra for *d-d* band comparison of possible Cu(II) products in acetone; $[(\text{DMM-tmpa})\text{Cu}^{II}(O_2^{\bullet-})]B(C_6F_5)_4$ (**2**) + phenol at low temperature, warmed up solution of **2** + phenol, $[(\text{DMM-tmpa})\text{Cu}^{II}(\text{OOH})]^+$ (**3**), $[(\text{DMM-tmpa})\text{Cu}^{II}(CH_3CN)](ClO_4)_2$, $[(\text{DMM-tmpa})\text{Cu}^{II}(CH_3CN)](ClO_4)_2$ + $^t\text{Bu}_4\text{OH}$, and **2** + $^t\text{Bu}_3\text{ArO}\cdot$.

6.18 MALDI-TOF Experiment

MALDI-TOF mass spectra were obtained using a Bruker AutoFlex III MALDI-TOF mass spectrometer. Samples were prepared in acetone and deposited on the target plate in the absence of any added matrix.

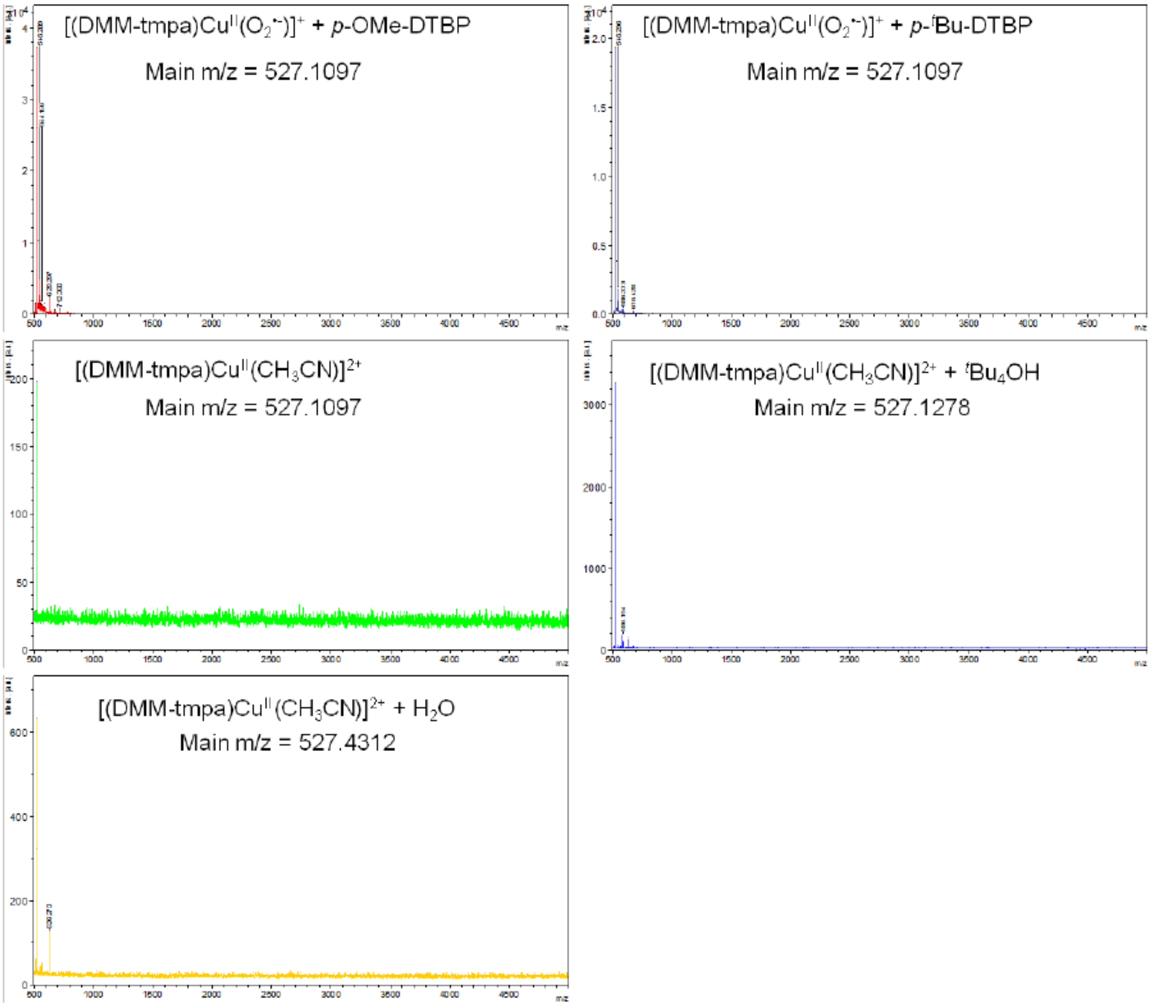

Figure S14. MALDI-TOF spectra of possible Cu(II) products following warming of reaction solutions of $[(\text{DMM-tmpa})\text{Cu}^{II}(\text{O}_2^{\bullet-})]^+$ (**2**) + phenol, $[(\text{DMM-tmpa})\text{Cu}^{II}(\text{CH}_3\text{CN})]^{2+}$, $[(\text{DMM-tmpa})\text{Cu}^{II}(\text{CH}_3\text{CN})]^{2+}$ + ^{t}Bu$_4$OH, and $[(\text{DMM-tmpa})\text{Cu}^{II}(\text{CH}_3\text{CN})]^{2+}$ + H_2O. In all cases the product observed m/z = ~ 527, corresponds to $[(\text{DMM-tmpa})\text{Cu}]^+$ most likely form reduction of the Cu(II) complex product actually formed.

6.19 Reactivity Study toward Catechol Derivatives

6.19.1 Reaction with 3,5-di-*tert*-butylcatechol

A Schlenk flask was charged with 10 mL of 0.25 mM acetone solution of [(DMM-tmpa)Cu^{I}(CO)]B(C_6F_5)$_4$ (**1**) in the glove box, and out of the glove box, the solution was immediately purged with $CO_{(g)}$ at room temperature. The solution was then cooled to the – 90 °C acetone/liquid nitrogen cooling bath and dioxygen was gently bubbled through the solution to generate [(DMM-tmpa)Cu^{II}($O_2^{\bullet-}$)]B(C_6F_5)$_4$ (**2**). After **2** was fully formed, Ar/Vacuum purge cycles (3X) were applied to remove excess dioxygen and a stock solution of 10 equiv 3,5-di-*tert*-butylcatechol was added. When the reaction ended, the reaction was quenched by passing the solution through an alumina column at low temperature. The resulting solution was dried under vacuum, and dissolved in ethyl acetate. Then 1 μL was injected into the GC-MS. The area ratio was converted to mole ratio to quantify the yield of 3,5-di-*tert*-butyl-1,2-benzoquinone which was 60%.

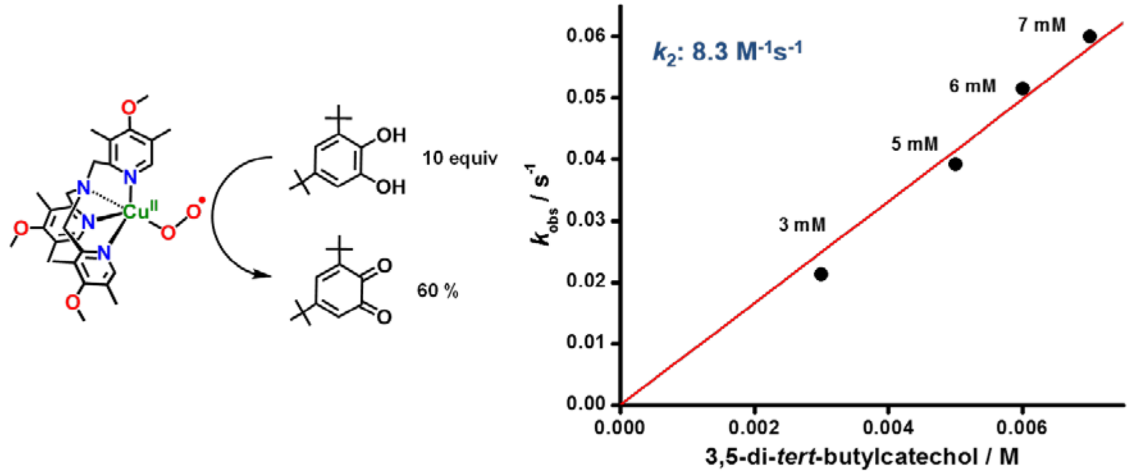

Figure S15. Left: Scheme for the oxidation of 3,5-di-*tert*-butylcatechol to 3,5-di-*tert*-butyl-1,2-benzoquinone by [(DMM-tmpa)Cu^{II}($O_2^{\bullet-}$)]$^+$. Right: Second-order-rate constants and fitting for the reaction of [(DMM-tmpa)Cu^{II}($O_2^{\bullet-}$)]$^+$ (**2**) and 3,5-di-*tert*-butylcatechol.

6.19.2 Kinetic studies with *p*-substituted-catechol series

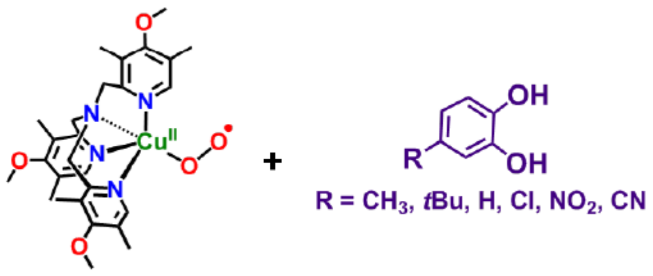

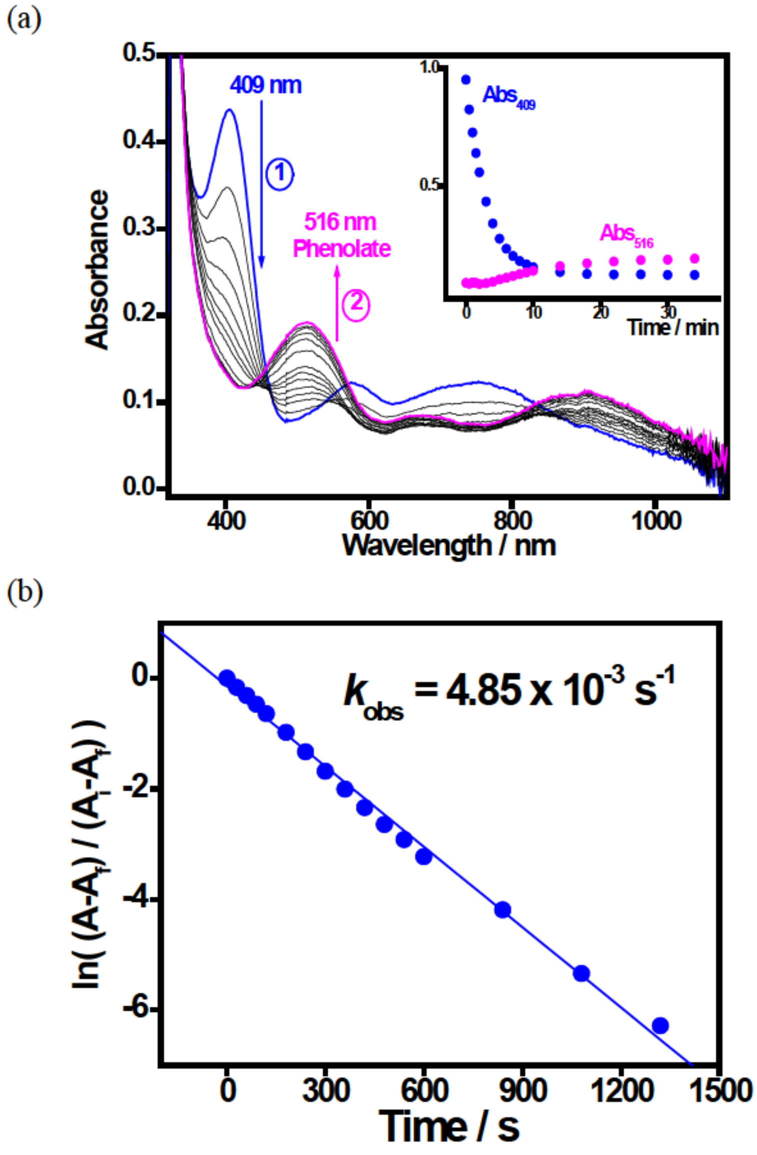

Figure S16. (a) UV-vis spectra of the reaction of 0.26 mM $[(\text{DMM-tmpa})\text{Cu}^{\text{II}}(\text{O}_2^{\bullet-})]^+$ (**2**) with 10 equiv of 4-methylcatechol in acetone at –90 °C. Inset: Time traces at 409 (complex **2**) and 516 nm (the product after 30 min; pink spectral line which is not yet identified). (b) Pseudo-first-order fitting of the reaction.

Table S2. Pseudo-first-order values of the reaction of $[(\text{DMM-tmpa})\text{Cu}^{\text{II}}(\text{O}_2^{\bullet-})]^+$ (**2**) with 4-substituted-catechol derivatives.

Substituents	M	k_{obs} (s^{-1})
OMe	0.00265	0.0495
	0.00398	0.0822
	0.0053	0.125
	0.00662	0.1527
Me	0.00265	0.0055
	0.00398	0.009
	0.0053	0.0126
	0.00662	0.0168
H	0.00398	0.0015
	0.00928	0.0027
	0.01325	0.0035
	0.01988	0.0044
Cl	0.00662	8.0×10^{-4}
	0.01325	0.0012
	0.01988	0.0018
CN	0.0130	1.78×10^{-4}

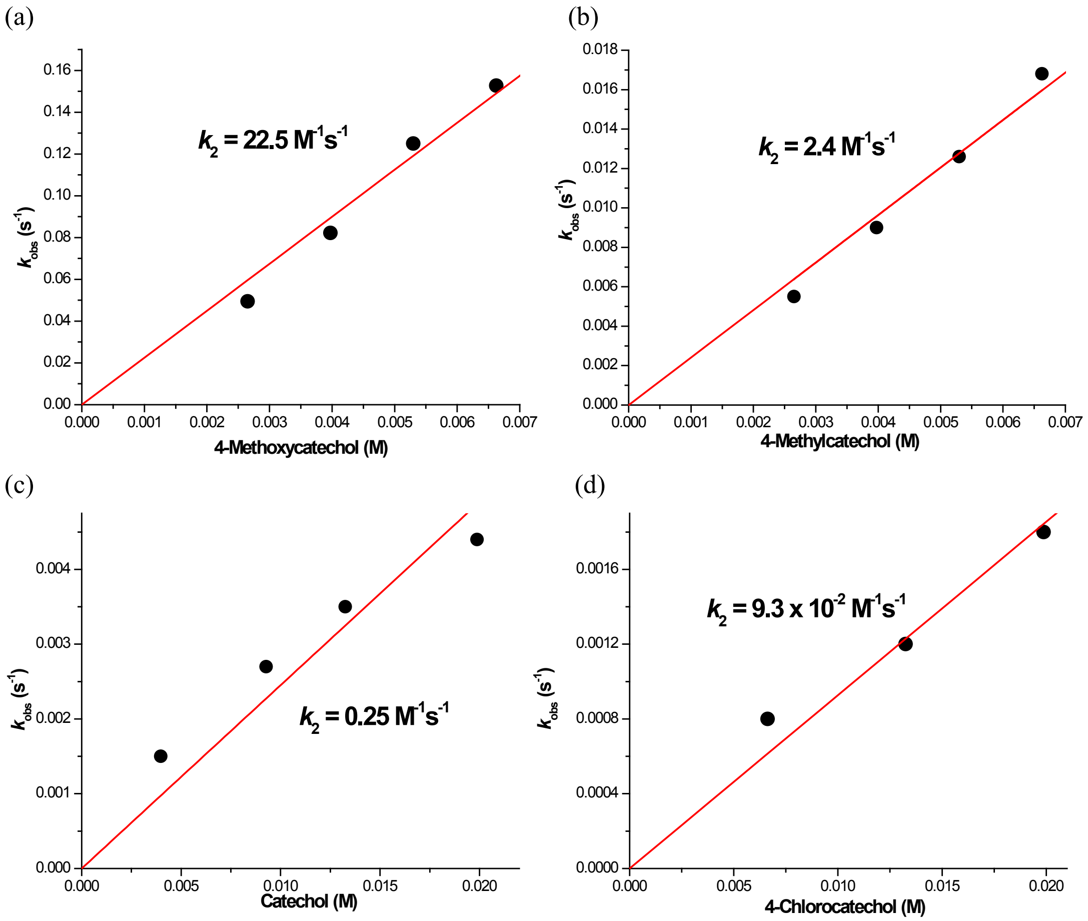

Figure S17. Second-order-rate constants and fitting for the reaction of $[(DMM\text{-}tmpa)Cu^{II}(O_2^{\bullet-})]^+$ (**2**) and (a) 4-methoxycatechol, (b) 4-methylcatechol, (c) catechol, and (d) 4-chlorocatechol.

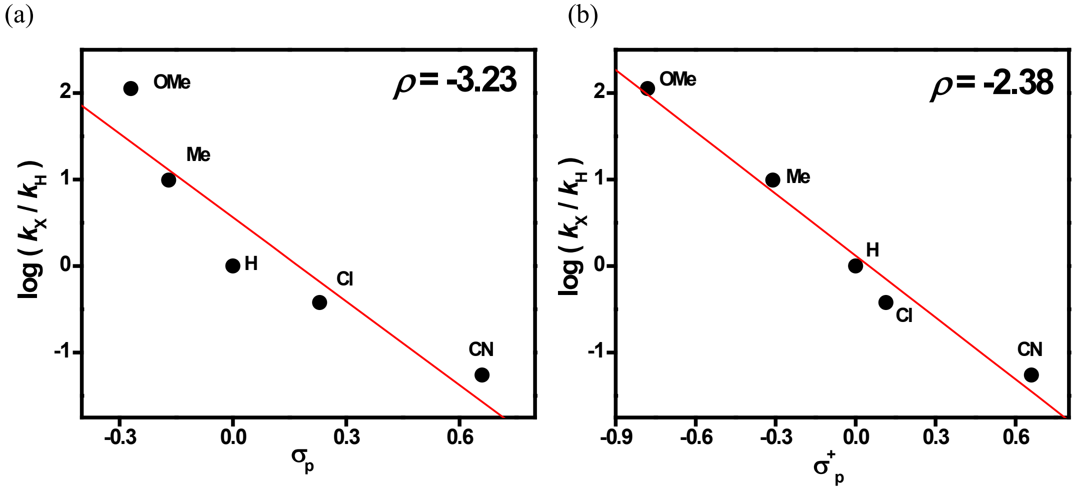

Figure S18. Hammett plots of the catechol reactions against (a) σ_P and (b) σ_P^+. One can conclude that in the rate determining step, possibly hydrogen-atom abstraction, **2** acts as an electrophile.

Chapter 3:

A N$_3$S$_{\text{(thioether)}}$-Ligated Cu$^{\text{II}}$-Superoxo with Enhanced Reactivity

This work was accomplished with the aid of the following collaborators and was published under the following citation:

Sunghee Kim, Jung Yoon Lee, Ryan E. Cowley, Jake W. Ginsbach, Maxime A. Siegler, Edward I. Solomon, and Kenneth D. Karlin

J. Am. Chem. Soc., **2015**, *137* (8), pp 2796-2799

Abstract

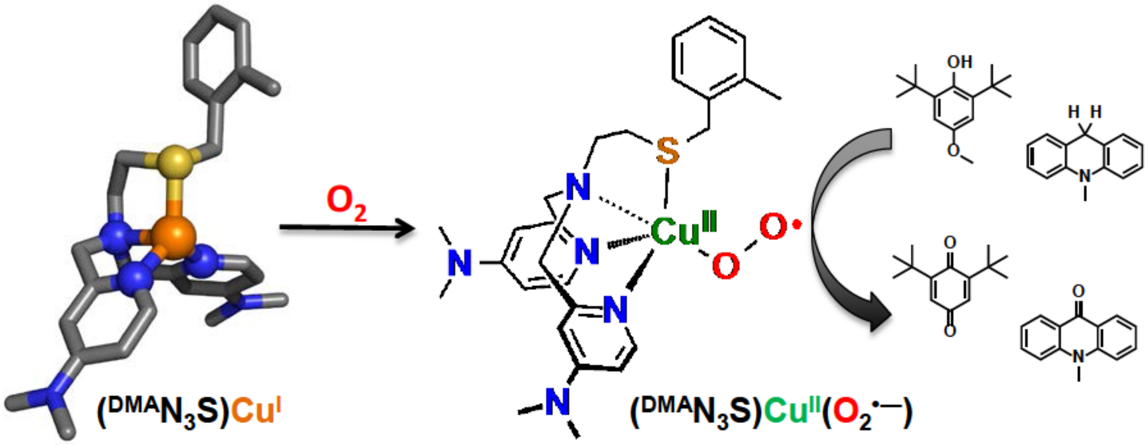
$(^{\text{DMA}}\text{N}_3\text{S})\text{Cu}^{\text{I}}$
O_2
S
N
N
N
N
Cu^{II}
O
O•
N
OH
H H
N
O
O
O
N
$(^{\text{DMA}}\text{N}_3\text{S})\text{Cu}^{\text{II}}(\text{O}_2^{\bullet -})$

Previous efforts to synthesize a cupric superoxide complex possessing a thioether donor have resulted in the formation of an end-on *trans*-peroxo-dicopper(II) species, $[\{(\text{Ligand})\text{Cu}^{\text{II}}\}_2(\mu\text{-1,2-O}_2^{2-})]^{2+}$. Redesign/modification of previous N$_3$S tetradentate ligands has now allowed for the stabilization of the monomeric, superoxide product possessing a S$_{\text{(thioether)}}$-ligation, $[(^{\text{DMA}}\text{N}_3\text{S})\text{Cu}^{\text{II}}(\text{O}_2^{\bullet -})]^+$ (**2**$^{\mathbf{S}}$), as characterized by UV-vis and

resonance Raman (rR) spectroscopies. This complex mimics the putative $Cu^{II}(O_2^{\bullet-})$ active species of the copper monooxygenase PHM and exhibits enhanced reactivity towards both O-H and C-H substrates in comparison to close analogues $[(L)Cu^{II}(O_2^{\bullet-})]^+$, where L contains only nitrogen donor atoms. Cu-$S_{(thioether)}$ ligation with its weaker donor ability (relative to an N-donor) are demonstrated by comparisons to the chemistry of analogue compounds.

1. Introduction

The copper monooxygenases peptidylglycine-α-hydroxylating monooxygenase (PHM) and dopamine-β-monooxygenase (DβM) possess a dicopper active site, but it is "noncoupled"; the two copper ions are about 11 Å apart.[1, 2] Extensive biochemical and biophysical research has shown that one copper ion (designated Cu_H or Cu_A) receives and passes electron reducing equivalents to the His_2Met $N_2S_{(thioether)}$ ligated Cu_M (or Cu_B) center, where O_2 and substrate binding occur. Recent computational analyses[3]lead to the hypothesis that an initial O_2-adduct, a Cu_M centered cupric superoxide $\{Cu^{II}(O_2^{\bullet-})\}$ moiety, forms from oxygenation of the fully reduced (Cu^I…Cu^I) enzyme. This species performs the H-atom abstraction of the peptide prohormone substrate (in PHM) leading to C–H hydroxylation and formation of the product hormone. Other reaction mechanisms suggesting other possible reactive intermediates being responsible for substrate C–H attack have been proposed.[4] In support of the importance of the $Cu^{II}(O_2^{\bullet-})$ reaction intermediate's involvement, a crystal structure obtained by Amzel and co-workers in the presence of a substrate inhibitor, reveals dioxygen bound to Cu_M in an end-on fashion,[2] as depicted in **Scheme 1a**. Undoubtedly, the thioether ligand plays a critical role in determining the electronic structure and functions of Cu_M site leading to C-H bond activation.[3] However, the precise role of Met coordination and the actual PHM reaction mechanism has yet to be fully elucidated.

Scheme 1. (a) Dioxygen-bound Cu_M site of PHM and (b) a new mononuclear cupric superoxo complex with thioether ligation.

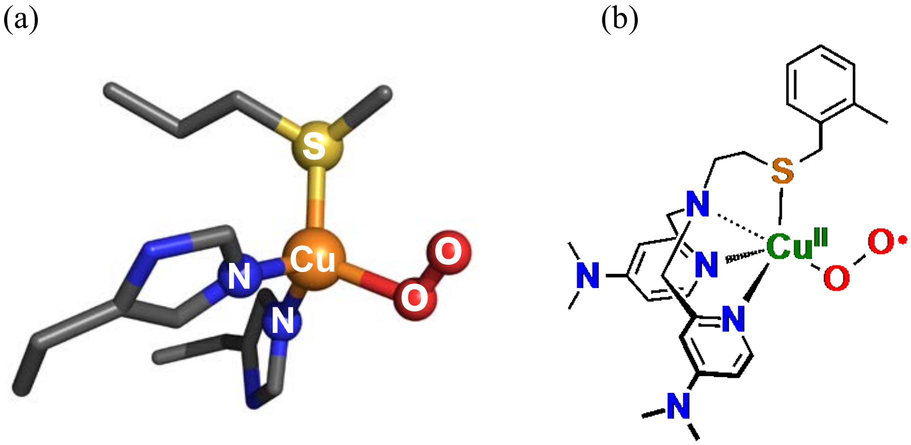

O_2-Adduct of Cu_M in PHM

$(^{DMA}N_3S)Cu^{II}(O_2^{\bullet-})$ (2^S)

Within the sub-field of copper-dioxygen synthetic bioinorganic chemistry, one long-standing goal has been to produce $Cu^{II}(O_2^{\bullet-})$ species that can be studied in detail, and to this end several cupric-superoxo complexes have been reported with ligands containing either three or four N-atoms.[5-7] In an attempt to mimic the active site donors of PHM and DβM, considerable effort has been devoted toward generating thioether containing tridentate or tetradentate ligands to study their Cu^I/O_2 reactivity.[8] In our own previous efforts we have been able to generate binuclear peroxo-dicopper complexes with $S_{(thioether)}$ ligation (**Scheme 2**),[9, 10] but there has been no report of a mononuclear $Cu^{II}(O_2^{\bullet-})$ species coordinated by a $S_{(thioether)}$ donor. Herein, for the first time we present the spectroscopic evidence and reactivity of the new mononuclear cupric superoxo complex,

($^{DMA}N_3S$)Cu^{II}($O_2^{\bullet-}$) (**2^S**) (**Scheme 1b**) possessing thioether S-ligation that exhibits enhanced reactivity towards both O-H and C-H substrates.

Scheme 2. Dicopper-dioxygen species possessing sulfur-containing ligands.

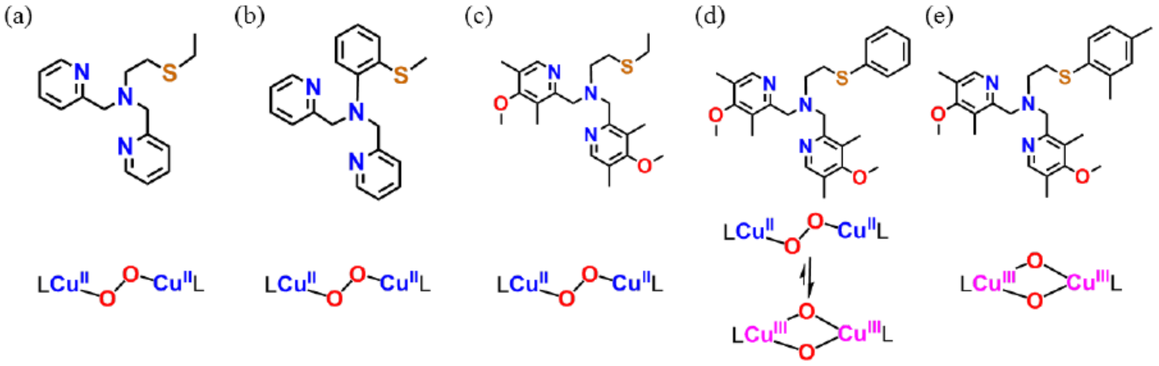

This new ligand, $^{DMA}N_3S$,[11] differs from our previously reported N_3S ligands in two important ways. First, it possesses highly electron-rich dimethylamino (DMA)[12] groups at the *para* position of the two pyridyl donors, a strategy from previously stabilized a mononuclear Cu^{II}($O_2^{\bullet-}$) complex containing N_4 tripodal tetradentate ligand.[6, 7, 13] The increased stability of a mononuclear O_2-adduct likely comes about as a result of an enhanced rate (constant) for formation of a the Cu^{II}($O_2^{\bullet-}$) complex, because of the ligand donor group, compared to the rate of reaction of the initially formed Cu^{II}($O_2^{\bullet-}$) species with a second ligand-Cu^{I} complex to give a peroxo-dicopper(II) complex, which is not as enhanced a reaction. Second, the thioether moiety is capped with a bulkier *o*-methyl benzyl substituent to slow dimerization relative to previous designs.[10]

2. Physical Properties of Cu-Complexes

Treatment of $^{DMA}N_3S$ with $[Cu^I(CH_3CN)_4]B(C_6F_5)_4$ in THF, followed by pentane addition leads to the isolation of bright yellow powders with formula $[(^{DMA}N_3S)Cu^I]B(C_6F_5)_4$ (**1**).[11] Single crystals could be grown from 2-methyltetrahydrofuran (MeTHF)/pentane at RT under Ar. As shown in **Figure 1a**, the cuprous complex is a four-coordinate monomer ligated by two pyridyl, one tertiary amine, and one thioether atom in a distorted pyramidal geometry providing a very open site for potential dioxygen binding. The Cu-S bond length in 1 (2.2327(5) Å) falls in the usual range (2.2 – 2.44 Å) for Cu^I–$S_{(thioether)}$ complexes.[9, 10] Many previously studied $N_3S_{(thioether)}$-Cu^I complexes form dimers in the solid state,[10] and it is the incorporation of the larger *o*-methylbenzyl group which may disfavor their formation.

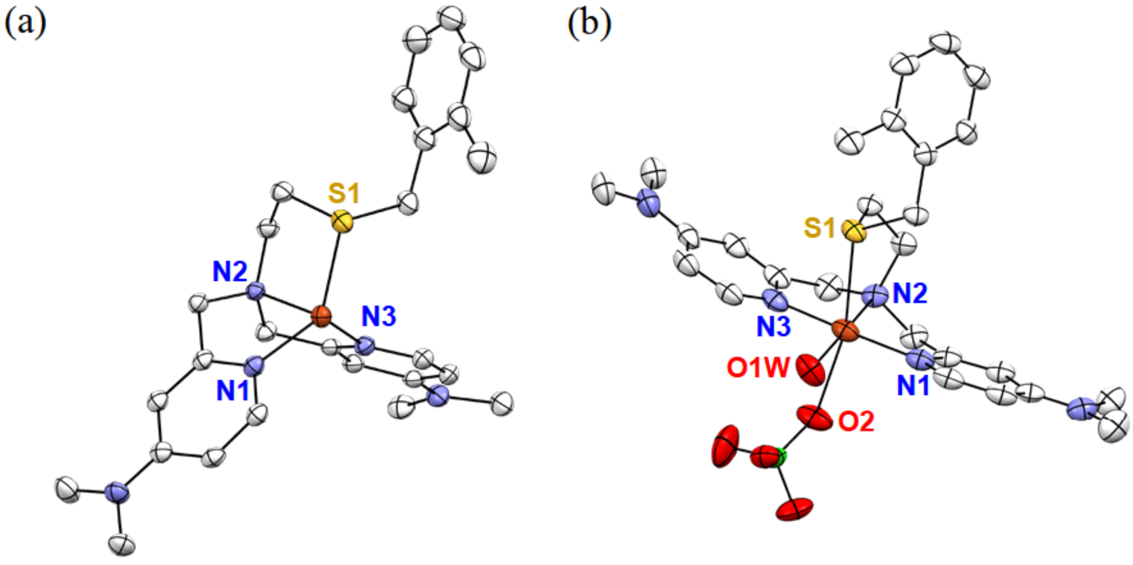

Figure 1. Displacement ellipsoid plots of the cations; (a) $[(^{DMA}N_3S)Cu^I]^+$ (**1**) and (b) $[(^{DMA}N_3S)Cu^{II}(H_2O)(ClO_4)]^+$ (**3**). Hydrogen atoms were removed for clarity.

Furthermore, the copper(II) complex $[(^{DMA}N_3S)Cu^{II}(H_2O)(ClO_4)](ClO_4)$ (**3**) (Figure 1b) was generated and structurally characterized.[11] A slightly distorted octahedral coordination is observed. The thioether donor group is found in an axial position with Cu-S bond distance of 2.6974(6) Å. Electron paramagnetic resonance (EPR) measurement on 3 reveals a standard axial spectrum of copper(II) complex.[11]

3. O_2 Chemistry of Cu(I)-Complexes

Bubbling O_2 into a MeTHF solution of **1** at –135 °C led to the immediate formation of a new species (λ_{max} = 425 nm) that rapidly (~50 s) converted to the thermodynamically more stable end-on *trans*-peroxo-dicopper(II) species $[\{(^{DMA}N_3S)Cu^{II}\}_2(\mu\text{-}1,2\text{-}O_2^{2-})]^{2+}$ (**2^P**) (**Figure 2**, top) exhibiting strong UV-vis absorptions at λ_{max} = 534 (6500 $M^{-1}cm^{-1}$) and 604 (6600 $M^{-1}cm^{-1}$) nm (**Figure 2**, bottom) consistent with the feature of previously

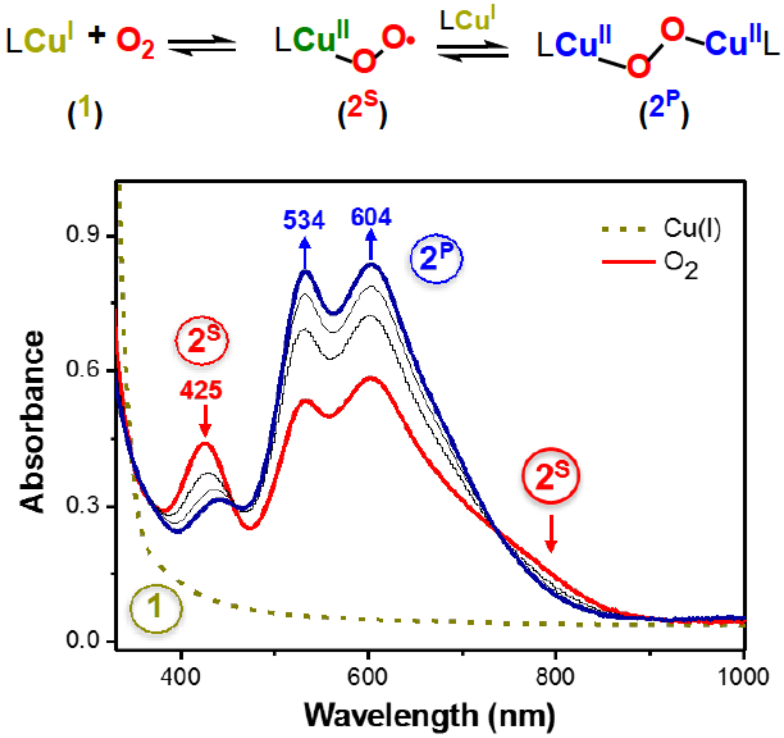

Figure 2. Low-temperature UV-vis absorption spectra of the reaction of **1** with O_2 at –135 °C in MeTHF (0.2 mM). The superoxo product **2^S** is observed immediately upon O_2 addition (red) and converted to the peroxo **2^P** (t = 50 s, blue).

synthesized $S_{(thioether)}$-ligated (μ-1,2-peroxo)Cu^{II}_2.[9, 10] The formulation of $\mathbf{2^P}$ is confirmed by rR spectroscopy ($\nu_{O\text{–}O}$ = 821 cm^{-1}, $\nu_{Cu\text{–}O}$ = 547 cm^{-1}).[11] Although the initially formed species has a short lifetime, the characteristic λ_{max} value of 425 nm and the transformation to a more stable (μ-1,2-peroxo)Cu^{II}_2, strongly suggest it is the S-ligated cupric superoxo species $[(^{DMA}N_3S)Cu^{II}(O_2^{\bullet-})]^+$ ($\mathbf{2^S}$).

Interestingly, when polar or potentially hydrogen-bonding solvents such as acetone, ethanol, methanol, or trifluoroethanol (TFE) are mixed with MeTHF, $[(^{DMA}N_3S)Cu^{II}\text{–}OO^{\bullet-}$

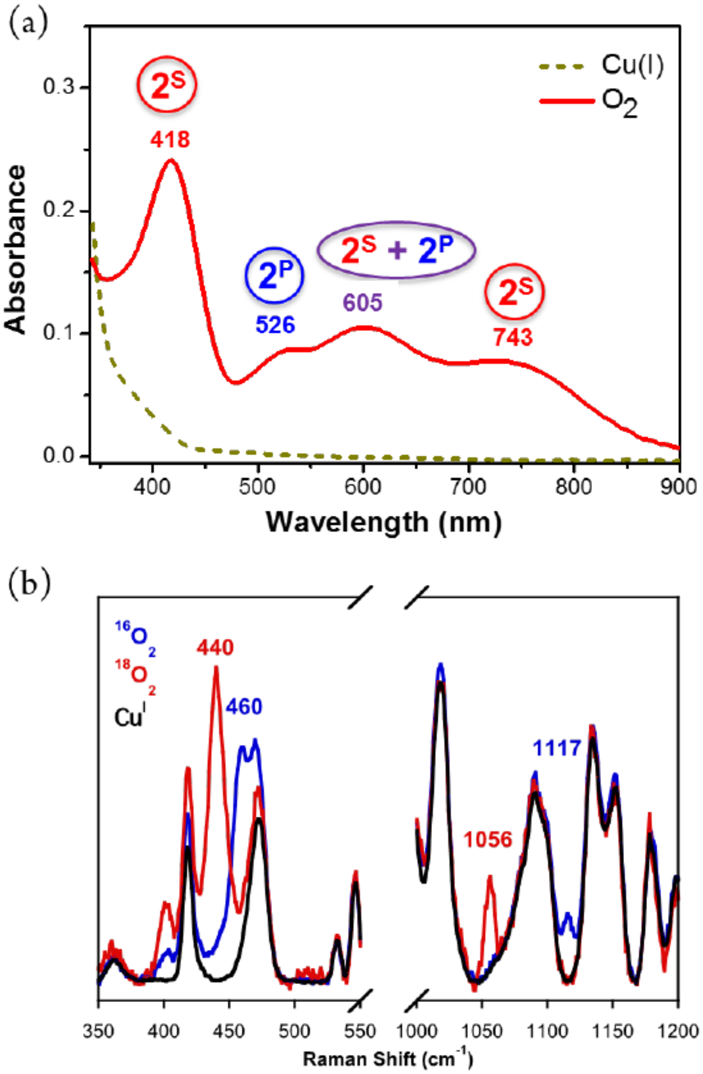

Figure 3. (a) Low-temperature (–135 °C) UV-vis absorption spectrum of $\mathbf{2^S}$ (containing ~11% $\mathbf{2^P}$, λ_{max} = 526 nm, ε = 6500) as recorded ~40 s after bubbling O_2 into a MeTHF:TFE (4:1) solution of **1** (0.098 mM), and (b) rR spectra of frozen $\mathbf{2^S}$ (0.62 mM, λ_{ex} = 413 nm, 77 K) in MeTHF:TFE (4:1).[11]

]$^+$ ($\mathbf{2^S}$) is much more persistent than is found in MeTHF only (**Figure 3a;** λ_{max} = 418, 605, 743 nm). There appears to be a shift of the equilibrium constant to the mononuclear superoxide over the binuclear *trans*-peroxo complex. This result could be due to the formation of a hydrogen bond between an O-atom of the superoxide ligand and the TFE solvent, as observed in a 'classical' cobalt(III)-superoxo complex with TFE.[14]

The rR spectra for $\mathbf{2^S}$ (λ_{ex} = 413 nm) reveal two dioxygen isotope sensitive vibrations (**Figure 3b**). An O–O stretch is observed at 1117 cm^{-1} which shifts to 1056 cm^{-1} upon $^{18}O_2$ substitution ($\Delta^{18}O_2 = -61$ cm^{-1}) and a Cu–O stretch at 460 cm^{-1} ($\Delta^{18}O_2 = -20$ cm^{-1}). The energy and isotope shifts of these vibrations confirm the assignment of $\mathbf{2^S}$ as an end-on superoxide species. In fact, these parameters closely match those for previously described cupric-superoxo complexes with tripodal tetradentate N_4 ligands (^{DMA}tmpa and ^{DMM}tmpa), (**Table 1**) both having $\nu_{O\text{–}O}$ = 1121 cm^{-1}.[6, 7] The species $\mathbf{2^S}$ is assigned as having an S = 1 (triplet) ground state by EPR spectroscopy. [11, 15]

4. Reactivity of $[(^{DMA}N_3S)Cu^{II}(O_2^{\bullet-})]^+$ ($\mathbf{2^S}$).

In MeTHF:TFE (4:1 v:v), an approximately 4:1 (mol/mol) equilibrium mixture of (2^S)/(2^P) forms within ~150 s following oxygenation of $[(^{DMA}N_3S)Cu^I]^+$ (1) at –135 °C. The ratio or relative amount of superoxo complex $\mathbf{2^S}$ to $\mathbf{2^P}$ was determined by first finding and calculating the molar absorptivity (ε) for a solution of pure $\mathbf{2^P}$ in MeTHF at –135 °C. {Note: as described, initial oxygenation of a solution of a known concentration of **1** gives the $\mathbf{2^S}/\mathbf{2^P}$ mixture but waiting 5 min leads to complete conversion to $\mathbf{2^P}$.} This mixture shows minimal decomposition over an hour and thus, we could carry out reactivity studies of $\mathbf{2^S}$ with the O–H and C–H substrates; 2,6-di-*tert*-butyl-4-methoxyphenol (*p*-OMe-DTBP) and

N-methyl-9,10-dihydroacridine ($AcrH_2$). Pseudo first-order kinetic behavior was observed upon addition of *p*-OMe-DTBP (with $t_{1/2} = 3$ min) or $AcrH_2$ ($t_{1/2} = 2$ min) as monitored by the disappearance of the 418 nm UV-vis band of $\mathbf{2}^{\mathbf{S}}$. Following workup at RT the products were analyzed as 2,6-di-*tert*-butyl-1,4-benzoquinone and 10-methyl-9-acridone, respectively.[11] Independent observations demonstrate that the complex $\mathbf{2}^{\mathbf{P}}$ is unreactive toward these substrates. Warming up the $\mathbf{2}^{\mathbf{S}}$ solution does not lead to sulfur oxygenation which occurs by bis(μ-oxo)Cu^{III}_2 species.[10]

Table 1. Comparison of LCu^{II}/LCu^{I} Redox Potentials and Reactivity of Derived $[(L)Cu^{II}(O_2^{\bullet-})]^+$ Complexes.

	^{DMA}tmpa[6]	^{DMM}tmpa[7]	$^{DMA}N_3S$
	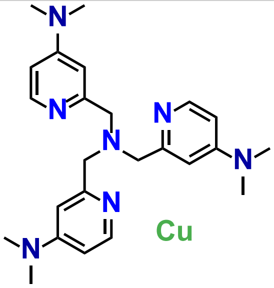	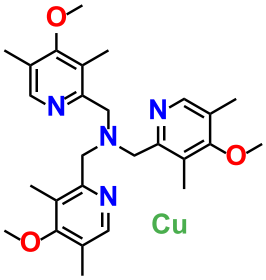	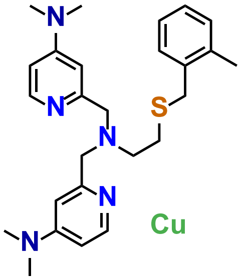
p-OMe-DTBP [a]	No [b]	No [b]	**Yes**
$AcrH_2$ [a]	No [b]	No [b]	**Yes**
$E_{1/2}$, mV [c]	-700	–570	–470

[a] Reaction comparisons of $[(L)Cu^{II}(O_2^{\bullet-})]^+$ complexes (MeTHF:TFE (4:1) at –135 ºC) toward substrates. [b] Reactions do occur, but only above –100 ºC, [c] $E_{1/2}$ (vs Fc^+/Fc) $[(L)Cu^{II}(solvent)](ClO_4)_2$ complexes as determined by cyclic voltammetry.[11]

To assess the effect of the thioether donor in $\mathbf{2}^{\mathbf{S}}$, we compared the reactivity of $(L)Cu^{II}(O_2^{\bullet-})$ complexes (L = ^{DMA}tmpa or ^{DMM}tmpa) toward the same substrates.[6, 7] Notably, both cupric superoxide complexes showed no reactivity under identical conditions (**Table 1**), although they do react above –100 ºC. Thus, $\mathbf{2}^{\mathbf{S}}$ with $S_{(thioether)}$-ligation is more reactive than the closely related N_4 superoxide compounds. The difference in reactivity is rationalized by the different donor strengths of the corresponding ligands. The substitution of a $S_{(thioether)}$ for a $N_{(pyridine)}$ donor decreases the ligand field strength, consistent with the

$Cu^{II/I}$ redox potentials for the separately isolated Cu^{II} complexes in which thioether coordination raises the reduction potential by 230 mV (**Table 1**).[11] As a result, we hypothesize that $\mathbf{2^S}$ is more electrophilic and hence better able to accept an H-atom from either an O–H or C–H substrate, as compared to the N_4 complexes.

5. Cu-S Interaction

The influence of the Cu–S interaction on the oxygenated products was further probed by comparing Cu/O_2 species with different donor atoms binding Cu. Three structurally analogous ligands were synthesized replacing the sulfur site with carbon, oxygen, and nitrogen (**Scheme 3**).[11] The isolated Cu^I complex with tridentate $^{DMA}N_3$ ligand exhibits a distinctive 382 nm absorption band[11] upon O_2 addition at –135 ºC in MeTHF. This absorption spectrum is consistent with a bis(μ-oxo)Cu^{III}_2 complex, which is known for many other products from low-temperature oxygenation of Cu^I-N_3 precursors.[10, 16] Under identical reaction conditions, oxygenation of the $Cu^I(^{DMA}N_3O)$, possessing three N-donors and an ether O-atom, leads to the initial formation of a (μ-1,2-peroxo)Cu^{II}_2 which rapidly (~ 1 min) converts to a bis(μ-oxo)Cu^{III}_2 species with very similar UV-vis spectrum as for the case with $^{DMA}N_3$.[10, 17] Thus, as seen before,[10, 18] the oxygen atom of the ether arm in $^{DMA}N_3O$ has an extremely weak to non-existent interaction with the copper ion in the oxygenated product. We find that for $Cu^I(^{DMA}N_4)$ in MeTHF (**Scheme 2c**), both Cu^{II}–superoxo and (μ-1,2-peroxo)Cu^{II}_2 complexes are generated[11] as in the case of $^{DMA}N_3S$. This strongly suggests that the $S_{(thioether)}$-atom donor of $^{DMA}N_3S$ ligand is coordinated in both Cu^{II}–superoxo/μ-1,2-peroxo complexes, $\mathbf{2^S}$ and $\mathbf{2^P}$. If it were not, a bis(μ-oxo)Cu^{III}_2 complex would prominently form. {Note: More direct confirmation of a Cu-$S_{(thioether)}$ bond such as by X-ray Absorption Spectroscopy, is not possible here, due to the short lifetime of $\mathbf{2^S}$ and the related fact that higher concentrations need only lead to transformation of $\mathbf{2^S}$ to $\mathbf{2^P}$.}

Scheme 3. Oxygenated products of ligand-Cu^I complexes.*

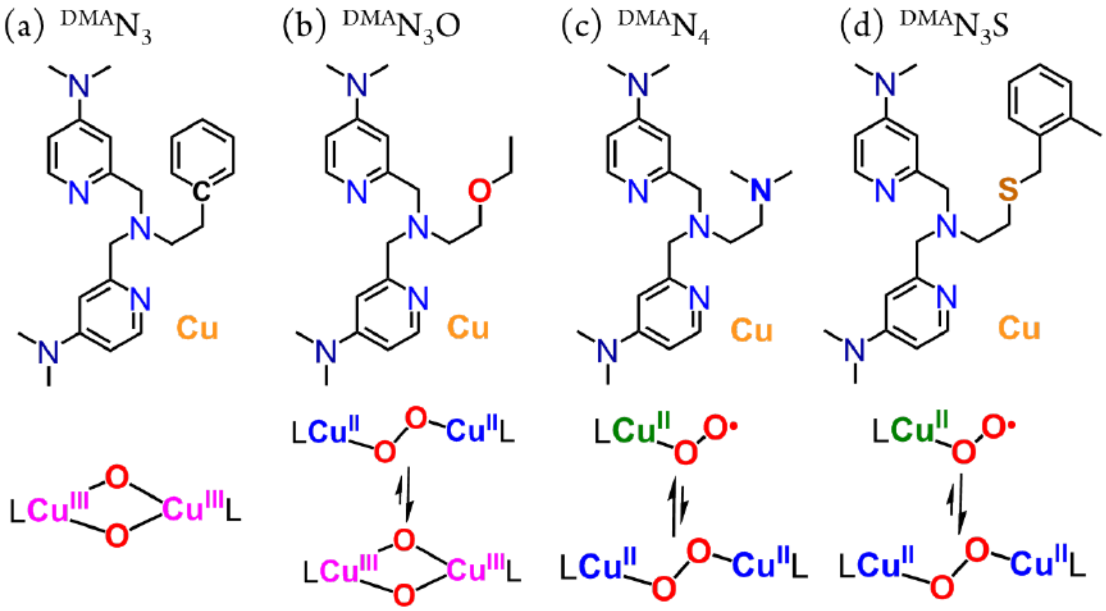

*See **SI** for CV's and redox potential values for the Cu^{II}/Cu^I complex couples for the $^{DMA}N_3$, $^{DMA}N_3O$, $^{DMA}N_4$ ligands.

6. Conclusion

In summary, $[(^{DMA}N_3S)Cu^{II}(O_2^{\bullet-})]^+$ ($\mathbf{2^S}$) is the first reported example of a cupric superoxo species supported by a $S_{(thioether)}$ donor. This advance has allowed us to determine that a superoxide species from an N_3S donor is more reactive towards O–H and C–H bonds than the corresponding N_4 complex. These results indicate that one role of the Met ligand in PHM and DβM may be to activate the superoxide species for reaction with substrates by increasing their electrophilicity. The synthesis of this species will also allow us to further consider the role of thioether ligation on critical downstream O_2-reduced (and protonated) derivatives, such as Cu^{II}-hydroperoxo and to further perform detailed kinetic analysis based on the preliminary reactivity study presented here.

7. References

1. Klinman, J. P., *Chem. Rev.* **1996,** *96*, 2541-2561; Klinman, J. P., *J. Biol. Chem.* **2006,** *281*, 3013-3016; Solomon, E. I.; Heppner, D. E.; Johnston, E. M.; Ginsbach, J. W.; Cirera, J.; Qayyum, M.; Kieber-Emmons, M. T.; Kjaergaard, C. H.; Hadt, R. G.; Tian, L., *Chem. Rev.* **2014,** *114* (7), 3659-3853.
2. Prigge, S. T.; Eipper, B.; Mains, R.; Amzel, L. M., *Science* **2004,** *304*, 864-867.
3. Chen, P.; Solomon, E. I., *J. Am Chem. Soc.* **2004,** *126*, 4991-5000; Chen, P.; Bell, J.; Eipper, B. A.; Solomon, E. I., *Biochemistry* **2004,** *43* (19), 5735-5747.
4. Crespo, A.; Marti, M. A.; Roitberg, A. E.; Amzel, L. M.; Estrin, D. A., *J. Am. Chem. Soc.* **2006,** *128* (39), 12817-12828; Yoshizawa, K.; Kihara, N.; Kamachi, T.; Shiota, Y., *Inorg. Chem.* **2006,** *45* (7), 3034-3041; Abad, E.; Rommel, J. B.; Kaestner, J., *J. Biol. Chem.* **2014,** *289* (20), 13726-13738.
5. Fujisawa, K.; Tanaka, M.; Morooka, Y.; Kitajima, N., *J. Am. Chem. Soc.* **1994,** *116* (26), 12079-12080; Würtele, C.; Gaoutchenova, E.; Harms, K.; Holthausen, M. C.; Sundermeyer, J.; Schindler, S., *Angew. Chem. Int. Ed.* **2006,** *45*, 3867-3869; Kunishita, A.; Kubo, M.; Sugimoto, H.; Ogura, T.; Sato, K.; Takui, T.; Itoh, S., *J. Am. Chem. Soc.* **2009,** *131* (8), 2788-2789; Donoghue, P. J.; Gupta, A. K.; Boyce, D. W.; Cramer, C. J.; Tolman, W. B., *J. Am. Chem. Soc.* **2010,** *132* (45), 15869-15871; Peterson, R. L.; Himes, R. A.; Kotani, H.; Suenobu, T.; Tian, L.; Siegler, M. A.; Solomon, E. I.; Fukuzumi, S.; Karlin, K.

D., *J. Am. Chem. Soc.* **2011,** *133* (6), 1702-1705; Pirovano, P.; Magherusan, A. M.; McGlynn, C.; Ure, A.; Lynes, A.; McDonald, A. R., *Angew. Chem. Intl. Ed.* **2014,** *53* (23), 5946-5950.

6. Maiti, D.; Fry, H. C.; Woertink, J. S.; Vance, M. A.; Solomon, E. I.; Karlin, K. D., *J. Am. Chem. Soc.* **2007,** *129* (2), 264-265.

7. Lee, J. Y.; Peterson, R. L.; Ohkubo, K.; Garcia-Bosch, I.; Himes, R. A.; Woertink, J.; Moore, C. D.; Solomon, E. I.; Fukuzumi, S.; Karlin, K. D., *J. Am. Chem. Soc.* **2014,** *136* (28), 9925-9937.

8. Kodera, M.; Kita, T.; Miura, I.; Nakayama, N.; Kawata, T.; Kano, K.; Hirota, S., *J. Am. Chem. Soc.* **2001,** *123* (31), 7715-7716; Zhou, L.; Nicholas, K. M., *Inorg. Chem.* **2008,** *47* (10), 4356-4367; Aboelella, N. W.; Gherman, B. F.; Hill, L. M. R.; York, J. T.; Holm, N.; Young, V. G.; Cramer, C. J.; Tolman, W. B., *J. Am. Chem. Soc.* **2006,** *128* (10), 3445-3458; Martínez-Alanis, P. R.; Sánchez Eguía, B. N.; Ugalde-Saldívar, V. M.; Regla, I.; Demare, P.; Aullón, G.; Castillo, I., *Chem. Eur. J.* **2013,** *19* (19), 6067-6079; Hoppe, T.; Josephs, P.; Kempf, N.; Wölper, C.; Schindler, S.; Neuba, A.; Henkel, G., *Z. Anorg. Allg. Chem.* **2013,** *639* (8-9), 1504-1511; Tano, T.; Mieda, K.; Sugimoto, H.; Ogura, T.; Itoh, S., *Dalton T* **2014,** *43* (12), 4871-4877.

9. Hatcher, L. Q.; Lee, D.-H.; Vance, M. A.; Milligan, A. E.; Sarangi, R.; Hodgson, K. O.; Hedman, B.; Solomon, E. I.; Karlin, K. D., *Inorg. Chem.* **2006,** *45* (25), 10055-10057; Lee, Y.; Lee, D.-H.; Park, G. Y.; Lucas, H. R.; Narducci Sarjeant, A. A.; Kieber-Emmons, M. T.; Vance, M. A.; Milligan, A. E.; Solomon, E. I.; Karlin, K. D., *Inorg. Chem.* **2010,** *49* (19), 8873-8885; Park, G. Y.; Lee, Y.; Lee, D.-H.; Woertink, J. S.; Sarjeant, A. A. N.; Solomon, E. I.; Karlin, K. D., *Chem. Comm.* **2010,** *46* (1), 91-93.

10. Kim, S.; Ginsbach, J. W.; Billah, A. I.; Siegler, M. A.; Moore, C. D.; Solomon, E. I.; Karlin, K. D., *J. Am. Chem. Soc.* **2014,** *136* (22), 8063-8071.

11. See Supporting Information.

12. Zhang, C. X.; Kaderli, S.; Costas, M.; Kim, E.-i.; Neuhold, Y.-M.; Karlin, K. D.; Zuberbühler, A. D., *Inorg. Chem.* **2003,** *42*, 1807-1824.

13. We believe the increased stability comes about as a result of great rate (constant) for formation of a $Cu^{II}(O_2^{\bullet -})$ complex, because of the ligand donor group, where the rate of reaction of $Cu^{II}(O_2^{\bullet -})$ with a second ligand-Cu^{I} species is not as enhanced a reaction.

14. Drago, R. S.; Cannady, J. P.; Leslie, K. A., *J. Am. Chem. Soc.* **1980,** *102* (19), 6014-6019.

15. Ginsbach, J. W.; Peterson, R. L.; Cowley, R. E.; Karlin, K. D.; Solomon, E. I., *Inorg. Chem.* **2013,** *52* (22), 12872-12874.

16. Mirica, L. M.; Ottenwaelder, X.; Stack, T. D. P., *Chem. Rev.* **2004,** *104*, 1013-1045; Hatcher, L. Q.; Karlin, K. D., *J. Biol. Inorg. Chem.* **2004,** *9*, 669-683.

17. Kieber-Emmons, M. T.; Ginsbach, J. W.; Wick, P. K.; Lucas, H. R.; Helton, M. E.; Lucchese, B.; Suzuki, M.; Zuberbühler, A. D.; Karlin, K. D.; Solomon, E. I., *Angew. Chem. Intl. Ed.* **2014,** *53* (19), 4935-4939.

18. Lucas, H. R.; Li, L.; Sarjeant, A. A. N.; Vance, M. A.; Solomon, E. I.; Karlin, K. D., *J. Am. Chem. Soc.* **2009,** *131* (9), 3230-3245.

8. Supporting Information

8.1 Materials and Methods

8.1.1 General

All materials used were commercially available analytical grade from Sigma-Aldrich, ChemBridge and TCI chemicals. Acetone, methanol, ethanol were distilled under an inert atmosphere over $CaSO_4$ and degassed under argon prior to use. Methylene chloride/Diethyl ether were used after being passed through a 60 cm long column of activated alumina (Innovative Technologies) under argon. Acetonitrile was stored under N_2 and purified via passage through 2 cm × 60 cm columns of activated alumina (Innovative Technologies Inc.). Inhibitor free tetrahydrofuran (THF), 2-methyltetrahydrofuran (MeTHF) and trifluoroethanol (TFE) were purchased from Sigma-Aldrich and distilled under argon from sodium/ benzophenone and degassed with argon prior to use. Pentane was freshly distilled from calcium hydride under an inert atmosphere and degassed prior to use. $[Cu^I(CH_3CN)_4]B(C_6F_5)_4$ was synthesized according to literature protocols,[1] and its identity and purity were verified by elemental analysis and/or ^{1}H-NMR. Synthesis and manipulations of copper salts were performed according to standard Schlenk techniques or in an MBraun glovebox (with O_2 and H_2O levels below 1 ppm).

8.1.2 Instrumentation

Bench-top low temperature UV–visible experiments were carried out on a Cary Bio-50 spectrophotometer equipped with a liquid nitrogen chilled Unisoku USP-203-A cryostat using a 1 cm modified Schlenk cuvette. NMR spectroscopy was performed on Bruker 300 and 400 MHz instruments with spectra calibrated to either internal tetramethylsilane (TMS) standard or to a residual protio solvent. EPR measurements were performed on an X-Band Bruker EMX CW EPR controlled with a Bruker ER 041 XG microwave bridge operating at the X-band (~9 GHz) in 5 mm quartz EPR tubes. ESI-Mass spectra were acquired using a Finnigan LCQDeca ion-trap mass spectrometer equipped with an electrospray ionization source (Thermo Finnigan, San Jose, CA). Single Crystal X-ray Diffraction was performed on suitable crystals of $[(^{DMA}N_3S)Cu^{I}]B(C_6F_5)_4$ (**1**), $[(^{DMA}N_3S)Cu^{II}(H_2O)](ClO_4)_2$ (**3**), and $[(^{DMA}tmpa)Cu^{II}(H_2O)](ClO_4)_2$ which were mounted either on the tip of a glass fiber or on a loop with a tiny amount of Paratone-N oil and transferred to a N_2 cold stream (110(2) K). GC-MS experiments were carried out and recorded using a Hewlett-Packard 6890 Series Gas Chromatograph System equipped with 5973N Mass Selective Detector. The GC-MS conditions for the product analysis were: Injector Port Temperature: 250 °C; Column Temperature: Initial Temperature 80 °C; Initial Time, 2 min; Final Temperature 280 °C; Final Time, 2 min; Gradient Rate 10 °C/min; Flow Rate: 14.2 mL/min; Ionization voltage: 1.3 kV. Resonance Raman (rR) Measurements. A 0.62 mM stock solution of copper(I) complexes was prepared in MeTHF or solvent mixture. A 500 μL aliquot of this copper(I) solution was added to the 5 mm NMR sample tube, capped with a septum, and chilled in a MeTHF/$N_2(l)$ bath. Oxygenation of the copper samples was achieved by slowly bubbling an excess of dioxygen through the solution using a Hamilton gas-tight syringe equipped with a three-way valve and needle outlet. Dioxygen, $^{16}O_2$ (Airgas OX UHP-300) or $^{18}O_2$ (Icon 6393), was added to an evacuated Schlenk flask fitted with a septum for the oxygenation reactions described above. The rR spectra were collected on a triple monochromator (Spex 1877 CP with 1200, 1800, and 2400 grooves/mm holographic spectrograph gratings) with a back-illuminated CCD (Princeton

Instruments ST-135). Samples were placed in a liquid nitrogen finger dewar (Wilmad) in a ~135° backscattering configuration and excitation was provided by a krypton ion laser (Coherent I90C-K) or Ti:sapphire laser (M Squared SolsTiS). Data were collected for 5 min at 20 mW of power (**2^{S}**) or 100 mW power (**2^{P}**) and samples were hand to minimize photodamage. Peak positions were determined from fitting the experimental data with Gaussian transitions using Peakfit Version 4. For the $[(^{DMA}N_3S)Cu^{II}–OO^{\bullet-}]^+$ rR spectra, the Cu^{I} spectrum was subtracted from both the $^{16}O_2$ and $^{18}O_2$ spectra and each transition was constrained to have an identical bandwidth.

8.2 Synthesis of Ligands

$^{DMA}N_3S$, 2-((((4-(dimethylamino)pyridin-2-yl)methyl)(2-((2-methylbenzyl)thio)ethyl)amino)methyl)-*N*,*N*-dimethylpyridin-4-amine. 2-(chloromethyl)-*N*,*N*-dimethylpyridin-4-amine hydrochloride (1.244 g, 6.007 mmol),[2] 2-[(2-methylbenzyl)thio]ethanamine (0.495 g, 2.730 mmol) and potassium carbonate (2.264 g, 16.382 mmol) in CH_3CN (120 mL) were placed in a 250 mL two-neck-flask. The mixture solvent was stirred for 4 days under Ar at 50 ~ 60 ºC. After removal of the solvent, crude brownish yellow solid was dissolved in 100 mL dichloromethane and washed with water three times. After drying over $MgSO_4$, the solution was filtered and removed by rotary evaporation. The resulting yellow oil was purified by column chromatography over Alumina (ethylacetate, MeOH = 7:1) yielding a pale yellow oil (0.471 g, 38 % yield) (R_f = 0.60). **^{1}H-NMR** (400 MHz, $CDCl_3$): δ 8.14-8.12 (d, 2H), 7.13-7.07 (m, 4H), 6.92 (s, 2H), 6.38-6.35 (d, 2H), 3.74 (s, 4H), 3.63 (s, 2H), 2.99 (s, 12H), 2.85-2.80 (t, 2H), 2.69-2.2.65 (t, 2H), 2.33 (s, 3H). **ESI-MS**, *m*/*z*: 450.48 ($L + H^+$).

$^{\mathrm{DMA}}\mathrm{N}_3$, 2-((((4-(dimethylamino)pyridin-2-yl)methyl)(phenethyl)amino)methyl)-*N*,*N*-dimethylpyridin-4-amine. The ligand was synthesized in the same way depicted above. The resulting red oil was purified by column chromatography over Alumina (CH_2Cl_2 : MeOH = 9:1) yielding a yellow powder (59 % yield) ($R_f = 0.65$). **^{1}H-NMR** (400 MHz, $CDCl_3$): δ 8.15-8.13 (d, 2H), 7.23-7.12 (m, 5H), 6.735-6.729 (d, 2H), 6.38-6.34 (q, 2H), 3.80 (s, 4H), 2.98 (s, 2H), 2.93 (s, 12H), 2.88 (s, 2H). **ESI-MS**, *m*/*z*: 390.98 ($L + H^+$).

$^{\mathrm{DMA}}\mathrm{N}_4$, N^1,N^1-bis((4-(dimethylamino)pyridin-2-yl)methyl)-N^2,N^2-dimethylethane-1,2-diamine. The ligand was synthesized in the same way depicted above. The resulting brown oil was purified by column chromatography three times over Alumina (CH_2Cl_2 : MeOH = 9:1) yielding a yellow oil (26 % yield) ($R_f = 0.75$). **^{1}H-NMR** (400 MHz, $CDCl_3$): δ 7.95-7.93 (d, 2H), 6.49-6.48 (d, 2H), 6.17-6.14 (m, 2H), 3.38 (s, 4H), 2.74 (s, 12H), 2.44 (s, 4H), 2.11 (s, 6H) **ESI-MS**, *m*/*z*: 357.81 ($L + H^+$).

$^{\mathrm{DMA}}\mathrm{N}_3\mathrm{O}$, 2-((((4-(dimethylamino)pyridin-2-yl)methyl)(2-ethoxyethyl)amino)methyl)-*N*,*N*-dimethyl-pyridin-4-amine. The ligand was synthesized in the same way depicted above using 2-ethoxyl ethanamine. The resulting yellow oil was purified by column chromatography over Alumina (CH_2Cl_2 : MeOH = 9:1) yielding a pale yellow powder (58 % yield) ($R_f = 0.60$). **^{1}H-NMR** (400 MHz, $CDCl_3$): δ 8.14-8.13 (d, 2H), 6.90-6.89 (d, 2H), 6.37-6.34 (q, 2H), 3.79 (s, 4H), 3.61-3.57 (t, 2H), 3.47-3.42 (q, 2H), 2.99 (s, 12H), 2.86-2.83 (t, 2H), 1.19-1.18 (t, 3H). **ESI-MS**, *m*/*z*: 358.25 ($L + H^+$).

Scheme S1. Ligand Synthesis Scheme

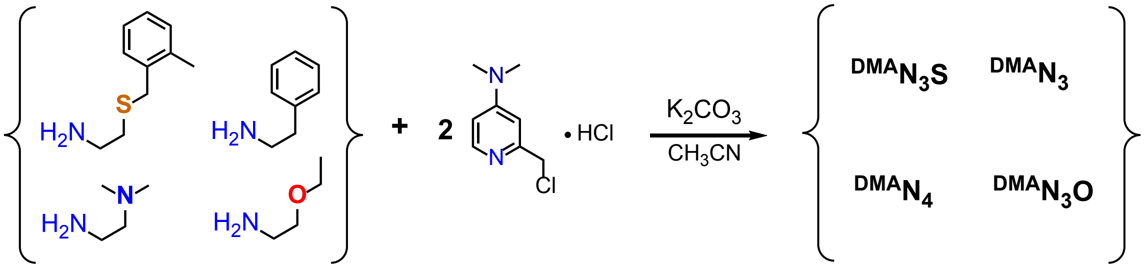

8.3 Synthesis of Copper (I)/(II) Complexes

$[(^{DMA}N_3S)Cu^I]B(C_6F_5)_4$ (1). In a 100 ml Schlenk flask in the glove box, 207 mg (0.228 mmol) of $[Cu^I(CH_3CN)_4]B(C_6F_5)_4$ were dissolved in 10 mL of THF. 102 mg (0.228 mmol) of **$^{DMA}N_3S$** ligand dissolved in approximately 7 mL of THF were added to the copper solution yielding a pale yellow solution. This yellow solution was allowed to stir for 5 min at which time approximately 100 mL of degassed pentane were added to the copper(I) solution. After 40 min, the supernatant was decanted and the pale yellow oil removed from the glove box and dried under vacuum for 10 min affording 211 mg of a yellow powder (77 % yield). *Single crystals were obtained by topping of dry pentane into a solution of the complex in THF* (See **Figure S2**). **^{1}H-NMR** (400 MHz, THF-d_8): δ 8.18-8.16 (d, 2H), 7.17-7.03 (d, 4H), 6.74-6.66 (d, 2H), 6.56 (s, 2H), 3.94-3.90 (m, 2H), 3.73 (s, 2H), 3.04 (s, 12H), 2.71-2.66 (m, 2H), 2.48 (s, 4H), 2.33 (s, 3H). **Elemental analysis**: ($C_{50}H_{35}BCuF_{20}N_5S$) Calculated: C (50.37), H (2.96), N (5.87); found: C (50.45), H (2.72), N (5.30).

$[(^{DMA}N_3)Cu^I]B(C_6F_5)_4$. 65 % yield. **^{1}H-NMR** (400 MHz, THF-d_8): δ 8.19-8.17 (d, 2H), 7.24-7.20 (d, 3H), 7.15-7.13 (d, 2H), 6.69-6.67 (q, 2H), 6.20-6.10 (d, 2H), 4.10-4.06 (d, 2H), 3.76-3.68 (t, 2H), 3.05 (s, 12H), 2.48 (s, 4H). **Elemental analysis**: ($C_{48}H_{31}BCuF_{20}N_5$) Calculated: C (50.92), H (2.76), N (6.19); found: C (50.68), H (2.92), N (5.89).

[($^{DMA}N_4$)Cu^I]$B(C_6F_5)_4$. 57 % yield. **^{1}H-NMR** (400 MHz, THF-d_8): δ 8.18-8.16 (d, 2H), 7.71-6.59 (m, 4H), 3.58 (s, 4H), 3.06-3.05 (d, 12H), 2.47 (s, 4H), 2.13-2.11 (d, 6H). **Elemental analysis**: ($C_{44}H_{32}BCuF_{20}N_6$) Calculated: C (48.08), H (2.93), N (7.65); found: C (47.31), H (3.02), N (7.17).

[($^{DMA}N_3O$)Cu^I]$B(C_6F_5)_4$. 85 % yield. **^{1}H-NMR** (400 MHz, THF-d_8): δ 8.17-8.15 (d, 2H), 6.63 (s, 4H, broad), 3.69-3.60 (t, 4H), 3.33-3.28 (q, 4H), 3.03 (s, 12H), 2.47 (s, 2H), 1.11-1.08 (t, 3H). **Elemental analysis**: ($C_{44}H_{31}BCuF_{20}N_5O$) Calculated: C (48.04), H (2.84), N (6.37); found: C (47.62), H (2.77), N (6.09).

[($^{DMA}N_3S$)Cu^{II}($OClO_3$)(H_2O)](ClO_4) (3). In a 100 mL Schlenk flask, 125 mg (0.278 mmol) of **$^{DMA}N_3S$** ligand was dissolved in 15 mL dry acetone. 103 mg (278 mmol) of $Cu^{II}(ClO_4)_2$•$6H_2O$ was dissolved in 15 mL dry acetone and then copper solution was added to **$^{DMA}N_3S$** solution. After stirring for 15 min at room temperature, the complex was precipitated as bluish green solid upon addition of diethyl ether (100 mL). The supernatant was decanted and the resulting blue solid was washed two times with diethyl ether and dried under vacuum to afford 149 mg of a copper(II) complex (73 % yield). *Single crystals were obtained by vapor diffusion of diethyl ether into a solution of the complex in acetone* (see **Figure S3**). **Elemental analysis**: ($C_{26}H_{39}Cl_2CuN_5O_9S$) Calculated: C (42.65), H (5.37), N (9.57); found: C (42.02), H (5.56), N (9.33). **EPR spectrum**: X-band (2 mM, ν

= 9.186 GHz) spectrometer in acetone at 70 K: $g_{\|} = 2.256$, $A_{\|} = 162$ G, $g\perp = 2.037$ (**Figure S1**).

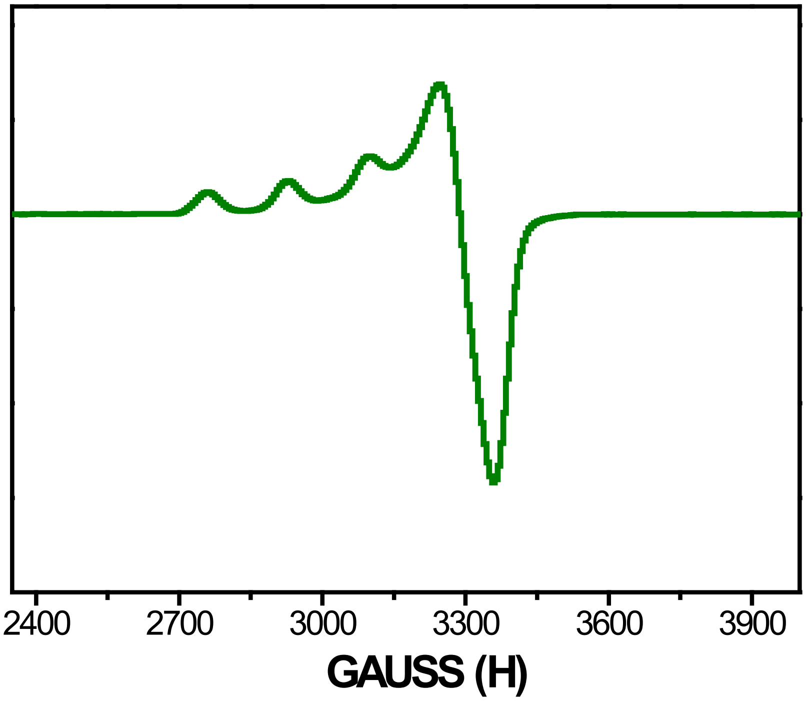

Figure S1. EPR spectrum of [($^{DMA}N_3S$)$Cu^{II}(OClO_3)(H_2O)$](ClO_4) (**3**) (2 mM).

[(^{DMA}tmpa)$Cu^{II}(OClO_3)(H_2O)$](ClO_4). In a 100 mL Schlenk flask, 210 mg (0.5 mol) of **^{DMA}tmpa** ligand prepared by reported method[2] was dissolved in 15 mL dry acetone. 185 mg (0.5 mol) of $Cu^{II}(ClO_4)_2$•$6H_2O$ was dissolved in 15 mL dry acetone and then copper solution was added to **^{DMA}tmpa** solution. After stirring for 15 min at room temperature, the complex was precipitated as bluish green solid upon addition of diethyl ether (100 mL). The supernatant was decanted and the resulting blue solid was washed two times with diethyl ether and dried under vacuum to afford 334 mg of a copper(II) complex (95 % yield). *Single crystals were obtained by vapor diffusion of diethyl ether into a solution of the complex in acetone* (see **Figure S4**). **Elemental analysis**: ($C_{24}H_{35}Cl_2CuN_7O_9$)

Calculated: C (41.18), H (5.04), N (14.01); found: C (41.11), H (5.30), N (13.80). **EPR spectrum**: X-band (2 mM, ν = 9.408 GHz) spectrometer in acetone at 70 K: $g_{||} = 2.207$, $A_{||} = 150$ G, $g\perp = 2.076$ (**Figure S2**).

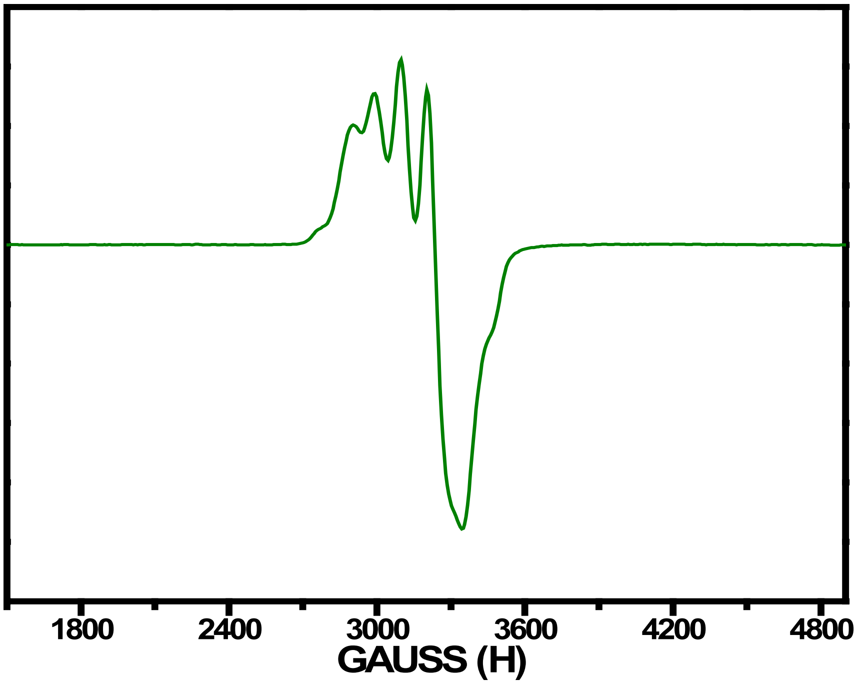

Figure S2. EPR spectrum of $[(^{DMA}tmpa)Cu^{II}(OClO_3)(H_2O)](ClO_4)$ (2 mM).

8.4 X-ray Crystallography

All reflection intensities were measured at 110(2) K using a SuperNova diffractometer (equipped with Atlas detector) with Cu *K*α radiation (λ = 1.54178 Å) under the program CrysAlisPro (Version 1.171.36.32 Agilent Technologies, 2013). The program CrysAlisPro was used to refine the cell dimensions and for data reduction. The structure was solved with the program SHELXS-2013 (Sheldrick, 2013) and was refined on F^2 with SHELXL-2013 (Sheldrick, 2013). Analytical numeric absorption correction based on a multifaceted crystal model was applied using CrysAlisPro for **1**. Empirical absorption correction using spherical harmonics implemented in SCALE3 ABSPACK scaling algorithm was applied using CrysAlisPro for **3**. The temperature of the data collection was controlled using the system Cryojet (manufactured by Oxford Instruments). The H atoms were placed at calculated positions using the instructions AFIX 23, AFIX 43 or AFIX 137 with isotropic displacement parameters having values 1.2 or 1.5 times *U*eq of the attached C atoms. In the structures of **3** and of [(^{DMA}tmpa)Cu^{II}(OClO$_3$)(H$_2$O)](ClO$_4$), the H atoms attached to O1W were found from difference Fourier maps, and their coordinates and isotropic temperature factors were refined freely.

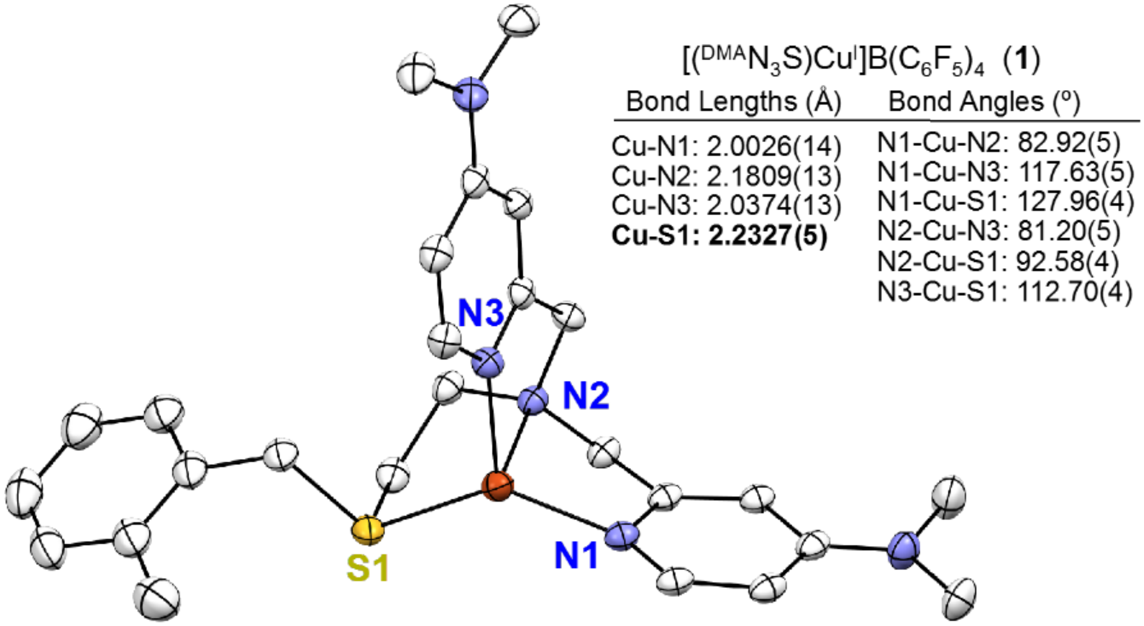

[(^{DMA}N$_3$S)Cu^I]B(C$_6$F$_5$)$_4$ (**1**)

Bond Lengths (Å)	Bond Angles (°)
Cu-N1: 2.0026(14)	N1-Cu-N2: 82.92(5)
Cu-N2: 2.1809(13)	N1-Cu-N3: 117.63(5)
Cu-N3: 2.0374(13)	N1-Cu-S1: 127.96(4)
Cu-S1: 2.2327(5)	N2-Cu-N3: 81.20(5)
	N2-Cu-S1: 92.58(4)
	N3-Cu-S1: 112.70(4)

Figure S3. Displacement ellipsoid plot (50% probability level) of [(^{DMA}N$_3$S)Cu^I]B(C$_6$F$_5$)$_4$ (**1**) at 110(2) K. The H atoms are omitted for the sake of clarity. The structure is ordered. [(^{DMA}N$_3$S)Cu^I]B(C$_6$F$_5$)$_4$ (**1**): Fw = 1192.24, irregular colorless lath, 0.54 × 0.18 × 0.08 mm^3, triclinic, *P*-1 (no. 2), a = 12.4367(3), b = 15.1159(3), c = 15.4174(4) Å, α = 69.996(2), β = 66.443(2), γ = 71.641(2)°, V = 2442.48(11) Å^3, Z = 2, D_x = 1.621 g cm^{-3}, μ = 2.115 mm^{-1}, T_{min}-T_{max}: 0.57–0.86. 32542 Reflections were measured up to a resolution of (sin $\theta/\lambda)_{max}$ = 0.62 Å^{-1}. 9586 Reflections were unique (R_{int} = 0.0232), of which 8727 were observed [$I > 2\sigma(I)$]. 708 Parameters were refined. $R1/wR2$ [$I > 2\sigma(I)$]: 0.0307/0.0785. $R1/wR2$ [all refl.]: 0.0342/0.0811. S = 1.024. Residual electron density found between −0.43 and 0.36 e Å^{-3}.

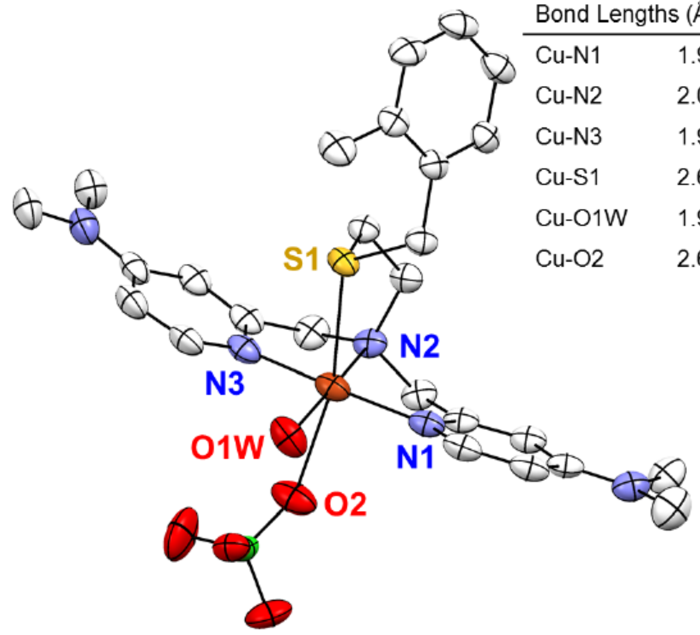

$[(^{DMA}N_3S)Cu^{II}(OClO_3)(H_2O)](ClO_4)$ (**3**)

Bond Lengths (Å)		Bond Angles (°)	
Cu-N1	1.977(2)	N1-Cu-N2	82.89(8)
Cu-N2	2.0256(19)	N1-Cu-N3	165.15(8)
Cu-N3	1.982(2)	N1-Cu-S1	103.25(5)
Cu-S1	2.6974(6)	N1-Cu-O1W	99.95(8)
Cu-O1W	1.9837(18)	N2-Cu-N3	83.66(8)
Cu-O2	2.693(2)	N2-Cu-S1	86.42(5)
		N2-Cu-O1W	172.62(8)
		N3-Cu-S1	82.12(5)
		N3-Cu-O1W	92.69(9)
		S1-Cu-O1W	99.46(6)
		O2-Cu-O1W	83.18(7)
		O2-Cu-N1	90.24(7)
		O2-Cu-N2	90.02(7)
		O2-Cu-N3	83.50(7)
		O2-Cu-S1	165.48(5)

Figure S4. Displacement ellipsoid plot (50% probability level) of $[(^{DMA}N_3S)Cu^{II}(H_2O)(OClO_3)](ClO_4)$ (**3**). The H atoms are omitted for the sake of clarity. The structure is mostly ordered. Both counterions are found to be disordered over two orientations. The occupancy factors of the major components of the disorder refine to 0.727(7) and 0.9465(18). $[(^{DMA}N_3S)Cu^{II}(H_2O)(OClO_3)](ClO_4)$ (3)**:** Fw = 730.10, blue lath, 0.35 × 0.15 × 0.10 mm³, monoclinic, $P2_1/c$ (no. 14), $a = 15.0863(2)$, $b = 11.06407(18)$, $c = 19.2816(3)$ Å, $\beta = 99.6221(14)$°, $V = 3173.13(8)$ Å³, $Z = 4$, $D_x = 1.528$ g cm⁻³, $\mu = 3.641$ mm⁻¹, abs. corr. range: 0.65–1.00. 25665 Reflections were measured up to a resolution of $(\sin \theta/\lambda)_{max} = 0.62$ Å⁻¹. 6227 Reflections were unique ($R_{int} = 0.0302$), of which 5302 were observed $[I > 2\sigma(I)]$. 496 Parameters were refined using 287 restraints. $R1/wR2$ $[I > 2\sigma(I)]$: 0.0355/0.0921. $R1/wR2$ [all refl.]: 0.0435/0.0990. S = 1.033. Residual electron density found between −0.50 and 0.81 e Å⁻³.

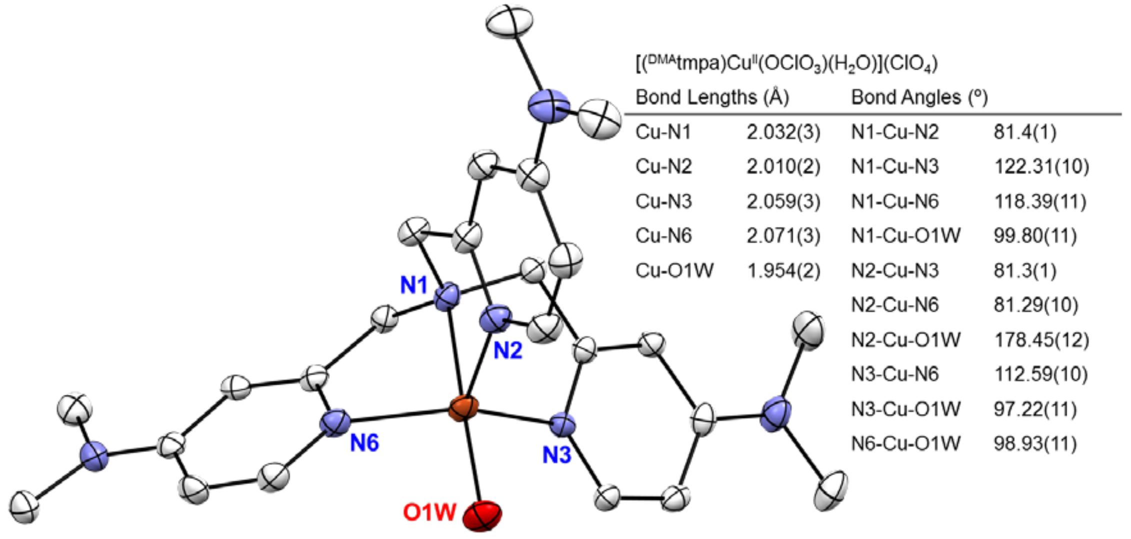

[(^{DMA}tmpa)Cu^{II}(OClO$_3$)(H$_2$O)](ClO$_4$)

Bond Lengths (Å)		Bond Angles (°)	
Cu-N1	2.032(3)	N1-Cu-N2	81.4(1)
Cu-N2	2.010(2)	N1-Cu-N3	122.31(10)
Cu-N3	2.059(3)	N1-Cu-N6	118.39(11)
Cu-N6	2.071(3)	N1-Cu-O1W	99.80(11)
Cu-O1W	1.954(2)	N2-Cu-N3	81.3(1)
		N2-Cu-N6	81.29(10)
		N2-Cu-O1W	178.45(12)
		N3-Cu-N6	112.59(10)
		N3-Cu-O1W	97.22(11)
		N6-Cu-O1W	98.93(11)

Figure S5. Displacement ellipsoid plot (50% probability level) of [(^{DMA}tmpa)Cu^{II}(OClO$_3$)(H$_2$O)](ClO$_4$). The H atoms are omitted for the sake of clarity. The structure is mostly ordered. One of the two crystallographically independent perchlorate counterions is found to be disordered over two orientations, and the occupancy factor of the major component of the disorder refines to 0.936(9). The absolute configuration was established by anomalous-dispersion effects in diffraction measurements on the crystal. The Flack parameter refines to -0.013(8). [(^{DMA}tmpa)Cu^{II}(OClO$_3$)(H$_2$O)](ClO$_4$): Fw = 700.03, green rod, 0.42 × 0.14 × 0.11 mm^3, hexagonal, $P6_5$ (no. 170), a = 15.05046(19), c = 22.7280(3) Å, V = 4458.52(13) Å^3, Z = 6, D_x = 1.564 g cm^{-3}, μ = 3.240 mm^{-1}, T_{min}-T_{max}: 0.486–0.752. 19557 Reflections were measured up to a resolution of $(\sin \theta/\lambda)_{max}$ = 0.62 Å^{-1}. 4703 Reflections were unique (R_{int} = 0.0323), of which 4565 were observed [$I > 2\sigma(I)$]. 430 Parameters were refined using 149 restraints. $R1/wR2$ [$I > 2\sigma(I)$]: 0.0248/0.0615. $R1/wR2$ [all refl.]: 0.0259/0.0623. S = 1.033. Residual electron density found between −0.23 and 0.21 e Å^{-3}.

8.5 Cyclic Voltammetry (CV) Data

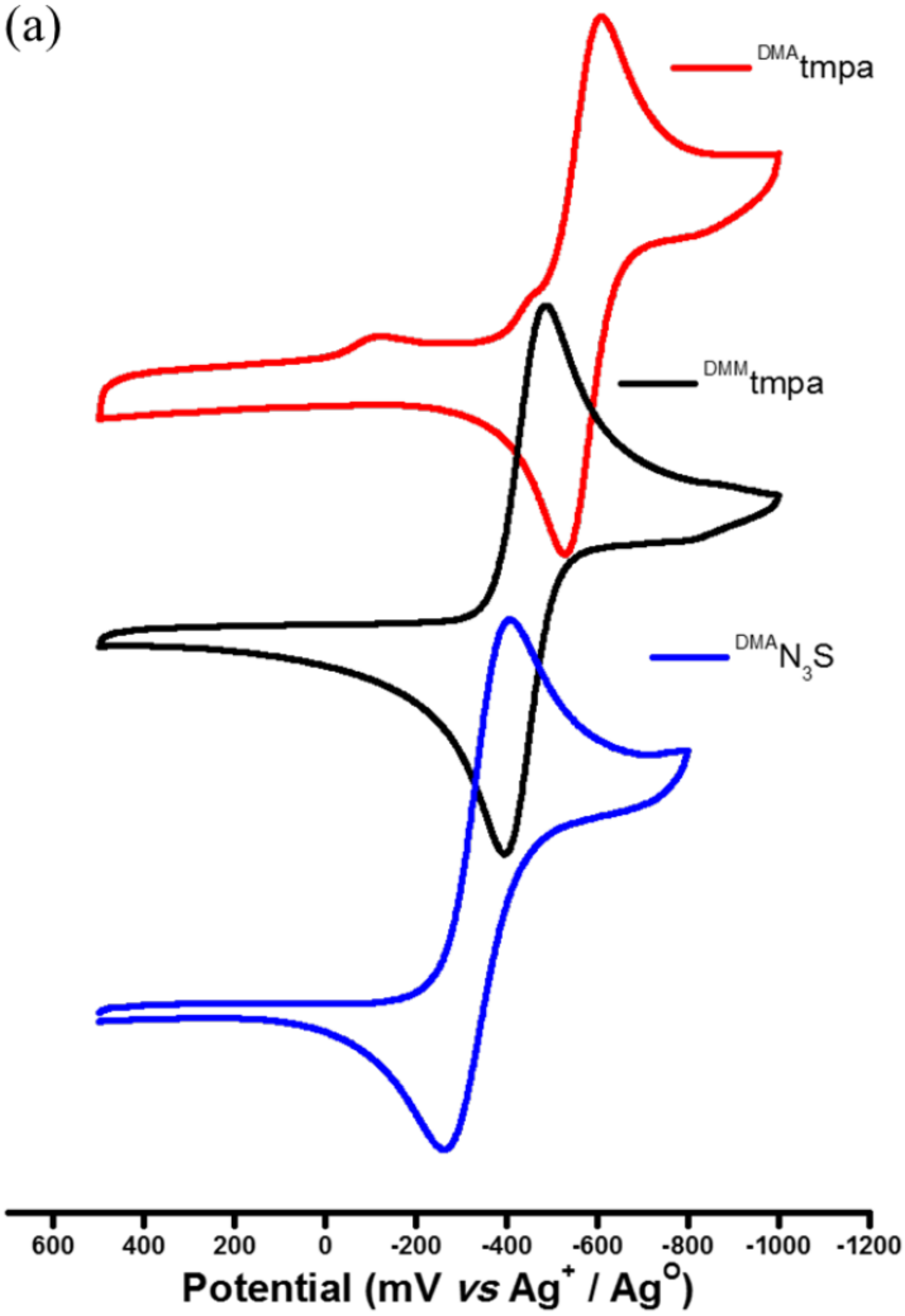

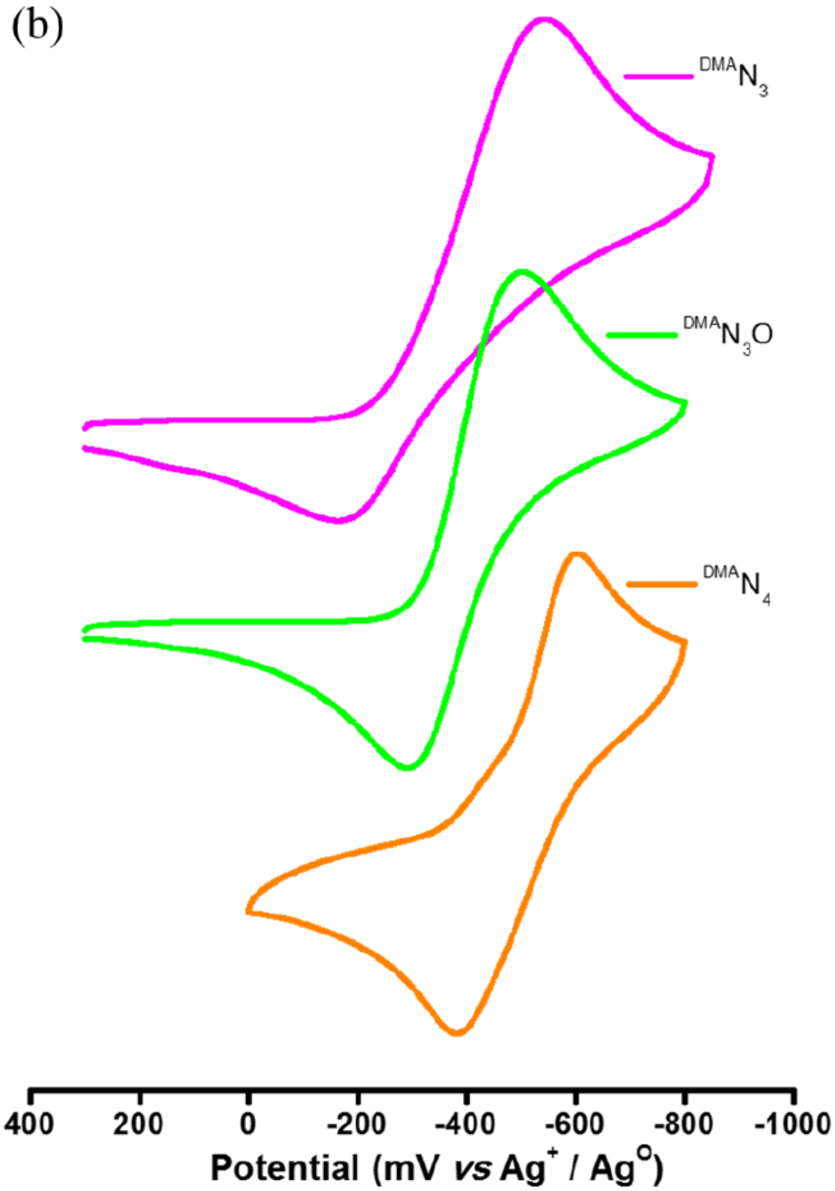

Figure S6. Cyclic voltammograms of ligand-Cu^{II} complexes in CH_3CN (mV *vs*. $[Fe(Cp)_2]^{+/0}$). Cu^{II} complexes (~ 1 mM) were employed for cyclic voltammetric measurements. CV measurements were undertaken in freshly distilled acetonitrile using a BAS 100B electrochemical analyzer with a glassy carbon working electrode and a platinum wire auxiliary electrode. Potentials were recorded versus a $Ag/AgNO_3$ electrode. Scans were run at 50 mV/s under Ar atmosphere using ca. 0.1 M $[Bu_4N][PF_6]$ as the supporting electrolyte.

8.6 Oxygenation of a $[(^{DMA}N_3S)Cu^{I}]^{+}$ (1) in MeTHF at -135 °C

In the glove box, 0.2 mM solution of $[(^{DMA}N_3S)Cu^{I}]B(C_6F_5)_4$ (**1**) was prepared in a 2.5 mL MeTHF, and the 1 cm Schlenk cuvette was sealed with a rubber septum. Out of the glove box and the cuvette was secured with a copper wire. The cell was transferred to the pre-cooled cryostat and chilled at –135 °C with a minimum of 10 minutes allowed for equilibration prior to oxygenation. The dioxygen was gently bubbled through the solution using long needle for 30 seconds forming mixture of $[(^{DMA}N_3S)Cu^{II}(O_2^{\bullet-})]^{+}$ ($\mathbf{2^S}$) and $[\{(^{DMA}N_3S)Cu^{II}\}_2(O_2^{2-})]^{2+}$ ($\mathbf{2^P}$). After 5 min, $\mathbf{2^S}$ is completely converted to $\mathbf{2^P}$ (**Figure 2**).

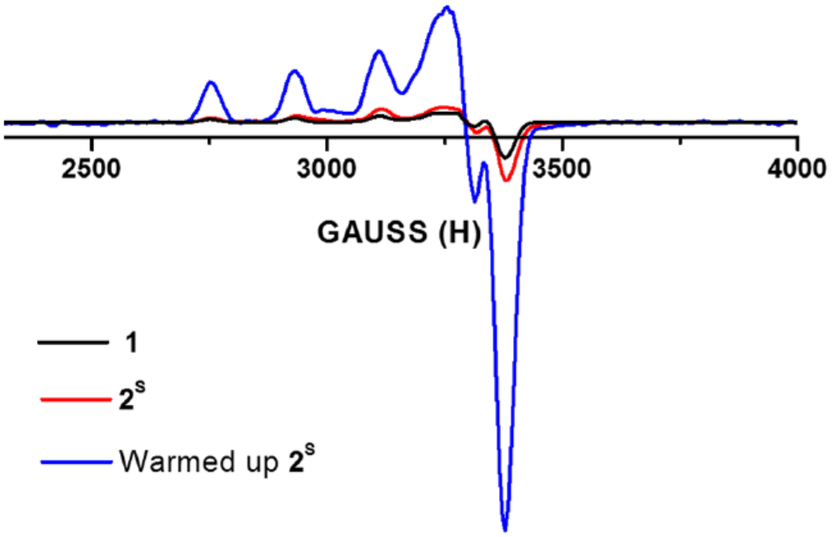

Figure S7. EPR spectra of $[(^{DMA}N_3S)Cu^{I}]B(C_6F_5)_4$ (**1**) (**black**), $[(^{DMA}N_3S)Cu^{II}(O_2^{\bullet-})]^{+}$ ($\mathbf{2^S}$) (**red**), and warmed up solution of $\mathbf{2^S}$ (**blue**) ($g_{\parallel} = 2.241$, $A_{\parallel} = 168$ G, $g_{\square} = 2.039$) taken with an X-band spectrometer ($\nu = 9.410$ GHz) in acetone at 70 K. Copper complex concentration: 0.1 mM. The spectra of **1** and $\mathbf{2^S}$ contain small amount of impurity of a typical copper(II) paramagnetic compound. The $[(L)Cu^{II}(O_2^{\bullet-})]^{+}$ complexes with N_4 tripodal tetradentate ligands have been shown to have S=1 triplet ground states, which usually do not exhibit EPR signals in typical X-band instrument conditions. $\mathbf{2^S}$ is EPR silent also assigned as an S = 1 species. On warming $\mathbf{2^S}$ to RT, a 'normal' Cu^{II} complex is generated, exhibiting a typical EPR signal at intensities expected.

8.7 Resonance Raman (rR) Data

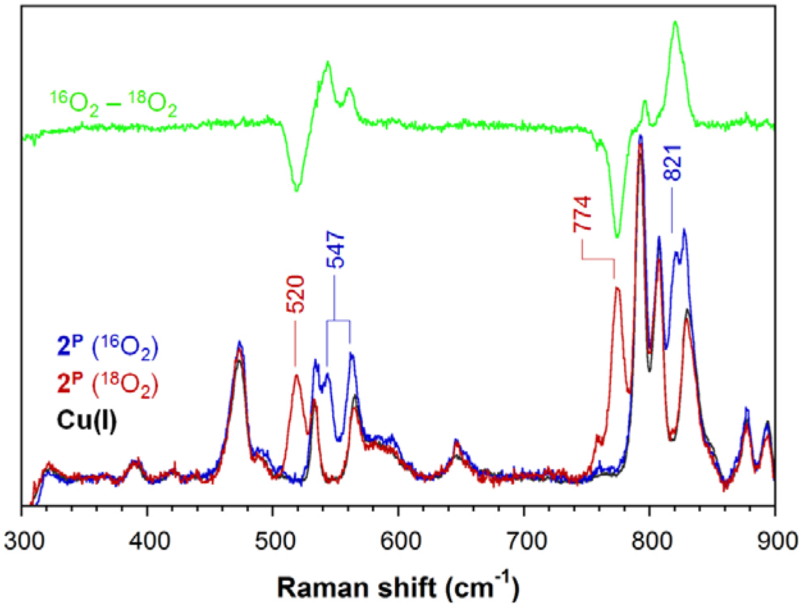

Figure S8. Resonance Raman spectra of $[\{(^{DMA}N_3S)Cu^{II}\}_2(\mu\text{-}1,2\text{-}O_2^{2-})]$ ($\mathbf{2^P}$) in MeTHF:acetone (4:1) with 720 nm excitation at 77 K. A control sample of $[(^{DMA}N_3S)Cu^{I}]B(C_6F_5)_4$ (**1**) in the same solvent mixture ("Cu(I)", black spectrum) is shown for comparison. The ^{16}O isotopologue of $\mathbf{2^P}$ shows two features at 544 and 561 cm^{-1} that are interpreted as a Fermi resonance of the ν(Cu–O) mode centered at the intensity-weighted average of 547 cm^{-1}.

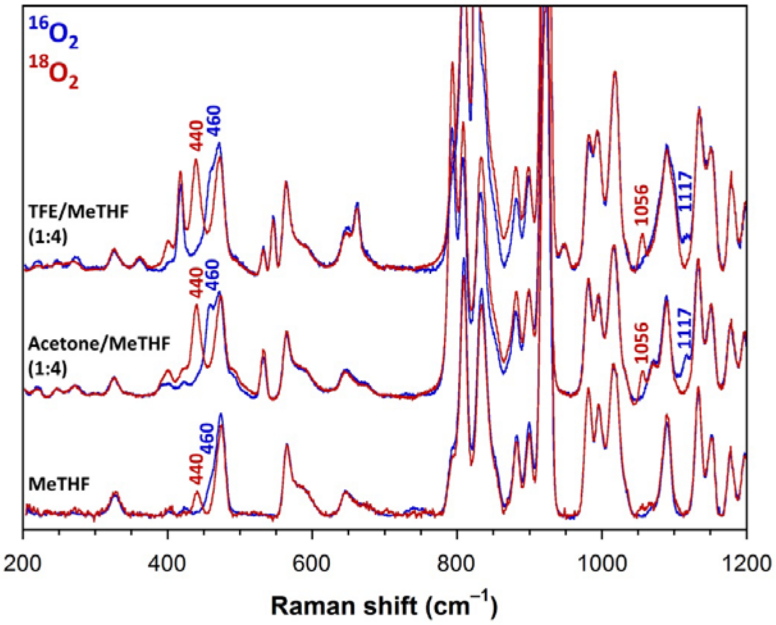

Figure S9. Comparison of resonance Raman spectra of $\mathbf{2^S}$ (413.1 nm) prepared in three solvent combinations (blue: $^{16}O_2$ spectra, red: $^{18}O_2$ spectra). The low concentration of $\mathbf{2^S}$ in neat MeTHF precluded observation of $\nu_{O\text{-}O}$.

8.8 Oxygenation of a [(^{DMA}N$_3$S)Cu^{I}]$^+$ (1) in 20 % Polar Solvents/MeTHF at -135 ºC

In the glove box, 0.15 mM solution of [(^{DMA}N$_3$S)Cu^{I}]B(C$_6$F$_5$)$_4$ (**1**) was prepared in a 2 mL MeTHF plus 0.5 mL polar solvents (acetone, ethanol, methanol, or TFE), and the 1 cm Schlenk cuvette was sealed with a rubber septum. Out of the glove box and the cuvette was secured with a copper wire. The cell was transferred to the pre-cooled cryostat and chilled at –135 °C with a minimum of 10 minutes allowed for equilibration prior to oxygenation. The dioxygen was gently bubbled through the solution using long needle for 40 seconds forming [(^{DMA}N$_3$S)Cu^{II}(O$_2^{\bullet-}$)]$^+$ (**2^S**) and small amount of [{(^{DMA}N$_3$S)Cu^{II}}$_2$ (O$_2^{2-}$)]$^{2+}$ (**2^P**).

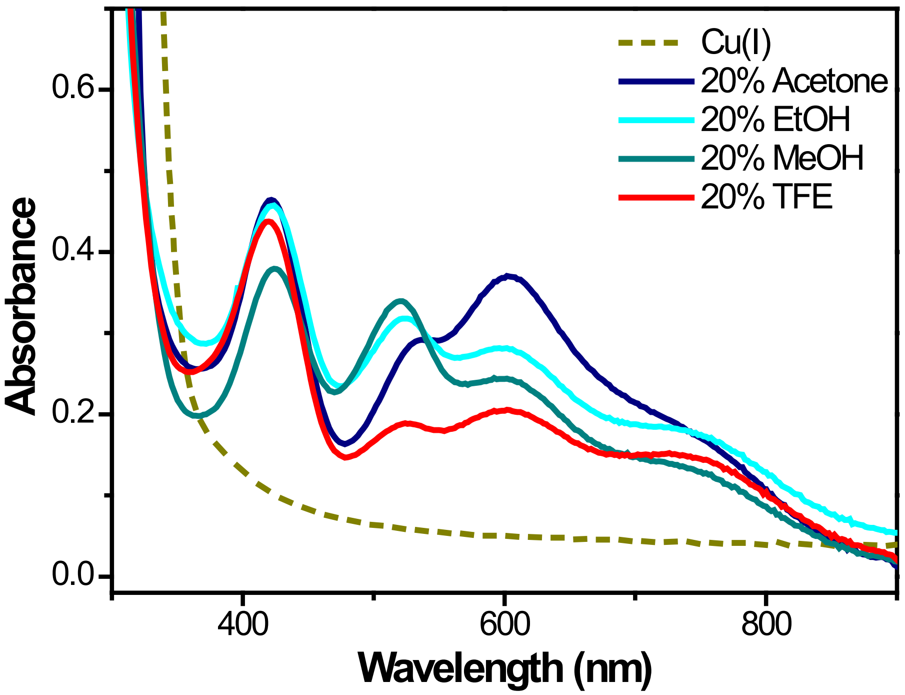

Figure S10. UV-vis spectra of **2^S** in mixed solvents of polar solvents with MeTHF at –135 ºC.

8.9 Reactivity Study and Product Analyses

In the glove box, 0.1 mM solution of $[(^{DMA}N_3S)Cu^I]B(C_6F_5)_4$ (**1**) was prepared in a 2.5 mL solvent mixture MeTHF:TFE (4:1), and the 1 cm Schlenk cuvette was sealed with a rubber septum. Out of the glove box and the cuvette was secured with a copper wire. The cell was transferred to the pre-cooled cryostat and chilled at –135 °C with a minimum of 10 minutes allowed for equilibration prior to oxygenation. The dioxygen was gently bubbled through the solution using long needle for 40 seconds forming $[(^{DMA}N_3S)Cu^{II}–OO^{\bullet-}]^+$ ($\mathbf{2}^S$). Reactivity studies were initiated by the addition of a stock solution of excessive substrates to the fully generated $\mathbf{2}^S$ after three times of Ar/Vacuum purge cycles. Pseudo-first-order rate plots were performed by observing the disappearance of 418 nm band to obtain plots of ln $[(A - A_f)/(A_i - A_f)]$ *vs* time(min).

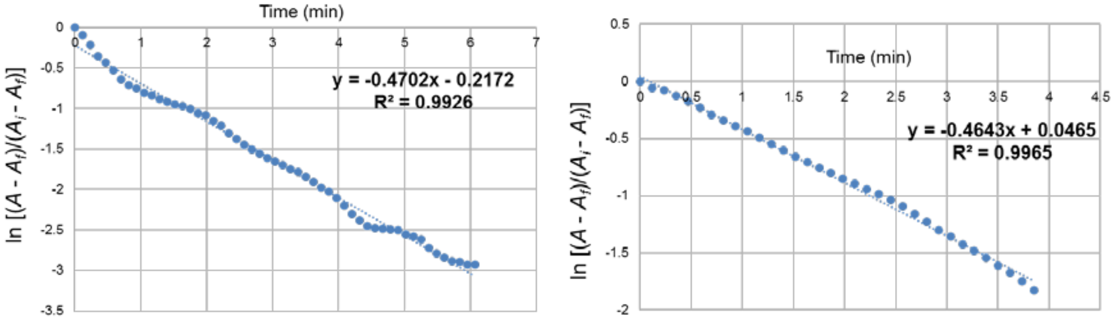

Figure S11. Pseudo-first-order plots for the reactions of $[(^{DMA}N_3S)Cu^{II}–OO^{\bullet-}]^+$ ($\mathbf{2}^S$) and *p*-OMe-DTBP (left panel)/$AcrH_2$ (right panel) to determine pseudo-first-order rate constants (k_{obs}'s). The k_{obs}'s are 0.470 min^{-1} and 0.464 min^{-1}, respectively.

8.9.1 Detection of the product from 2^S + 2,6-di-*tert*-butyl-4-methoxyphenol (*p*-OMe-DTBP) by GC-MS

When the reaction ended, the Schlenk cuvette was warmed up to room temperature (RT). The solvent was removed *in vacuo*, redissolved in 1.5 mL of the solvent and transferred in a GC-MS vial. Then 1 μL was injected into the GC-MS. The retention time of 2,6-di-*tert*-butyl-1,4-benzoquinone is 7.8 min, and that of *p*-OMe-DTBP is 8.9 min.

8.9.2 Identification of the product from 2^S + N-methyl-9,10-dihydroacridine ($AcrH_2$) by ^{1}H-NMR

When the reaction ended, the Schlenk cuvette was warmed up to RT. The solvent was removed *in vacuo*, redissolved in 2 mL of CH_2Cl_2, and the solution was loaded on silica gel column eluting 0 ~ 10 % gradient of CH_2Cl_2:MeOH. Unreacted $AcrH_2$ obtained from the first fraction eluted by 100% CH_2Cl_2. The product was obtained from the last fraction eluted by 9:1 (CH_2Cl_2:MeOH) eluent. (R_f = 0.50, CH_2Cl_2) **^{1}H-NMR** (400 MHz, $CDCl_3$): δ 8.58-8.57 (d, 2H), 7.77-7.73 (t, 2H), 7.57-7.55 (d, 2H), 7.34-7.30 (t, 2H), 3.93 (s, 3H). The spectrum is perfectly matched with that of 10-methyl-9-acridone authentic sample.[3]

8.10 Comparison of Cu/O₂ Adducts of Different Ligands

(a)

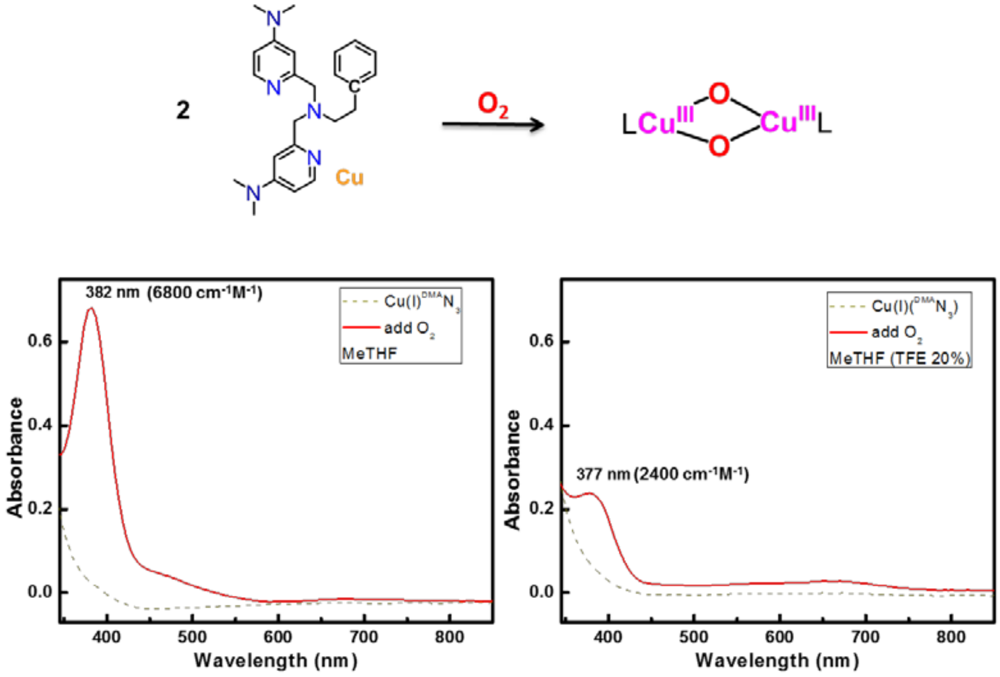

(b)

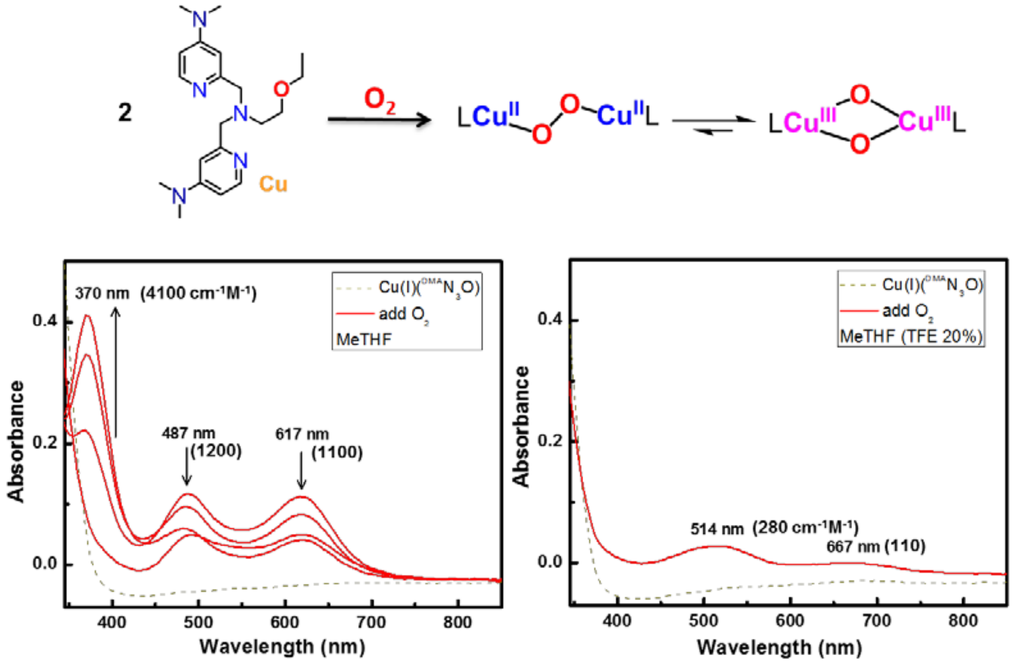

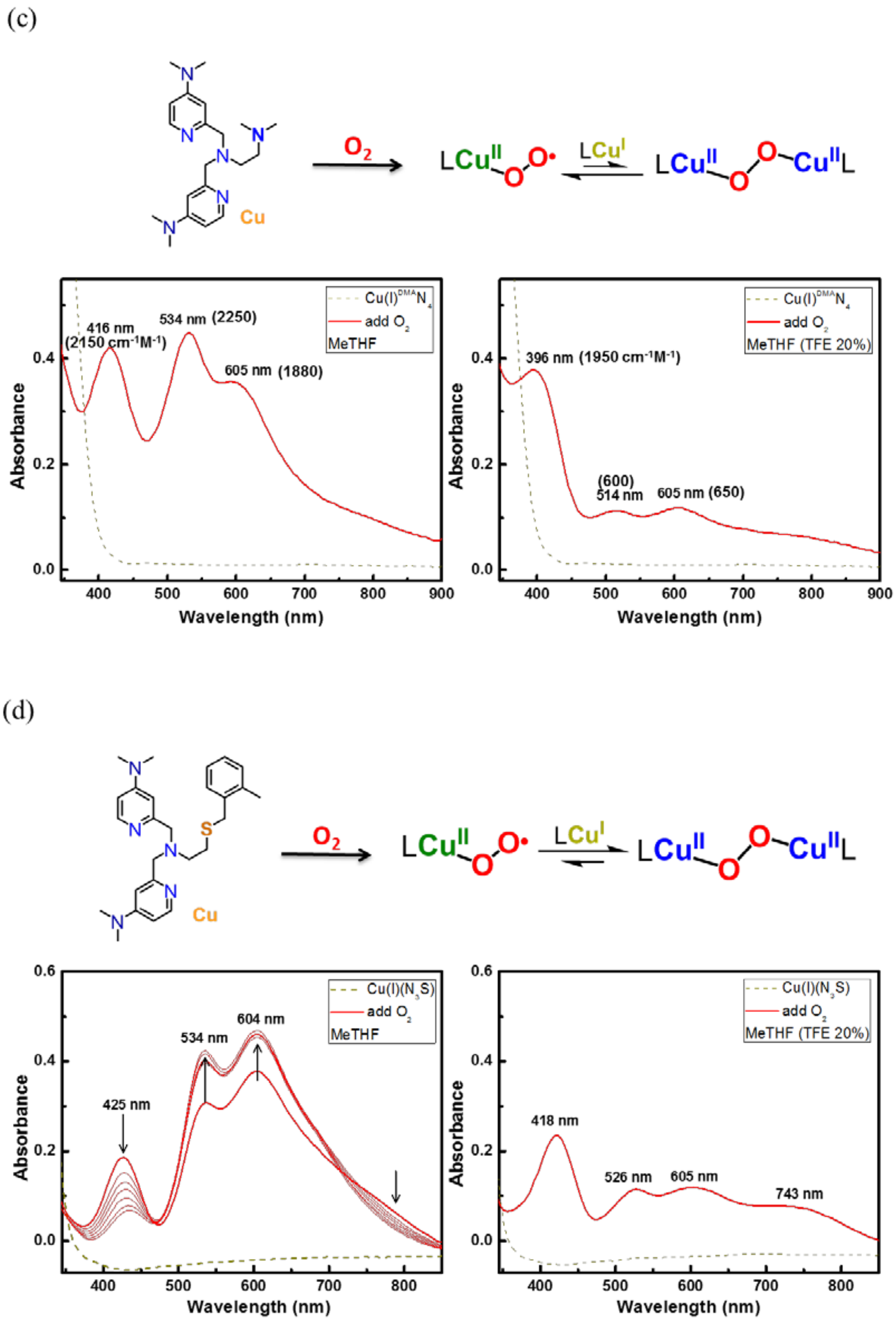

Figure S12. UV-vis spectra of oxygenated adducts of Cu^{I} complexes with different ligand ($^{DMA}N_3$, $^{DMA}N_3O$, $^{DMA}N_4$ and $^{DMA}N_3S$) under different solvent with identical concentrations (–135 ºC). (See **Scheme 2**)

8.11 DOSY NMR Experiments

Table S1. DOSY Derived Diffusion Coefficients (*D*) of Mono- and Dinuclear Cu(I) Complexes in THF-d_8 ($D_{\text{THF-d8}} = 10^{-8.50}$ m^{2}s^{-1}). The NMR spectroscopic technique Diffusion Ordered Spectroscopy (DOSY) utilizes pulsed field gradients to measure the translational diffusion of molecules. The measured diffusion constant is a function of the hydrodynamic radius of the molecule, as given by the Stokes-Einstein equation.

Complex	Log $D = 10^D$ [m^2/s]		Ref.
$[(^{DMA}N_3S)Cu^I]B(C_6F_5)_4$ (1)	$10^{-9.09} = 8.128 \times 10^{-10}$	Monomer	This work
$[(^{DMM}ESE)Cu^I]\ B(C_6F_5)_4$	$10^{-9.08} = 8.317 \times 10^{-10}$	Monomer	4
$[(TMPA)Cu^I(CH_3CN)]$ $B(C_6F_5)_4$	$10^{-9.07} = 8.609 \times 10^{-10}$	Monomer	4
$[(N5)Cu^I_2](B(C_6F_5)_4)_2$	$10^{-9.33} = 4.677 \times 10^{-10}$	Dimer	4
$[(XYL\text{-}H)Cu^I_2](B(C_6F_5)_4)_2$	$10^{-9.31} = 4.897 \times 10^{-10}$	Dimer	4

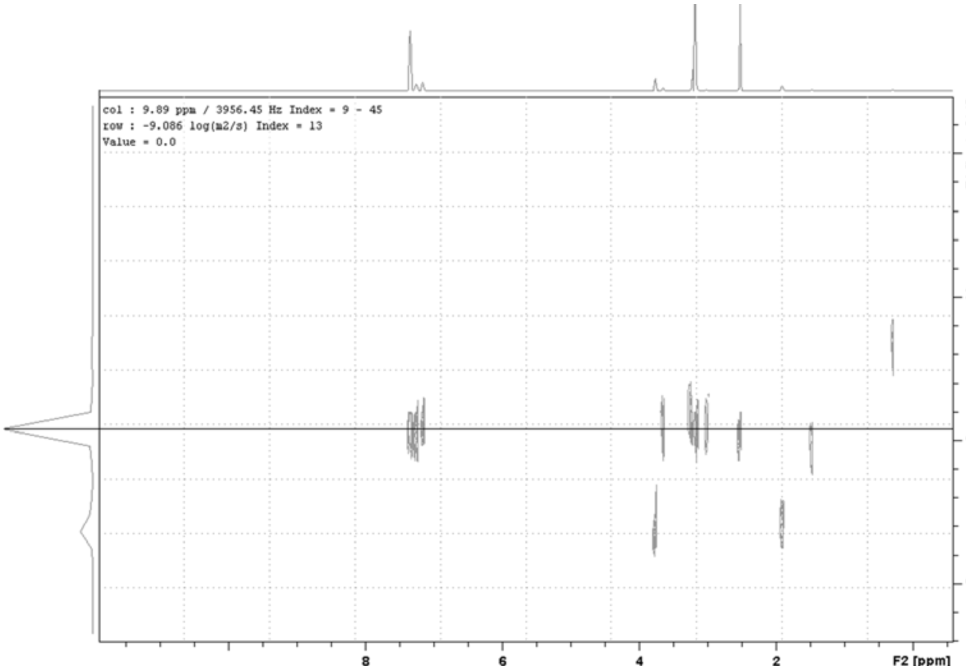

Figure S13. DOSY NMR data of $[(^{DMA}N_3S)Cu^I]B(C_6F_5)_4$ (**1**), affording a diffusion coefficient (*D*) of $D = 10^{-9.09}$ m^{2}s^{-1} ($D_{\text{THF-d8}} = 10^{-8.50}$).

8.12 References

(1) Liang, H.-C.; Kim, E.; Incarvito, C. D.; Rheingold, A. L.; Karlin, K. D. *Inorg. Chem.* **2002**, *41*, 2209.

(2) Zhang, C. X.; Kaderli, S.; Costas, M.; Kim, E.-i.; Neuhold, Y.-M.; Karlin, K. D.; Zuberbühler, A. D. *Inorg. Chem.* **2003**, *42*, 1807.

(3) Lee, J. Y.; Lee, Y.-M.; Kotani, H.; Nam, W.; Fukuzumi, S. *Chem. Commun.* **2009**, *14*, 704.

(4) Kim, S.; Ginsbach, J. W.; Billah, A. I.; Siegler, M. A.; Moore, C. D.; Solomon, E. I.; and Karlin, K. D. *J. Am. Chem. Soc.* **2014**, *136*, 8063.

Chapter 4:

Primary Cu^I/O_2 Adduct with Tunable H-bonding from Secondary Coordination

This work was accomplished with the aid of the following collaborators:

Sunghee Kim, Ryan E. Cowley, Maxime A. Siegler, Edward I. Solomon, and Kenneth D. Karlin

Abstract

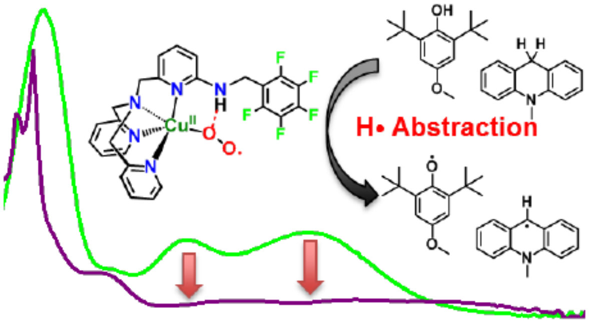

Investigation into the coordination chemistry and reactivity studies are performed with stable primary Cu^I/O_2 species featuring an intramolecular hydrogen bonding substituent, $(^X BA)Cu^{II}(O_2^{\bullet -})$ (^{X}**S**). The stability of ^{X}**S** compounds are ascribed to internal H-bonding from the secondary coordination sphere to the proximal superoxide 'O' atom. The ^{X}**S** complexes were characterized by UV−vis and resonance Raman spectroscopies. Direct evidence of hydrogen atom transfer from phenol substrates by ^{X}**S** complexes was obtained, and enhanced reactivity for copper(II) superoxo complexes possessing electron-withdrawing groups (i.e., X) compared with other $Cu^{II}(O_2^{\bullet -})$ analogues was observed. This

behavior is discussed and correlated to the H-bonding ability of ^{X}BA ligands and the copper ion centered redox behavior of varying ^{X}S.

1. Introduction

Mononuclear copper(II)-oxygen adducts have aroused much interest due to their consequence in chemistry of copper enzymes which contain monocopper active center. Lytic polysaccharide monooxygenases (LPMOs), peptidylglycine-α-hydroxylating monooxygenase (PHM) and dopamine-*β*-monooxygenase (D*β*M) have been known to be responsible for oxidative cleavage of C-H bond, while galactose oxidase and copper amine oxidase are involved in O-H bond activation (**Figure 1**).[1]

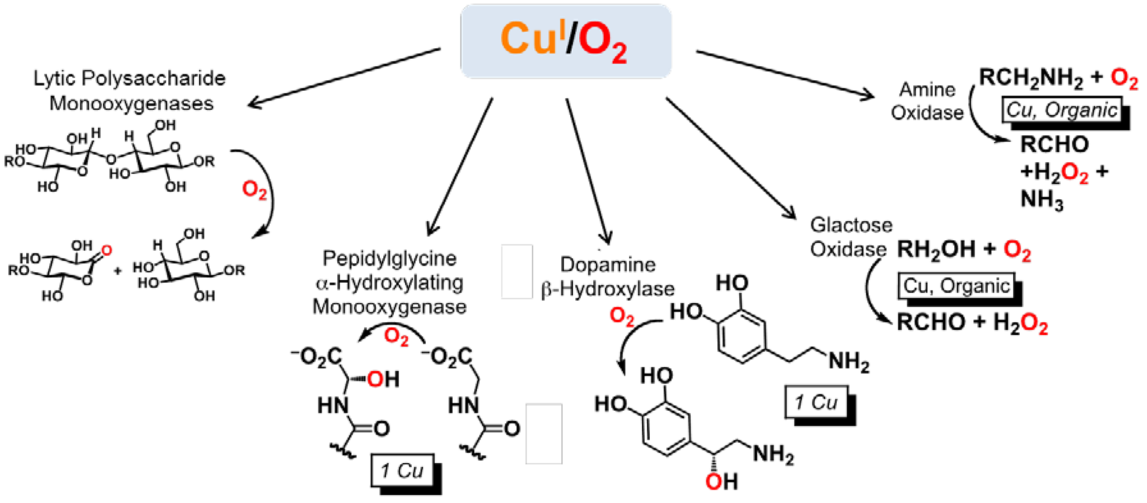

Cu^{I}/O$_2$
Lytic Polysaccharide Monooxygenases
O$_2$
Pepidylglycine α-Hydroxylating Monooxygenase
O$_2$
1 Cu
Dopamine β-Hydroxylase
O$_2$
1 Cu
Glactose Oxidase
RH$_2$OH + O$_2$
Cu, Organic
RCHO + H$_2$O$_2$
Amine Oxidase
RCH$_2$NH$_2$ + O$_2$
Cu, Organic
RCHO +H$_2$O$_2$ + NH$_3$

Figure 1. Metalloenzymes containing mononuclear copper active sites and their biological functions by O_2 activation.[2]

A primary Cu^{I}/O$_2$ adduct, Cu^{II}($O_2^{\bullet-}$), is produced from the internal electron transfer between a reduced copper ion and O_2. Then, sequential electron-proton addition from substrates may lead to a Cu^{II}(OOH) species. Further H-atom transfer may afford a cupric oxyl (Cu^{II}-O• ↔ Cu^{III}=O) species by O–O bond homolysis (**Scheme 1**). All three species have been regarded as reactive intermediates which are capable of C–H or O–H bond activation in nature.[2-4]

Scheme 1. O_2-Derived copper adducts proposed as reactive intermediates.

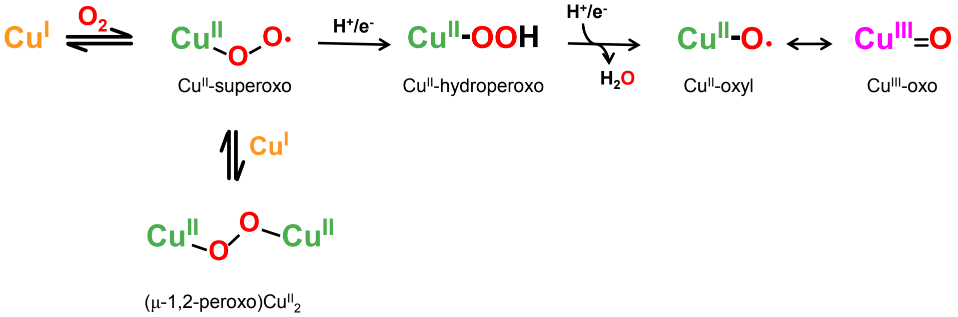

X-ray crystallography reveals that the oxygen-derived form of copper center in PHM exists as an end-on type superoxide moiety[5] and many enzymatic studies have indicated that the $Cu^{II}(O_2^{\bullet-})$ species is more likely to be the reactive species for the C–H/O–H bond oxidation of the substrates.[3] For that reason, synthetic cupric superoxo model systems have been developed and examined to elucidate chemical/physical properties and reactivity of $Cu^{II}(O_2^{\bullet-})$ complexes.[6-12] However, it has been challenging to observe species $Cu^{II}(O_2^{\bullet-})$ spectroscopically since the reactions of $Cu^{II}(O_2^{\bullet-})$ with a second mole-equiv of the starting ligand Cu(I) complex rapidly leads to dicopper(II) *trans*-peroxo species which are thermodynamically more stable (**Scheme 1**).[13] Therefore, bioinorganic chemists have made great efforts to stabilize synthetic ligand-$Cu^{II}(O_2^{\bullet-})$ complexes by redesigning the ligands and adjusting the reaction conditions. In general, there are two strategies in modifying ligands; (i) adding electron-donating groups, in our case where pyridyl-alkylamine ligands are prominently employed, to the *para*- positions on the pyridyl groups of the ligand in order to suppress the further reactions of ligand-$Cu^{II}(O_2^{\bullet-})$ with other copper(I) complexes (**Figure 2a** and **b**),[7, 8] and (ii) adding potential hydrogen-bonding moiety to the secondary coordination sphere to stabilize the proximal oxygen atom of the superoxide anion ligand (**Figure 2c**).[9] The latter method has been extensively precedent by Masuda's group to generate stable synthetic copper(II) hydroperoxo complexes (**Figure 2d** and **e**).[14] They found that the hydrogen bonding interaction with the proximal oxygen of the Cu^{II}(OOH) results in stabilization of the complex, while the interaction with the distal 'O' atom reduces the stability and rather enhances the activity (**Scheme 2**).[15, 16] These results have inspired other research groups to try to obtain critical insights into the roles of hydrogen bonding interactions not only for the Cu^{II}(OOH) species, but also for all other plausible dioxygen-derived metal complexes. Thus, the strategy of adding H-bond groups to ligand constructions has been also applied by our group.

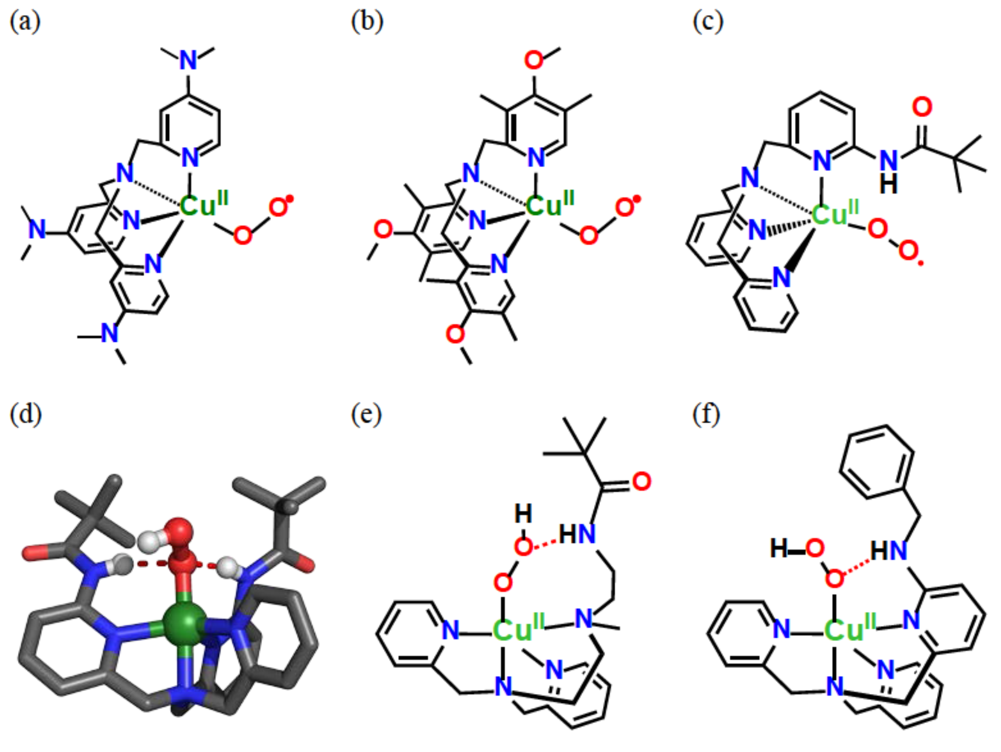

Figure 2. (a)[7] and (b)[8]: Primary Cu^I/O_2 adducts stabilized by electron-donating groups, (c): mononuclear cupric superoxo species stabilized by potential H-bonding pivalamido group, $[(^{PV}tmpa)Cu^{II}(O_2^{\bullet-})]^+$ [9] (d) the X-ray crystallographic structure of $Cu^{II}(O_2H)$ possessing two pivalamido groups,[17] (e) $Cu^{II}(O_2H)$ activated by H-bond with distal O-atom,[16] and (f) $(^{H}BA)Cu^{II}(O_2H)$.[18]

Scheme 2. Mononuclear copper(II)-hydroperoxo complexes, which are stabilized by a H-bond interaction with the proximal oxygen (left)[17] and destabilized by a interaction with the distal oxygen (right).[16]

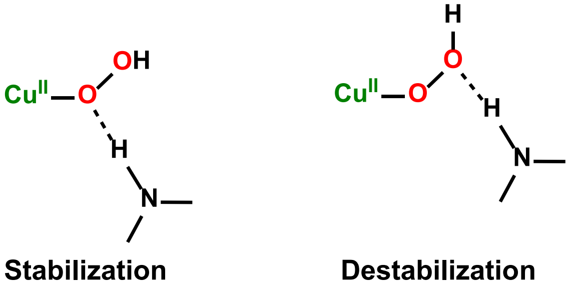

Our group has described Cu^{II}(O$_2^{\bullet-}$) possessing pivalamido group, a good proton donor, on the ligand which may form relatively strong intramolecular H-bonds with the proximal O-atom of the superoxide ion resulting in stabilizing the Cu^{II}(O$_2^{\bullet-}$) complex (**Figure 2c**).[9] In an effort to search for ligands having adjustable hydrogen bonding strength, to obtain greater insights, a substituted benzyl amino moiety was utilized instead of an amido group, which may provide for poorer hydrogen bonding than in the amide (**Figure 2c**). A new ligand series (^{X}BA) (**Chart 1**), possessing potential H-bonding groups, was designed and synthesized by modifying the ^{H}BA ligand previously employed to produce a copper(II) hydroperoxo complex (**Figure 2f**).[18] To provide new insights into the hydrogen bond-stabilized Cu/O$_2$ species including the effect of electron-donating/withdrawing groups on the secondary coordination sphere (benzyl amino arm), primary dioxygen-derived copper adducts of these ^{X}BA ligands were generated and characterized.

Chart 1. ^{X}BA ligands utilized in this study.

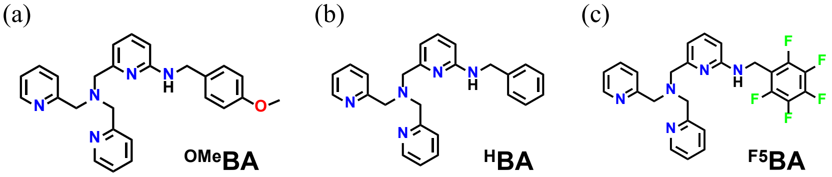

2. Physical Properties of Cu-Complexes

2.1 Geometry and Crystal Structure

The ^{OMe}BA and ^{F5}BA ligands are metallated with $[Cu^I(CH_3CN)_4]SbF_6$ yielding single crystals which could be grown from acetone/diethyl ether at room temperature in the dry box and the complex was structurally determined by single crystal X-ray diffraction analysis. As illustrated in **Figure 3a**, the cuprous complex, $[(^{OMe}BA)Cu^I]^+$ (**^{OMe}1**) is a four-coordinate monomer ligated by three pyridyl and one tertiary amine in a distorted pyramidal geometry providing a very open site for potential dioxygen binding.

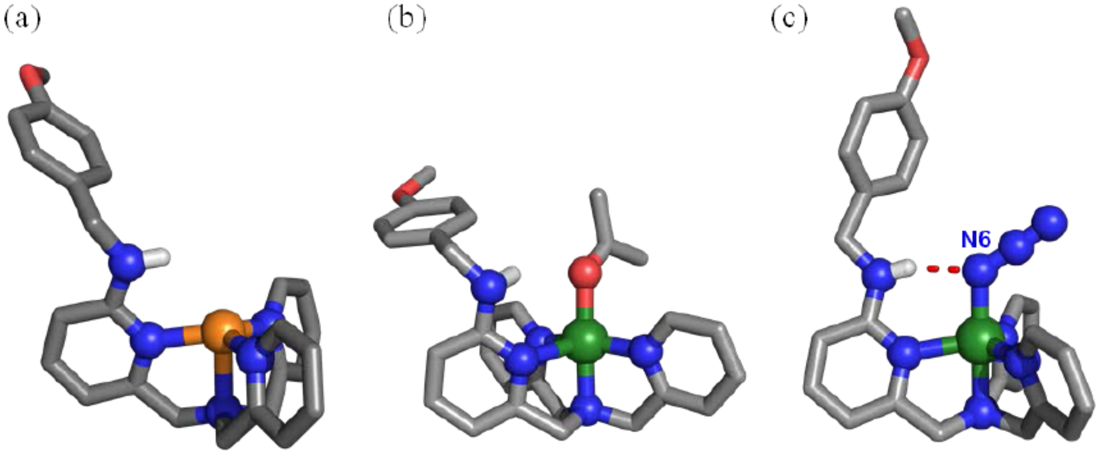

Figure 3. X-ray crystallographically derived structures of; (a) $[(^{OMe}BA)Cu^I]^+$ (**^{OMe}1**), (b) $[(^{OMe}BA)Cu^{II}(CH_3COCH_3)]^{2+}$ (**^{OMe}2**) and (c) $[(^{OMe}BA)Cu^{II}(N_3)]^+$ (**^{OMe}3**). Hydrogen atoms were removed for clarity. Displacement ellipsoid plots of the cations are illustrated in Supporting Information.

The copper(II) complex $[(^{OMe}BA)Cu^{II}(CH_3COCH_3)](ClO_4)_2$ (**^{OMe}2**) presents a distorted square pyramidal (SP) coordination with $\tau = 0.31$ ($\tau = 0$ for idealized SP geometries) (**Figure 3b**). Compared to the close analog $[(^{H}BA)Cu^{II}(CH_3COCH_3)]^{2+}$ (**^{H}2**) which displays distorted trigonal-bipyramidal (TBP) geometry with $\tau = 0.83$,[18] *para*-substitution of the benzyl amine moiety in the secondary coordination sphere changes the Cu^{II} structures from a slightly distorted TBP to distorted SP geometries (Note: the τ value for **^{F5}2** is 0.19). Electron paramagnetic resonance (EPR) measurements show a signature spectrum for a copper(II) complex TBP coordination (i.e., "reverse" axial) ($g_{\parallel}$ = 2.07, $g_{\perp}$= 2.22, $A_{\perp}$ = 108 G) (**Figure S1**).

Furthermore, an azide ion bound copper(II) complex, $[(^{OMe}BA)Cu^{II}(N_3)]^+$ (**^{OMe}3**), was prepared as a structural model complex for $[(^{OMe}BA)Cu^{II}(O_2^{\bullet-})]^+$ (**^{OMe}S**), for the purpose of closer examination of the hydrogen-bonding present. The addition of one equivalent of NaN_3 to an acetone solution of **^{OMe}2** results in an immediate color change of the solution from blue to green, indicating coordination of azide as a fifth ligand. The single crystal of **^{OMe}3** was grown from acetone/pentane through a slow diffusion process at room temperature (**Figure 3c**). In the structure derived from X-ray crystallography, a hydrogen bond (2.059 Å) was observed between the H-atom from the benzyl amino –NH group and the proximal N-atom of the N_3^- ion. The τ value (= 0.87) indicates that the **^{OMe}3** exists in slightly distorted TBP (τ = 1.00 for idealized TBP geometries) geometry. The N(azido)–N(amino) distance was determined as 2.876 Å and the N-H...N(azido) angle as 161.93°. The electronic absorption spectrum of **^{OMe}3** exhibits an intense band in the UV region (403 nm, 1760 M^{-1} cm^{-1}) which can be assigned as a ligand-to-metal charge-transfer (LMCT) transition from the bound azide anion to the cupric ion. In addition, two d-d transition bands were observed, at 662 nm (280 M^{-1} cm^{-1}) and 882 nm (250 M^{-1} cm^{-1}) (**Figure S2**).

2.2 Redox Potentials of $[(^{X}BA)Cu^{II}(CH_3COCH_3)](ClO_4)_2$ (^{X}2) Complexes

To elucidate correlation of hydrogen bonding effect from secondary coordination sphere and electrophilicity relative to observed reactivity (see below), $Cu^{II/I}$ redox potentials for the isolated ligand-Cu^{II} complexes formulated as

$[(^{X}BA)Cu^{II}(CH_3COCH_3)](ClO_4)_2$ (**^{X}2**) (see Supporting Information) were measured and compared (**Figure S8**). The redox potentials of **^{OMe}2**, **^{H}2** and **^{F5}2** were –360, –350 and –330 mV (vs $Fc^{+/0}$), respectively. As a result, $[(^{F5}BA)Cu^{II}(CH_3COCH_3)](ClO_4)_2$ (**^{F5}2**) displays the most positive reduction potentials out of **^{X}2** series, so that we can hypothesize that electron-withdrawing groups on the secondary coordination sphere may make the superoxide ligand oxidant more electrophilic, thus a better oxidant, and hence potentially a better acceptor of an H-atom (H^+/e^-) from either an O–H or C–H substrate, as compared to the **^{OMe}S** or **^{H}S** complexes. Reactivity studies of the various $(^{X}BA)Cu^{II}(O_2^{\bullet-})$ (**^{X}S**) complexes toward O–H or C–H substrates will be discussed below.

3. O_2 Chemistry of Cu(I)-Complexes

For cryogenic low temperature experiments, $[(^{X}BA)Cu^{I}]B(C_6F_5)_4$ (**^{X}1**) complexes, i.e., with $B(C_6F_5)_4^-$ as counter-anion, were utilized for better solubility of copper(I) complexes in 2-methyltetrahydrofuran (2-MeTHF) in order to carry out experiments at –135 ºC. Treatment of the ^{X}BA ligands (substituents X = OMe, H, F_5) with $[Cu^{I}(CH_3CN)_4]B(C_6F_5)_4$ in THF, followed by pentane addition resulting in precipitation, led to the isolation of bright yellow powders with formula $[(^{X}BA)Cu^{I}]B(C_6F_5)_4$ (**^{X}1**).

Upon oxygenation of $[(^{X}BA)Cu^{I}]B(C_6F_5)_4$ (**^{X}1**) complex by bubbling $O_{2\,(g)}$ into a MeTHF solutions at –50 ºC, a stable end-on *trans*-peroxo dicopper(II) species, $[\{(^{X}BA)Cu^{II}\}_2(\mu\text{-}1,2\text{-}O_2^{2-})]^{2+}$ (**^{X}P**), forms and exhibits strong UV-vis absorptions at λ_{max} = 493~503 nm (4800 $M^{-1}cm^{-1}$) (**Figure S9**) consistent with the typical feature of tris(2-pyridylmethyl)amine (tmpa) ligand-based *trans*-peroxo dicopper(II) complexes.[13, 18] The formulation of $[\{(^{H}BA)Cu^{II}\}_2(\mu\text{-}1,2\text{-}O_2^{2-})]^{2+}$ (**^{H}P**) has been confirmed by resonance Raman (rR) spectroscopy in a previous report (ν_{O-O} = 843 cm^{-1}, ν_{Cu-O} = 540 cm^{-1}).[18]

The cupric superoxo complexes $[(^{X}BA)Cu^{II}(O_2^{\bullet-})]^{+}$ (**^{X}S**) were generated by oxygenation at cryogenic temperature, –135 ºC, by vigorously bubbling $O_{2\,(g)}$ for 40 s to minimize the formation of **^{X}P**. These new species **^{X}S**'s have characteristic charge transfer bands at λ_{max} = 417~420 nm (3500 M^{-1}cm^{-1}) and are stable at –135 ºC for hours (**Figure 4**). As illustrated in **Figure 4**, $[(^{OMe}BA)Cu^{II}(O_2^{\bullet-})]^{+}$ (**^{OMe}S**) and $[(^{H}BA)Cu^{II}(O_2^{\bullet-})]^{+}$ (**^{H}S**) contain approximately 20 % of $[\{(^{OMe}BA)Cu^{II}\}_2(\mu\text{-}1,2\text{-}O_2^{2-})]^{2+}$ (**^{OMe}P**) and **^{H}P** based on their known extinction coefficients (**Figure S9**). Only $[(^{F5}BA)Cu^{II}(O_2^{\bullet-})]^{+}$ (**^{F5}S**), possessing electron-withdrawing groups on the ligand, forms a pure copper(II) superoxo species showing three primary absorption bands at 417, 600 and 748 nm with ε = 3500, 810 and 800 M^{-1} cm^{-1}, respectively (**Figure 4**).

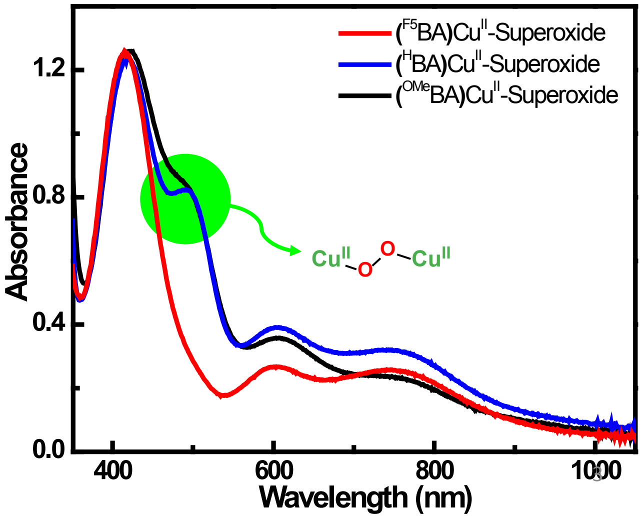

Figure 4. Low-temperature UV-vis absorption spectra of the reaction of **^{X}1** (X = OMe, H, and F5) with O_2 at –135 ºC in MeTHF (0.37 mM). The superoxo products **^{X}S**'s are observed after adding O_2 by bubbling for 40 s.

In continuing collaborations with the group of Prof. E. I. Solomon at Stanford University, rR spectroscopic studies were carried out on $[(^{F5}BA)Cu^{II}(O_2^{\bullet-})]^+$ (**^{F5}S**) (77 K, λ_{ex} = 413 nm) revealing two dioxygen isotope sensitive vibrations (**Figure 5**). An O-O vibration is observed at 1126 cm^{-1} as a single peak upon oxygenation by $^{16}O_2$ (**Figure 5B**, blue), while $^{18}O_2$ isotopic substitution exhibits two features (**Figure 5B**, red). This latter phenomenon is ascribed to a Fermi resonance between the $^{18}O_2$ vibration and a non-enhanced mode at similar energy. From the energy and intensity of the two observed mixed-modal features, the ^{18}O-^{18}O stretch was calculated to occur at 1062 cm^{-1}. Thus, we can say that O-O stretch shifted to lower energy by 64 cm^{-1} upon isotopic substitution, consistent with classical superoxo-bound mononuclear copper species. Notably, these values are higher than those found for tetradentate tmpa ligand-based cupric superoxo

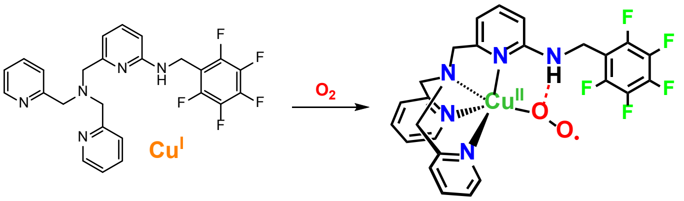

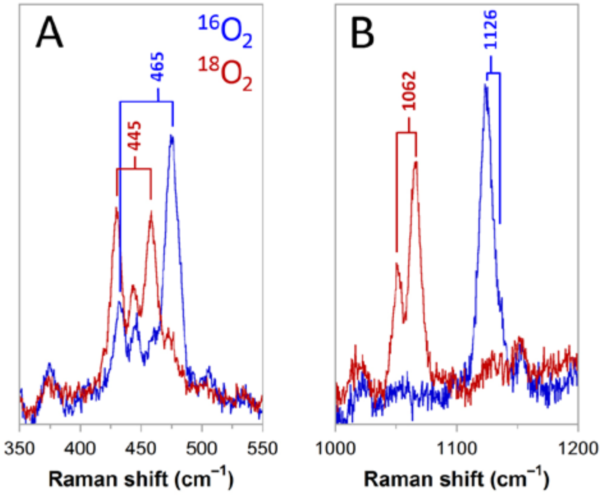

Figure 5. Solvent-subtracted resonance Raman spectra of complex **^{F5}S** (0.7 mM) measured in frozen MeTHF (77 K, λ_{ex} = 413 nm) showing A: ν(Cu–O) and B: ν(O–O) regions. Blue, $^{16}O_2$; red, $^{18}O_2$.

complexes with no hydrogen bond moiety (**Table 1**).[7, 8] An additional isotope sensitive vibrations attributed to the Cu-O stretch also showed two peaks with an intensity distribution that changed with isotope substitution at the lower-energy region as a result of a Fermi resonance. A Cu-^{16}O stretch occurs at 465 cm^{-1} which shifted to 445 cm^{-1} ($\Delta^{18}O_2$ = –20 cm^{-1}) with $^{18}O_2$.

Table 1. The redox potentials of LCu^{II} complexes and rR values of LCu^{II}($O_2^{\bullet-}$), where L is tmpa-based tripodal N_4 ligand.

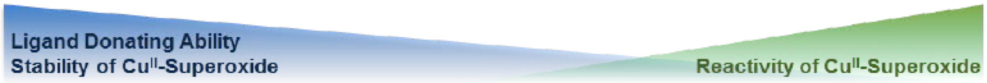
Ligand Donating Ability
Stability of Cu^{II}-Superoxide
Reactivity of Cu^{II}-Superoxide

Ligands	^{DMA}tmpa	^{DMM}tmpa	^{PV}tmpa	tmpa	^{H}BA [c]	^{F5}BA [c]
	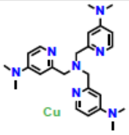	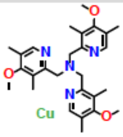	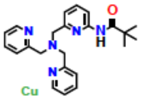	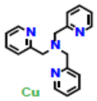	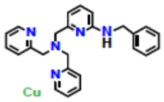	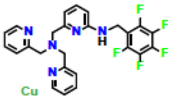
$E_{1/2}$ [a]	–700	–570	–520	–420	–350	–330
$\nu_{O\text{-}O}/\nu_{Cu\text{-}O}$ [b]	1121/472	1121/474	1130/482	1117/ -	1123/460	1126/465

[a] mV vs Fc$^{+/0}$, redox potentials of LCu^{II} complexes. [b] measured by rR spectroscopy. [c] This work.

4. Reactivity of [(^{X}BA)Cu^{II}($O_2^{\bullet-}$)]$^{+}$ (^{X}S) Complexes

Many synthetic cupric superoxo species have been investigated with respect to their reactivity toward small molecules such as C–H or O–H bond containing substrates.[6-12] Most of them are known to oxidize a very narrow range of substrates, possessing relatively weak C–H (e.g., 1-benzyl-1,4-dihydronicotinamide, BNAH, a NADH analog)[9] or O–H (e.g., *p*-substituted-2,6-di-*tert*-butylphenols, *p*-X-DTBP's) bond dissociation energies (BDEs).[7, 8, 10] Only one tridentate Cu^{II}($O_2^{\bullet-}$) complex, developed by Itoh and co-workers,[11] has been reported for its capability to hydroxylate an intramolecular benzylic position, or react with *para*-substituted phenols.[12] To obtain a broader perspective on how the hydrogen bonding effects the chemical properties of $[(^{X}BA)Cu^{II}(O_2^{\bullet-})]^+$ (**^{X}S**) complexes, the reactivity studies toward various substrates have been carried out (**Chart 2**). We find that the H-bond moiety of the BA ligand is able to stabilize $Cu^{II}(O_2^{\bullet-})$, and at the same time, enhance its reactivity.

Chart 2. O-H/C-H bond containing substrates utilized in the reactivity study.

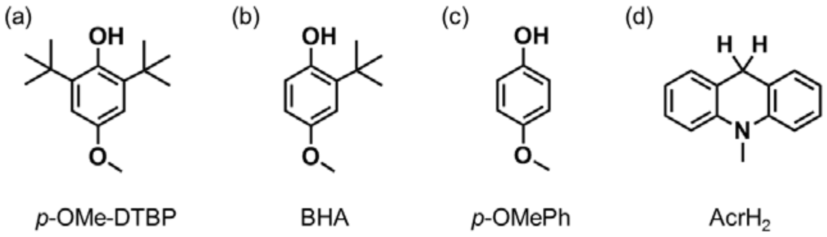
(a)
OH
O
p-OMe-DTBP
(b)
OH
O
BHA
(c)
OH
O
p-OMePh
(d)
H H
N
AcrH2

4.1 The Oxidation of Phenol Derivatives

The detailed reactivities and mechanism of the oxidation of the *para*-substituted-2,6-di-*tert*-butylphenol series (*p*-X-DTBP's) by copper(II) superoxo species have been

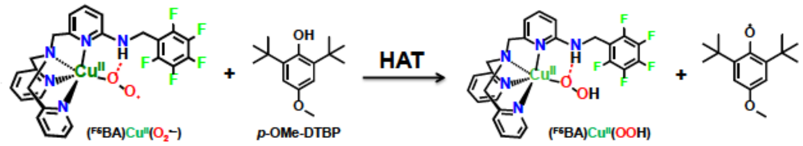
N
N
N
N
H
Cu^II
O
O
F
F
F
F
F
(F5BA)Cu^II(O2−)
+
OH
O
p-OMe-DTBP
HAT
OH
(F5BA)Cu^II(OOH)
+

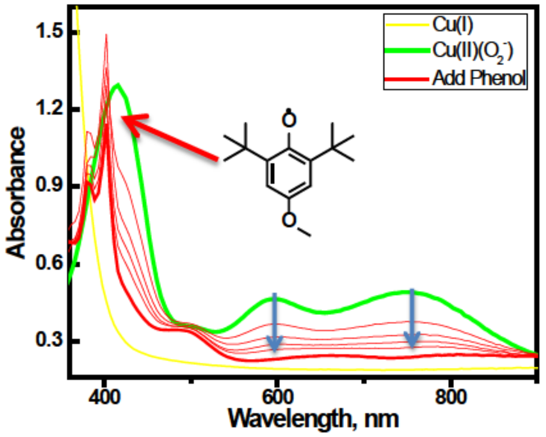

Figure 6. Low-temperature UV-vis absorption spectra of the reaction of ^{F5}**S** with 75 equiv *p*-OMe-DTBP at –135 °C in MeTHF (0.37 mM).

extensively investigated due to its readily oxidizable weak O–H BDE (e.g., 79.6 kcal mol^{-1} for *p*-OMe-DTBP[19]).[7, 8] To compare the $[(^{X}BA)Cu^{II}(O_2^{\bullet-})]^+$ complexes' (^{X}**S**'s) reactivity with previously reported synthetic tetradentate tmpa ligand-based cupric superoxide analogues,[7, 8] *p*-OMe-DTBP was utilized as substrate. When an excess of *p*-OMe-DTBP was added to the ^{X}**S** complexes, the distinctive phenoxyl radical absorption band was observed (**Figure 6**), indicating hydrogen atom abstraction occurs, which thus supports the mechanism previously proposed based on kinetic/thermodynamic results.[8] Compared to $Cu^{II}(O_2^{\bullet-})$ analogues without a hydrogen bond moiety, which do not react at the identical reaction conditions (–135 °C), ^{X}**S** shows enhanced reactivity toward *p*-OMe-DTBP, which is attributed to hydrogen bonding effect. The final organic product was identified as 2,6-di-*tert*-butyl-1,4-benzoquinone (DTBQ), using gas chromatography-mass spectrometry (GC-MS) (**Scheme 3**).

Scheme 3. Final major products of phenol oxidation reactions.

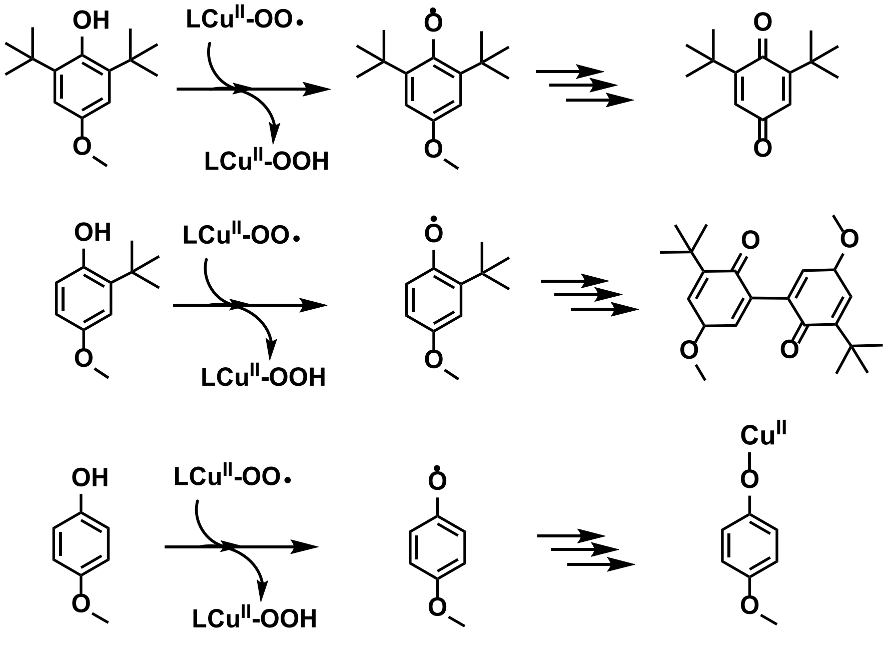

We also performed a reactivity study of $[(^{X}BA)Cu^{II}(O_2^{\bullet-})]^+$ ($^{X}\mathbf{S}$) utilizing the substrate 3-*tert*-butyl-4-hydroxyanisole (BHA). which contains fewer electron-donating substituents (**Chart 2**). As expected, the oxidation of BHA by $^{X}\mathbf{S}$'s was slower than the reaction with *p*-OMe-DTBP (**Table 2**) which is consistent with the larger O-H BDE (80.3 kcal mol^{-1}) reported for BHA.[20] The $[(^{F5}BA)Cu^{II}(O_2^{\bullet-})]^+$ ($^{F5}\mathbf{S}$) complex having electron-withdrawing groups on the ligand reacts faster than $^{OMe}\mathbf{S}$ or $^{H}\mathbf{S}$ complexes. A phenoxyl radical peak was detected only in the case of the reaction between $^{OMe}\mathbf{S}$ and BHA by UV-vis spectroscopy. Observed rate constants (k_{obs}'s) deduced from pseudo-first-order fitting are given in **Table 2**. The BHA has been known to undergo free radical mechanism affording dimer species (**Scheme 3**),[21] and that was the case in this reaction, as confirmed by GC-MS analysis.

Table 2. Physical properties of phenol derivatives and rate constants of reaction with $Cu^{II}(O_2^{\bullet-})$ complexes.

	p-OMe-DTBP	BHA	*p*-OMePh
BDE (kcal mol^{-1})	79.6	80.3	85.2
Redox Potential [a]	530 mV	570 mV	640 mV
$[(^{OMe}BA)Cu^{II}(O_2^{\bullet-})]^+$ ($^{OMe}\mathbf{S}$)	nd	5.72×10^{-3} s^{-1}	4.6×10^{-3} M^{-1}s^{-1}
$[(^{H}BA)Cu^{II}(O_2^{\bullet-})]^+$ ($^{H}\mathbf{S}$)	nd	1.03×10^{-2} s^{-1}	5.2×10^{-3} M^{-1}s^{-1}
$[(^{F5}BA)Cu^{II}(O_2^{\bullet-})]^+$ ($^{F5}\mathbf{S}$)	nd	1.90×10^{-2} s^{-1}	0.01 M^{-1}s^{-1}

[a] mV *vs* Fc$^+$/Fc.
nd – the reactions were too fast to be measured.

Furthermore, the findings in a reactivity study of $[(^{X}BA)Cu^{II}(O_2^{\bullet-})]^+$ ($^{X}\mathbf{S}$) complexes toward *para*-methoxyphenol (*p*-OMePh), possessing a comparably strong O-H BDE (85.2 kcal mol^{-1}),[19] implies that $^{X}\mathbf{S}$ complexes are better oxidants than previously described tripodal tetradentate N_4 $Cu^{II}(O_2^{\bullet-})$ species, those not possessing an internal potential H-bonding moiety.[7, 8] The kinetic studies were carried out by monitoring the disappearance of the 750 nm band of superoxo species at 138 K. The decay behaviors observed fit to pseudo-first-order kinetics and yield observed rate constants (k_{obs}'s) which were linear with respect to the substrate concentrations as shown in **Figure S13**. The second-order-rate constants (k_2's) were obtained as 4.6 x 10^{-3}, 5.2 x 10^{-3}, 0.01 M^{-1} s^{-1} for $^{\mathbf{OMe}}\mathbf{S}$, $^{\mathbf{H}}\mathbf{S}$, and $^{\mathbf{F5}}\mathbf{S}$, respectively (**Table 2**). As expected, the species $^{\mathbf{F5}}\mathbf{S}$ exhibits higher reactivity than other derivatives ($^{\mathbf{OMe}}\mathbf{S}$ or $^{\mathbf{H}}\mathbf{S}$) indicating that the substituents in the secondary coordination sphere affect the reactivity of $Cu^{II}(O_2^{\bullet-})$. Although no organic final product was observed from the GC-MS experiments, UV-vis spectra reveal that a copper(II)-phenolate species is produced upon warming, and that this is stable for weeks at room temperature. The same behavior was observed from the reaction of tridentate N_3 cupric superoxo system with *para*-substituted phenols, studied by Itoh and co-workers.[12] They suggested the reaction mechanism as depicted in **Scheme 4**, where release of dioxygen and hydrogen peroxide from the disproportionation of hydroperoxyl radical occurs.

Scheme 4. Itoh's proposed reaction mechanism.

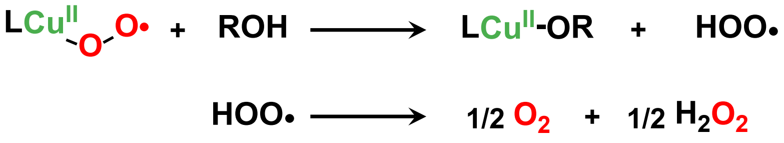

4.2 The Reaction with N-methyl-9,10-dihydroacridine (AcrH$_2$)

As a hydrogen atom source from a substrate with C─H bond, N-methyl-9,10-dihydroacridine (AcrH$_2$) was employed. The addition of AcrH$_2$ to the $[(^{X}BA)Cu^{II}(O_2^{\bullet-})]^+$ ($^{\mathbf{X}}\mathbf{S}$) solutions led to formation of radical species and *trans*-peroxo-dicopper(II) species, as monitored by UV-vis spectroscopy (**Figure S14**). The radical observed (as a high energy very sharp band at ~ 400 nm) is supposed to be the acridinyl radical This initial result suggests what what is occurring is similar to that observed for the case of $[(^{PV}tmpa)Cu^{II}(O_2^{\bullet-})]^+$ (**Figure 2c**),[9] which reacts with BNAH producing BNA^+ and the dicopper(II) *trans*-peroxo complex (**Scheme 5**). Further studies are required.

Scheme 5. Proposed pathways of the reaction of $Cu^{II}(O_2^{\bullet-})$ and NADH analogues.[9]

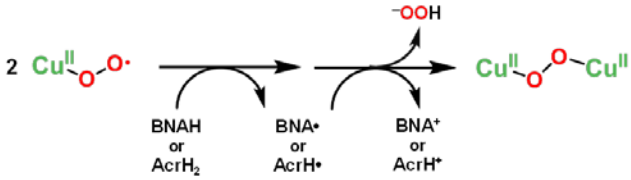

5. Conclusion

The new synthetic cupric superoxo complexes, $[(^{X}BA)Cu^{II}(O_2^{\bullet-})]^+$ (**^{X}S**), possessing tunable hydrogen bond moieties, have been generated and characterized. A hydrogen bond forming between the ligand N-H group and the proximal oxygen atom of ligated superoxide ion stabilizes the $Cu^{II}(O_2^{\bullet-})$ species and at the same time, enhanced their reactivity toward substrates. We suggest that when present, electron-withdrawing groups in the secondary coordination sphere of the **^{X}S** complex allow the Cu^{II}-superoxo complexes to be more electrophilic so that they act as a good hydrogen atom acceptor. The observance of radical species upon substrate reactions directly proves that copper(II) superoxo complexes are capable of hydrogen atom abstraction chemistry. Future experimental or computational studies are required to provide more details concerning the H-bonding to the superoxide moiety, as well as the *para*-benzyl substituent effects upon copper complex redox potentials and H-bonding.

6. References

1. Peterson, R. L.; Kim, S.; Karlin, K. D., In *Comprehensive Inorganic Chemistry II (Second Edition)*. Oxford: Elsevier: Amsterdam: 2013; pp 149-177, http://dx.doi.org/10.1016/B978-0-08-097774-4.00309-0.

2. Mirica, L. M.; Ottenwaelder X.; Stack T.D., *Chem. Rev.* 2004, *104* (2), 1013-1046.

3. Itoh, S., *Curr. Opin. Chem. Biol.* 2006, *10* (2), 115-122.

4. Hatcher, L.; Karlin, K., *J. Biol. Inorg. Chem.* 2004, *9* (6), 669-683.

5. Prigge, S. T.; Eipper, B. A.; Mains, R. E.; Amzel, L. M., *Science* 2004, *304* (5672), 864-867.

6. Würtele, C.; Gaoutchenova, E.; Harms, K.; Holthausen, M. C.; Sundermeyer, J.; Schindler, S., *Angew. Chem. Int. Ed.* 2006, *45*, 3867-3869; Woertink, J. S.; Tian, L.; Maiti, D.; Lucas, H. R.; Himes, R. A.; Karlin, K. D.; Neese, F.; Würtele, C.; Holthausen, M. C.; Bill, E.; Sundermeyer, J.; Schindler, S.; Solomon, E. I., *Inorg. Chem.* 2010, *49* (20), 9450-9459.

7. Maiti, D.; Fry, H. C.; Woertink, J. S.; Vance, M. A.; Solomon, E. I.; Karlin, K. D., *J. Am. Chem. Soc* 2006, *129* (2), 264-265.

8. Lee, J. Y.; Peterson, R. L.; Ohkubo, K.; Garcia-Bosch, I.; Himes, R. A.; Woertink, J.; Moore, C. D.; Solomon, E. I.; Fukuzumi, S.; Karlin, K. D., *J. Am. Chem. Soc* 2014, *136* (28), 9925-9937.

9. Peterson, R. L.; Himes, R. A.; Kotani, H.; Suenobu, T.; Tian, L.; Siegler, M. A.; Solomon, E. I.; Fukuzumi, S.; Karlin, K. D., *J. Am. Chem. Soc* 2011, *133* (6), 1702-1705.

10. Kim, S.; Lee, J. Y.; Cowley, R. E.; Ginsbach, J. W.; Siegler, M. A.; Solomon, E. I.; Karlin, K. D., *J. Am. Chem. Soc* 2015, *137* (8), 2796-2799.

11. Kunishita, A.; Kubo, M.; Sugimoto, H.; Ogura, T.; Sato, K.; Takui, T.; Itoh, S., *J. Am. Chem. Soc* 2009, *131* (8), 2788-2789.

12. Tano, T.; Okubo, Y.; Kunishita, A.; Kubo, M.; Sugimoto, H.; Fujieda, N.; Ogura, T.; Itoh, S., *Inorg. Chem.* 2013, *52* (18), 10431-10437.

13. Karlin, K. D.; Wei, N.; Jung, B.; Kaderli, S.; Zuberbuehler, A. D., *J. Am. Chem. Soc* 1991, *113* (15), 5868-5870.

14. Wada, A.; Harata, M.; Hasegawa, K.; Jitsukawa, K.; Masuda, H.; Mukai, M.; Kitagawa, T.; Einaga, H., *Angew. Chem. Int. Ed.* 1998, *37* (6), 798-799; Yamaguchi, S.; Masuda, H., *Sci. Technol. Adv. Mater.* 2005, *6* (1), 34-47.

15. Yamaguchi, S.; Wada, A.; Nagatomo, S.; Kitagawa, T.; Jitsukawa, K.; Masuda, H., *Chem. Lett.* 2004, *33* (12), 1556-1557.

16. Yamaguchi, S.; Nagatomo, S.; Kitagawa, T.; Funahashi, Y.; Ozawa, T.; Jitsukawa, K.; Masuda, H., *Inorg. Chem.* 2003, *42* (22), 6968-6970.

17. Yamaguchi, S.; Wada, A.; Funahashi, Y.; Nagatomo, S.; Kitagawa, T.; Jitsukawa, K.; Masuda, H., *Eur. J. Inorg. Chem.* 2003, *2003* (24), 4378-4386.

18. Kim, S.; Saracini, C.; Siegler, M. A.; Drichko, N.; Karlin, K. D., *Inorg. Chem.* 2012, *51* (23), 12603-12605.

19. Bordwell, F. G.; Zhang, X.-M., *J. Phys. Org. Chem.* 1995, *8* (8), 529-535.

20. Amorati, R.; Pedulli, G. F.; Valgimigli, L.; Johansson, H.; Engman, L., *Organic Letters* 2010, *12* (10), 2326-2329.

21. Kadoma, Y.; Ito, S.; Yokoe, I.; Fujisawa, S., *In Vivo* 2008, *22* (3), 289-296.

7. Supporting Information

7.1 Materials and Methods

7.1.1 General

All materials used were commercially available analytical grade from Sigma-Aldrich, ChemBridge and TCI chemicals. Acetone was distilled under an inert atmosphere over $CaSO_4$ and degassed under argon prior to use. Methylene chloride/Diethyl ether were used after being passed through a 60 cm long column of activated alumina (Innovative Technologies) under argon. Acetonitrile was stored under N_2 and purified via passage through 2 cm × 60 cm columns of activated alumina (Innovative Technologies Inc.). Inhibitor free tetrahydrofuran (THF) and 2-methyltetrahydrofuran (MeTHF) were purchased from Sigma-Aldrich and distilled under argon from sodium/ benzophenone and degassed with argon prior to use. Pentane was freshly distilled from calcium hydride under an inert atmosphere and degassed prior to use. $[Cu^I(CH_3CN)_4]B(C_6F_5)_4$ was synthesized according to literature protocols,[1] and its identity and purity were verified by elemental analysis and/or ^{1}H-NMR. Synthesis and manipulations of copper salts were performed according to standard Schlenk techniques or in an MBraun glovebox (with O_2 and H_2O levels below 1 ppm).

7.1.2 Instrumentation

Bench-top low temperature UV–visible experiments were carried out on a Cary Bio-50 spectrophotometer equipped with a liquid nitrogen chilled Unisoku USP-203-A cryostat using a 1 cm modified Schlenk cuvette. NMR spectroscopy was performed on Bruker 300 and 400 MHz instruments with spectra calibrated to either internal tetramethylsilane (TMS) standard or to a residual protio solvent. EPR measurements were performed on an X-Band Bruker EMX CW EPR controlled with a Bruker ER 041 XG microwave bridge operating at the X-band (~9 GHz) in 5 mm quartz EPR tubes. ESI-Mass spectra were acquired using a Finnigan LCQDeca ion-trap mass spectrometer equipped with an electrospray ionization source (Thermo Finnigan, San Jose, CA). Single Crystal X-ray Diffraction was performed on suitable crystals, which were mounted either on the tip of a glass fiber or on a loop with a tiny amount of Paratone-N oil and transferred to a N_2 cold stream (110(2) K). Resonance Raman (rR) Measurements. A stock solution of copper(I) complexes was prepared in MeTHF. A 500 μL aliquot of this copper(I) solution was added to the 5 mm NMR sample tube, capped with a septum, and chilled in a pentane/N_2(*l*) bath. Oxygenation of the copper samples was achieved by slowly bubbling an excess of dioxygen through the solution using a Hamilton gas-tight syringe equipped with a three-way valve and needle outlet. Dioxygen, $^{16}O_2$ (Airgas OX UHP-300) or $^{18}O_2$ (Icon 6393), was added to an evacuated Schlenk flask fitted with a septum for the oxygenation reactions described above. Resonance Raman spectra were collected on a triple monochromater (Spex 1877 CP with 1200, 1800, and 2400 grooves/mm holographic spectrograph gratings) with a back-illuminated CCD (Princeton Instruments ST-135). Samples were placed in a liquid nitrogen finger dewar (Wilmad) in a ~135° backscattering configuration and excitation was provided by an argon ion laser (Innova Sabre 25/7) and a krypton ion laser (Coherent I90C-K). Data were collected for 5 min at 20 mW of power and samples were hand spun for data collected at 380 nm. Peak positions were determined from fitting the experimental data with Gaussian transitions using Peakfit Version 4.

7.2 Synthesis of Ligands

All ^{X}BA series ligands are synthesized as in the literature[2] using *para*-substituted benzaldehydes.

^{OMe}BA, 6-((bis(pyridin-2-ylmethyl)amino)methyl)-N-(4-methoxybenzyl)-pyridin-2-amine. (85 % yield) (R_f = 0.8 at 100 % ethyl acetate). ^{1}H-NMR (400 MHz, $CDCl_3$): δ 8.52 (d, 2H), 7.64-7.62 (d, 4H), 7.40-7.36 (t, 1H), 7.12-7.11 (t, 2H), 6.90-6.76 (d, 3H), 6.24-6.22 (d, 1H), 4.42 (s, 2H), 3.90 (s, 4H), 3.80 (s, 3H), 3.71 (s, 2H).

^{F5}BA, 6-((((3,4-dihydropyridin-2-yl)methyl)(pyridin-2-ylmethyl)amino)methyl)-N-((perfluorophenyl) methyl)pyridin-2-amine. (78 % yield) (R_f = 0.6 at ethyl acetate: MeOH = 5:1). ^{1}H-NMR (400 MHz, $CDCl_3$): δ 8.50-8.49 (d, 2H), 7.65-7.58 (m, 4H), 7.41-7.37 (t, 1H), 7.13-7.10 (d, 2H), 6.87-6.85 (d, 1H), 6.33-6.31 (d, 1H), 4.92 (t, 1H), 4.65-4.63 (d, 2H), 3.86 (s, 4H), 3.69 (s, 2H). ESI-MS, *m*/*z*: 450.48 (L + H^+).

6.3 Synthesis of Copper (I)/(II) Complexes

$[(^{H}BA)Cu^{I}]B(C_6F_5)_4$ (**^{H}1**) and $[(^{H}BA)Cu^{II}(CH_3COCH_3)](ClO_4)_2$ (**^{H}2**) were synthesized as in the literature.[2]

$[(^{OMe}BA)Cu^{I}]B(C_6F_5)_4$ (^{OMe}1). In a 100 ml Schlenk flask in the glove box, 207 mg (0.228 mmol) of $[Cu^{I}(CH_3CN)_4]B(C_6F_5)_4$ were dissolved in 10 mL of THF. One equivalent of ^{OMe}BA ligand was dissolved in approximately 7 mL of THF were added to the copper solution yielding a pale yellow solution. This yellow solution was allowed to stir for 5 min at which time approximately 100 mL of degassed pentane were added to the copper(I) solution. After 40 min, the supernatant was decanted and the pale yellow oil removed from the glove box and dried under vacuum for 10 min affording yellow powder (70 % yield). Elemental analysis: ($C_{50}H_{27}BCuF_{20}N_5O$) Calculated: C (51.41), H (2.33), N (6.00); found: C (49.69), H (2.58), N (5.62). ^{1}H-NMR (400 MHz, THF-d_8): δ 8.70-8.68 (d, 2H), 7.94-7.89 (m, 2H), 7.50-7.42 (m, 5H), 7.24-7.22 (d, 2H), 6.86-6.83 (d, 2H), 6.60-6.52 (q, 2H), 4.52-4.50 (m, 2H), 4.40-4.04 (q, 4H), 4.02 (s, 2H), 3.76 (s, 3H).

[(^{F5}BA)Cu^{I}]B(C_6F_5)$_4$ (^{F5}1). 77 % yield. Elemental analysis: ($C_{49}H_{22}BCuF_{25}N_5$) Calculated: C (47.85), H (1.80), N (5.69); found: C (47.32), H (2.01), N (5.24). ^{1}H-NMR (400 MHz, THF-d_8): δ 8.71-8.69 (d, 2H), 7.97-7.91 (t, 2H), 7.52-7.46 (m, 4H), 7.41-7.36 (t, 1H), 6.60-6.58 (d, 1H), 6.49-6.47 (d, 1H), 4.70-4.68 (d, 2H), 4.56-4.50 (d, 2H), 4.00 (s, 3H), 3.93 (s, 1H).

[(^{OMe}BA)Cu^{II}(CH_3COCH_3)](ClO_4)$_2$ (^{OMe}2). 85 % yield. *Single crystals were obtained by slow diffusion of diethyl ether into a solution of the complex in acetone* (**Figure S5**). Elemental analysis: ($C_{29}H_{33}Cl_2CuN_5O_{10}$) Calculated: C (46.69), H (4.46), N (9.39); found: C (46.92), H (4.85), N (9.27). EPR spectrum (**Figure S1a**): X-band (ν = 9.186 GHz) spectrometer in acetone at 70 K: $g_{||} = 2.07$, $g_{\perp} = 2.22$, $A_{\perp} = 108$ G.

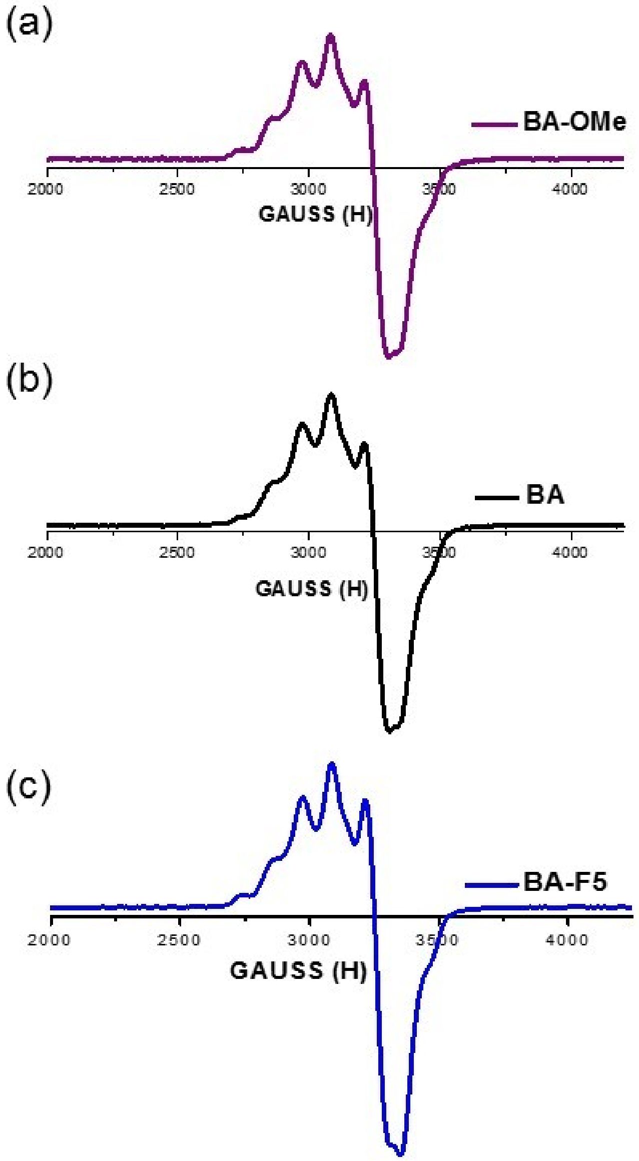

Figure S1. EPR spectra of ^{OMe}**2** and ^{F5}**2** complexes taken with an X-band spectrometer (ν = 9.186 GHz) in acetone at 70 K. Copper(II) complex concentration: 2 mM.

$[(^{F5}BA)Cu^{II}(CH_3COCH_3)](ClO_4)_2$ + $[(^{F5}BA)Cu^{II}(H_2O)](ClO_4)_2$ (^{F5}2). 69 % yield. *Single crystals were obtained by slow diffusion of diethyl ether into a solution of the complex in acetone* (**Figure S6**). Elemental analysis: ($C_{53}H_{52}Cl_4Cu_2F_{10}N_{10}O_{18}$) Calculated: C (40.39), H (3.33), N (8.89); found: C (40.44), H (3.35), N (8.65). EPR spectrum (**Figure S1b**): X-band (ν = 9.186 GHz) spectrometer in acetone at 70 K: $g_{||}$ = 2.07, $g_{\perp}$ = 2.22, $A_{\perp}$ = 108 G.

[(^{OMe}BA)Cu^{II}(N_3)]ClO_4 (^{OMe}3). To a acetone solution of [(^{OMe}BA)Cu^{II}(CH_3COCH_3)](ClO_4)$_2$ (^{OMe}**2**), one equivalent of sodium azide (NaN_3) solution in water was added. The immediate color change from blue to green indicates ligation of azide ion. The solution was filtered through cotton and single crystals were obtained by slow diffusion of pentane into a solution of the complex in acetone (**Figure S2**).

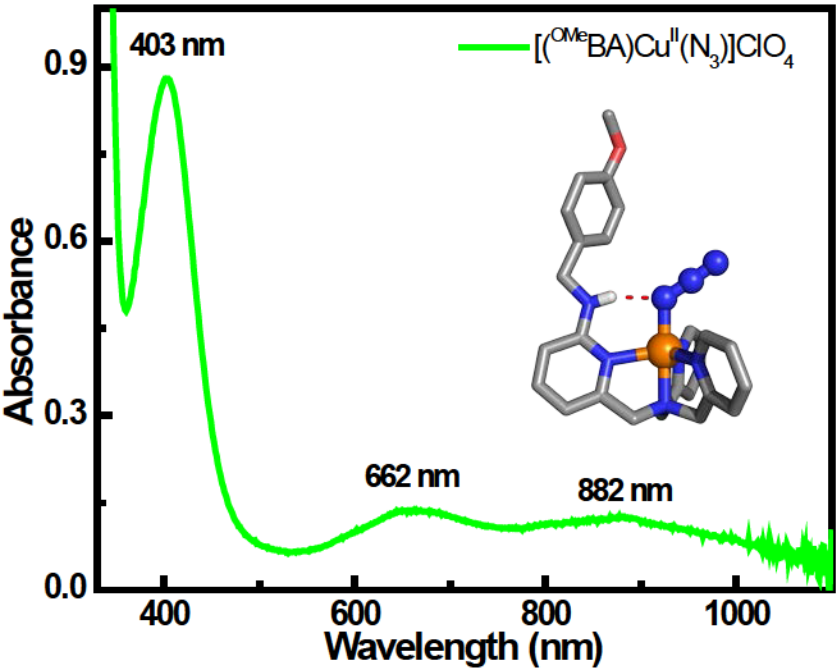

Figure S2. UV-vis spectrum of [(^{OMe}BA)Cu^{II}(N_3)]ClO_4 (^{OMe}**3**) At room temperature.

7.4 X-ray Crystallography

All reflection intensities were measured at 110(2) K using either a KM4/Xcalibur (detector: Sapphire3) with enhance graphite-monochromated Mo *K*α radiation (λ = 0.71073 Å) for $[(^{OMe}BA)Cu^{II}(CH_3COCH_3)](ClO_4)_2$, $[(^{Cl}BA)Cu^{II}(CH_3COCH_3)](ClO_4)_2$, and $[(^{OMe}BA)Cu^{I}]SbF_6$ or a SuperNova diffractometer (equipped with Atlas detector) with Cu *K*α radiation (λ = 1.54178 Å) for $[(^{F5}BA)Cu^{II}(CH_3COCH_3)(OClO_3)](ClO_4)$, $[(^{F5}BA)Cu^{I}]_2(SbF_6)_2$, and $[(^{OMe}BA)Cu^{II}(N_3)](ClO_4)$ under the program CrysAlisPro (Versions 1.171.34.44/1.171.33.55/1.171.36.32/ 1.171.37.31 Agilent Technologies, 2010-2014). The same program was used to refine the cell dimensions and for data reduction.. The structure was solved with the program SHELXS-97/2013 (Sheldrick, 2008) and was refined on F^2 with SHELXL-97/2013 (Sheldrick, 2008). Analytical numeric absorption correction based on a multifaceted crystal model was applied using CrysAlisPro. The temperature of the data collection was controlled using the system Cryojet (manufactured by Oxford Instruments). The H-atoms were placed at calculated positions (unless otherwise specified) using the instructions AFIX 23, AFIX 43, AFIX 123 or AFIX 137 with isotropic displacement parameters having values 1.2 or 1.5 times *U*eq of the attached C atoms.

[(^{OMe}BA)Cu^{I}]SbF$_6$: The structure is ordered. The absolute configuration was established by anomalous-dispersion effects in diffraction measurements on the crystal, and the flack parameter refines to 0.046(11) (Flack, 1983). Crystal data: Fw = 724.82, yellow block, 0.44 × 0.32 × 0.22 mm^3, monoclinic, *Cc* (no. 9), $a = 23.5199(4)$, $b = 8.88829(9)$, $c = 15.2449(3)$ Å, $\beta = 121.459(2)°$, $V = 2718.53(10)$ Å^3, $Z = 4$, $D_x = 1.771$ g cm^{-3}, $\mu = 1.847$ mm^{-1}, abs. corr. range: 0.542–0.725. 23096 Reflections were measured up to a resolution of (sin $\theta/\lambda)_{max} = 0.65$ Å^{-1}. 6193 Reflections were unique ($R_{int} = 0.0536$), of which 5926 were observed [$I > 2\sigma(I)$]. 363 Parameters were refined with 2 restraints. $R1/wR2$ [$I > 2\sigma(I)$]: 0.0260/0.0631. $R1/wR2$ [all refl.]: 0.0272/0.0634. S = 1.117. Residual electron density found between −0.60 and 0.50 e Å^{-3}.

[(^{OMe}BA)Cu^{I}]$^+$

Bond Lengths (Å)		Bond Angles (°)	
Cu-N1	2.004(3)	N1-Cu-N2	83.49(9)
Cu-N2	2.185(2)	N1-Cu-N3	116.30(10)
Cu-N3	2.011(2)	N1-Cu-N4	119.46(10)
Cu-N4	2.002(2)	N2-Cu-N3	83.03(9)
		N2-Cu-N4	82.47(9)
		N3-Cu-N4	119.84(10)

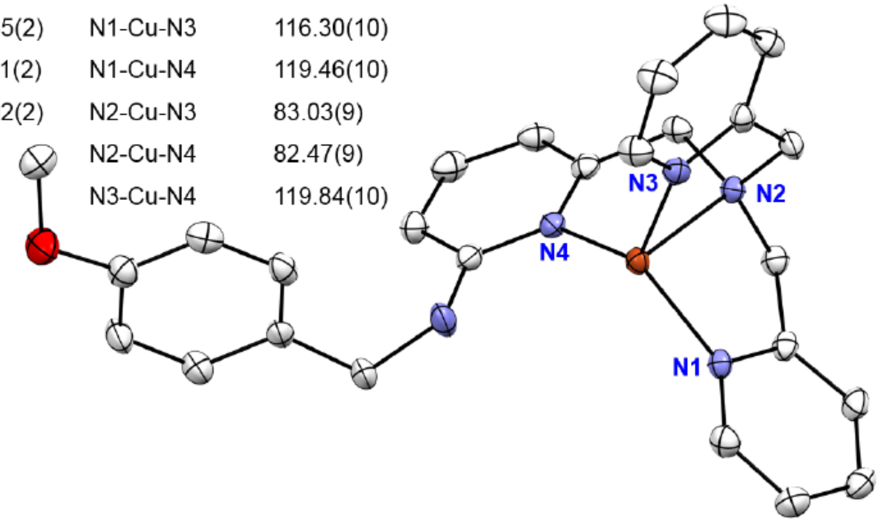

Figure S3. Displacement ellipsoid plot (50% probability level) of the cation [(^{OMe}BA)Cu^{I}]$^+$ at 110(2) K. H atoms are omitted for clarity. A list of relevant bond distances and angles is also provided.

[(^{F5}BA)Cu^I]$_2$: The asymmetric unit contains three crystallographically independent Cu^I dimers, seven SbF_6^- counterions (two of those are found at sites of inversion symmetry, and thus their occupancy factors are constrained to be 0.5), and two lattice diethylether solvent molecules (one molecule is fully occupied and the other molecule has an occupancy factor refining to 0.748(8)). The structure is partly disordered. Three of the seven counterions (Sb1, Sb4 and Sb6) are found to be disordered over two orientations. The occupancy factors of the major components of the disorder refine to 0.555(6) (Sb1), 0.5 (Sb4, constrained to be one half as this counterion is found at sites of inversion symmetry) and 0.633(7) (Sb6'). One counterion ion (Sb5) is disordered over three orientations, and the three occupancy factors refine to 0.741(2), 0.121(2) and 0.1380(19). Two of the three crystallographically dimers are also found partially disordered: two $-C_6F_5$ groups (C20A/G$\rightarrow$F5A/G and C20E/H$\rightarrow$F5E/H) and one $-CH_2C_6F_5$ (C19F/I$\rightarrow$F5F/I) group are disordered over two orientations, and the occupancy factors of the major components refine to 0.831(9), 0.720(15), and 0.538(6), respectively. Some electron density in the asymmetric unit – *i.e.*, some amount of disordered acetone solvent molecules with partial occupancy – has been taken out in the final refinement (SQUEEZE details are provided in the CIF file). The crystal that was mounted on the diffractometer was non-merohedrally twinned. The diffraction patterns of components 1 and 2 are related by a twofold axis around the vector 0.0000a* - 0.7071b* + 7071c*. Data integration of both components was performed using CrysAlisPro (Version 1.171.37.31 Agilent Technologies, 2014), and a HKLF 5 file was made. In order to perform the SQUEEZE procedure, the detwinning option was set in SHELXL-2013 via a LIST 8 style FCF. The BASF scale factor refines to 0.2896(5). Crystal data: Fw = 1612.69, small orange-yellow block, 0.27 × 0.13 × 0.12

mm^3, triclinic, P-1 (no. 2), a = 19.8184(3), b = 23.5255(4), c = 23.9366(3) Å, α = 112.2691(15), β = 106.5181(13), γ = 102.1115(14) °, V = 9245.5(3) Å^3, Z = 6, D_x = 1.738 g cm^{-3}, μ = 8.667 mm^{-1}, abs. corr. range: 0.232–0.504. 105437 Reflections were measured up to a resolution of $(\sin \theta/\lambda)_{max}$ = 0.62 Å^{-1}. 42032 Reflections were unique (R_{int} = 0.0322), of which 34974 were observed [$I > 2\sigma(I)$]. 3039 Parameters were refined using 2918 restraints. $R1/wR2$ [$I > 2\sigma(I)$]: 0.0433/0.1087. $R1/wR2$ [all refl.]: 0.0505/0.1117. S = 0.986. Residual electron density found between −1.00 and 1.45 e Å^{-3}.

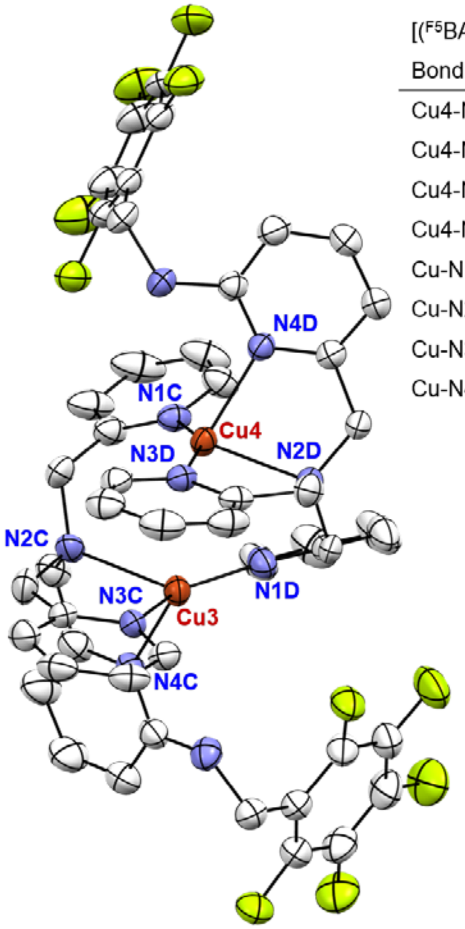

$[(^{F5}BA)Cu^{I}]_2^{2+}$

Bond Lengths (Å)		Bond Angles (°)	
Cu4-N1C	1.953(4)	N4D-Cu4-N1C	101.08(17)
Cu4-N2D	2.223(4)	N4D-Cu4-N3D	99.41(16)
Cu4-N3D	1.980(4)	N4D-Cu4-N2D	76.66(16)
Cu4-N4D	2.195(4)	N1C-Cu4-N3D	150.06(19)
Cu-N1D	1.955(4)	N1C-Cu4-N2D	123.61(19)
Cu-N2C	2.241(4)	N3D-Cu4-N2D	82.33(18)
Cu-N3C	1.974(4)	N2C-Cu3-N1D	124.38(19)
Cu-N4C	2.202(4)	N2C-Cu3-N3C	83.46(17)
		N2C-Cu3-N4C	75.91(17)
		N1D-Cu3-N3C	148.7(2)
		N1D-Cu3-N4C	102.37(18)
		N3C-Cu3-N4C	98.05(17)

Figure S4. Displacement ellipsoid plot (50% probability level) of the cation $[(^{F5}BA)Cu^{I}]_2^{2+}$ at 110(2) K. H atoms are omitted for clarity. A list of relevant bond distances and angles is also provided. **References**: Sheldrick, G. M. (2008). *Acta Cryst.* A64, 112-122; Flack, H.D. (1983). *Acta Cryst.* A39, 876-881.

$[(^{OMe}BA)Cu^{II}(CH_3COCH_3)](ClO_4)_2$: The structure is mostly ordered. One of the two perchlorate counterions is found to be disordered over two orientations. The occupancy factor for the major component of the disorder refines to 0.676(6). The coordinates and the isotropic temperature factor of the H atom located on N5 (*i.e.*, H5) were refined freely. The distances N5−H5 was restrained to be 0.88(3) Å. Crystal data: Fw = 746.04, blue thick lath, $0.55 \times 0.38 \times 0.14$ mm^3, triclinic, P-1 (no. 2), $a = 10.30467(12)$, $b = 12.82297(16)$, $c = 13.46088(15)$ Å, $\alpha = 74.6747(10)$, $\beta = 76.6381(10)$, $\gamma = 69.2379(11)°$, $V = 1585.30(3)$ Å^3, $Z = 2$, $D_x = 1.563$ g cm^{-3}, $\mu = 0.923$ mm^{-1}, T_{min}–T_{max}: 0.671–0.897. 35137 Reflections were measured up to a resolution of $(\sin \theta/\lambda)_{max} = 0.65$ Å^{-1}. 7310 Reflections were unique ($R_{int} = 0.0542$), of which 6505 were observed [$I > 2\sigma(I)$]. 471 Parameters were refined with 136 restraints. $R1/wR2$ [$I > 2\sigma(I)$]: 0.0332/0.0933. $R1/wR2$ [all refl.]: 0.0373/0.0954. S = 1.046. Residual electron density found between −0.56 and 0.44 e Å^{-3}.

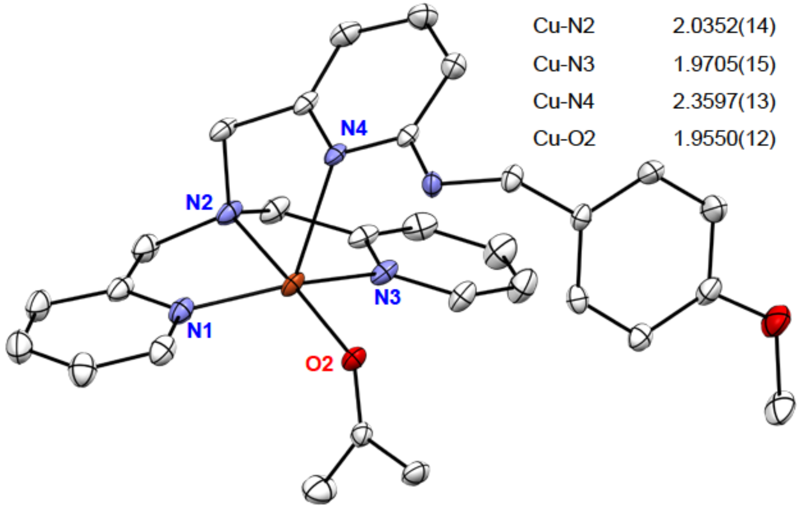

$[(^{OMe}BA)Cu^{II}(CH_3COCH_3)]^{2+}$

Bond Lengths (Å)		Bond Angles (°)	
Cu-N1	1.9812(15)	N1-Cu-N2	83.23(6)
Cu-N2	2.0352(14)	N1-Cu-N3	158.68(6)
Cu-N3	1.9705(15)	N1-Cu-N4	110.27(5)
Cu-N4	2.3597(13)	N1-Cu-O2	96.33(5)
Cu-O2	1.9550(12)	N2-Cu-N3	84.58(6)
		N2-Cu-N4	82.06(5)
		N2-Cu-O2	177.37(5)
		N3-Cu-N4	85.19(5)
		N3-Cu-O2	95.05(5)
		N4-Cu-O2	100.51(5)

Figure S5. Displacement ellipsoid plot (50% probability level) of the cation $[(^{OMe}BA)Cu^{II}(CH_3COCH_3)]^{2+}$ at 110(2) K. H atoms are omitted for clarity. A list of relevant bond distances and angles is also provided.

[(^{F5}BA)Cu^{II}(CH$_3$COCH$_3$)(OClO$_3$)](ClO$_4$): The structure is ordered. The H atom attached to N5 was found from difference Fourier map, and its coordinates and isotropic temperature factor were refined freely. Crystal data: Fw = 805.98, blue block, 0.18 × 0.15 × 0.12 mm^3, monoclinic, $P2_1/c$ (no. 14), a = 20.0003(2), b = 10.59484(12), c = 15.22292(19) Å, β = 99.1402(12)°, V = 3184.78(6) Å^3, Z = 4, D_x = 1.681 g cm^{-3}, μ = 3.338 mm^{-1}, T_{min}-T_{max}: 0.651–0.733. 21345 Reflections were measured up to a resolution of (sin $\theta/\lambda)_{max}$ = 0.62 Å^{-1}. 6240 Reflections were unique (R_{int} = 0.0225), of which 5812 were observed [$I > 2\sigma(I)$]. 456 Parameters were refined. $R1/wR2$ [$I > 2\sigma(I)$]: 0.0274/0.0717. $R1/wR2$ [all refl.]: 0.0297/0.0737. S = 1.018. Residual electron density found between −0.49 and 0.55 e Å^{-3}.

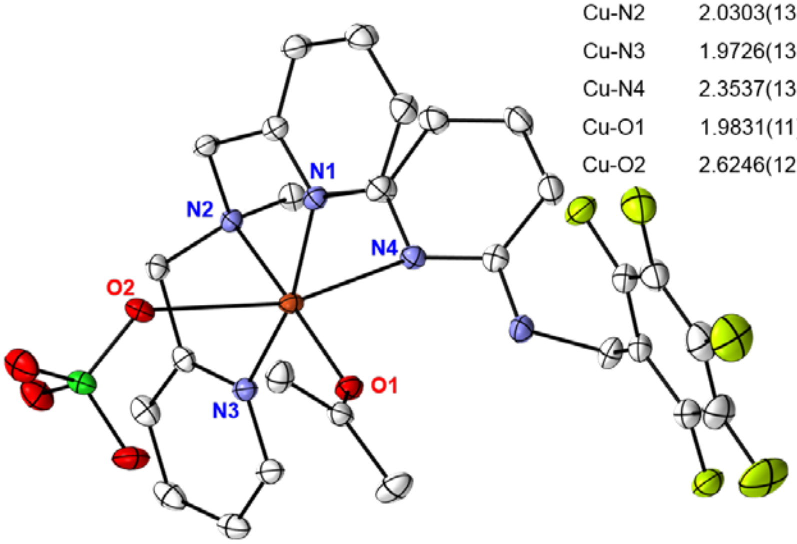

[(^{F5}BA)Cu^{II}(CH$_3$COCH$_3$)(OClO$_3$)]$^+$

Bond Lengths (Å)		Bond Angles (°)	
Cu-N1	1.9957(13)	N1-Cu-N2	84.24(5)
Cu-N2	2.0303(13)	N1-Cu-N3	166.05(6)
Cu-N3	1.9726(13)	N1-Cu-N4	82.55(5)
Cu-N4	2.3537(13)	N1-Cu-O1	98.51(5)
Cu-O1	1.9831(11)	N1-Cu-O2	88.32(4)
Cu-O2	2.6246(12)	N2-Cu-N3	82.81(5)
		N2-Cu-N4	82.24(5)
		N2-Cu-O1	177.20(5)
		N2-Cu-O2	83.20(4)
		N3-Cu-N4	100.77(5)
		N3-Cu-O1	94.49(5)
		N3-Cu-O2	85.03(4)
		N4-Cu-O1	97.58(5)
		N4-Cu-O2	163.51(4)

Figure S6. Displacement ellipsoid plot (50% probability level) of the cation [(^{F5}BA)Cu^{II}(CH$_3$COCH$_3$)(OClO$_3$)]$^+$ at 110(2) K. H atoms are omitted for clarity. A list of relevant bond distances and angles is also provided.

[(${}^{\mathrm{OMe}}$BA)Cu$^{\mathrm{II}}$(N$_3$)](ClO$_4$): The structure is partly disordered. The perchlorate counterion is found to be disordered over three orientations, and the occupancy factors of the three components of the disorder refine to 0.660(3), 0.207(3) and 0.133(2). The crystal lattice contains some amount of lattice solvent molecules (acetone). In the asymmetric unit, one molecule is found at sites of inversion symmetry, and its occupancy factor is constrained to be 0.5. The H atom attached to N5 was found from difference Fourier map, and its coordinates and isotropic temperature factor were refined freely.

Specified hydrogen bonds (with esds except fixed and riding H)

D-H	H...A	D...A	<(DHA)	
0.85(2)	2.06(2)	2.877(3)	162(2)	N5-H5...N6

Crystal data: Fw = 659.58, green lath, 0.38 × 0.24 × 0.09 mm^3, monoclinic, $P2_1/c$ (no.14), a = 8.9508(3), b = 15.9140(6), c = 20.6679(9), β = 100.984(4)°, V = 2890.1(2) Å^3, Z = 4, D_x = 1.516 g cm^{-3}, μ = 0.904 mm^{-1}, $T_{\min}$–$T_{\max}$: 0.779–0.932. 22613 Reflections were measured up to a resolution of $(\sin \theta/\lambda)_{\max}$ = 0.65 Å^{-1}. 6635 Reflections were unique (R_{int} = 0.0328), of which 5598 were observed [$I > 2\sigma(I)$]. 506 Parameters were refined using 424 restraints. $R1/wR2$ [$I > 2\sigma(I)$]: 0.0383/0.0921. $R1/wR2$ [all refl.]: 0.0491/0.0975. S = 1.105. Residual electron density found between -0.49 and 0.42 e Å^{-3}.

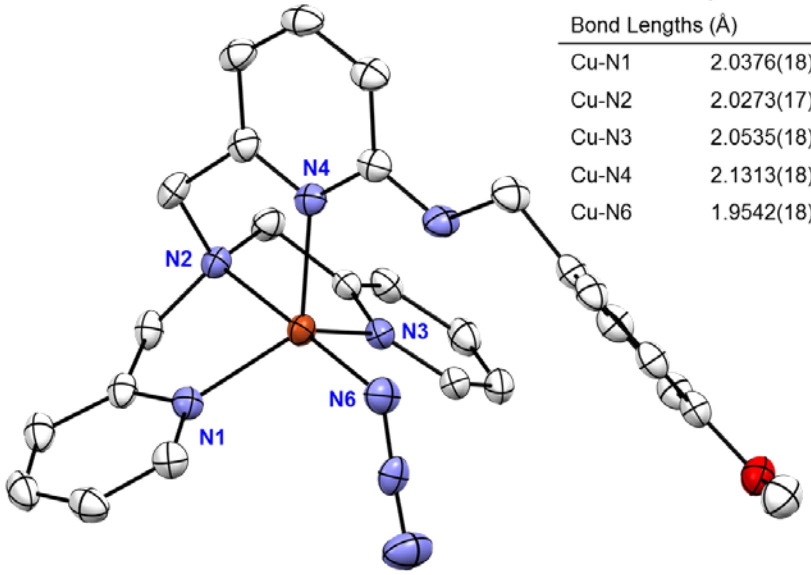

$[(^{OMe}BA)Cu^{II}(N_3)]^+$

Bond Lengths (Å)		Bond Angles (°)	
Cu-N1	2.0376(18)	N1-Cu-N2	81.83(7)
Cu-N2	2.0273(17)	N1-Cu-N3	126.77(7)
Cu-N3	2.0535(18)	N1-Cu-N4	117.51(7)
Cu-N4	2.1313(18)	N1-Cu-N6	97.30(8)
Cu-N6	1.9542(18)	N2-Cu-N3	82.08(7)
		N2-Cu-N4	81.04(7)
		N2-Cu-N6	179.04(8)
		N3-Cu-N4	109.44(7)
		N3-Cu-N6	98.79(8)
		N4-Cu-N6	99.03(7)

Figure S7. Displacement ellipsoid plot of the cation $[(^{OMe}BA)Cu^{II}(N_3)]^+$ at 110(2) K. H atoms are omitted for clarity. A list of relevant bond distances and angles is also provided.

Reference: Sheldrick, G. M. (2008). Acta Cryst. A64, 112-122.

7. 5 Cyclic Voltammetry (CV) Data

Ligand-Cu^{II} complexes (~ 1 mM) were employed for cyclic voltammetric measurements. CV measurements were undertaken in freshly distilled acetonitrile using a BAS 100B electrochemical analyzer with a glassy carbon working electrode and a platinum wire auxiliary electrode. Potentials were recorded versus a Ag/AgNO$_3$ electrode. The voltammograms are plotted *versus* the Fe(Cp)$_2^{+/0}$ potential which was measured as an external standard. Scans were run at 50 mV/s under Ar atmosphere using ca. 0.1 M [Bu$_4$N][PF$_6$] as the supporting electrolyte.

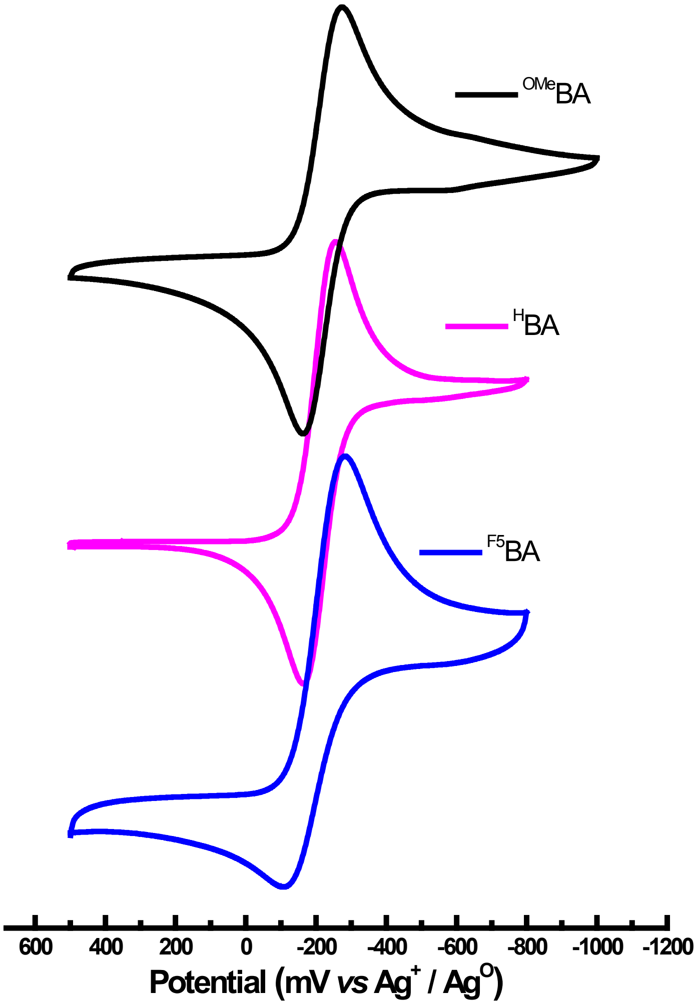

Figure S8. Cyclic voltammograms for copper(II) complexes in CH$_3$CN (mV *vs*. [Fe(Cp)$_2$]$^{+/0}$).

7.6 Oxygenation of a $[(^{DMA}N_3S)Cu^I]^+$ (1) in MeTHF at -50 °C

In the glove box, 0.1 mM solution of $[(^{X}BA)Cu^I]B(C_6F_5)_4$ (^{X}**1**, X = F5, H, OMe) was prepared in a 2.5 mL MeTHF, and the 1 cm Schlenk cuvette was sealed with a rubber septum. Out of the glove box and the cuvette was secured with a copper wire. The cell was transferred to the pre-cooled cryostat and chilled at –50 °C with a minimum of 15 minutes allowed for equilibration prior to oxygenation. The dioxygen was gently bubbled through the solution using long needle for 15 seconds forming a $[\{(^{X}BA)Cu^{II}\}_2\,(O_2^{2-})]^{2+}$ (^{X}**P**).

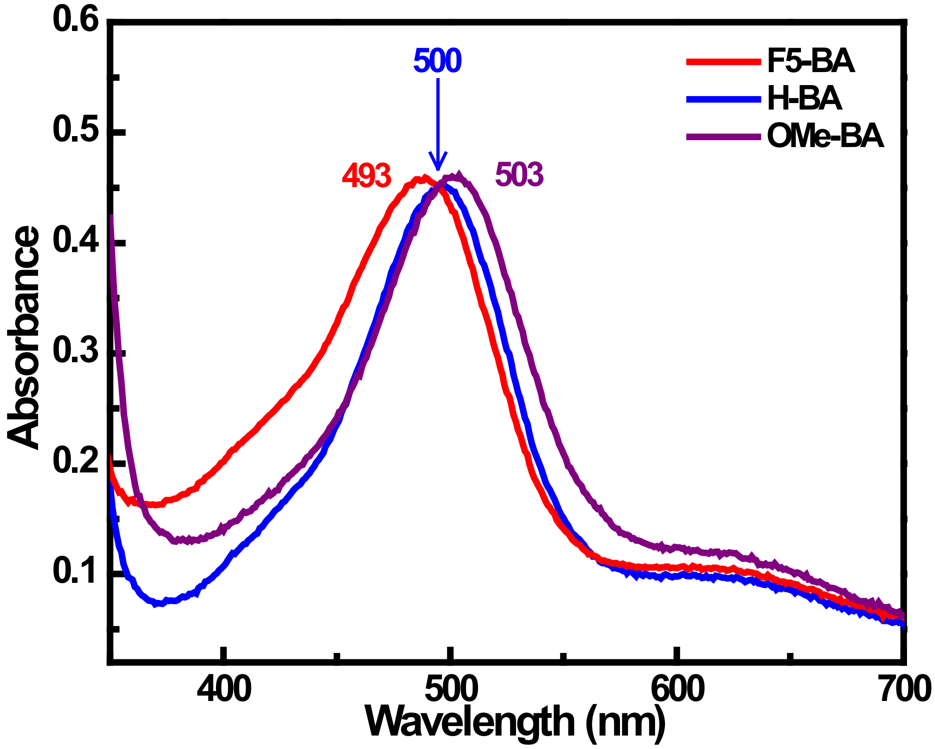

Figure S9. Low-temperature UV-vis absorption spectra of the reaction of ^{X}**P** (X=OMe, H, and F5) with O_2 at –50 °C in MeTHF (0.1 mM).

7.7 Resonance Raman (rR) Data

The resonance Raman spectrum of $[(^{H}BA)Cu^{II}(O_2^{\bullet-})]^{+}$ (**^{H}S**) (**Figure S9**, 77 K, 413 nm) shows two overlapping features in the O-O stretching region with an isotope-dependent intensity distribution (~3:1 with $^{16}O_2$; ~2:3 with $^{18}O_2$), consistent with Fermi resonances of both ν(^{16}O–^{16}O) and ν(^{18}O–^{18}O) with a nonenhanced mode at similar energy and of the same symmetry. From the energies and intensities of the two mixed-mode features (**Figure S10a**), the pre-interaction energy of ν(^{16}O–^{16}O) was calculated to be 1123 cm^{-1} (ν(^{18}O–^{18}O) = 1059; Δ = -64 cm^{-1}). The ν(Cu-O) region also showed a Fermi resonance in each isotopologue, and a similar analysis (**Figure S10b**) revealed ν(Cu-^{16}O) at 460 cm^{-1} (ν(Cu-^{18}O) = 443 cm^{-1}, Δ = -17 cm^{-1}).

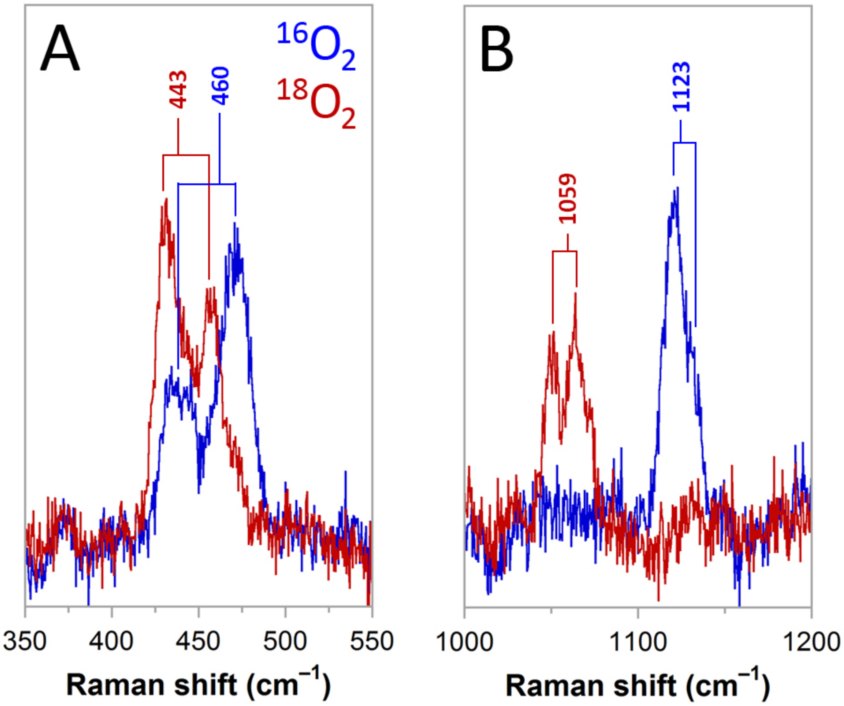

Figure S10. Solvent-subtracted resonance Raman spectra of MeTHF solutions of (BA)CuO$_2$ (77 K, λ_{ex} = 413 nm) showing the (A) ν(Cu–O) and (B) ν(O–O) regions.

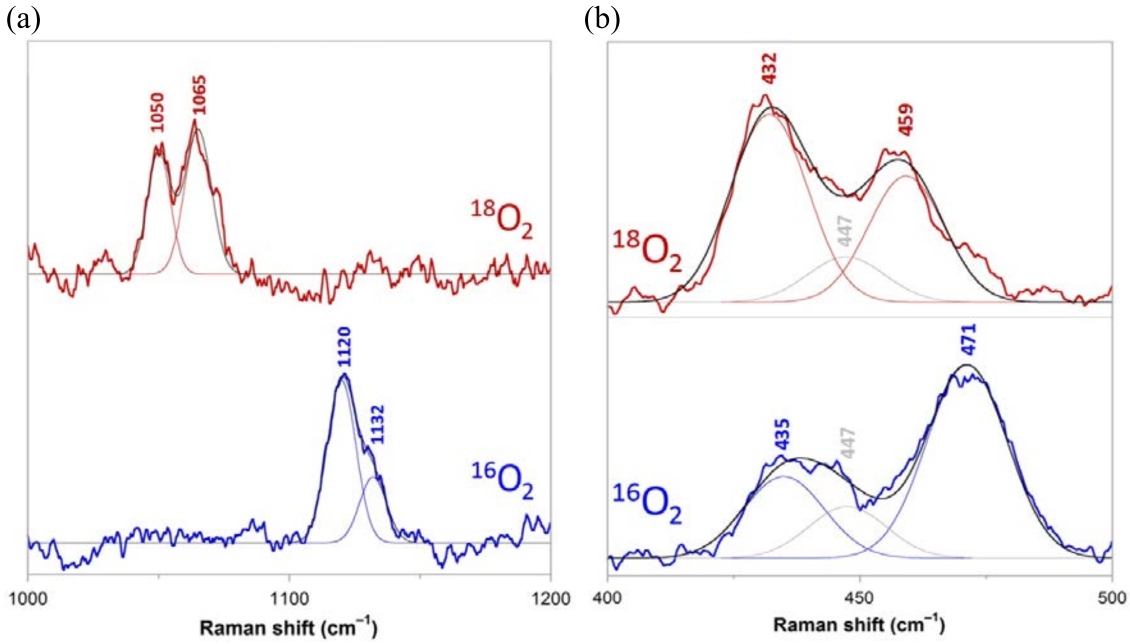

Figure S11. Gaussian fit of the two Fermi-mixed (a) ν(O-O) modes of $[(^{H}BA)Cu^{II}(O_2^{\bullet-})]^+$ (**^{H}S**) (relative intensities 72:28 ($^{16}O_2$) and 42:58 ($^{18}O_2$)), and (b) ν(Cu-O) modes (relative intensities 70:30 ($^{16}O_2$)). An isotope-insensitive feature occurs at 447 cm^{-1}.

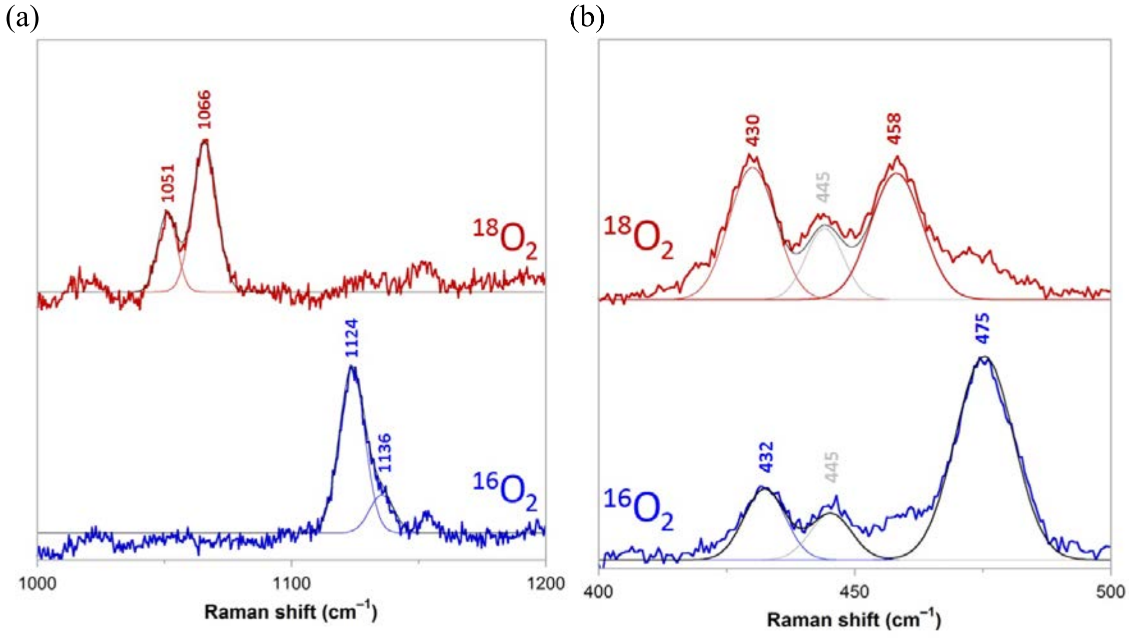

Figure S12. Gaussian fits of the two Fermi-mixed (a) ν(O-O) modes of $[(^{F5}BA)Cu^{II}(O_2^{\bullet-})]^+$ (**^{F5}S**) (relative intensities 82:18 ($^{16}O_2$) and 29:71 ($^{18}O_2$)) and (b) ν(Cu-O) modes (relative intensities 75:25 ($^{16}O_2$) and 53:47 ($^{18}O_2$)). An isotope-insensitive feature occurs at 445 cm^{-1} in the spectra.

7.8 Reactivity Study

In the glove box, 0.37 mM solution of $[(^{X}BA)Cu^{I}]B(C_6F_5)_4$ (^{X}**1**) was prepared in a 2.5 mL MeTHF, transferred to a 1 cm Schlenk cuvette and the cuvette was sealed with a rubber septum. Out of the glove box the cuvette was secured with a copper wire. The cell was transferred to the pre-cooled cryostat and chilled at –135 °C with a minimum of 15 minutes allowed for equilibration prior to oxygenation. The dioxygen was gently bubbled through the solution using long needle for 40 seconds forming $[(^{X}BA)Cu^{II}(O_2^{\bullet-})]^+$ (^{X}**S**). Reactivity studies were initiated by the addition of a stock solution of substrates to the fully generated ^{X}**S**. Pseudo-first-order rate plots were performed by observing the disappearance of 750 nm band to obtain k_{obs}'s from plots of ln $[(A - A_f)/(A_i - A_f)]$ *vs* time(s). Second-order-rate constants were obtained from the linear plots of k_{obs}'s against the substrate concentration (**Figure S13**).

(a)

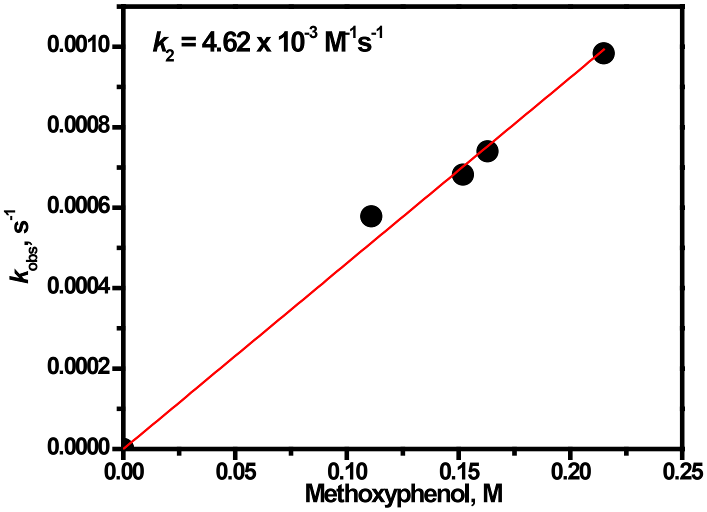

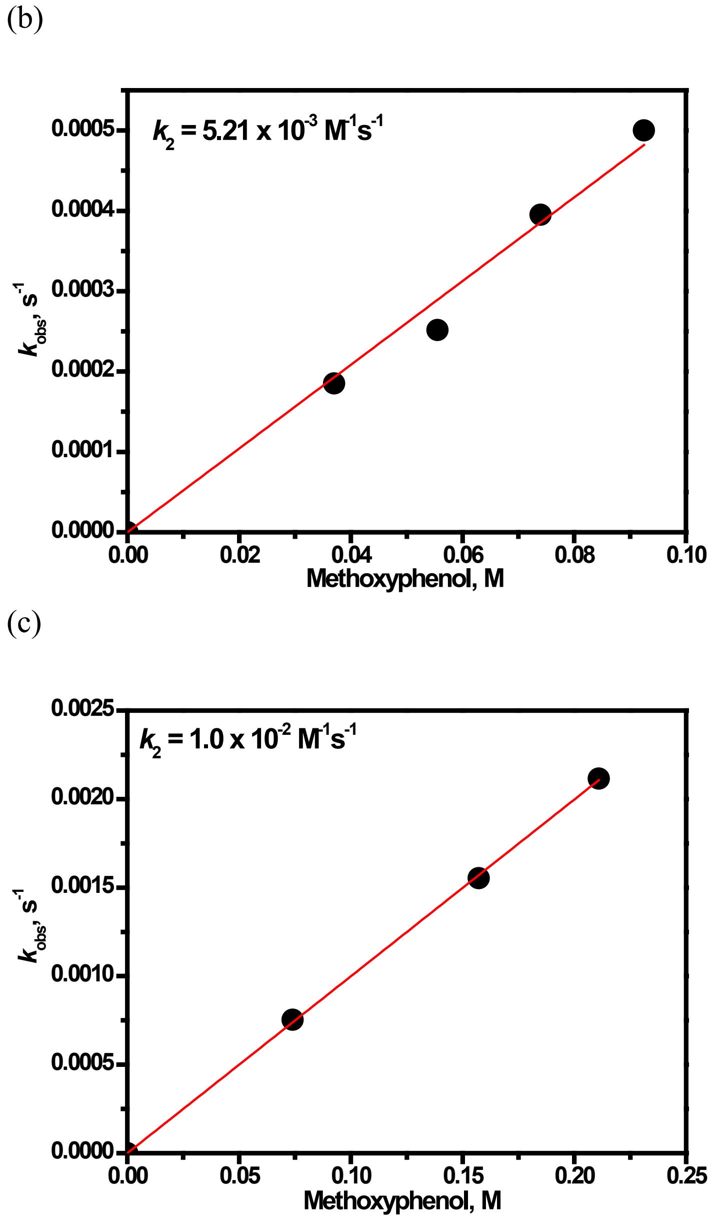

Figure S13. Plots of k_{obs}'s against the concentrations of *p*-OMePh for the reaction of (a) $[(^{OMe}BA)Cu^{II}(O_2^{\bullet-})]^+$ ($^{\mathbf{OMe}}\mathbf{S}$), (b) $[(^{H}BA)Cu^{II}(O_2^{\bullet-})]^+$ ($^{\mathbf{H}}\mathbf{S}$), and (c) $[(^{F5}BA)Cu^{II}(O_2^{\bullet-})]^+$ ($^{\mathbf{F5}}\mathbf{S}$).

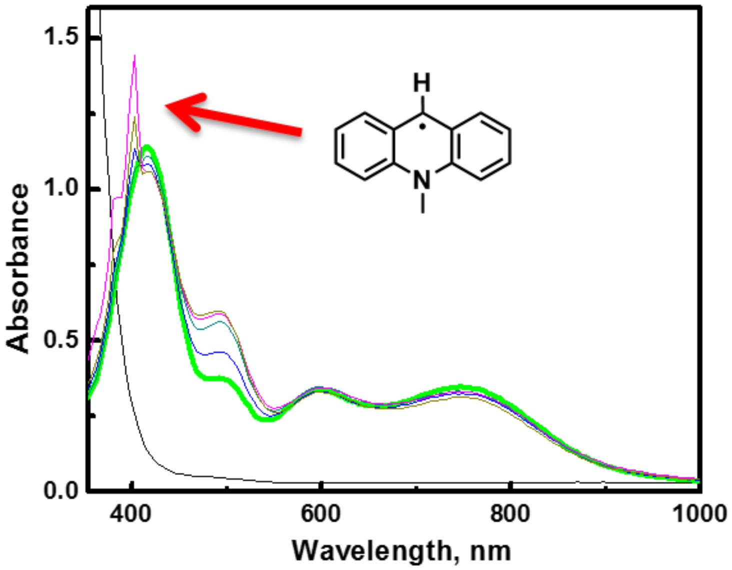

Figure S14. UV-vis spectra for the reaction of [(^{F5}BA)Cu^{II}($O_2^{\bullet-}$)]$^+$ (**^{F5}S**) and 125 equiv N-methyl-9,10-dihydroacridine ($AcrH_2$) affording generation of radical species (most likely the acridinyl radical) and *trans*-peroxo dicopper(II) complexes.

7.9 References

(1) Liang, H.-C.; Kim, E.; Incarvito, C. D.; Rheingold, A. L.; Karlin, K. D. *Inorg. Chem.* **2002**, *41*, 2209.

(2) Kim, S.; Saracini, C.; Siegler, M. A.; Drichko, N.; Karlin, K. D., *Inorg. Chem.* **2012**, *51*, 12603.

Chapter 5:

Dioxygen-Derived Copper Species Ligated by His-Braced Peptide Ligands

This work was accomplished with the aid of the following collaborators:

Jake W. Ginsbach, Zakaria Halime, Edward I. Solomon, and Kenneth D. Karlin

Abstract

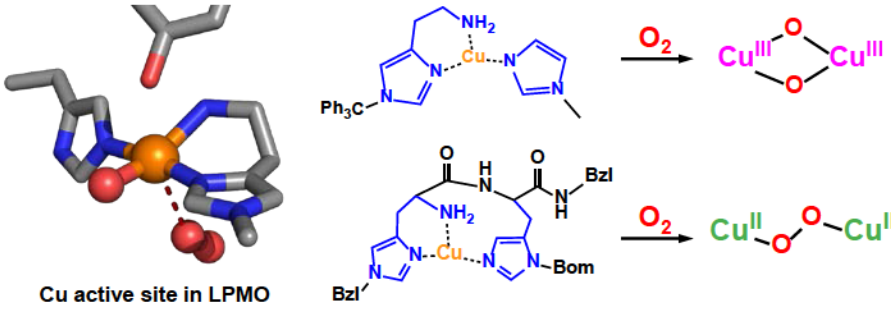
Cu active site in LPMO
NH$_2$
Cu
N
N
N
N
Ph$_3$C
O$_2$
Cu^{III}
O
O
Cu^{III}
O
H
N
O
Bzl
N
H
NH$_2$
N
N
Cu
N
N
Bom
Bzl
O$_2$
Cu^{II}
O
O
Cu^{II}

As many enzymatic X-ray crystallographic studies reveal a unique ‘His-brace’ coordination environment at copper active sites in various lytic polysaccharide monooxygenases (LPMOs), the necessity for synthetic copper-histidine complexes has been apparent, in order to elucidate their physical/chemical properties and oxidative chemistry. Thus, a new dipeptide and histamine ligands mimicking the ‘His-brace’ moiety have been developed. Oxygen-derived copper species coordinated by these ligands are determined as (*trans*-peroxo)Cu^{II}_2 and (bis-μ-oxo)Cu^{III}_2 complexes based on UV-vis and resonance Raman spectroscopies.

1. Introduction

Metal-peptide model systems have for some time aroused the special interests of (bio)chemists since almost all the ligands at copper active sites of metalloproteins are amino acids – more often tyrosine, histidine, methionine and cysteine (**Figure 1**). In particular, histidine (His) is the most important ligand commonly found in almost all copper-containing enzymes.

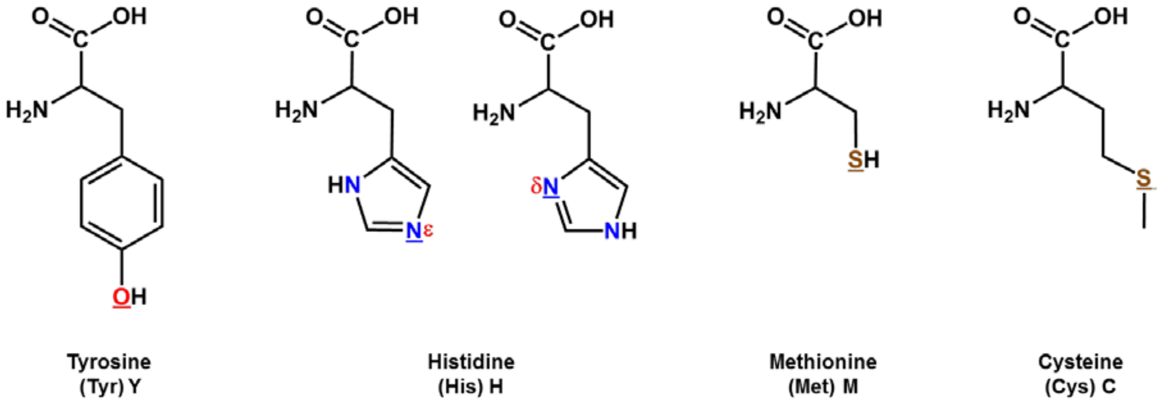

Figure 1. Amino acids commonly found at copper active site as ligand donors. Donor atoms are colored and underlined.

X-ray crystallographic studies of copper enzymes reveal that many copper ions at active sites are ligated by histidine-containing dipeptide or tripeptide motifs. The imidazole group of histidine ligands can bind to copper active sites through either δN_{His} or εN_{His} nitrogen atoms, see **Figure 1**. For example, the catalytic Cu_M or Cu_B active site of peptidylglycine-α-hydroxylating monooxygenase (PHM) and dopamine-β-monooxygenase (DβM) bind to εN_{His} and εN_{His} sites of two histidines and a methionine[1] while Cu_H or Cu_A electron-transfer center is coordinated by three δN_{His} sites (**Table 1**). The monocopper center of particulate methane monooxygenase (pMMO) is ligated by two

Table 1. Binding sites of His's at Cu centers in enzymes.

Enzymes	Cu active sites	Binding sites of histidines
PHM (DβM)	Cu_H (Cu_A)	δ, δ, δ
	Cu_M (Cu_B)	ε, ε
pMMO	Monocopper	δ, δ
	Dicopper	δ, ε for one/ δ with N-termini for another
SOD		δ, ε
LPMOs		ε, δ with N-termini

histidines through a bidentate $\delta N_{His}\delta N_{His}$ binding motif, while the dicopper active site contains one copper ion binding to δN_{His} and εN_{His} positions and the second copper ion chelated by an N-terminal histidine referred to as a 'His-brace': the δN_{His} and the amino terminus ($-NH_2$) (**Figure 2b**)[2-4] as an asymmetrical motif.[4-6] The binding motif with δN_{His} and εN_{His} sites is also observed in copper-zinc superoxide dismutase (CuZn-SOD) associated with Lou Gehrig's disease.[2,7] Very recent enzymatic studies exhibit that lytic polysaccharide monooxygenases (LPMOs) possess a mononuclear Cu center that binds to a His via εN imidazole ligation plus a His-brace (**Figure 2a**).[8,9,10] These three nitrogen donors form a nearly T-shaped coordination.[11] Some biochemists[12] suggest the pMMO active site may contain only one copper, coordinated by the His-brace and one another His residue as in LPMOs (**Figure 2a**), since closer examination of the dicopper centers of pMMO in X-ray structures reveals two very tilted Cu-N_{His} bonds (with the Cu-N vector reaching far out of the plane of the imidazole ring), not reasonable for inorganic coordination structures. Furthermore, although it is not relevant to the Cu/O_2 chemistry, there is a copper resistance protein CopC, a copper carrier involved in copper homeostasis, which displays 'His-brace' chelation (**Figure 2c**).[13]

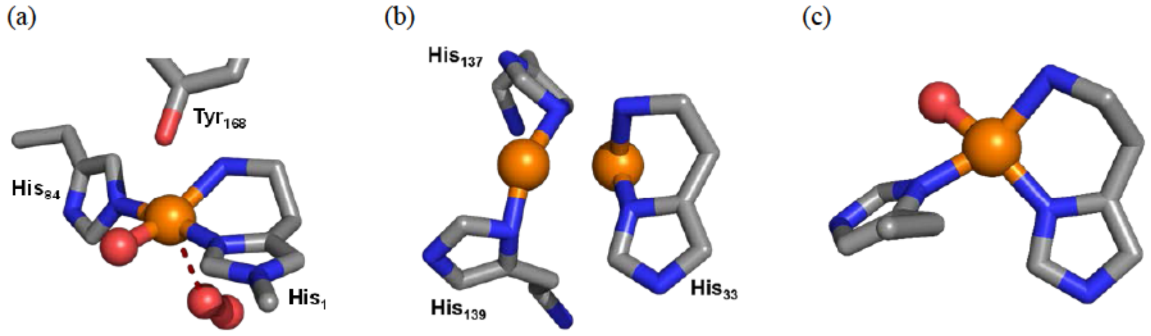

Figure 2. (a) Copper active site of one of the lytic polysaccharide monooxygenase proteins in the cellulose-active fungal AA9 group (PDB: 4EIR)[10]. A putative superoxide moiety is observed at 3.0 Å from the Cu center. (b) Dicopper active sites found in pMMOs (PDB: 1YEW)[2]. (c) Structure of CopC (copper resistance protein, bacterial blue copper protein, copper carrier) (PDB: 2C9Q)[13]

The regioselectivity, the imidazole tautomeric preferences, involved in the binding to the copper ion, are critical in determining the functions and properties of the enzymes because of differences in decisive steric and/or electronic effects, proximity to other His ligands, the ability to deprotonate the N-H bond and other factors. However, there are only very few model studies in the literature which address the chemistry associated with copper(I) or copper(II) in different histidine binding mode.[14] Thus, structural and associated physical-spectroscopic, reactivity toward O_2 and H_2O_2, as well as redox behavior of varying copper-peptide systems, are important topics to investigate.

In fact, the Karlin group has previously reported studies on Cu^I complexes of both modified histidylhistidine dipeptide[15] and His-Gly-His tripeptides[16] showing that a switch in the imidazole tautomer can radically influence the reactivity of a Cu(I) center. Both dipeptides (δN_{His} vs εN_{His} availability) adopt a linear two-coordinate N_{His}-Cu^I-N_{His} environment and copper complex coordinated by two δN_{His} shows redox behavior only when additional imidazole is added. The results provided a detailed understanding for the functioning of the Cu_H electron-transfer site of PHM. Accordingly, it has been reported that copper complex coordinated by two εN_{His} sites of HGH tripeptides exhibits redox behavior and oxidative chemistry toward O_2 and H_2O_2, while Cu^I ligated by a δN_{His}-Gly-δN_{His} tripeptide does not show reactivity with small molecules.

Yet, it is less well understood how this unique 'His-brace' moiety affects copper centers' chemical/physical properties or reactivities toward small molecules; O_2 or H_2O_2. Only recently, Stack and co-workers contributed to develop oxygen-derived copper species coordinated by a bidentate ligands including a primary amine (-NH_2) which affords dicopper(III) bis-μ-oxo species.[18] Both experimental and computational studies lead to conclusions that the small –NH_2 ligand allows for strong Cu-N bonding relative to –NR_2 and achievement of Cu high-valency. Also, the small –NH_2 ligand also allows a substrate to approach to the (bis-μ-oxo)Cu_2^{III} species. More recently, the group found that the ligands are further exchanged upon addition of histamine which indicates (bis-μ-oxo)Cu_2^{III} complexes coordinated by histamine are thermodynamically more stable than those ligated by primary amines (See below).[19]

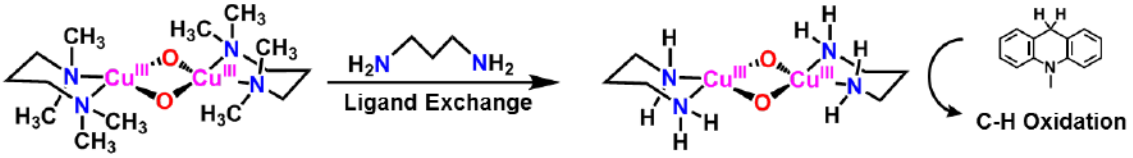

Figure 3. A high-valent dicopper(III) species **O** ligated by the primary amine, 1,3-propylenediamine, is capable of H-atom abstraction from the C–H bond in 9,10-dihydromethylacridine.

Since pMMO contains an asymmetric dicopper active site, two different mixed-valent bis(μ-oxo)$Cu^{II}Cu^{III}$ and (μ-oxo)(μ-hydroxo)$Cu^{II}Cu^{III}$ formulations have been suggested as intermediates which have enhanced reactivity; those conclusions are based on computational chemistry results..[4, 6, 20, 21, 22] However, neither species has ever been directly synthesized or identified, thus such entities remain as important synthetic targets.

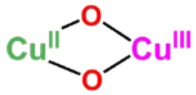

bis(μ-oxo)Cu^{II}Cu^{III}

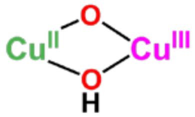

(μ-oxo)(μ-hydroxo)Cu^{II}Cu^{III}

Here, in this chapter, new peptide ligands which mimic His-braced copper active sites have been designed and synthesized. With resulting biomimetic copper complexes, characterization and reactivity studies, for example Cu^I/O_2, Cu^I/H_2O_2 interactions, studies on Cu-oxygen species added to acids/substrates will be carried out in order to understand their properties and oxidative chemistry. The overall goal is to elucidate the O_2-and oxidative chemistry of copper ion in these particular 'His-brace' coordination environments.

2. Cu-dipeptide Complex Chemistry

2.1 Dipeptide Ligand Design

A new dipeptide ligand (NδHεH) (**Chart 1**) was designed based on the coordination environment found at the copper active center in lytic polysaccharide monooxygenases (LPMOs), which can be chelated by one histidine with an available site at the δ position, plus N-terminal primary amine group and the other histidine with available coordination to the nitrogen at the ε position, as stated above (**Figure 2a**). The NδHεH ligand contains three possible 'N'-atom donors to Cu ion, where the C-terminus group is protected by benzyl amino group to avoid any likelihood of terminal group carboxylate Cu-coordination. Starting from the left side of the ligand diagram (**Chart 1**), each εN_{His} and δN_{His} binding sites of imidazole groups are specifically blocked using benzyl (Bzl) and benzyloxymethyl acetal (Bom) protecting groups, respectively, thus the other (δN_{His} and εN_{His}) sites are available for metal coordination. (See Supporting Information for synthesis.) The Cu^I complexes of peptide ligands featuring the 'N-brace' have been generated and investigated for elucidation of their physical/chemical properties.

Chart 1. The ligands utilized in this study; NδHεH (left) and BocδHεH (right). Nitrogen donors are underlined.

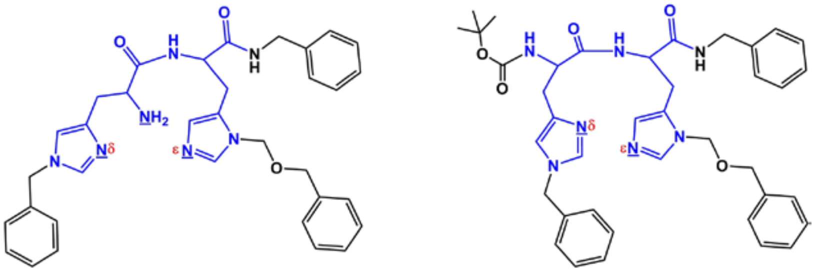

2.2 Oxygen-Derived Copper Species in Different Solvent Systems

The $[(N\delta H\varepsilon H)Cu^I]^+$ complex forms different oxygen-derived copper species upon oxygenation in different solvents. Bubbling $O_{2\,(g)}$ into a tetrahydrofuran (THF) solution of $[(N\delta H\varepsilon H)Cu^I]^+$ at –100 ºC led to the slow formation of a new species (**Cpd A**) with two distinctive absorption bands; λ_{max} = 454 and 608 nm with $\varepsilon_{apparent}$ = 2500 and 1200 $M^{-1}cm^{-1}$, respectively (**Figure 3a**) (Note: ε values assume a binuclear Cu complex formulation of **Cpd A**, but are given per/copper; thus irrespective of the formulation $\varepsilon = Abs./[Cu_{initial}]$ (assuming a one cm pathlength for the absorption experiment). The new dark green **Cpd A** complex was stable for hours at at –100 ºC. In 2-methyltetrahydrofuran (MeTHF) at –135 ºC, **Cpd A** forms quickly, apparently being the first species to form, but then it converts to an another new species, **Cpd B**, featuring a bright green color in solution (λ_{max} = 349 nm, 1140 M^{-1}cm^{-1} and 580 nm **Figure 3b**). In acetone as a much more polar solvent, **Cpd A** was not observed, only the bright green species was generated which is presumed to be **Cpd B** (λ_{max} (sh) = 344 and 570 nm, 1280 and 110 M^{-1}cm^{-1}, **Figure 3c**). Electron paramagnetic resonance (EPR) spectroscopic studies reveal that both **Cpd A** and **Cpd B** are EPR silent (**Figure S1**). Thus, those species can be presumed to be either dicopper or mononuclear copper(II) superoxo complexes.

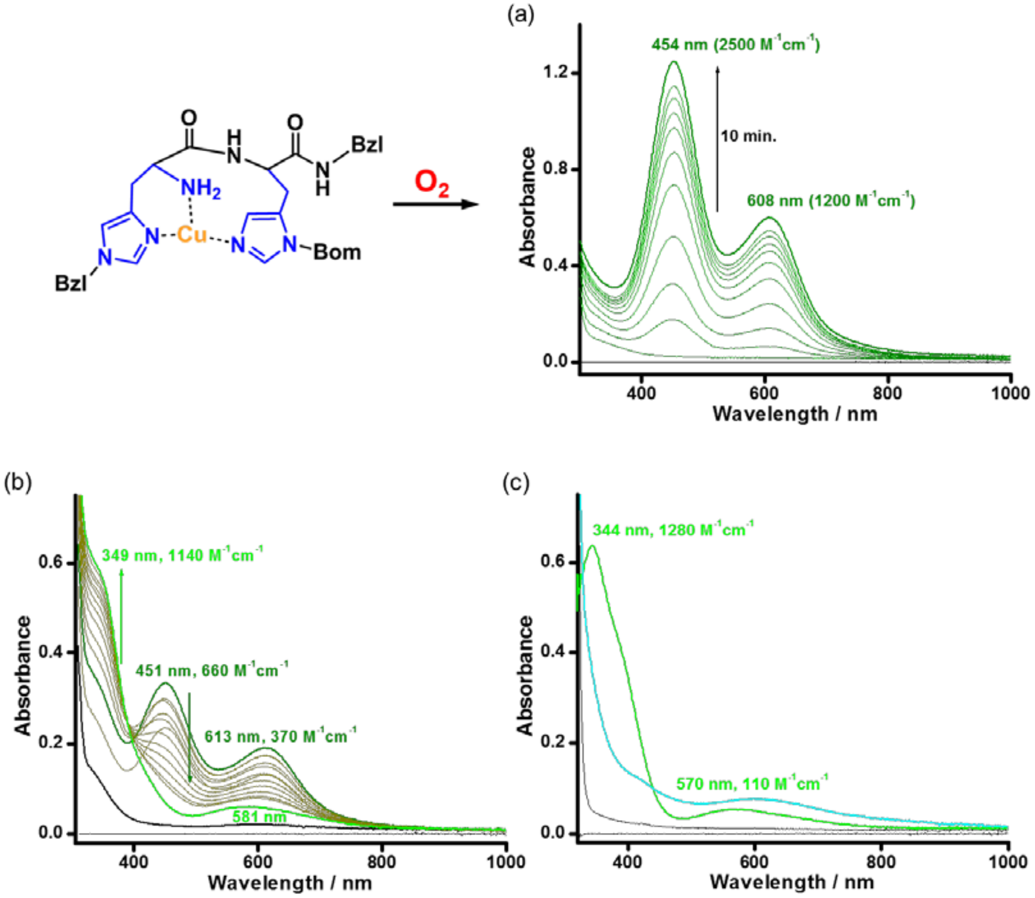

Figure 4. Low-temperature UV-vis absorption spectra of the oxygenated products of [(NδHεH)Cu^{I}]$^{+}$ species in (a) THF at –100 °C forming **Cpd A** (final most absorbing green line spectrum); (b) MeTHF at –135 °C showing conversion of **Cpd A** (dark green lines) to **Cpd B** bright lighter green line spectrum; the black spectrum is that for the starting Cu(I) complex; and (c) **Cpd B** (green line) in acetone at –90 °C, the aqua blue line spectrum is that obtained after warmup to RT.

Cpd A was characterized by resonance Raman (rR) spectroscopy and could be assigned as being an end-on *trans*-peroxo dicopper(II) species, formulated as $[\{(N\delta H\varepsilon H)Cu^{II}\}_2(\mu\text{-}1,2\text{-}O_2^{2-})]^{2+}$. Laser excitation of oxygenated samples of **Cpd A** yielded an O-O stretch observed at 815 cm^{-1} which shifted to lower energy (771 cm^{-1}) upon isotopic substitution using $^{18}O_2$ (**Figure 4b**). These parameters closely match those known for many $(\mu\text{-}1,2\text{-}O_2^{2-})Cu^{II}_2$ complexes; they are well precedented.[23] However, the intense characteristic charge-transfer bands are blue-shifted and the apparent absorptivity (ε) values calculated (vide supra) are extremely low compared to most literature values. For example, the originally characterized end-on *trans*-peroxo dicopper complex, $[\{(tmpa)Cu^{II}\}_2(\mu\text{-}1,2\text{-}O_2^{2-})]^{2+}$ (tmpa = tris(2-pyridylmethyl)amine), has an absorptivity of 11550 M^{-1} cm^{-1} for the strongest charge-transfer transition, that at 525 nm.

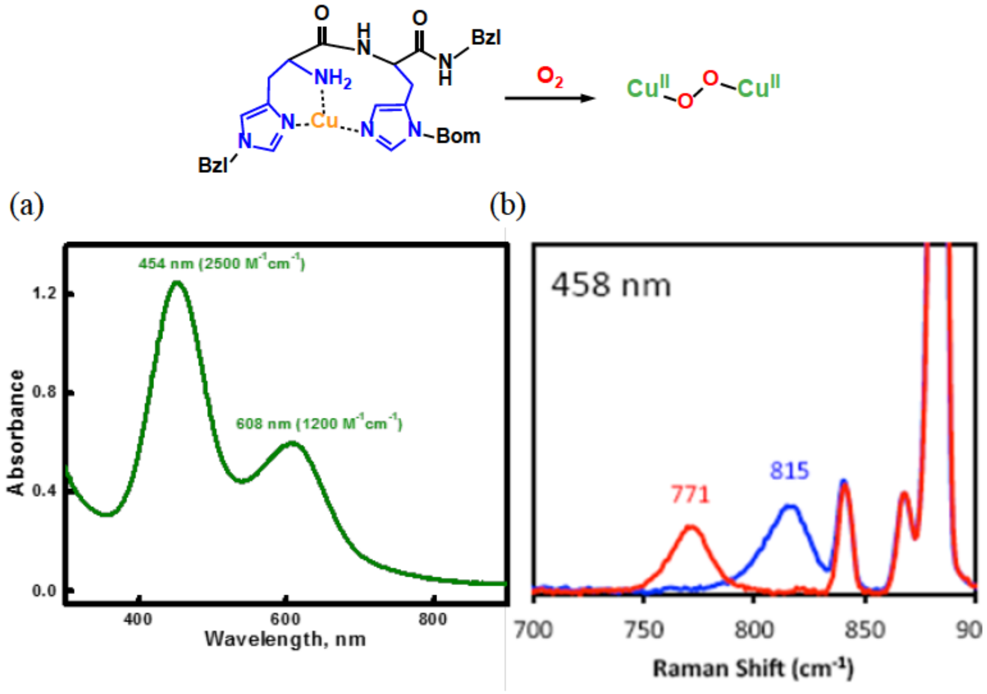

Figure 5. (a) Low-temperature UV-vis absorption spectrum of the oxygenated products of $[(N\delta H\varepsilon H)Cu^{I}]^{+}$ species Cpd A in THF at –100 °C and (b) resonance Raman spectra λ_{ex} = 458 nm.

To understand whether the N-termini (–NH_2) moiety has an effect on Cu^I/O_2 chemistry, a dipeptide analog with no primary amine also has been synthesized (BocδHεH, **Chart 1**). The –NH_2 group was protected by *tert*-butyloxycarbonyl (Boc) group so that the ligand has only two possible nitrogen donors for copper ion; δN_{His} and εN_{His} bonding sites. The BocδHεH ligand was metallated and the Cu^I complex was isolated to study its oxidative chemistry. The oxygenated copper(I) complex does not form *trans*-peroxo species (**Cpd A**). It forms a metastable species which is presumed to be **Cpd B** or something else. From this simple control experiment, we are able to assume that N-termini plays an important role in its dioxygen reactivity.

2.3 Reactivity of the $[\{(N\delta H\varepsilon H)Cu^{II}\}_2(\mu\text{-}1,2\text{-}O_2^{2-})]^{2+}$ Complex

Cu_2O_2 (*trans*-μ-1,2-peroxo)Cu^{II}_2 species have been considered relatively inert in their reactivity toward external substrates. There are only a few reports that describe the aliphatic C-H activations of external substrates (e.g., toluene and ethylbenzene) effected by (μ-1,2-O_2^{2-})Cu^{II}_2 complexes.[24] **Cpd A** does not exhibit reactivity toward various substrates; O-H bond substrates (phenol derivatives), C-H bond substrates (BNAH, xanthene, ethylbenzene), strong reductants (cobaltocene), triphenylphosphine, thioanisole, or 2,2,6,6-tetramethylpiperidinol (TEMPO-H).

2.4 Protonation of *trans*-Peroxo Dicopper(II) Complex

To better understand the chemical behavior of the new copper-oxygen initial product, $[\{(N\delta H\varepsilon H)Cu^{II}\}_2(\mu\text{-}1,2\text{-}O_2^{2-})]^{2+}$ (**Cpd A**), it was protonated using strong acid. The addition of 0.1 ~ 0.5 equivalent of perchloric acid or trifluoroacetic acid to **Cpd A** at

–100 °C led to the clean conversion to a new bright green species displaying a sharp absorption band at 334 nm (2000 M^{-1} cm^{-1}). When 0.5 ~ 1 equivalent of acid was added, the new peak decayed, and the similar behavior was observed from the protonation of synthetic cupric superoxo complex.[26] At this time, we cannot be sure about the nature of the 334 nm product as it does not match up will with other Cu_2O_2 type complexes, nor are the spectral properties similar to known hydroperoxo [(ligand)Cu^{II}-OOH]$^+$ complexes; also, see below.

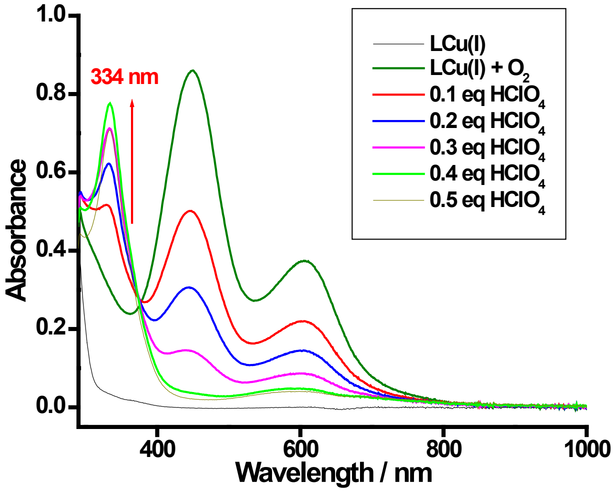

Figure 6. Low-temperature UV-vis absorption spectra for the protonation of $[\{(N\delta H\varepsilon H)Cu^{II}\}_2(\mu\text{-}1,2\text{-}O_2^{2-})]^{2+}$ (**Cpd A**) by perchloric acid, $HClO_4$ in THF at –100 °C.

2.5 Generation of Mononuclear Cupric Hydroperoxide Species

As copper(II)-hydroperoxo complexes are of interest as possible enzyme active intermediates capable of substrate oxidative behavior, a green colored species, which is presumed to possess a $[(N\delta H\varepsilon H)Cu^{II}(OOH)]^+$ formulation in THF at –80 °C, was generated by addition of 1.5 ~ 10 equiv H_2O_2 to the solution of $[(N\delta H\varepsilon H)Cu^{I}]^+$ (**Figure 6a**); this follows another recently reported procedure to generate Cu^{II}-OOH species.[23] The mononuclear cupric hydroperoxo complex is presently characterized by its (i) UV-vis features, λ_{max} = 357 nm (ε = 2100 $M^{-1}cm^{-1}$), assignable to a $^{-}OOH \rightarrow Cu^{II}$ LMCT absorption based on the correspondence with a number of literature examples;[23, 27] a *d-d* transition band observed at 590 nm (ε = 250 $M^{-1}cm^{-1}$) (**Figure 6a**) and (ii) distinctive mononuclear type axial EPR spectrum, $g_{\parallel} = 2.28$, $g_{\perp} = 2.05$, $A_{\parallel}$ = 164G; 77 K (**Figure 6b**).

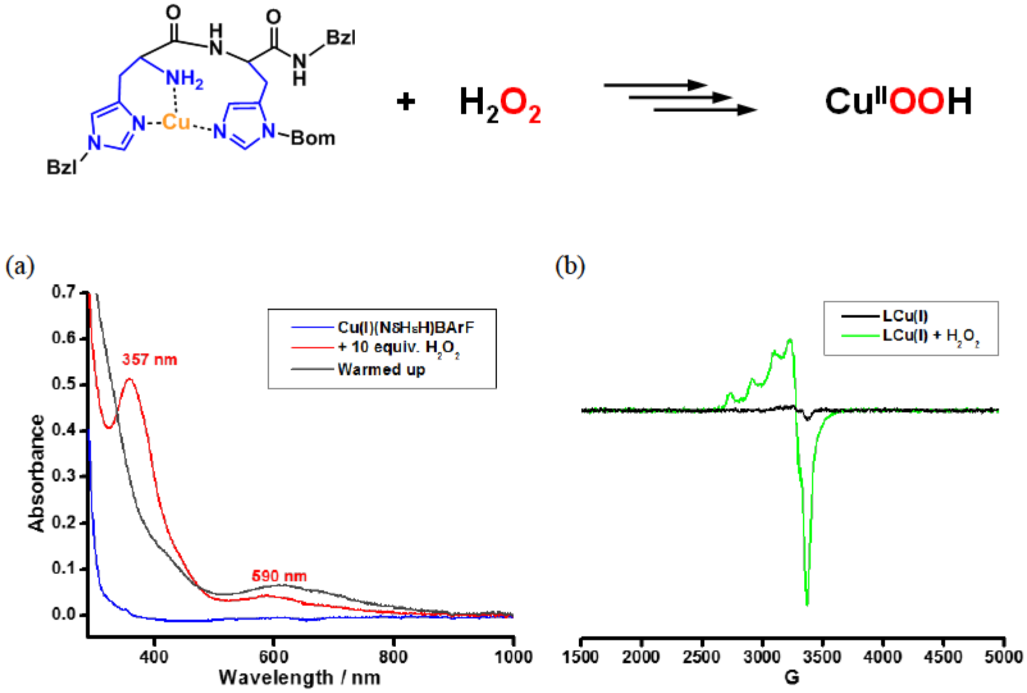

Figure 7. (a) Low-temperature UV-vis absorption spectra of 0.25 mM $[(N\delta H\varepsilon H)Cu^{II}(OOH)]^{+}$ in THF at - 80 °C and its warmed-up solution, and (b) EPR spectra of the $[(N\delta H\varepsilon H)Cu^{II}(OOH)]^{+}$ complex.

3. Cu^{I}/O_2 Chemistry of a (^{Trt}His)Cu(I) Complex

A modified histamine was used as a ligand to produce synthetic oxygen-derived Cu-complexes which may form at the copper centers of LPMO of pMMO. A εN_{Im} binding site of the histamine was blocked by a trityl ($-C(C_6H_5)_3$) group for copper ion coordinating to the

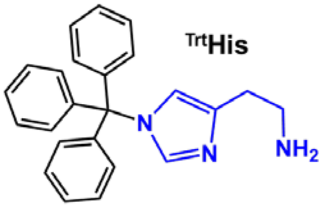

open site at the δN_{Im} position and for improving the solubility in organic solvents (See Supporting Information for the synthesis). The ligand ^{Trt}His was metallated with one equiv $[Cu^{I}(CH_3CN)_4]B(C_6F_5)_4$ and the resulting copper(I) complex isolated (but not yet fully characterized.

The isolated copper(I) complex of ^{Trt}His shows only a very slow reaction with only modest intensities observed when reacted with dioxygen at –135 °C in MeTHF (**Figure 7a** blue spectrum), forming a new species, presumed to be (bis-μ-oxo)Cu^{III}_2, featuring a 366 nm band with relatively low extinction coefficient ($\varepsilon = 3000\ M^{-1}cm^{-1}$; also see the observed spectral changes shown in **Figure S5**. Very recently, a similar behavior was described by Stack and co-worker[19] for the follow-up study of high-valent dicopper(III) bis(μ-oxide) compounds with primary-amine (1,3-diaminopropane) ligation (**Figure 3**). The addition of histamine led to ligand exchange indicating that the (bis-μ-oxo)Cu_2^{III} core coordinated by histamine is thermodynamically more stable. This species exhibits an absorption band at 363 nm ($\varepsilon = 2780\ M^{-1}cm^{-1}$) which is comparable to our results. The extinction coefficient

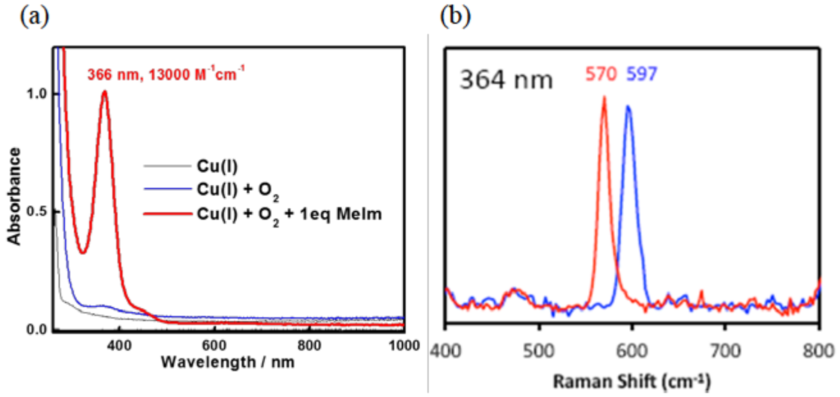

Figure 8. (a) Low-temperature UV-vis absorption spectra of the oxygenated products of $[(^{Trt}His)Cu^{I}]^+$ species with or without one equiv 1-methylimidazole in MeTHF at –135 °C and (b) resonance Raman spectra of the bis-μ-oxo dicopper(III) complex ($\lambda_{ex} = 364$ nm).

values are much lower than those for synthetic (bis-μ-oxo)Cu^{III}_2 complexes investigated previously.[28]

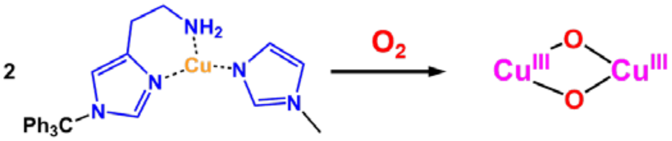

However, in the presence of one equivalent of 1-methylimidazole, the 366 nm absorption band increased greatly (ε = 13000 $M^{-1}cm^{-1}$). The species was identified by rR spectroscopic experiments displaying a Cu-O vibration observed at 597 cm^{-1} which is shifted to 570 cm^{-1} upon isotopic substitution by using $^{18}O_{2(g)}$ (**Figure 7b**) The energy and isotope shifts of the vibrations confirm the assignment of the species as a dicopper(III) (bis-μ-oxo) complex. Both parameters from UV-vis and rR spectroscopic data well fit those for many synthetic (bis-μ-oxo)Cu^{III}_2 complexes possessing tridentate ligands for copper, as previously reported.[28] In addition, the extinction coefficient is consistent with many (bis-μ-oxo)Cu^{III}_2 species known. From the results, we hypothesize that His-braced reduced copper ion may need additional imidazole ligation in order to be fully oxygenated by molecular oxygen, as occurs in the copper active site of LPMOs (see Figure 2).

4. Conclusion and Future Directions

To elucidate the function and properties of 'His-brace' moiety which exists in LPMOs and pMMOs, a dipeptide and histamine ligands that mimic the His-braced copper centers were synthesized, copper(I) complexes generated and preliminary oxygenation chemistry tested. Oxygen-derived species are identified as trans-peroxo dicopper(II) and bis-μ-oxo dicopper(III) complexes, respectively. These results combined with more detailed future studies, are hoped to provide insights into the reason that the unique 'His-brace' chelation is in particular selected by nature.

5. References

1. Prigge, S. T.; Kolhekar, A. S.; Eipper, B. A.; Mains, R. E.; Amzel, L. M., *Science* **1997,** *278* (5341), 1300-1305; Chen, P.; Solomon, E. I., *Proc. Natl. Acad. Sci. USA* **2004,** *101* (36), 13105-13110.

2. Lieberman, R. L.; Rosenzweig, A. C., *Nature* **2005,** *434* (7030), 177-182.

3. Culpepper, M. A.; Rosenzweig, A. C., *Crit. Rev. Biochem. Mol. Biol.* **2012,** *47* (6), 483-492.

4. Himes, R.; Barnese, K.; Karlin, K., *Angew. Chem. Intl. Ed.* **2010,** *49* (38), 6714-6716.

5. Himes, R. A.; Karlin, K. D., *Curr. Opin. Chem. Biol.* **2009,** *13* (1), 119-131.

6. Culpepper, M. A.; Cutsail Iii, G. E.; Gunderson, W. A.; Hoffman, B. M.; Rosenzweig, A. C., *J. Am. Chem. Soc.* **2014,** *136* (33), 11767-11775.

7. Himes, R. A.; Karlin, K. D., *Curr. Opin. Chem. Biol.* **2009,** *13* (1), 119-131.

8. Vaaje-Kolstad, G.; Westereng, B.; Horn, S. J.; Liu, Z.; Zhai, H.; Sørlie, M.; Eijsink, V. G. H., *Science* **2010,** *330* (6001), 219-222; Beeson, W. T.; Phillips, C. M.; Cate, J. H. D.; Marletta, M. A., *J. Am. Chem. Soc.* **2011,** *134* (2), 890-892.

9. Hemsworth, G. R.; Henrissat, B.; Davies, G. J.; Walton, P. H., *Nat Chem Biol* **2014,** *10* (2), 122-126; Gudmundsson, M.; Kim, S.; Wu, M.; Ishida, T.; Momeni, M. H.; Vaaje-Kolstad, G.; Lundberg, D.; Royant, A.; Ståhlberg, J.; Eijsink, V. G. H.; Beckham, G. T.; Sandgren, M., *J. Biol. Chem.* **2014,** *289* (27), 18782-18792.

10. Li, X.; Beeson Iv, William T.; Phillips, Christopher M.; Marletta, Michael A.; Cate, Jamie H. D., *Structure* **2012,** *20* (6), 1051-1061.

11. Kjaergaard, C. H.; Qayyum, M. F.; Wong, S. D.; Xu, F.; Hemsworth, G. R.; Walton, D. J.; Young, N. A.; Davies, G. J.; Walton, P. H.; Johansen, K. S.; Hodgson, K. O.; Hedman, B.; Solomon, E. I., *Proc. Natl. Acad. Sci.* **2014**, 8797–8802.

12. Quinlan, R. J.; Sweeney, M. D.; Lo Leggio, L.; Otten, H.; Poulsen, J.-C. N.; Johansen, K. S.; Krogh, K. B. R. M.; Jørgensen, C. I.; Tovborg, M.; Anthonsen, A.; Tryfona, T.; Walter, C. P.; Dupree, P.; Xu, F.; Davies, G. J.; Walton, P. H., *Proc. Natl. Acad. Sci.* **2011,** *108* (37), 15079-15084.

13. Zhang, L.; Koay, M.; Maher, M. J.; Xiao, Z.; Wedd, A. G., *J. Am. Chem. Soc.* **2006,** *128* (17), 5834-5850.

14. Karlin, S.; Zhu, Z.-Y.; Karlin, K. D., *Proc. Natl. Acad. Sci.* **1997,** *94* (26), 14225-14230; Karlin, K. D.; Zhu, Z.-Y.; Karlin, S., *J. Biol. Inorg. Chem.* **1998,** *3* (2), 172-187.

15. Himes, R. A.; Park, G. Y.; Barry, A. N.; Blackburn, N. J.; Karlin, K. D., *J. Am Chem. Soc.* **2007,** *129* (17), 5352-5353.

16. Park, G. Y.; Lee, J. Y.; Himes, R. A.; Thomas, G. S.; Blackburn, N. J.; Karlin, K. D., *J. Am Chem. Soc.* **2014,** *136* (36), 12532-12535.

17. Timari, S.; Kallay, C.; Osz, K.; Sovago, I.; Varnagy, K., *Dalton Trans.* **2009,** (11), 1962-1971.

18. Citek, C.; Lin, B.-L.; Phelps, T. E.; Wasinger, E. C.; Stack, T. D. P., *J. Am. Chem. Soc.* **2014,** *136* (41), 14405-14408.

19. Citek, C.; Gary, J. B.; Wasinger, E. C.; Stack, T. D. P., *J. Am. Chem. Soc.* **2015,** *137* (22), 6991-6994.

20. Chan, S. I.; Yu, S. S.-F., *Acc. Chem. Res.* **2008,** *41* (8), 969-979; Himes, R. A.; Karlin, K. D., *Proc. Natl Acad. Sci. USA* **2009,** *106* (45), 18877-18878.

21. Shiota, Y.; Yoshizawa, K., *Inorg, Chem.* **2009,** *48* (3), 838-845.

22. Shiota, Y.; Juhász, G.; Yoshizawa, K., *Inorg. Chem.* **2013,** *52* (14), 7907-7917.

23. Kim, S.; Saracini, C.; Siegler, M. A.; Drichko, N.; Karlin, K. D., *Inorg. Chem.* **2012,** *51* (23), 12603-12605.

24. Lucas, H. R.; Li, L.; Sarjeant, A. A. N.; Vance, M. A.; Solomon, E. I.; Karlin, K. D., *J. Am. Chem. Soc.* **2009,** *131* (9), 3230-3245; Würtele, C.; Sander, O.; Lutz, V.; Waitz, T.; Tuczek, F.; Schindler, S., *J. Am. Chem. Soc.* **2009,** *131* (22), 7544-7545.

25. Thompson, J. S.; Calabrese, J. C., *Inorg. Chem.* **1985,** *24* (20), 3167-3171.

26. Peterson, R. L.; Ginsbach, J. W.; Cowley, R. E.; Qayyum, M. F.; Himes, R. A.; Siegler, M. A.; Moore, C. D.; Hedman, B.; Hodgson, K. O.; Fukuzumi, S.; Solomon, E. I.; Karlin, K. D., *J. Am. Chem. Soc.* **2013,** *135* (44), 16454-16467.

27. Wada, A.; Harata, M.; Hasegawa, K.; Jitsukawa, K.; Masuda, H.; Mukai, M.; Kitagawa, T.; Einaga, H., *Angew. Chem. Int. Ed.* **1998,** *37*, 798-799; Yamaguchi, S.; Wada, A.; Nagatomo, S.; Kitagawa, T.; Jitsukawa, K.; Masuda, H., *Chem. Lett.* **2004,** *33* (12), 1556-1557; Mizuno, M.; Honda, K.; Cho, J.; Furutachi, H.; Tosha, T.; Matsumoto, T.; Fujinami, S.; Kitagawa, T.; Suzuki, M., *Angew. Chem. Intl. Ed.* **2006,** *45* (41), 6911-6914; Maiti, D.; Narducci Sarjeant, A. A.; Karlin, K. D., *J. Am. Chem. Soc.* **2007,** *129* (21), 6720-6721; Yamaguchi, S.; Nagatomo, S.; Kitagawa, T.; Funahashi, Y.; Ozawa, T.; Jitsukawa, K.; Masuda, H., *Inorg. Chem.* **2003,** *42* (22), 6968-6970; Yamaguchi, S.; Masuda, H., *Sci. Technol. Adv. Mat.* **2005,** *6* (1), 34-47; Fujii, T.; Naito, A.; Yamaguchi, S.; Wada, A.;

Funahashi, Y.; Jitsukawa, K.; Nagatomo, S.; Kitagawa, T.; Masuda, H., *Chem. Comm.* **2003,** (21), 2700-2701.

28. Que, J. L.; Tolman, W. B., *Angew. Chem. Int. Ed.* **2002,** *41* (7), 1114-1137; Itoh, S.; Nakao, H.; Berreau, L. M.; Kondo, T.; Komatsu, M.; Fukuzumi, S., *J. Am. Chem. Soc.* **1998,** *120*, 2890-2899; Shearer, J.; Zhang, C. X.; Zakharov, L. N.; Rheingold, A. L.; Karlin, K. D., *J. Am. Chem. Soc.* **2005,** *127* (15), 5469-5483; Maiti, D.; Woertink, J. S.; Narducci Sarjeant, A. A.; Solomon, E. I.; Karlin, K. D., *Inorg. Chem.* **2008,** *47* (9), 3787-3800; Mahapatra, S.; Halfen, J. A.; Wilkinson, E. C.; Pan, G.; Wang, X.; Young, J., V. G.; Cramer, C. J.; Que, J., L.; Tolman, W. B., *J. Am. Chem. Soc.* **1996,** *118*, 11555-11574; Liang, H.-C.; Zhang, C. X.; Henson, M. J.; Sommer, R. D.; Hatwell, K. R.; Kaderli, S.; Zuberbuehler, A. D.; Rheingold, A. L.; Solomon, E. I.; Karlin, K. D., *J. Am Chem. Soc.* **2002,** *124* (16), 4170-4171.

6. Supporting Information

6.1 Materials and Methods

6.1.1 General

All materials used were commercially available analytical grade from Advanced ChemTech, Novabiochem, Cambridge Isotopes and Sigma-Aldrich. Acetone, methanol, ethanol were distilled under an inert atmosphere over $CaSO_4$ and degassed under argon prior to use. Methylene chloride and diethyl ether were used after being passed through a 60 cm long column of activated alumina (Innovative Technologies) under argon. Dimethylformamide (DMF, HPLC grade) was used from freshly opened bottles without further purification. Inhibitor free tetrahydrofuran (THF) and 2-methyltetrahydrofuran (MeTHF) were purchased from Sigma-Aldrich and distilled under argon from sodium/ benzophenone and degassed with argon prior to use. Pentane was freshly distilled from calcium hydride under an inert atmosphere and degassed prior to use. $[Cu^I(CH_3CN)_4]B(C_6F_5)_4$ was synthesized according to literature protocols.[1] Ligands were stored in freezers (–32 °C) in vials wrapped with Teflon tape prior to use. Preparation and handling of air-sensitive materials were carried out under an argon atmosphere by using standard Schlenk techniques, within a MBraun Labmaster 130 inertatmosphere drybox filled with prepurified N_2 (Airgas).

6.1.2 Instrumentation

Bench-top low temperature UV–visible experiments were carried out on a Cary Bio-50 spectrophotometer equipped with a liquid nitrogen chilled Unisoku USP-203-A cryostat using a 1 cm modified Schlenk cuvette. NMR spectroscopy was performed on

Bruker 300 and 400 MHz instruments with spectra calibrated to either internal tetramethylsilane (TMS) standard or to a residual protio solvent. EPR measurements were performed on an X-Band Bruker EMX CW EPR controlled with a Bruker ER 041 XG microwave bridge operating at the X-band (~9 GHz) in 5 mm quartz EPR tubes. ESI-Mass spectra were acquired using a Finnigan LCQDeca ion-trap mass spectrometer equipped with an electrospray ionization source (Thermo Finnigan, San Jose, CA). For resonance Raman (rR) measurements, a 0.5 ~ 1 mM stock solution of copper(I) complexes was prepared in the solvent. A 500 μL aliquot of this copper(I) solution was added to the 5 mm NMR sample tube, capped with a septum, and chilled in a cooling bath. Oxygenation of the copper samples was achieved by slowly bubbling an excess of dioxygen through the solution using a Hamilton gas-tight syringe equipped with a three-way valve and needle outlet. Dioxygen, $^{16}O_2$ (Airgas OX UHP-300) or $^{18}O_2$ (Icon 6393), was added to an evacuated Schlenk flask fitted with a septum for the oxygenation reactions described above. Resonance Raman spectroscopic studies were carried out at Stanford University, in collaboration with the group of Professor E. I. Solomon in the Chemistry department. Spectra were collected on a triple monochromator (Spex 1877 CP with 1200, 1800, and 2400 grooves/mm holographic spectrograph gratings) with a back-illuminated CCD (Princeton Instruments ST-135). Samples were placed in a liquid nitrogen finger dewar (Wilmad) in a ~135° backscattering configuration and excitation was provided by a krypton ion laser (Coherent I90C-K) or Ti:sapphire laser (M Squared SolsTiS). Data were collected for 5 min at 20 mW of power (**2^S)** or 100 mW power (**2^P**) and samples were hand to minimize photodamage. Peak positions were determined from fitting the experimental data with Gaussian transitions using Peakfit Version 4.

6.2 Ligand Synthesis

6.2.1 NεHis (**Scheme S1**)[2]

Boc-His(Bom)-OH (3.00 g, 8.1 mmol) was dissolved in DMF (25 ml) and 1 equiv of 2-(1*H*-benzotriazol-1-yl)-1,1,3,3-tetramethyluronium hexafluorophosphate (HBTU), 1 equiv of 1-hydroxybenzotriazole (HOBt), and 2 equiv of diisopropylethylamine (DIPEA) were added under $Ar_{(g)}$. After 10 min, benzyl amine (0.80 g, 7.3 mmol) was added and the reaction stirred under $Ar_{(g)}$ at room temperature. After 16 hrs, the reaction mixture was evaporated under reduced pressure, dissolved in CH_2Cl_2 (40 ml), washed with saturated $Na_2CO_{3(aq)}$ three times, saturated $NaCl_{(aq)}$ once, dried ($MgSO_4$) and finally evaporated under reduced pressure. A white solid product was dissolved in 20 ml of 50% trifluoroacetic acid (TFA)-CH_2Cl_2 and stirred at room temperature. After 4 hrs, the mixture was made basic condition (pH 8) with saturated $NaHCO_{3(aq)}$. The organic phase was washed with saturated $NaCl_{(aq)}$ and dried with $MgSO_4$ and evaporated under reduced pressure. The residue was purified by silica gel column chromatography (eluent: CH_2Cl_2:MeOH = 10:1, $R_f = 0.5$) to give a white solid product (0.51 g, 64%). ^{1}H-NMR ($CDCl_3$) δ 7.65 (s, 1H), 7.49 (d, J = 10 Hz, 1H), 7.24 (m, 10H), 6.91 (d, J = 9.2 Hz, 1H), 5.27 (td, 2H, J = 10.2, 45.2 Hz), 4.47 (m, 4H), 3.65 (m, 1H), 3.27 (m, 1H), 2.88 (m, 1H), 1.52 (s, 1H); ^{13}C-NMR ($CDCl_3$) δ 173.484, 138.484, 138.181, 136.065, 128.593, 128.214, 128.022, 127.806, 127.611, 127.335, 73.158, 69.960, 54.285, 43.103, 29.256; ESI-MS $M+H^+$ $C_{21}H_{25}N_4O_2$ exp m/z: 365.24 (100%), 366.24 (24.8%), 357.24 (4.5%), calc m/z: 365.20 (100.0%), 366.20 (24.6%), 367.20 (3.2%).

Scheme S1. Synthesis of the NεH.

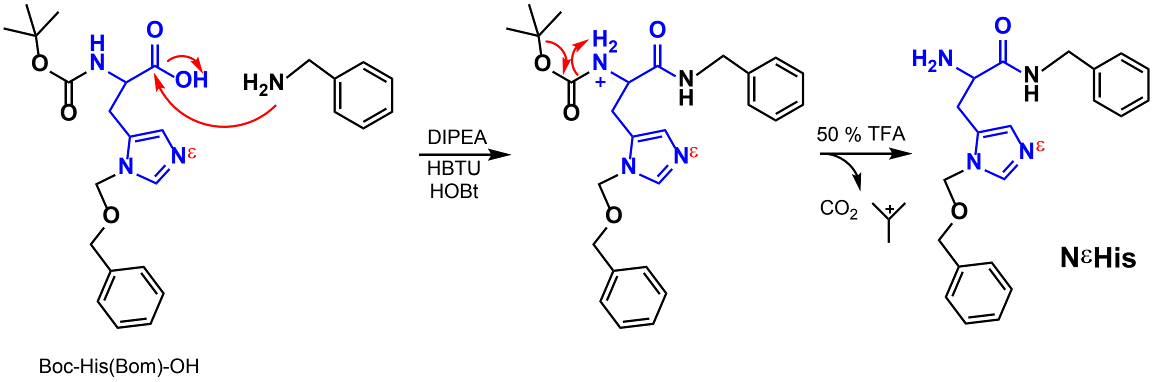

6.2.2 Ligand NδHεH (**Scheme S2**)

The NεHis (1.3 g, 3.1 mmol) was dissolved in DMF (35 ml) and 1.2 equiv of HBTU, 1.2 equiv of HOBt, 2 equiv of DIPEA, and Boc-His(Bzl)-OH (1.08 g, 3.13 mmol) were added and the reaction stirred under $Ar_{(g)}$ at room temperature. After 16 hrs, the reaction mixture was evaporated under reduced pressure, dissolved in CH_2Cl_2 (50 ml), washed with saturated $Na_2CO_{3(aq)}$ three times, saturated $NaCl_{(aq)}$ once, dried ($MgSO_4$) and finally the solvent was removed by evaporation under reduced pressure. The residue was purified by silica gel column chromatography (eluent: CH_2Cl_2:MeOH = 10:1, R_f = 0.55) to give a light yellow solid product (0.48 g, 70%). This was dissolved in 20 ml of 50% trifluoroacetic acid (TFA)-CH_2Cl_2 and stirred at room temperature. After 4 hrs, the mixture was adjusted to be under basic conditions (pH 9) using saturated a $NaOH_{(aq)}$ solution. The organic phase was washed with saturated $NaCl_{(aq)}$ and dried with $MgSO_4$ and evaporated under reduced pressure. The residue was purified by silica gel column chromatography (eluent: CH_2Cl_2:MeOH = 10:1, R_f = 0.37) to give a yellowish white solid product (1.39 g, 76%). ^{1}H-NMR (CD_2Cl_2) δ 7.77 (t, 1H), 7.65 (d, 1H), 7.36 (s, 1H), 7.29-7.03 (m, 16H), 6.69 (s, 1H), 6.59 (s, 1H), 5.24-5.15 (m, 2H), 4.55-4.54 (q, 1H), 4.36-4.34 (m, 2H), 4.31-

4.18 (m, 2H), 3.42 (br s, 4H), 3.07-3.05 (m, 2H) 2.82-2.67 (m, 4H); ESI-MS M+H$^+$ $C_{34}H_{37}N_7O_3$ exp m/z: 591.74 (100 %), 592.75 (31.7 %), 593.72 (3.2 %), calc m/z: 591.30 (100.0 %), 592.30 (36.8 %), 593.30 (3.9 %).

Scheme S2. Synthetic pathway to the ligand NδHεH.

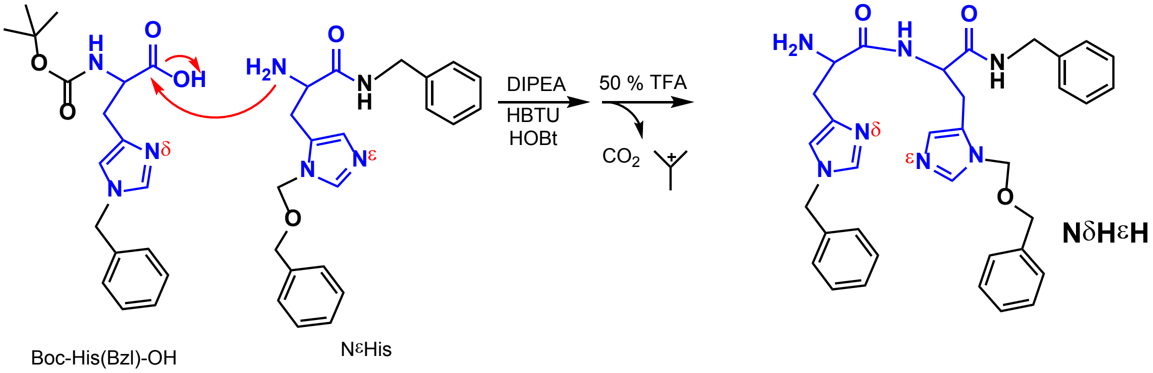

Boc-His(Bzl)-OH
NεHis
DIPEA
HBTU
HOBt
50 % TFA
CO2
NδHεH

6.2.3 The ligand triphenylmethylhistamine (**^{Trt}His**) synthesized as in the literature.[3]

His-Phth. ^{1}H NMR (DMSO): δ 11.9 (br s, 1H), 7.83 (s, 4H), 7.50 (s, 1H), 6.81 (s, 1H), 3.81-3.77 (t, 2H), 2.85-2.81 (t, 2H).

Scheme S3. Synthetic pathway to protect the primary amino group; the precursor His-Phth

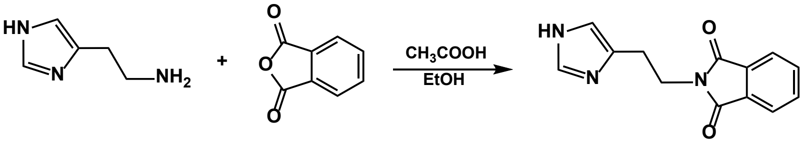

CH3COOH
EtOH

^{Trt}His-Phth ^{1}H NMR ($CDCl_3$): δ 7.83-7.81 (m, 2H), 7.72-7.70 (m, 2H), 7.35-7.34 (d, 1H), 7.31-7.26 (m, 9H), 7.10-7.07 (m, 6H), 6.55 (s, 1H), 4.01-3.97 (t, 2H), 2.99-2.95 (t, 2H).

Scheme S4. Synthetic pathway to block the εN$_{histamine}$ with trityl group

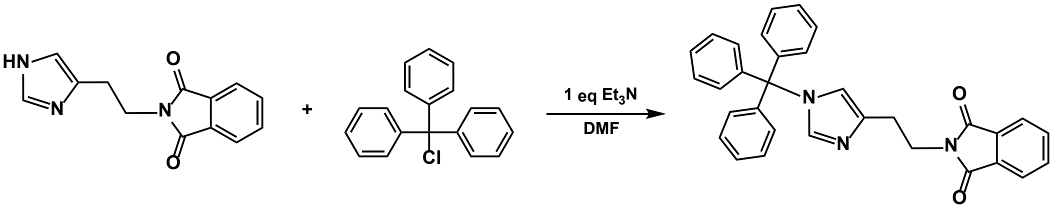

^{Trt}His (Triphenylmethylhistamine ^{1}H NMR ($CDCl_3$): δ 7.39 (s, 1H), 7.35-7.33 (t, 9H), 7.18-7.14 (m, 6H), 6.61 (s, 1H), 3.00-2.97 (t, 2H), 2.70-2.67 (t, 2H), 1.48 (br s, 2H).

Scheme S5. Deprotection of the phthalimide moiety affording the ^{Trt}His ligand

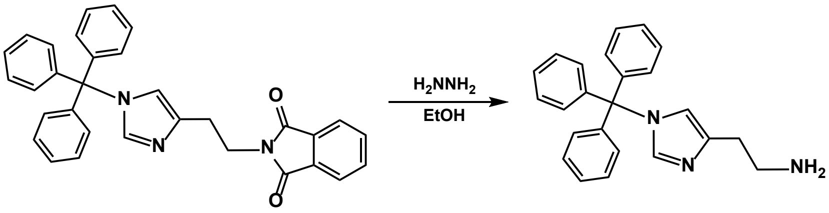

6.3 Synthesis of Copper(I) Complexes

[Cu^I(NδHεH)]B(C_6F_5)$_4$. [Cu^I(CH_3CN)$_4$]B(C_6F_5)$_4$ (0.453 g, 0.5 mmol) and NδHεH (0.3 g, 0.51 mmol) are dissolved in THF (6 ml) in 100 ml Schlenk flask in a glove box. This mixture was stirred for 20 min then pentane (100 ml) was added to precipitate. The solid was decanted and washed two times with 50 ml of pentane. The Schlenk flask was sealed with rubber septum and taken out of the glove box. The rubber septum was sealed with copper wire and dried under vacuum yielding a white solid product. (Yield: 0.55 g, 83%). ESI-MS [Cu(NδHεH)]$^+$ $C_{34}H_{37}CuN_7O_3$ exp m/z: 654.29 (100.0 %), 656.48 (73.5 %), 655.39 (67.1 %), 657.74 (33.5%), calc m/z: 654.23 (100.0 %), 656.22 (52.9 %), 655.23

(39.9 %), 657.23 (19.0 %). Anal. Calcd. for $C_{58}H_{37}BCuF_{20}N_7O_3$: C, 52.21; H, 2.80; N, 7.35; Found: C, 52.45; H, 2.74; N, 6.73.

[Cu^I(^{Trt}His)]$B(C_6F_5)_4$. [Cu^I(CH_3CN)$_4$]$B(C_6F_5)_4$ (0.28 g, 0.31 mmol) and ^{Trt}His (0.1 g, 0.3 mmol) are dissolved in THF (5 ml) in 100 ml Schlenk flask in dry box. This mixture was stirred for 10 min then pentane (100 ml) was added to precipitate. The solid was decanted and washed two times with 50 ml of pentane. The Schlenk flask was sealed with rubber septum and taken out of the glove box. The rubber septum was sealed with copper wire and dried under vacuum yielding a white solid. (Yield: 0.22 g, 68 %). Characterization will be carried out.

6.4 Generation of Cpd A and Cpd B

In the glove box, 0.5 mM solution of [(NδHεH)Cu^I]$B(C_6F_5)_4$ was prepared in a 2.5 mL THF, and the 1 cm Schlenk cuvette was sealed with a rubber septum. Out of the glove box and at room temperature, the cuvette was secured with a copper wire. The cell was transferred to the pre-cooled cryostat and chilled at –135 ~ –90 °C with a minimum of 15 minutes allowed for equilibration prior to oxygenation. The dioxygen was gently bubbled through the solution using long needle for 10 seconds forming **Cpd A** or **Cpd B**.

6.5 EPR Experiments

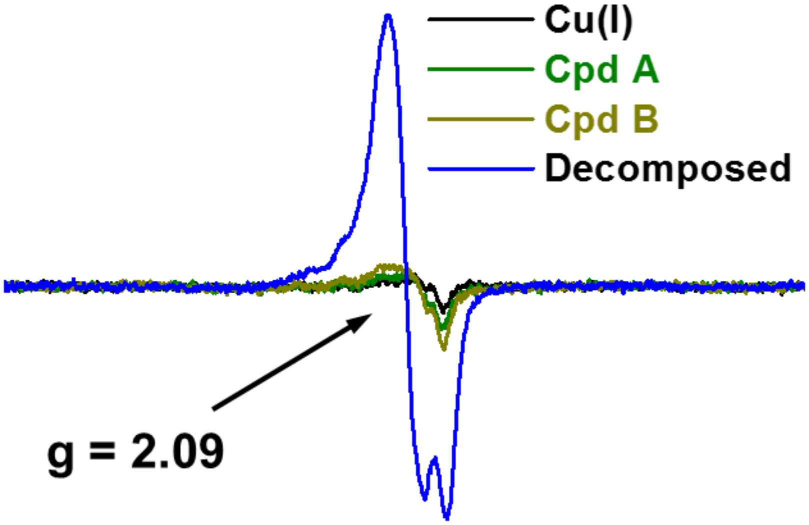

Figure S1. EPR spectra of [(NδHεH)Cu^{I}]B(C_6F_5)$_4$, Cpd A, Cpd B, and decomposed product in THF (2 mM).

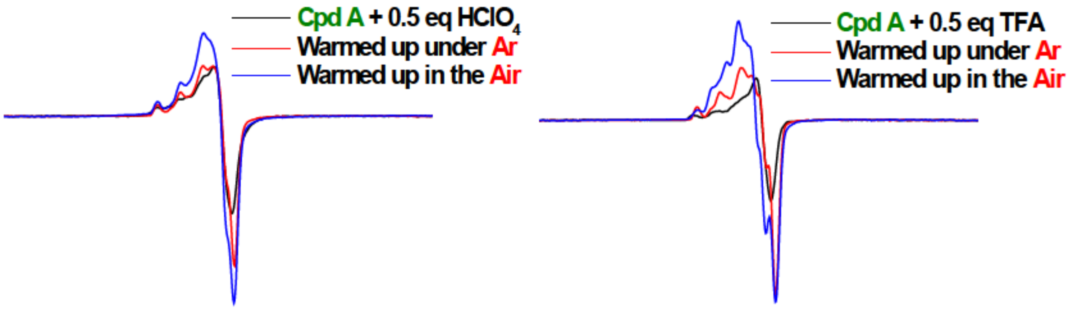

Figure S2. EPR spectra of protonation of **Cpd A** with half equivalent of (a) $HClO_4$; X-band (ν = 9.431 GHz) spectrometer in THF at 70 K: $g_{||}$ = 2.28, $A_{||}$ = 150 G, $g\perp$ = 2.05 and (b) trifluoroacetic acid (TFA); X-band (ν = 9.431 GHz) spectrometer in THF at 70 K: $g_{||}$ = 2.28, $A_{||}$ = 145 G, $g\perp$ = 2.06.

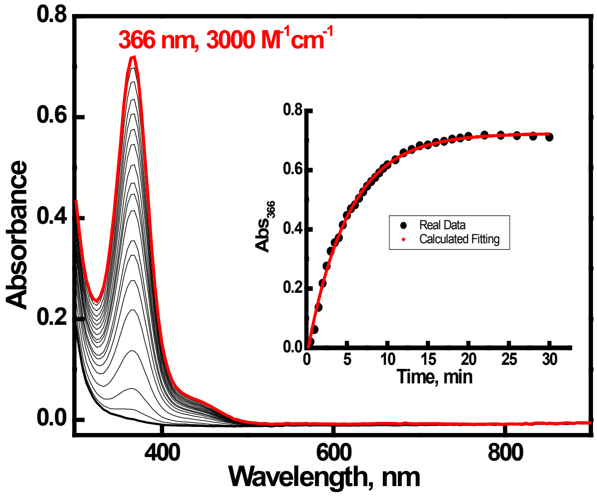

Figure S3. UV-vis spectra for oxygenation of $(^{\mathrm{Trt}}\mathrm{His})\mathrm{Cu}^{\mathrm{I}}$ in MeTHF solution at –135 °C without addition of 1-methylimidazole. (0.24 mM).

6.6 References

(1) Liang, H.-C.; Kim, E.; Incarvito, C. D.; Rheingold, A. L.; Karlin, K. D. *Inorg. Chem.* **2002**, *41*, 2209.

(2) Park, G. Y.; Lee, J. Y.; Himes, R. A.; Thomas, G. S.; Blackburn, N. J.; Karlin, K. D. *J. Am. Chem. Soc.*, **2014**, *136*, 12532.

(3) Lee, Y.; Park, G. Y.; Lucas, H. R.; Vajda, P. L.; Kamaraj, K.; Vance, M. A.; Milligan, A. E.; Woertink, J. S.; Siegler, M. A.; Narducci Sarjeant, A. A.; Zakharov, L. N.; Rheingold, A. L.; Solomon, E. I.; Karlin, K. D., *Inorg. Chem.* **2009,** *48* (23), 11297.

Curriculum Vitae

The Johns Hopkins University
Lee, Jung Yoon
July 21, 2015

EDUCATIONAL HISTORY

Ph.D. expected	2015	Department of Chemistry Mentor: Kenneth D. Karlin PhD	Johns Hopkins University, USA
M.A.	2012	Department of Chemistry Mentor: Kenneth D. Karlin PhD	Johns Hopkins University, USA
M.S.	2010	Chemistry and Nano Science Mentor: Wonwoo Nam PhD	Ewha Womans University, Seoul, Korea
B.S.	2008	Department of Chemistry Mentor: Wonwoo Nam PhD	Ewha Womans University, Seoul, Korea

PROFESSIONAL EXPERIENCE

Dissertation Research	September 2010 – July 2015	Laboratory of Kenneth D. Karlin Johns Hopkins University
Teaching Assistant	September 2010 – May 2012	Introductory Chemistry Johns Hopkins University
Research Internship	February 2010 – June 2010	Laboratory of Wonwoo Nam Ewha Womans University
Research Assistant	March 2009 – February 2010	Laboratory of Wonwoo Nam Ewha Womans University
Cooperative Research	2008 – 2009 (four weeks)	Laboratory of Takashi Ogura University of Hyogo, Japan
Cooperative Research	January 2008 (three weeks)	Laboratory of Shun Fukuzumi Osaka University, Osaka, Japan
Undergraduate Research	December 2007 – February 2008	Laboratory of Wonwoo Nam Ewha Womans University
Undergraduate Research	June 2007 – August 2007	Laboratory of Wonwoo Nam Ewha Womans University

ACEDEMIC HONORS

Drs. Eugene W. Zeltman and Susan C. Zeltman Fellowship	Summer 2015
Shepard Memorial Travel Fund for ACS Meeting	Spring 2015
Division of Inorganic Chemistry (DIC) of the ACS Travel Award	Spring 2015

PEER-REVIEWED PUBLICATION

J. Y. Lee, and K. D. Karlin*; "Elaboration of Copper-Oxygen Mediated C–H Activation Chemistry in Consideration of Future Fuel and Feedstock Generation"
Curr. Opin. Chem. Biol. **2015***, 25*, 184 (*Review Article)*

S. Kim, J. W. Ginsbach, **J. Y. Lee**, R. L. Peterson, J. Liu, M. A. Siegler, A. A. Sarjeant, E. I. Solomon*, and K. D. Karlin*; "Amine Oxidative N-Dealkylation via Cupric Hydroperoxide Cu–OOH Homolytic Cleavage Followed by Site-Specific Fenton Chemistry"
J. Am. Chem. Soc. **2015***, 137,* 2867 (*Article)*

S. Kim, **J. Y. Lee**, R. Cowley, J. W. Ginsbach, M. A. Siegler, E. I. Solomon,* and K. D. Karlin*; "A $N_3S_{(thioether)}$-Ligated Cu^{II}-Superoxo with Enhanced Reactivity"
J. Am. Chem. Soc. **2015***, 137,* 2796 (*Communication)*

J. Y. Lee, R. L. Peterson, K. Ohkubo, I. Garcia-Bosch, R. A. Himes, J. Woertink, C. D. Moore, E. I. Solomon*, S. Fukuzumi*, and K. D. Karlin*; "Mechanistic insights into the oxidation of substituted phenols *via* hydrogen atom abstraction by a cupric superoxo complex"
J. Am. Chem. Soc. **2014**, *136*, 9925 (*Article)*

G. Y. Park, **J. Y. Lee**, R. A. Himes, N. J., G. S. Thomas, Blackburn and K. D. Karlin*; "Copper-Peptide Complex Structure and Reactivity when Found in Conserved His-X_{aa}-His Sequences"
J. Am. Chem. Soc. **2014**, *136*, 12532 (*Communication)*

C. J. Rolle III, S. Kim, **J. Y. Lee,** K. D. Karlin*; "Highlights and Directions in Copper-Dioxygen Chemistry of Bioinorganic Relevance"
Bull. Jpn. Soc. Coord. Chem. **2013**, *62*, 40 (*Review Article)*

J. Cho, R. Sarangi, H. Y. Kang, **J. Y. Lee**, M. Kubo, T. Ogura, E. I. Solomon, W. Nam*; "Synthesis, structural, and spectroscopic characterization and reactivities of mononuclear cobalt(III)-peroxo complexes"
J. Am. Chem. Soc. **2010**, *132*, 16977 (*Article)*

C. Arunkumar, Y.-M. Lee, **J. Y. Lee**, S. Fukuzumi* and W. Nam*; "Hydrogen-atom abstraction reactions by manganese(V)- and manganese(IV)-oxo porphyrin complexes in aqueous solution"
Chem.–Eur. J. **2009**, *15*, 11482 (*Full Paper)*

J. Y. Lee, Y.-M. Lee, H. Kotani, W. Nam* and S. Fukuzumi*; "High-valent manganese(V)–oxo porphyrin complexes in hydride transfer reactions"
Chem. Commun. **2009**, 704 (*Communication)*

A.-R. Han, Y. J. Jeong, Y. Kang, **J. Y. Lee**, M. S. Seo and W. Nam*; "Direct evidence for an iron(IV)-oxo porphyrin π-cation radical as an active oxidant in catalytic oxygenation reactions"
Chem. Commun. **2008**, 1076 (*Communication)*

SCIENTIFIC PRESENTATIONS

J. Y. Lee et al.; "Evolution of Thioether S-Ligated Primary Cu^I/O_2 Adducts: The 1st Example of Cu^{II}-Superoxo Species with Enhanced Reactivity"
249th ACS Meeting in Denver **2015**

J. Y. Lee, R. L. Peterson, K. Ohkubo, I. Garcia-Bosch, E. I. Solomon, S. Fukuzumi, and K. D. Karlin; "Mechanistic Insights into the Oxidation/Oxygenation of Phenols *via* Rate-limiting Hydrogen Atom Transfer by a Cupric-Superoxo Complex"
33rd Summer Symposium in Molecular Biology at Penn State **2014**

J. Y. Lee et al.; "Copper-Oxidase Reactivity Mimetic Behavior: Oxidation/Oxygenation of Phenols by a Copper(II)-Superoxo Complex"
Gordon Research Seminar (*Data Blitz*) **2014**

J. Y. Lee, R. L. Peterson and K. D. Karlin; "Copper-Oxidase Reactivity Mimetic Behavior: Oxidation/Oxygenation of Phenols by a Copper(II)-Superoxo Complex"

Gordon Research Seminar (Poster) **2014**

J. Y. Lee, C. Arunkumar, Y.-M. Lee, S. Fukuzumi, W. Nam; "Reactivity of high-valent manganese-oxo porphyrin complexes under aqueous and organic System"

The 14th International Conference on Biological Inorganic Chemistry **2009**

J. Y. Lee, Y.-M. Lee, W. Nam, S. Fukuzumi; "Study of high-valent manganese(V)-oxo porphyrin complexes in the hydride transfer reactions"

The 3rd Korean Bioinorganic Chemistry Symposium **2009**

J. Y. Lee, Y.-M. Lee, S. Fukuzumi, W. Nam; "Mechanistic studies on the hydride transfer reactions of high-valent manganese(V)-oxo porphyrin intermediates"

The 4th Asian Biological Inorganic Chemistry Conference **2008**

CURRENT PROJECTS

"Primary Cu^{I}/O_2 Adduct with Tunable H-bond from Secondary Coordination Sphere Exhibiting Direct Evidence of H-Atom Transfer"

Manuscript in Preparation

"Lytic Polysaccharide Monooxygenases (LPMOs) Model Systems: 'His-Braced' Copper-peptide Complexes and Oxidative Chemistry"

Manuscript in Preparation

"An Investigation into a Stable Thioether-Ligated Cu^{II}-Superoxo Complex and Alcohol Effect"